# High Resolution Spectroscopy of Erbium Doped Solids

**Miloš Rančić**


**A thesis submitted for the degree of**
**Doctor of Philosophy at**
**The Australian National University**

**July 2018**

# Declaration

This thesis is an account of research undertaken between October 2011 and February 2018 at the Department of Laser Physics, Research School of Physical Sciences, The Australian National University, Canberra, Australia. Except where acknowledged in the customary manner, the material presented in this thesis is, to the best of my knowledge, original and has not been submitted in whole or part for a degree in any university.

Miloš Rančić

July 2018

# Acknowledgements

Firstly, I would like to thank my supervisor Dr Matthew Sellars for his insight and guidance during the past eight years. His dedication to research is unrivalled.

I would further like to acknowledge all the students, post-docs and prof's with whom I've shared an office, experiment or headache over that time. Grace, Kate, Sara, James, John, Rose, Michael, Prithvi, Matt, Matt, Adam, Charlotte, Marcus and Neil from LPC, Chunming, Gabe, Qi and Sven from UNSW, Olivier from my brief stint at DQS, and a shout-out to Sebastian and Mike at UC for their timely theoretical support in all matters erbium. Special thanks also goes to Morgan, for the many hours he spent proof-reading this thesis.

A PhD, however, is more than just time spent doing experiments and writing up results. It requires a supportive family that's given you the means and opportunity to aim for the stars, whether you realise it or not. Mum, you never doubted me for a second, and always pushed me to do better. Dad, you did the same in your own half-arsed way. I want to thank my sister for the time we spent together and lessons I learned. I want to thank my Aunt for having a welcoming home, no matter where she was, and David for being there at the hardest times.

Finally, I want thank my beautiful wife for sharing all of life's ups and downs over these past six years. It's gone by like a flash, so hopefully we'll fit everything in over the next sixty.

As required, I acknowledge the Australian Government for their financial support

# Abstract

This thesis investigates the potential of Er:YSO and Er:Si for quantum communication and computation applications. Erbium uniquely possess optical transitions in the 1.5 $\mu$m region, making it suitable for both fibre telecommunication and silicon photonics.

The properties of the $I_{15/2} \leftrightarrow I_{13/2}$ optical transition in Er:YSO have already been extensively studied. Over two decades ago, improvements in $Er^{3+}$ dephasing time at 1.5 $\mu$m were achieved by applying a 5T field along the D1 axis. More recently, a record 4.4 ms coherence time on the same optical transition was achieved using a 7T field.

These investigations, among others, illustrate that large Er electron spins become thermally polarised with sufficient magnetic field. However, no long lived and coherent spin transitions associated with the Er ions had previously been identified, and such transitions are necessary for on-demand quantum state storage.

To address this requirement, the optical and hyperfine transition properties of $^{167}$Er:YSO were investigated in large magnetic fields. In a field of 7T, spectral hole lifetimes of 1 minute and hyperfine population lifetimes of 12 minutes were observed. These measurements illustrate the effect of spin-lattice relaxation in this system, and how it can be mitigated.

Efficient spin-polarisation of the entire $^{167}$Er hyperfine ensemble is also demonstrated. This is the first such demonstration in rare earth systems, and a key requirement for broadband optical storage. Moreover, a 1.3 second coherence time was recorded for an $^{167}$Er:YSO hyperfine transition at 7T and 1.4 K. This is an improvement of several orders-of-magnitude over previous coherence measurements on spin-transitions in Er doped solids. This is also sufficient for maximal entanglement rates in quantum repeater networks that span distances of 1000 km or greater.

With an optical transition at 1.5 $\mu$m, Er is also an ideal candidate to connect silicon based quantum computers to the future quantum Internet. In particular, single Er:Si ions could be used to develop an optical-spin bus between P:Si qubits and fibre based quantum networks.

Presented here is the first spectroscopic investigation of single Er:Si ions. This required a novel opto-electronic approach to single ion detection, where the Er ions are implanted into a nanometre scale fin-shaped Field Effect Transistor. With this approach it was

possible to develop high resolution optical spectra, where both the electronic and hyperfine levels of individual Er ions were resolved.

Long optical and spin coherence times are also important requirements for an optical-spin bus. To address the first requirement, an investigation of the optical lineshape was undertaken. Here it was determined that sources of Stark noise external to the transistor channel contribute a significant amount to optical homogeneous linewidth. However, the dominant noise contribution was determined to be short-range (from within the 30 nm wide channel) and the total homogeneous linewidth was measured to be 50 MHz.

The site structure of an individual Er:Si ion was then analysed, using magnetic field rotation patterns and optical transitions between multiple crystal field levels. This site was determined to have approximately axial ($C_3$) symmetry. The purpose of this study was to determine a magnetic field regime in which the Er electrons spin can be polarised, which is necessary for realising of long hyperfine lifetimes and coherence times.

# Contents

# List of publications

1. C. Yin, M. Rancic, G. de Boo, N. Stavrius, J.C. McCallum, M. J. Sellars and S. Rogge, Optical addressing of an individual erbium ion in silicon, *Nature, 417. 91-94, (2013)*

2. M. Rancic, M. P. Hedges, R. L. Ahlefeldt and M. J. Sellars, Coherence time of over a second in a telecom-compatible quantum memory storage material, *Nature Physics, 14, 50–54, (2018)*

3. M. Rancic, J. Stuart, M. P. Hedges, and M. J. Sellars. Inexpensive fibre-optic frequency reference for high resolution optical spectroscopy. *Manuscript in preparation*

4. B-B Xu, A. C. Bedoya, M. Rancic, C. Yin, G. de Boo, B. Morrison, B. Johnson, J. C. McCallum, B. J. Eggleton, M. J. Sellars and S. Rogge, High-Q phosphorus doped optical cavity for qubit devices, *Manuscript in preparation*

5. Q. Zhang, C. Yin, G. Hu, G. de Boo, M. Rancic, B. C. Johnson, J. C. McCallum, J. Du, M. J. Sellars and S. Rogge, Single rare-earth ions as atomic-scale probes in ultra-scaled transistors, *Manuscript in preparation*

Chapter 1

# Introduction

There has been extensive interest in using rare earth optical centres for quantum communication and quantum computing applications. This thesis focuses on the potential of using cryogenically cooled erbium doped materials for these applications. Among the rare earths, Er uniquely possess optical transitions in the 1550 nm region. This wavelength lies within the transparency window of both silicon and silica fibres, so Er is ideally suited for linking quantum computers over the future quantum Internet.

Before going into further detail I will briefly outline the history, motivation and concept of quantum computation. Following this will be a discussion of the state-of-the-art in silicon based quantum computing, the platform of interest for this thesis. Finally, the chapter concludes with a description of fibre-based quantum communication, and the potential for Er to satisfy a crucial role in quantum repeater technology.

## 1.1 A brief history of quantum computing

Even with the myriad of applications for which we utilise digital computers, there exist many kinds of problems they deal with poorly. The reason boils down to computational efficiency. In simplest terms, efficiency is a measure of how long a computer will need to solve a problem as you increase the problem size. Increasing the problem size may be a matter of simply increasing the resolution or parameter space, but it can also mean adding extra dimensions or calculation steps. This increase will inevitably require extra resources in terms of power, time or memory. An algorithm is deemed efficient if the increase in resources required can be bounded by some finite polynomial which is a function of problem size. In all other cases, the computation is deemed inefficient.

In fact, there exist technologies which purposefully exploit computational inefficiency. The typical example is Rivest-Shamir-Adleman (RSA) encryption. Developed in 1977, this encryption method is based on the sharing of 'public keys' over an open network [1].

These public keys are simply the product of two large primes, which form the unknown 'private keys' equivalent to a password. Although forming a public key from a private key is a straight-forward multiplication, the reverse process of deciphering the private key with just the public key is inefficient. Even though many mathematicians and computer scientists have worked on this problem, there is currently no known algorithm for a digital computer to find prime factors of a large number in polynomial time.

For this reason, RSA encryption protocols are ubiquitous in our daily lives. When we check our email, log onto Facebook, or electronically transfer money, RSA encryption is often keeping our information secure. Moreover, as the decades pass and processing power steps inexorably forwards, simply adding a few more bits to the size of the encryption keys is all that is needed to maintain the same level of security. This made RSA encryption elegant and future-proof, or so it seemed. Attempting to solve this apparently intractable problem turned out to be a key driver of research into quantum computation. Almost 20 years after the invention of RSA, a solution was found. In 1994, a researcher at Bell Labs named Peter Shor developed an efficient algorithm to crack RSA encryption, but it had to run on a quantum computer [2].

Although Shor's discovery could be considered a pivotal moment in the field, the birth of quantum computation dates back to the early 1980's. In 1982 notable physicist Richard Feynman pointed out that a computer based on the laws of quantum mechanics should outperform a digital simulation of a quantum system [3]. Then, in 1985, computer scientist David Deutsch postulated the notion of a universal quantum computer that can simulate any physical system, or another computer [4]. While digital computers then functioned (and still do) on a collection of two state systems called bits, quantum computers were designed for two-state quantum systems called quantum-bits, or qubits for short.

A fundamental advantage of quantum computers over their digital counterparts is their potential for massive parallelism. An N-qubit quantum computer represents a $2^N$ dimensional space, and can execute potentially $2^N$ simultaneous operations. A digital processor can only perform linear calculations, regardless of the physical system on which its implemented. Thus, the amount of digital processing power required to simulate an N-qubit system grows exponentially with N.

With the advent of Shor's algorithm, organisations relying on data security were suddenly presented with potential 'quantum' attacks on their privacy. Ironically though, quantum mechanics saved the day again with the promise of fundamentally secure net-

works and crypto-keys. Shor's factoring algorithm spurred research into Quantum Key Distribution (QKD) and quantum repeater systems, which are described in Section 1.3 below.

Fortunately QKD has made great commercial strides in the last decade, while quantum computers have not [5, 6]. Tapping into the resources of quantum computing has proven a much greater challenge. Today, more than 30 years since conception, the best demonstration of a quantum computer has a mere 14 qubits [7]. A 14 qubit computer is very limited in it's capabilities; to find the prime factors of the number 15, Shor's algorithm requires at least 21 qubits [8]. The reason for this seemingly slow progress is due to the complexity of a truly universal quantum computer. Such a device must conform to a strict set of requirements, known as the Di-Vicenzo criteria [9]:

1. *The system must have well defined qubits, and be scalable.*
2. *There must be a way of initialising the system to a well-known state*
3. *The coherence time must be much longer than the gate operation time*
4. *A universal set of logic gates must exist*
5. *There must be a way to read out a single qubit*

Since Di-Vicenzo stated his original 5 criteria, two more have been added in order to integrate quantum computers into quantum communication networks [10]:

6. *There must be a way of converting between stationary and flying qubits*
7. *There must be a way of transmitting flying qubits between locations*

These last two requirements could be addressed by an Er based optical interface, and this forms one of the foci of this thesis. Erbium has an unpaired electron which makes it predisposed to strong interactions with nearby qubit-ions. If these interactions can be controlled, then Er can act as a interface or 'bus' between stationary qubits and flying qubits, potentially addressing the $6^{\text{th}}$ Di-Vicenzo criterion. This is especially true in materials such as silicon, where absorption of 1550 nm photons is very low, and this will be explored in greater detail at the end of this section. Moreover, fibre optic repeater networks could then transmit these flying qubits between distant quantum computers, fulfilling the $7^{\text{th}}$ criterion. The next subsection will present an overview of recent milestones towards quantum computers in silicon and explain the future role of Er in this architecture.

## 1.2 Quantum computing in Silicon

A wide variety of physical systems have been suggested as a platform for quantum computation, with Di-Vicenzo's criteria in mind. Notable systems currently under investigation include individually trapped ions, quantum dots, linear optics and superconducting circuits [7, 9, 11, 12]. The focus of this thesis, however, is on Er impurity dopants in silicon (Er:Si). In particular, I investigate whether such a platform can satisfy the $6^{\text{th}}$ and $7^{\text{th}}$ Di-Vicenzo criteria.

Silicon is an excellent scaffold for dopant based quantum computing, and many researchers call it a solid-state vacuum. This is because extremely pure Si crystals can be manufactured free of the nuclear spins that cause quantum noise. Indeed, phosphorus dopants in Si have shown great promise as computing spin-qubits, and many of the Di-Vicenzo criteria have already been met with this platform. Although Er:Si could be developed as a platform for quantum computation itself, it can also be used in hybrid systems such as a phosphorus-erbium architecture.

To this end, a concept for a phosphorus-erbium based device is presented at the conclusion of this section. This device would aim to demonstrate the $6^{\text{th}}$ and $7^{\text{th}}$ Di-Vicenzo criteria. The next few paragraphs, however, outline key demonstrations of Di-Vicenzo's criteria already achieved with P:Si. The timeline of these demonstrations is shown in Figure 1.1, and most have been achieved in parallel (and literally next door) to the Er:Si work within the Centre for Quantum Computation and Communication ($\text{CQC}_2\text{T}$) at the University of New South Wales (UNSW).

This outline begins with the first spectroscopy of individual P:Si dopants. In it's most common configuration, phosphorus has an unpaired electron and neutron $\left({}^{31}\text{P}\right)$. In 2010 Morello et al. were the first to resolve the electronic-spin states of P:Si in a field of 1.5T [13]. This demonstration realised the $5^{\text{th}}$ Di-Vicenzo criterion, and was achieved by placing the phosphorus atom inside a Single Electron Transistor (SET). These transistors are nanometre scale Fin-shaped Field-Effect Transistors (FinFETs), and are sensitive to electrostatic perturbations induced by changes in the electron-spin state (see Section 3.4). SET technology has since become an integral component of single-impurity systems in Si, including the Er:Si experiments presented in this thesis.

Following the initial work of Morello et al, in 2012 the precision placement of individual phosphorus dopants was demonstrated [14]. Rather than using ion beam implantation, a single phosphorus dopant was controllably placed in the silicon lattice with $\sim$0.5 nm

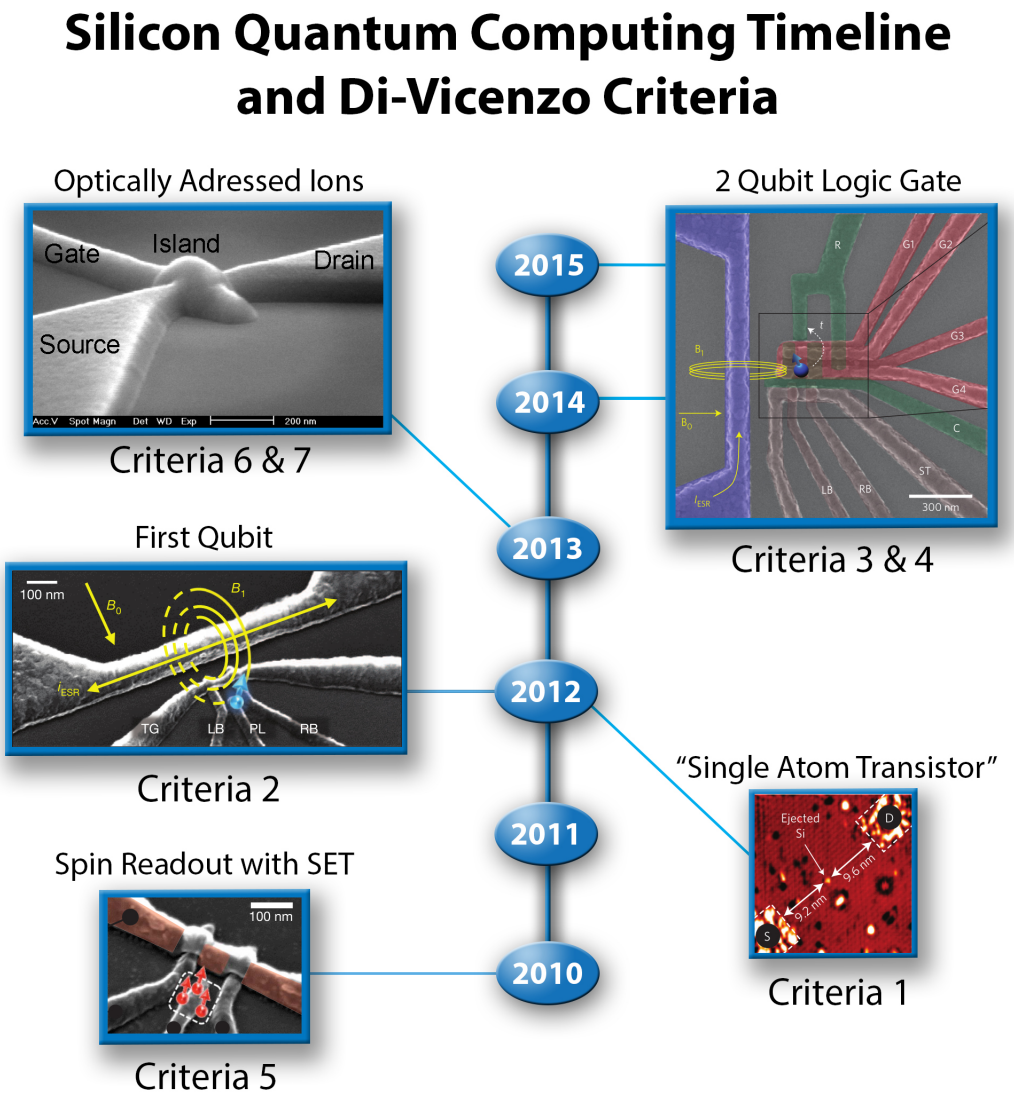


**Figure 1.1:** Timeline of the Si devices developed by $CQC_2T$, at the University of New South Wales (UNSW), Sydney. The devices were lithographically etched on a Si/SiO substrate using standard industry techniques, for the most part. With the exception of the 'Single Atom Transistor', the Er and P dopants were implanted by ion beam. Only the FinFET device on the top right contains Er ions, all other devices are P based and the location of the individual dopants are shown by small pointed balls. Yellow rings indicate microwave fields generated by metallic strip-lines.

accuracy using a scanning-tunnelling microscope tip. Dubbed the world's first single-atom transistor, it was a major step towards realising the 1$^{st}$ Di-Vicenzo criterion.

The next step was to demonstrate control over the P spins. This was achieved by adding microwave strip-lines to the P:Si devices. In a magnetic field of 1.5T, microwave pulses were used to manipulate the electron-spin state of a single phosphorus dopant [15]. This achievement realised the 2$^{nd}$ Di-Vicenzo criterion, and for the first time a phosphorus dopant could truly be called a qubit.

In 2014 the researchers at CQC$_2$T began incorporating isotopically enriched $^{28}$Si into their devices. Natural abundance Si contains 5% nuclear spin-$1/2$ $^{29}$Si. This isotope is the primary source of decoherence for any P qubits in a refined crystal: measurements of bulk P:Si enriched with 99.995% $^{28}$Si demonstrated a coherence time of 3 hours for a hyperfine transition of $^{31}$P [16]. By utilising this isotopically enriched material in devices with single P dopants, Muhonen et al. achieved electronic and hyperfine coherence times of 500 ms and 35 seconds, respectively [17].

Although these coherence times were shorter than those measured in bulk P:Si, they were the longest observed for any single dopant in solid state. Moreover, the limitation came from external equipment, rather than sources intrinsic to the device. In particular, the problem was caused by thermal fluctuations in the microwave field and instabilities in the static magnetic field. While both noise sources could be reduced further, these coherence times were already six orders-of-magnitude longer than the gate operation times, satisfying the 3$^{\text{rd}}$ Di-Vicenzo criterion.

The last relevant demonstration, by Veldhorst et al, was a two-qubit Controlled-Not (CNOT) gate [18]. This gate flips the spin state of the second qubit, conditional on the state of the first. The truth table for this logic-gate is presented in Table 1.1. CNOT gates are very useful for quantum computation because they are universal; any arbitrary computation can be performed by combining CNOT gates. However, the qubits used to accomplish the CNOT gate were not P dopants. Instead they were 'quantum dots', which are electrons trapped inside arrays of electrodes. The electrodes are very similar to those that form the basis of the SET devices, because they generate steep potentials in a small volume.

Although the nature of the potential well differs between quantum dots and phosphorus dopants, the techniques used to demonstrate CNOT gates were identical. Strong magnetic fields were used to define the energy levels of the electron-spin, using the Zeeman effect [19]. Microwave pulses were then used to initialise and manipulate these spin-qubits. This was an important step towards achieving the 4$^{\text{th}}$ (and only remaining) Di-Vicenzo criterion for the P:Si architecture.

An important aspect of these demonstrations was their use of Complimentary Metal on Insulator (CMOS) manufacturing. Adapting the industrial CMOS process solves many of the issues regarding the economies-of-scale for quantum computers. Even with this advantage, however, key issues remain for the P:Si architecture. One of the most pressing

| **Input** | | **Output** | |
|---|---|---|---|
| Control Qubit | Target Qubit | Control Qubit | Target Qubit |
| $\|\downarrow\rangle$ | $\|\downarrow\rangle$ | $\|\downarrow\rangle$ | $\|\downarrow\rangle$ |
| $\|\downarrow\rangle$ | $\|\uparrow\rangle$ | $\|\downarrow\rangle$ | $\|\uparrow\rangle$ |
| $\|\uparrow\rangle$ | $\|\downarrow\rangle$ | $\|\uparrow\rangle$ | $\|\uparrow\rangle$ |
| $\|\uparrow\rangle$ | $\|\uparrow\rangle$ | $\|\uparrow\rangle$ | $\|\downarrow\rangle$ |

**Table 1.1:** The logic table for a CNOT quantum gate. The spin states of the ions $|\uparrow\rangle$ and $|\downarrow\rangle$ are equivalent to logical 1's and 0's respectively.

issues is that of 'spin-transport'. The basic operations of a quantum computer rely on qubits interacting coherently over the entire length of the chip, which could be $\mu$m-cm. Unfortunately the interaction qubits in the P:Si architecture are highly localised electrons, with a radius of only ten nanometres.

Spin-transport represents an interesting and important area of research, and although no solution has yet been demonstrated, there has been significant progress in this area [20–22]. The aim of thesis, however, is to help solve the problem of transporting qubits over much greater distances. As mentioned at the start of this section, Er dopants in Si show great promise as candidates to satisfy the $6^{\text{th}}$ and $7^{\text{th}}$ Di-Vicenzo criteria. To this end, the following section outlines the direction in which this Er:Si research is headed.

### 1.2.1 The role of erbium in quantum computing

The previous section illustrated a collective effort towards a P:Si computing architecture, based on Di-Vicenzo's original 5 criteria. This thesis, however, is focused on extending this P:Si architecture to encompass all 7 criteria by using Er:Si. Silicon is transparent to 1550 nm light in much the same way as optical fibres. With a band-gap of around 1.1 eV (1100 nm), photons don't have enough energy at this wavelength to excite electrons from valence band. In comparison, phosphorus has a more energetic optical transition at 1078 nm which has considerably higher absorption. Because of this, the optically excited state of P:Si is weakly bound and isn't suitable for quantum information processing [23].

The first result achieved towards Er:Si integration was in 2013 [24]. Using a similar device to that of the P:Si experiment in 2010 (see Figure 1.1), our research group demonstrated the laser-induced detection of single Er spins. This detection was achieved by resonantly exciting the optical transition of individual Er ions. Most of the energy used to excite these optical transitions ends up in the transistor channel. This energy can mobilise charges, which are detected by the SET. Thus, laser-induced optical excitation of Er

generates a clear electrical signal. Chapter 5 outlines the recent progress and results of these Er implanted SET devices. The remainder of this section describes a long-term goal of this research programme.

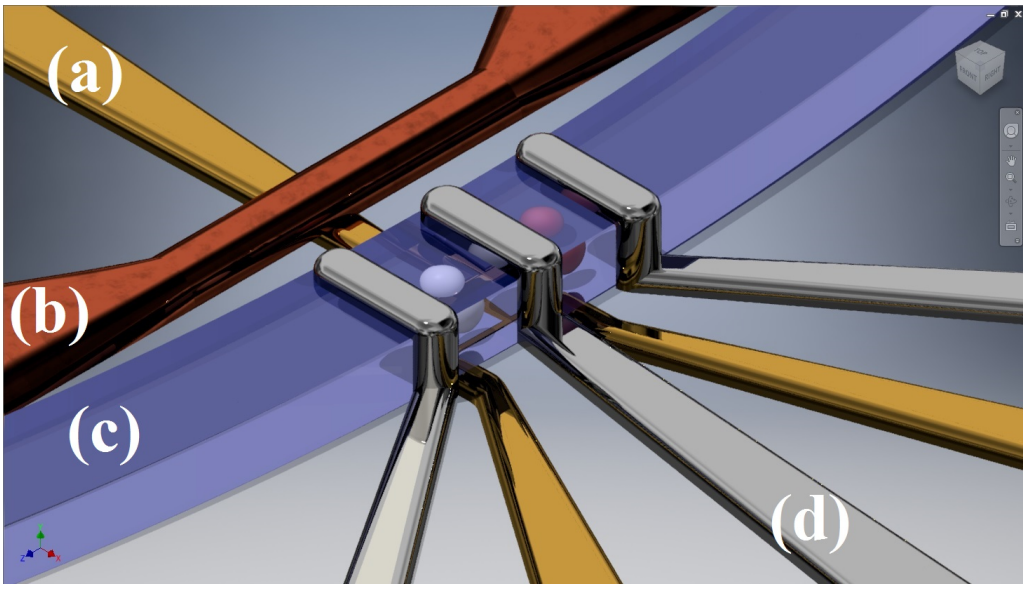


**Figure 1.2:** The concept for an optical bus based on an Er **(pink sphere)** and P **(white sphere)** quantum logic gate. **(a)** The gold coloured electrodes form an SET, which is buried under the device to ensure close proximity to the ions. **(b)** A conductive strip-line drives the microwave frequency transitions of either ion. **(c)** An isotopically enriched $^{28}$Si optical ring resonator strongly couples the Er ion to the telecom optical mode. **(d)** Stark shifting electrodes are used to rapidly tune the Er and P transition energies.

This goal relies on two key results demonstrated in this thesis [24]. Firstly, an SET can determine the precise optical and spin transition energies of an Er ion. Secondly, narrow-band lasers can drive those optical transitions. These results pave the way for a coherent P:Si optical interface. To illustrate this point, consider a pair of magnetically coupled Er and P ions. These ions can form a two-qubit CNOT gate, similar to the quantum dot system demonstrated in 2015 [18]. Here the Er acts as the control qubit, with logical qubit states $|\downarrow\rangle$ and $|\uparrow\rangle$ representing the optical levels of the ion. The state of the Er qubit can be manipulated by photons. Such photons can originate from an Er qubit in the same silicon chip ( a mere $\mu$m away) or from a quantum computer 1000 km away, connected though optical fibre. A conceptual device for realising both these scenarios is illustrated in Figure 1.2. This device is a type of Er-P 'optical-spin bus' and goes a long way towards demonstrating the 6$^{\text{th}}$ and 7$^{\text{th}}$ Di-Vicenzo criteria.

For such a device to function correctly, the Er ion must absorb single photons with great efficiency. For this reason the Er ions are placed in an optical resonator, which

significantly enhances the Er-photon coupling strength. Furthermore, good functionality of the CNOT gate relies on tunability of the Er-P and Er-photon interactions. This can be achieved by placing electrodes around the P and Er ions, and using the Stark effect to bring these ions into and out-of resonance [25].

The performance of this optical-bus will also depend on the coherence properties of the Er ions, and coherence times sufficiently long for this application have been demonstrated in Er:YSO [26]. However, similar results have not been achieved with Er:Si. Thus, demonstrating long coherence times is one of the major outstanding challenges for realising an Er:Si based quantum device. To realise this goal, an obvious approach would involve techniques that have proven successful for Er:YSO. This involves the use of large magnetic fields, and will be discussed shortly in the second part of the Introduction.

This approach also relies on accurate knowledge of the Er energy structure. Unfortunately, this information is not available for the single Er ions in Si investigated here. This is primarily due to Er forming complexes with other dopants in the Si crystal, such as oxygen and boron. While the structure of pure Er:Si is known, many of the Er complexes in Si remain undetermined [27, 28].

This issue is compounded further by the specific manufacturing process used for the devices studied here. For these devices, the dopants are added to the Si by ion implantation. This is a standard technique, and is usually followed by a high-temperature 'annealing' process. Annealing repairs damage to the Si crystal caused by implantation, but also destroys the SET. For this reason only low-temperature annealing is used on these devices. This leads to large variations in structure from one ion to the next, due to the disordered implantation process. To address this issue, detailed spectroscopic studies of each Er ion must be undertaken. These studies help determine the local structure around each ion, and are a major part of the Er:Si research undertaken in Chapter 5.

By understanding the local structure or 'crystal-field' of these single Er ions, one can predict the magnetic-field dependence of their energy levels. As was mentioned previously, long coherence times have been achieved in Er:YSO using large magnetic-fields, which is the reason for this analysis. Replicating these results also brings us to the second focal point of this thesis: demonstrating long hyperfine coherence times in Er:YSO. Achieving this result in Er:YSO would fulfil a key requirement for long-distance quantum communication. The remainder of the Introduction discusses this requirement and several others, in the context of telecommunication technology.

## 1.3 Erbium and the quantum Internet

Over the past two decades humanity has become interconnected to an extent never seen before, by an invention called simply 'the Internet'. In essence, the Internet allows people to transmit information over vast distances with incredible ease. This ability has made it a powerhouse of social and economic development: Internet related commerce accounted for 21 per cent of GDP growth in mature economies between 2006-2011 [29]. This digital revolution of the 21$^{\text{st}}$ century has now spurred billion dollar investments in quantum technologies, aimed at unlocking similar economic potential [30]. Along with quantum computing, the future 'quantum Internet' will play a major role in this technological platform [31, 32].

Indeed, several hundred million dollars have recently been invested in technologies to distribute quantum information over vast distances [33, 34]. Most recently, a satellite launched by the Chinese Academy of Science (CAS) managed to established a quantum link across 1200 km [35]. While this represents an order-of-magnitude improvement over previous records, a satellite based quantum network has several key limitations [36]. Photon qubits can only be transmitted during night, and only between two location with line-of-sight to the satellite. This limits the entanglement range to about 4000 km.

Thus, it is far more likely the future quantum Internet will mimic the established digital Internet. This consists of cheap[1], robust[2], and future-proof fibre optic interconnects [37,38]. For this reason CAS has also invested in a quantum fibre network, to operate in tandem with their satellite network. Connecting Beijing and Shanghai over a distance of 2000 km, this fibre network relies on both quantum and digital interconnects.

Historically, fibre networks have also relied on erbium. Almost 40 years ago it was discovered that fused silica fibres have a window of minimum loss in the 1550 nm wavelength region, at around 0.2 dB/km [39]. In the 1980's the telecom industry began exploiting this property for long distance optical networks, and now erbium doped solids are lighting up literally millions of kilometres of fibre optic cable around the globe [40]. When you type something into google and hit enter, your question will pass through at least a handful of Erbium Doped Fibre Amplifiers (EDFAs) as it travels across the oceans. These amplifiers transform your whisper into a shout, many times over [41, 42].

While Er has demonstrated its usefulness for digital transmission, it's still an open

[1] SMF-28 telecom fibre costs approximately \$10/km when purchased in commercial quantities.

[2] Photons do not experience electromagnetic interference or cross-talk. Optic fibres can be used in high voltage or strongly magnetic environments and degrade more slowly than copper cabling

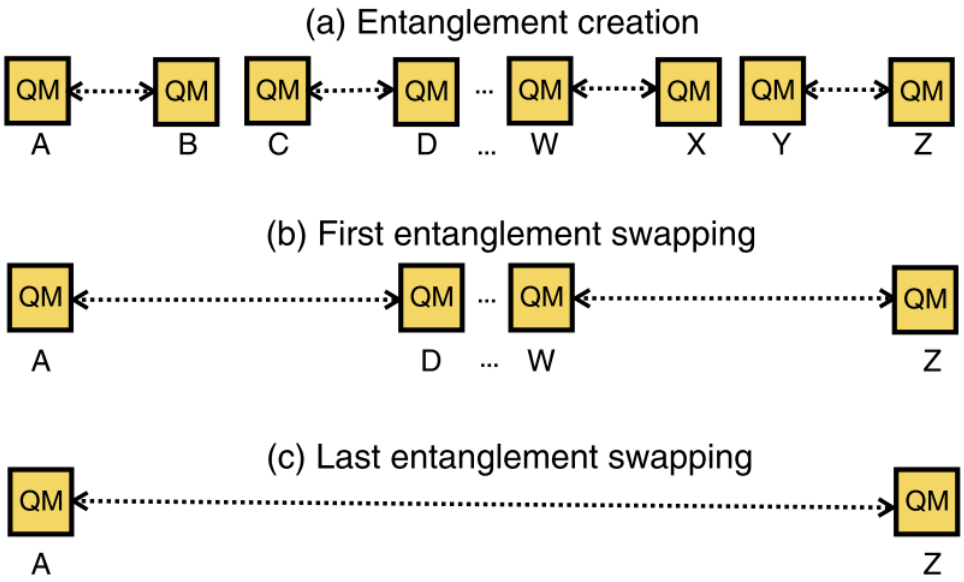


**Figure 1.3:** The process of generating quantum entanglement across a repeater network by using entanglement 'swapping'. **(a)** Entanglement is first created independently over short links between repeater nodes with quantum memories, labelled **QM**. **(b)** Entanglement is then swapped between neighbouring links such that the locations A and D, ... , W and Z share entanglement. **(c)** Swapping operations are performed successively until entanglement is established between A and Z. Figure reproduced from Ref [44]

question whether it might be useful for quantum networks. To help answer this question, this thesis investigates the properties of erbium in Yttrium Orthosilicate (YSO), for quantum repeater applications.

### 1.3.1 Quantum repeaters

A quantum repeater can be considered a device, architecture, or protocol whose purpose is to establish quantum correlations over large distances [43]. The transmission of quantum information is achieved via entanglement: a strong quantum correlation between two distant qubits. Individual repeater 'nodes' form the basic elements of long-distance quantum networks. In most repeater implementations the data is transmitted by entanglement-swapping amongst nodes (see Figure 1.3).

Other than transmitting data between quantum computers, an advantage of quantum networks is the provable security of information [45]. As was mentioned in the previous section, entangled pairs of photons can be exploited for cryptography. These photon qubits can be used for Quantum Key Distribution (QKD) between large institutions such as banks or government agencies, where security is paramount. An example of a commercial point-

to-point QKD system is shown in Figure 1.4, where entanglement is not strictly required.

Without repeaters, however, the loss in fibre limits the range of QKD to approximately 100 km. The Chinese Academy of Science side-stepped this problem by using 'trusted' nodes between these short fibre links. These nodes convert quantum correlations to classical data. Although this might be sufficient for cryptography, end-to-end network entanglement is required to connect distant quantum computers. If the trusted nodes in the CAS network could be replaced with true repeater nodes, the value and functionality of their network would increase dramatically.

The first step towards realising a quantum repeater is the development of a quantum memory. This is because repeater nodes act as data buffers, storing quantum information while entanglement is being established end-to-end. For cryogenically cooled memories, repeaters are best implemented using the 'second generation' approach [46]. With this approach a memory must satisfy several important requirements:

1. *Compatibility with the low-loss telecom bands at 1310/1550 nm.*

2. *A storage time longer than the network transmission time. For a global network, this should be at least 100 ms.*

3. *Efficient, low-noise storage and retrieval of flying qubits.*

4. *Broadband absorption and multimode capacity, to achieve high data transmission rates.*

With these requirements in mind, the rare earths (elements 57 to 71 on the periodic table) have demonstrated several important memory characteristics [47–50]. No single system, however, has simultaneously addressed all the requirements of a repeater memory. The remainder of this chapter explores the progress made towards these requirements, and highlights the potential of Er to satisfy them all.

### 1.3.2 Telecommunication networks

To date, none of the memories which satisfy criteria 2-4 operate directly in a telecom band. Because of this limitation, several strategies for achieving telecom compatibility have been proposed. The first is wavelength-conversion, where light at the memory wavelength is converted to a low-loss telecom wavelength [51–55]. The second technique is slightly more nuanced. A quirk of quantum mechanics allows for data to be stored, in the form of

entangled photons, even though these photons haven't travelled a great distance. Instead, the photons stored in the memories just need to be *entangled* with photons that travelled a great distance. This raised the idea of producing entangled photons at two different wavelengths: one at the memory wavelength and the other at telecom. This concept is illustrated in Figure 1.5, where memories and photon-sources are combined to mitigate transmission loss at visible wavelengths.


**Figure 1.4:** The commercial Cerberis QKD system sold by IDQ in Geneva, Switzerland. Two such rack mounted units are able to generate and share 1 cryptographic key per minute, via a telecom fibre link, up to a distance of 100 km.

While these techniques may one day prove commercially viable, they are relatively complicated and current implementations greatly impede memory performance. The highest efficiency demonstrated for wavelength conversion was 94% but no measurement of conversion fidelity was performed [56]. Moreover, non-degenerate photons have only been stored in memories with low efficiencies or short coherence times [49,57,58]. For this reason, developing Er based memories has been very appealing. With fibre losses as low as 0.15 dB/km at 1550 nm, repeater stations for an Er based network could be spaced 100 km apart and still be loss tolerant [59, 60]. Moreover, a system operating at a single wavelength enables integration of photon sources and memories using techniques such as Rephased Amplified Spontaneous Emission (RASE) [61].

An Er based approach can also take full advantage of existing 1550 nm technology. At this wavelength there's a wide variety of cheap, robust and integrated optical components. These include lasers, amplifiers, high frequency optical modulators and switches, as well as passive fibre components such as dense spectral filters, couplers, circulators, cavities and mirrors. As telecom infrastructure grows and develops, this repertoire continues to expand at a respectable rate.

Finally, the large size of 1550 nm optical modes also helps reduce absorption from

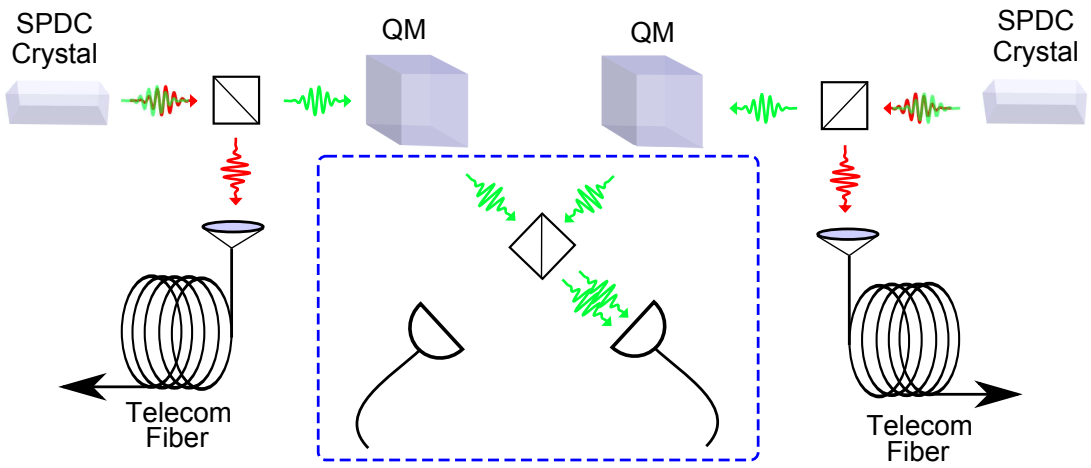


**Figure 1.5:** A quantum repeater node that utilises non-degenerate Spontaneous Parametric Down Conversion (SPDC). Pairs of entangled photons are generated at telecom wavelength **(red)** and visible wavelength **(green)**. The telecom photons are transmitted down optic fibres to be entangled at the neighbouring nodes. The visible photons are stored locally in the memories. **Blue inset:** Once entanglement has been established with the neighbouring nodes (via the telecom photons) the memories release their stored photons simultaneously. By sending these photons through a beamsplitter, one performs a projective measurement. This indirectly entangles the photons sent to neighbouring nodes on the left and right, and is one approach to the entanglement-swapping procedure outlined in Figure 1.3

optical surface roughness. This is an important consideration for commercial solid-state repeater implementations. In particular, integrated waveguide architectures offer a scalable approach for 'memory-on-a-chip' implementations [62, 63]. While such waveguides exhibit losses of several dB/cm at visible wavelengths, 0.1 dB/cm has been demonstrated at 1550 nm [64].

### 1.3.3 The state-of-the-art for Er based memories

From the information presented so far, it should be clear that an Er based quantum memory is a highly desirable thing. Yet there has not been an Er memory demonstration which achieved the storage time or efficiency required for repeater applications (see Section 6.1). This shortcoming has not been from lack of effort though. There have been several attempts to develop practical Er memories over the past decade, and here I will detail the best results so far.

In 2010, Lauritzen et al. attempted an Er memory using the Gradient Echo Memory (GEM) technique, but achieved a storage efficiency of only 0.25% with a 600 ns storage time [65]. In comparison, an similar experiment with praseodymium achieved 69% efficiency for a storage time of 1.3 $\mu s$ [47]. With a different approach called the Revival of a Silenced

Echo (ROSE), Dajczgewand et al. demonstrated a much higher efficiency of 40% [66]. However, the coherence time with ROSE is limited to 4.4 ms and achieving efficiencies much greater than 40% will be difficult. Moreover, neither of these attempts achieved quantum state storage.

There has only been one demonstration of quantum storage in an Er doped material. This was achieved by Saglamyurek et al. in 2015, where they used an Atomic Frequency Comb (AFC) delay line to demonstrate a very high storage fidelity of 97%. However, their efficiency and storage time was limited to 1% and 50 ns respectively, because of the glass fibres they used [50].

In all of these demonstrations low efficiency was a major issue. The problem has arisen because the Er ensembles cannot be prepared for photon storage. This preparation step is usually achieved with a technique called spectral holeburning (see Section 3.1.1). Here a laser is used to make sharp absorption features for capturing light, by exciting unwanted ions into unused spin-states. Due to the magnetic interactions between Er ions, however, these features only last for about 100 ms. In these demonstrations it took a similar amount of time to move the ions with the laser, so holeburning in Er could be likened to filling a bucket full of holes.

The majority of attempts at an Er based memory have also shown that the dense ensembles of Er electron spins have an adverse effect on quantum state storage. The electron spin dynamics cause large magnetic interactions in the crystal, which in turn shorten transition lifetimes and coherence times. One way to mitigate this problem is to polarise, or 'freeze', the electron spins. Once these spins are frozen, however, they can no longer be manipulated to store quantum information.

With the electron spins frozen, one must consider alternative energy transitions for storing quantum information. One such candidate is the nuclear spin of $^{167}$Er, and this forms the focus of this thesis. There have already been several demonstration of Er electron spin polarisation using large magnetic fields [26, 67, 68], but the hyperfine transition properties of $^{167}$Er have not been investigated in this regime. These transitions are adversely affected by the fluctuating electron-spins in zero field; coherence times and transition lifetimes were measured to be only $O(1\,\mu\text{s})$ and $O(100\,\text{ms})$ respectively [69].

This thesis investigates whether the electronic spin dynamics still dominate in the high field regime. If this is indeed the case, one might observe a significant improvement in hyperfine coherence times and lifetimes. It remains an outstanding question, however, as

hyperfine transitions are also susceptible to other dynamics. In particular, the effect of both nuclear spin cross-relaxation and lattice coupling might dominate in large fields. These processes are detailed in Section 2.4, and while they are less perturbative than electron spin fluctuations, their effects on hyperfine transitions are not attenuated by magnetic fields. Thus, a large portion of Chapter 4 is dedicated to quantifying their effect on hyperfine transitions in the high field regime.

### 1.3.4 Broadband quantum memories

The final requirement for a practical memory is a rapid rate of photon storage. The data rate is limited by the absorption bandwidth of the memory, due to the Fourier relationship between frequency and time. Moreover, the common approach for generating entangled photon pairs will typically produce photons with GHz - THz bandwidths [70].

To address these issues, there have been several demonstrations of large bandwidth storage in rare earth systems [49, 57]. In demonstrations where GHz bandwidth photons were stored, highly disordered materials were utilised. In particular, Er doped glass has delayed 6 GHz photons at telecom wavelengths by using a two-level AFC [50]. The two-level AFC is advantageous in these disordered materials becauseit can use the entire absorption bandwidth of the memory, if an appropriate ancillary level is used for spectral shaping. One side-effect of this technique is that storage times are determined before the photons are captured. Hence, the two-level AFC is a type of delay-line rather than an on-demand memory. Furthermore, the large static disorder in glass leads to dynamic disorder in the form of Two Level Systems (TLS). These two level systems perturb the rare earth ions, leading to short coherence times in these materials. Thus, the longest coherence time observed in Er doped fibre is 50 ns.

Conversely, materials that have demonstrated large storage efficiencies and long coherence times have only stored MHz bandwidth photons [47, 71, 72]. Such bandwidths would limit single-channel data rates to kbits/s. To achieve broadband storage in these materials, the missing ingredient is spin hyper-polarisation. This is a method for driving the ensemble of ions into a single spin state, and is detailed in Section 3.1. Nuclear spin hyper-polarisation in rare earths, however, requires hyperfine spacings larger than the inhomogeneous broadening (see Section 2.3). In many crystals the inhomogeneous broadening is greater than 100 MHz, while long coherence times are achieved in systems with hyperfine spacing of only a few MHz. Er:YSO on the other hand, exhibits GHz hyperfine

spacings. In-fact, Chapter 4 presents the first demonstration of efficient hyper-polarisation in a rare earth system, opening the path to several broadband storage techniques.

A promising broadband storage technique requiring hyper-polarisation is off-resonant Raman absorption. Here the flying qubits are slightly detuned from the memory absorption, and a strong off-resonant laser pulse is used to store them. In this system, the storage bandwidth is no longer determined by the absorption profile of the memory and THz storage has been demonstrated in diamond [73]. The most efficient and low-noise demonstration, however, is with Cs vapour. Photons at 850 nm have been stored in this vapour with bandwidths up to 1.8 GHz [74]. Cs vapour has not been considered for quantum repeater applications itself, however, due to the inconvenient absorption wavelength and $\mu s$ coherence times.

A second potential avenue of investigation for broadband absorption is the gradient echo memory. This method utilises field gradients, either electric or magnetic, to broaden the absorption of the memory. Furthermore, GEM has demonstrated the highest storage efficiency for quantum memories both in solids and gases [47,72]. With the ability to hyper-polarise the rare earth ensemble, a key roadblock to broadband storage in solid-state GEM has been removed. Electric field gradient of kV/mm are sufficient for GHz bandwidth[3] in Er:YSO. These gradients remain below the dielectric breakdown limit, and can be achieved with 100V potentials in a waveguide architecture.

## 1.4 Thesis outline

From the overview presented in this chapter, it should be clear that Er doped solids show great potential for quantum communication. The investigations presented here aim to help realise this goal, and the thesis is organised as follows:

Chapter 2 gives the basic theory of rare earth spectroscopy relevant to the remainder of the thesis. It presents a derivation of the optical, electronic and hyperfine structure in rare earth ions, as well as the important dynamic interactions which affect the lifetimes and coherence times of these transitions.

Chapter 3 describes the experimental techniques used throughout the thesis, including the optical pumping approaches used to manipulate the Er:YSO ensemble and the frequency modulation spectroscopy used for imaging the same ensemble. This chapter also

[3]Based on the electric field susceptibility of 500 kHz/Vmm [68]

introduces the SET technology used in the spectroscopic investigations of Er:Si.

Chapters 4 and 5 detail the main experimental results of the thesis. Chapter 4 investigates the optical and hyperfine transition properties of $^{167}$Er:YSO in large magnetic fields, with the aim of improving the hyperfine transition lifetimes and coherence times.

Chapter 5 demonstrates the addressing of individual Er:Si ions via the $I_{15/2} \leftrightarrow I_{13/2}$ optical transition, and investigates the optical coherence properties and level structure of these ions.

Chapter 6 concludes with an analysis of repeater performance, given the $^{167}$Er coherence times measured here. It also discusses the relevance of $^{167}$Er:YSO for long term information storage, and Er:Si for optical communication.

Chapter 2

# The spectroscopy of rare earth ions

Erbium ($_{68}$Er) is a member of the rare earth elements, also known as the lanthanides. The lanthanide series ranges from lanthanum ($_{57}$La) through to lutetium ($_{71}$Lu). The lanthanides long fascinated spectroscopists due to their narrow optical lines in solid-state, and this property makes them uniquely suited for quantum applications. Indeed, these lines were so narrow that it wasn't until tunable lasers were introduced in the 1970's that the inhomogeneous linewidths could be readily probed [75].

This chapter aims to familiarise the reader with the basic properties of rare earth ions, and their key interactions within solid-state hosts. Section 2.1 presents an overview of the relevant physical and chemical properties of rare earth ions, and the effect these have on the optical spectrum. This overview is followed by a derivation of the $Er^{3+}$ valence shell Hamiltonian in Section 2.2. The parameters of this Hamiltonian are used to analyse the crystal-field structure of a single Er:Si ion, presented in Chapter 5. Sections 2.3 and 2.4 then introduce the dynamic interactions that affect the coherence properties of rare earth ions. An understanding of these interactions is critical to achieving the long lifetimes and coherence times presented in Chapter 4. The chapter concludes with some background information about the energy transfer processes of Er:Si in Section 2.5, motivating the charge detection technique applied in Chapter 5.

## 2.1 Physical and chemical properties

In solids, the lanthanides become highly electro-positive and often take on the 3+ charge configuration, a rule which holds for Er in both Si and YSO. The trivalent lanthanides can be described by the electronic configuration $[\mathrm{Xe}]\,4f^n$ where $n$ ranges from 0 to 14. The valence electrons successively fill the $4f$ shell in the lanthanide series, even though this shell is buried below the $5s$ and $5p$ shells, as shown in Figure 2.1.

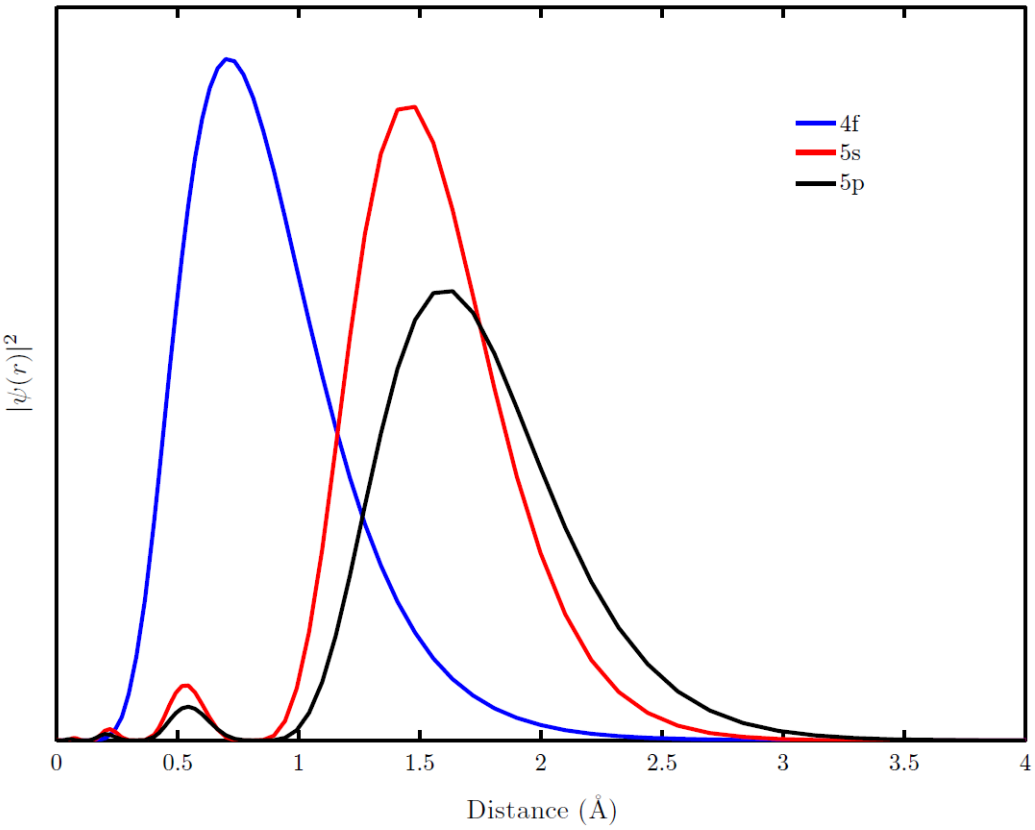


**Figure 2.1:** The radial electronic probability distribution for the triavalent ion $Pr^{3+}$. All the trivalent rare earths exhibit similar radial distributions. Figure reproduced from Ref [63].

Thus, the eight electrons in the $n = 5$ shell screen the valence electrons from external perturbations. As the optical transitions of rare earths are intra $4f$, this screening attenuates any perturbations from the crystal environment and narrows the optical transition linewidths. $Er^{3+}$ in particular has demonstrated one of the narrowest homogeneous optical linewidths of any rare earth in solid state, with $\Gamma_h$ =73 Hz [76].

Furthermore, the atomic radii of the lanthanides gradually decrease from lightest to heaviest, a trend known as the lanthanide contraction, shown in Table 2.1. This contraction occurs because of the relatively close proximity of the $4f$ shell to the nucleus, added to the repulsion of the outer $5s$ & $5p$ electrons. This causes a 20% contraction across the series, so the atomic radius of $Er^{3+}$ is 98.5% that of $Y^{3+}$. Of all the rare earths, only trivalent holmium ($Ho^{3+}$) and dysprosium ($Dy^{3+}$) are a better match for $Y^{3+}$. This similarity is important for minimising strain broadening in YSO as Er substitutionally dopes for Y (see Section 2.3).

| Atomic number | Element | Electron configuration $RE^{3+}$ | Ground state $RE^{3+}$ | Ionic radius $RE^{3+}$ (pm) |
|---|---|---|---|---|
| 21 | Sc | $3d^0$ | $^1S_0$ | 87 |
| 39 | Y | $4d^0$ | $^1S_0$ | 101.9 |
| 57 | La | $4f^0 5s^2 5p^6$ | $^1S_0$ | 116.0 |
| 58 | Ce | $4f^1 5s^2 5p^6$ | $^2F_{5/2}$ | 114.3 |
| 59 | Pr | $4f^2 5s^2 5p^6$ | $^3H_4$ | 112.6 |
| 60 | Nd | $4f^3 5s^2 5p^6$ | $^4I_{9/2}$ | 110.9 |
| 61 | Pm | $4f^4 5s^2 5p^6$ | $^5I_4$ | 109.3 |
| 62 | Sm | $4f^5 5s^2 5p^6$ | $^6H_{5/2}$ | 107.9 |
| 63 | Eu | $4f^6 5s^2 5p^6$ | $^7F_0$ | 106.6 |
| 64 | Gd | $4f^7 5s^2 5p^6$ | $^8S_{7/2}$ | 105.3 |
| 65 | Tb | $4f^8 5s^2 5p^6$ | $^7F_6$ | 104.0 |
| 66 | Dy | $4f^9 5s^2 5p^6$ | $^6H_{15/2}$ | 102.7 |
| 67 | Ho | $4f^{10} 5s^2 5p^6$ | $^5I_8$ | 101.5 |
| 68 | Er | $4f^{11} 5s^2 5p^6$ | $^4I_{15/2}$ | 100.4 |
| 69 | Tm | $4f^{12} 5s^2 5p^6$ | $^3H_6$ | 99.4 |
| 70 | Yb | $4f^{13} 5s^2 5p^6$ | $^2F_{7/2}$ | 98.5 |
| 71 | Lu | $4f^{14} 5s^2 5p^6$ | $^1S_0$ | 97.7 |

**Table 2.1:** Properties of trivalent rare earth ions. The electron configurations start at the valence shell for each ion. The ionic radii given are for an eight coordinate ion from Ref [77], table re-printed with permission from Ref [78].

## 2.2 The 4*f*-shell Hamiltonian

The optical transitions of the lanthanides are those between the electronic states of the $4f$-shell, and this section presents a Hamiltonian which models these levels. The derivation of this Hamiltonian begins with the potential of a free-ion $H_{\mathrm{FI}}$. It was previously explained that the valence $4f$-shell lies below the chemically-active $5s$ and $5p$ shells. Because of this, the atomic energy levels vary just a few percent among different crystals and the eigenstates of the free-ion form an excellent basis for rare earths in novel materials. The degenerate multiplets of the free-ion are often labelled using Russell-Sanders symbols:

$$^{2S+1}L_J$$

Here $S$ and $L$ correspond to the total projections of spin and orbital momenta for a given electronic configuration of the $4f$-shell. The coupled total momentum $J$ is defined $|L-S| \leq J \leq L+S$, and for $Er^{3+}$ there are 41 distinct $|L,S,J\rangle$ multiplets. Most of these

are visible in the classic Dieke diagram, shown in Figure 2.2. Once the ion is implanted in a solid, the interaction with the crystal-field ($H_{\mathrm{CF}}$) breaks the $2J+1$ degeneracy of each multiplet. However, the screening of the $4f$ -shell means that $H_{\mathrm{CF}}$ is a small perturbation of $H_{\mathrm{FI}}$. Because of this, the treatment of the crystal-field perturbation in Section 2.2.2 predicts the $2J+1$ substructure of each multiplet well. For ions with nuclear structure, such as $^{167}$Er, it is also necessary to include the nuclear-electronic and nuclear-quadrupole interactions $H_{\mathrm{HF}}$ and $H_{\mathrm{Q}}$. These two terms are introduced in Section 2.2.3. The complete $4f$-shell Hamiltonian can thus be written in order of decreasing perturbation:

$$H_{4f} = H_{\mathrm{FI}} + H_{\mathrm{CF}} + H_{\mathrm{HF}} + H_{\mathrm{Q}} \tag{2.1}$$

Development of the $4f$-shell Hamiltonian based on this approach has been documented extensively [79–81], and this section closely follows this standard approach. In Chapter 5, the $4f$-shell Hamiltonian will be used to characterise the site symmetry of a single Er ion in silicon. The software suite Python Crystal Field (PYCF) is used to perform this analysis. Developed by S. Horvath, PYCF is a numerical solver that can perform automated fits to the $4f$-Hamiltonian using optical transition data [82]. Further detail is left to Appendix A.

### 2.2.1 The free ion

The Hamiltonian of an $N$-electron atom (or ion) can be described by equation (19.1-1) of Weissbluth [79]:

$$H_{\mathrm{FI}} = \sum_{i=1}^{N} \left[ \underbrace{\frac{p_i^2}{2m}}_{\text{kinetic}} - \underbrace{\frac{Ze^2}{r_i}}_{\text{nuclear}} + \underbrace{\xi\left(r_i\right) l_i \cdot s_i}_{\text{spin-orbit}} \right] + \sum_{i<j}^{N} \underbrace{\frac{e^2}{r_{i,j}}}_{\text{e}^- \text{ repulsion}} \tag{2.2}$$

Each electron $i$ in Hamiltonian (2.2) is influenced by only four physical effects, if we ignore relativistic corrections. Moreover, the first three terms are only functions of individual electrons $i$. If this were true of all four Hamiltonian components, the eigenstates could be expressed as tensor products of single-electron wavefunctions:

$$\Psi = \psi_1 \otimes \psi_2 \otimes \cdots \otimes \psi_N \tag{2.3}$$

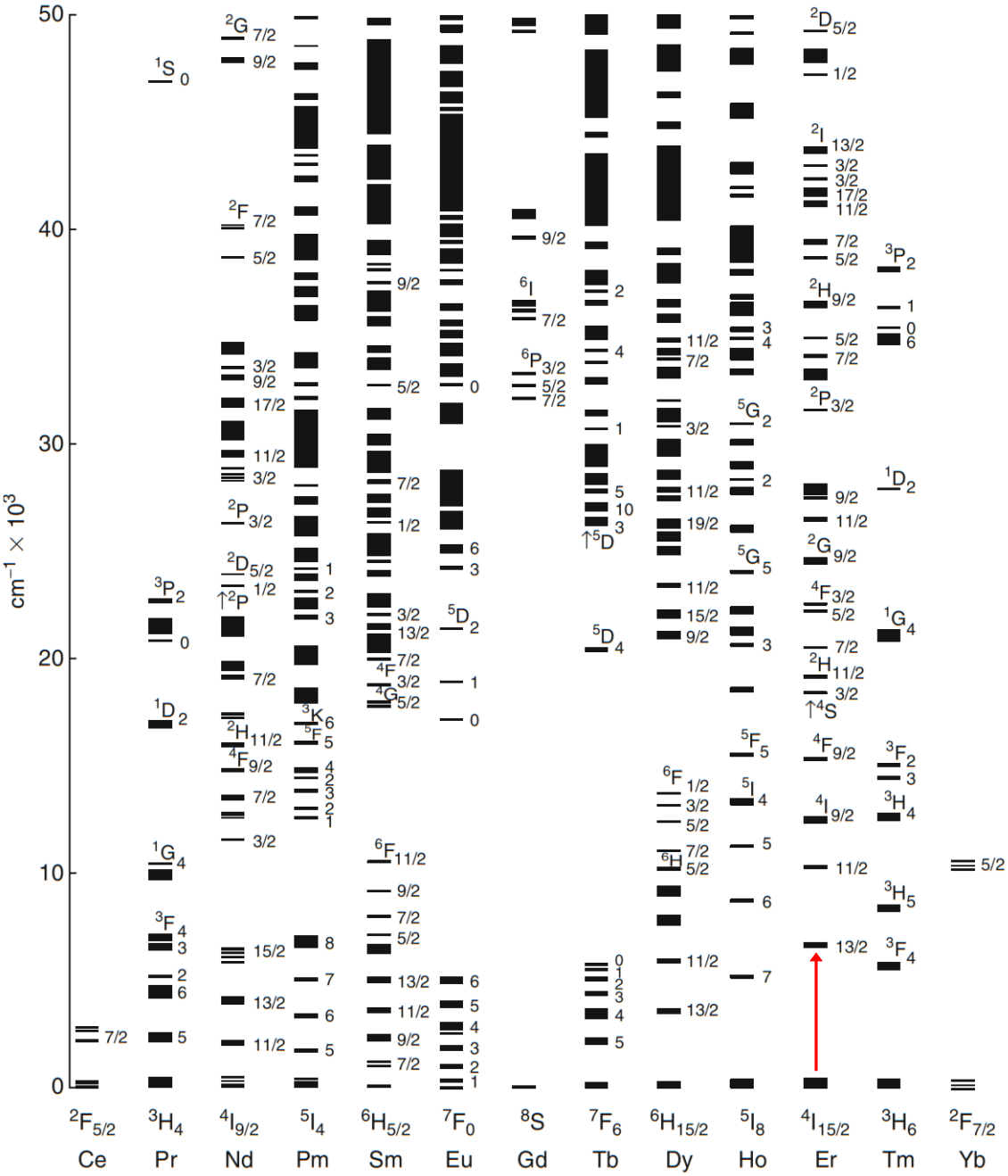


**Figure 2.2:** Theoretical Dieke diagram showing the $4f$ electronic levels of trivalent rare earths in $LaF_3$, based on the free-ion and crystal-field Hamiltonian [83]. The thickness of the levels indicates the crystal-field splitting of each free-ion multiplet. The ${}^4I_{15/2} \rightarrow {}^4I_{13/2}$ transition relevant to this thesis is highlighted in red, with a transition energy of around 1538 nm. Figure modified from Ref [84].

Unfortunately, the electron-electron Coulomb repulsion is comprised of two-electron operators and hinders this separation of variables. The electron repulsion is also too large to be treated as a perturbation of the single-electron product states. To solve this dilemma, one turns to the central field approximation.

### The central field approximation

The goal of this approximation is to re-express the Coulomb repulsion $H_C$ as a combination of centro-symmetric and asymmetric contributions. Thus, the dominant centro-symmetric Coulomb interaction becomes a separable single-electron operator expression. In particular, this interaction can be represented as the spherical average of the repulsion for each pair of electrons:

$$H_C = \sum_{i<j}^{N} \frac{e^2}{r_{i,j}} \quad = \quad \underbrace{\left\langle \sum_{i<j}^{N} \frac{e^2}{r_{i,j}} \right\rangle}_{\text{symmetric}} \quad + \quad \underbrace{H'_{\mathrm{C}}}_{\text{asymmetric}}$$

and the small asymmetric contribution $H'_C$ can then be treated as a perturbation. Rewriting Hamiltonian (2.2) in terms of these two components we get:

$$H = \sum_{i=1}^{N} \left[ \frac{p_i^2}{2m} - \frac{Ze^2}{r_i} \right] + \left\langle \sum_{i<j}^{N} \frac{e^2}{r_{i,j}} \right\rangle + H_{\mathrm{SO}} + H'_{\mathrm{C}}$$

The symmetric Coulomb repulsion now represents a sum of spherical single-electron operators. Thus, it can be combined with the nuclear potential into a new single-electron operator $U$:

$$H_{\mathrm{FI}} = \underbrace{\sum_{i=1}^{N} \left[ \frac{p_i^2}{2m} - U\left(r_i\right) \right]}_{\text{hydrogenic}} + \underbrace{H_{\mathrm{SO}} + H'_{\mathrm{C}}}_{\text{perturbations}} \tag{2.4}$$

Expression (2.4) allows the free-ion Hamiltonian to be solved by separation of variables. In particular, the 'hydrogenic' component of Hamiltonian (2.4) can be re-expressed as $N$ single-electron Schrödinger equations:

$$\left( \frac{p_i^2}{2m} - U\left(r_i\right) \right) \psi_i = E_i \psi_i \tag{2.5}$$

Except for the term $U(r)$, equation (2.5) is identical to the time-independent Schrödinger equation for hydrogen. The solution to the hydrogen Hamiltonian can be expressed analytically, and is often derived in undergraduate texts such as Griffiths [85]. Separation of variables are again used decompose each wavefunction into radial and angular components: $\psi\left(n, \theta, \phi\right) = R_{nl}(r) Y_l^{m_l}(\theta, \phi)$.

The angular components are comprised of the well-known spherical harmonics:

$$Y_l^{m_l}(\theta,\phi) = (-1)^{m_l}\left[\frac{(2l+1)\,(l-1)!}{4\pi\,(l+m_l)!}\right]^{\frac{1}{2}} P_l^{m_l}\left[\cos(\theta)\right] e^{im_l\phi} \tag{2.6}$$

Where the $P_q^k(x)$ in expression (2.6) are the associated Legendre polynomials. The radial function $R(r)$ depends on the unknown potential $U(r)$ and cannot be solved analytically. For our purposes, however, determining $R(r)$ is unnecessary as $n$ and $l$ are the same for all $4f$ electrons and so shift all the levels equally. This centre-of-mass change does not affect the intra-$4f$ optical transitions and so cannot be observed.

The final consideration for these hydrogenic wavefunctions is the spin $\boldsymbol{s}$. For a single-electron, only two spin states are possible with spin-projections $m_s = -1/2$ or $+1/2$. This is incorporated into the spinor $\xi(m_s)$ and the complete single-electron wavefunction is expressed:

$$\psi_{n,l,m_l,m_s}(r,\theta,\phi) = R_{nl}(r)\, Y_l^{m_l}(\theta,\phi)\,\xi(m_s)$$

Recall that the end goal of this section is to construct the many-body wavefunction $\Psi$. This can now be accomplished using the form given in equation (2.3). Electrons are fermions, so the eigenstates of the many-electron wavefunction must be anti-symmetric combinations of the single-electron states $(n,l,m_l,m_s)$. Such combinations can be expressed using Slater determinants, (cf. Chapter 11 of Weissbluth [79]):

$$\Psi(\lambda_1,\lambda_2,\cdots,\lambda_N) = \frac{1}{\sqrt{N!}}\begin{vmatrix} \psi_1(\lambda_1) & \psi_2(\lambda_1) & \cdots & \psi_N(\lambda_1) \\ \psi_1(\lambda_2) & \psi_2(\lambda_2) & \cdots & \psi_N(\lambda_2) \\ \vdots & \vdots & & \vdots \\ \psi_1(\lambda_N) & \psi_2(\lambda_N) & \cdots & \psi_N(\lambda_N) \end{vmatrix}$$

Here the subscripts $i$ and $\lambda_j$ correspond to the $(n,l,m_l,m_s)$ components of electron $i$ and the $(r,\theta,\phi)$ co-ordinates of electron $j$, respectively. With only the hydrogenic potential (2.5), the energies of the $4f$ -shell would be completely degenerate; they are defined only by the principal quantum number $n$ and angular momentum $l$. However, off-diagonal matrix elements are introduced into the Hamiltonian by the perturbations $H_{\mathrm{SO}}$ and $H'_{\mathrm{C}}$.

### Intermediate LS coupling

When dealing with perturbations, a common approach is to diagonalise the Hamiltonian in a basis that commutes with the dominant perturbation. This approach is used because it simplifies both the Hamiltonian and eigenstate vectors by reducing the number of off-diagonal Hamiltonian parameters. There are several distinct bases, or 'coupling schemes', that have been developed for dealing with perturbations to the free-ion Hamiltonian, and these are detailed in Chapter 1 of Liu [81]. The term 'scheme' is used because all subsequent interactions will have noticeably different parametrisations with different coupling schemes, and several common schemes will be described briefly here.

Diagonalising a Hamiltonian which includes the spin-orbit perturbation is often achieved with $jj$ coupling. This coupling scheme is so named because $H_{\mathrm{SO}}$ commutes with the electronic momentum of each electron $j$, and the total momentum of the ion $J$:

$$\boldsymbol{j}_i = \boldsymbol{l}_i + \boldsymbol{s}_i \qquad\qquad J = \sum_{i=1}^{N} \boldsymbol{j}_i$$

$$[H_{\mathrm{SO}}, j_i] = 0 \quad (\forall i \in N) \qquad\qquad [H_{\mathrm{SO}}, J] = 0$$

Unfortunately, $H'_{\mathrm{C}}$ doesn't commute with the momentum $j$ of individual electrons. Instead $H'_{\mathrm{C}}$ commutes with the atomic spin, orbital and total momenta:

$$S = \sum_{i=1}^{N} \boldsymbol{s}_i \qquad\qquad L = \sum_{i=1}^{N} \boldsymbol{l}_i$$

$$\left[H'_{\mathrm{C}}, S\right] = 0 \qquad \left[H'_{\mathrm{C}}, L\right] = 0 \qquad \left[H'_{\mathrm{C}}, J\right] = 0$$

This alternate scheme is called $LS$ coupling, and forms the preferred basis for the $4f$-Hamiltonian in rare earths. The magnitude of $H_{\mathrm{SO}}$ and $H'_{\mathrm{C}}$, however, are similar in rare earths so neither $L, S$ nor $j$ are 'good' quantum numbers. To diagonalise the Hamiltonian for the rare earths, one uses the 'intermediate' $LS$ coupling regime. Here, the Hamiltonian is diagonalised in the $L, S, J$ basis, but the energy eigenstates must be expressed as linear combinations of $L$ and $S$:

$$\Psi(n, l, J, m_J) = \sum_{\tau, L, S} a_{\tau, L, S} |n, l, \tau, L, S, J, m_J\rangle \tag{2.7}$$

In representation (2.7) there is an additional quantum number $\tau$, called the seniority number. This is required to distinguish unique states that happen to have the same $L$ and $S$ values, an accidental degeneracy introduced in the breakdown of $4f$ states into the $LS$ basis. The value of $\tau$ for every eigenstate of the $4f^N$ configuration is listed in Table (1.3) of Liu [81]. In the case of $Er^{3+}$, the $^2$D, $^2$F, $^2$G and $^2$H states are doubly-degenerate. Furthermore, the coefficients for each eigenstate can be determined from the following:

$$a_{\tau,L,S} = \sum_{\tau',L',S'} \langle n, l, \tau, L, S, J, m_J | H_{\mathrm{SO}} + H'_{\mathrm{C}} | n, l, \tau', L', S', J', m'_J \rangle \delta(J, J') \delta(m_J, m'_J)$$

### Parametrising the perturbations

To calculate the free-ion energy levels, the perturbation $H'_{\mathrm{C}}$ and $H_{\mathrm{SO}}$ must be expressed in operator form. The asymmetric Coulomb perturbation $H'_{\mathrm{C}}$ can be expressed as the difference between the total and symmetric Coulomb terms:

$$H'_C = \underbrace{\sum_{i<j}^{N} \frac{e^2}{r_{i,j}}}_{\text{total}} - \underbrace{\sum_{i=1}^{N} \left( \frac{Ze^2}{r_i} - U(r_i) \right)}_{\text{symmetric}}$$

The asymmetric Coulomb perturbation can be parameterised by noting, once again, that the radial functions $U(r)$ and $e^2/r$ shift all the $4f$ states equally. This implies that $H_{\mathrm{C}}$ and $H'_{\mathrm{C}}$ have identical effects on the spectrum, so $H'_{\mathrm{C}}$ can be parametrised using exactly the same components as $H_{\mathrm{C}}$. Following the Section 1.3.1 of Liu [81], the complete Coulomb perturbation $H_{\mathrm{C}}$ can be expressed as follows:

$$H_{\mathrm{C}} = \sum_{i<j}^{N} \sum_{k=0}^{\infty} \frac{r_<^k}{r_>^{k+1}} \left( \sum_{q=-k}^{k} (-1)^q \, \mathrm{C}_q^k(i) \, \mathrm{C}_{-q}^k(j) \right) \tag{2.8}$$

For each pair of electrons $i, j$ in expression (2.8), the $r_>$ ($r_<$) correspond to the greater (lesser) of $r_i$ or $r_j$. The terms $C_q^k$ are proportional to the spherical harmonics (2.6), and for the $n^{th}$ electron:

$$C_q^k(n) = \sqrt{\frac{4\pi}{2k+1}} Y_q^k(\theta_n, \phi_n) \tag{2.9}$$

The terms in equation (2.8) have exclusively radial or angular dependence.

The solution thus lends itself to separation of variables, and the matrix elements are expressed using a sum of two functions:

$$\langle n, l, \tau, L, S, J, m_J | H_{\mathrm{C}} | n, l, \tau', L', S', m'_J \rangle = \sum_{k=0}^{\infty} F^k \left( nl, nl \right) f_k \left( l, l \right)$$

The solutions to the angular function $f$ is given by equation (1.24) of Liu [81]:

$$f_k \left( l, l \right) = \frac{1}{2} \left( 2l + 1 \right)^2 \begin{pmatrix} l & k & l \\ 0 & 0 & 0 \end{pmatrix}^2 \times \left\{ \frac{1}{2L+1} \sum_{\tau' L'} |\langle l^N \tau L S || \mathbf{U}^{(k)} || l^N \tau L' S' \rangle| - \frac{N}{2l+1} \right\}$$

where the open brackets $(\cdots)$ represent the Wigner 3j symbol. Due to the selection rules of the Wigner 3j symbol, $f_k$ is only non-zero for even values of $k$ where $0 \leq k \leq 2l$. Given that $l = 3$ for all $4f$ electrons, this gives $k = 0, 2, 4, 6$. Additionally, the matrix elements of the unitary operator $\mathbf{U}^{(k)}$ are tabulated by Nielson & Koster [86]. The solutions of the radial function $F$ are the Slater integrals, expressed by equation (1.22) of Liu [81]:

$$F^k \left( nl, nl \right) = e^2 \int_0^{\infty} \int_0^{\infty} \frac{r_<^k}{r_>^{k+1}} R_{nl} \left( r_i \right)^2 R_{nl} \left( r_j \right)^2 dr_i dr_j$$

Unlike the angular components, the constants $F^k$ are determined experimentally by fitting to the free-ion levels shown in a Dieke diagram (Figure 2.2). With this approach, the Slater parameters for $Er^{3+}$ have already been determined in many materials [82, 87]. This completes the parametrisation of $H'_{\mathrm{C}}$, and we now arrive at the spin-orbit perturbation:

$$H_{\mathrm{SO}} = \sum_{i=1}^{N} \xi \left( r_i \right) l_i \cdot s_i$$

Just like the Coulomb repulsion term, the spin-orbit interaction is amenable to angular and radial separation of variables:

$$\langle n, l^N, \tau, L, S, J, m_J | H_{\mathrm{SO}} | n, l^N, \tau', L', S', J', m'_J \rangle = \zeta_{nl} A_{\mathrm{SO}} \left( nl \right)$$

The solution to the angular component is once again stated by Liu, in equation (1.28) [81]:

$$A_{\mathrm{SO}}\left(nl\right) = (-1)^{L+S'+J}\left(2l+1\right)\delta\left(J,J'\right)\delta\left(m_J,m'_J\right)\sqrt{\left(2l+1\right)\left(l+1\right)l} \times \left\{ \begin{array}{ccc} L & S & J \\ S' & L' & 1 \end{array} \right\} \langle \tau LS||\mathbf{V}^{(11)}||\tau L'S'\rangle$$

In the formulation above, the brackets $\{\cdots\}$ represent the Wigner 6j symbol and the values of the unitary operator $\mathbf{V}^{(11)}$ are tabulated once again by Nielson & Koster [86]. Finally, the radial component is described by equation (1.29):

$$\zeta_{nl} = \int_0^\infty R_{nl}(r_i)^2 \xi\left(r_i\right) dr_i$$

### Corrections to the free-ion Hamiltonian

While Hamiltonian (2.2) is considered a good approximation for rare earths, attempts at fitting experimental spectra usually deviate by several hundred $\mathrm{cm}^{-1}$ [80]. Better fits are obtained by including more physical interactions, although not from first principles. Instead these interactions are parametrised as simple correction factors, based on their symmetries and the effect they have on the spectrum.

The first of these corrections deal with the contribution from Coulomb repulsion of non-$4f^n$ configurations. Describing the electronic configuration of rare earths as $4f^n$ eigenstates is only an approximation. Energy level fits can be improved by accounting for mixing with excited configurations such as $4f^{n+1}5p^5$. The first set of correction factors $(\alpha,\beta,\gamma)$ identified by Trees, Rajnak and Wybourne deal with this inter-configurational mixing [88, 89]. These factors account for two electron interactions[1] of the same form as $H'_{\mathrm{C}}$:

$$H_{\mathrm{c1}} = \alpha L\left(L+1\right) + \beta G\left(G_2\right) + \gamma G\left(R_7\right)$$

In the above equation, the last two functions correspond to the eigenstates of the Casimir operators acting on the $G_2$ and $R_7$ groups. They can be found in Tables 2-6 and 2-7 of Wybourne [80]. Since the initial work of Wybourne, it became common to account for three-electron interactions as well.

[1] In particular, $H_{\mathrm{c1}}$ deals with configurations of the same parity. The effect of configurations with differing parity (such as $4f^{n+1}5s^1$, etc) are already absorbed by the Slater parameters $F^k$.

For the same type of inter-configuration mixing an additional six parameters, whose constants are labelled $T_i$, account for the three-body interactions:

$$H_{c2} = \sum_{i=2,3,4,6,7,8} T^i t_i$$

Here each $t_i$ is a three-body operator, for which the matrix elements have been published by Hansen et al. [90]. The final set of corrections to the free-ion Hamiltonian compensate for spin-spin and spin-other-orbit interactions, and were identified by Judd et al. [91]:

$$H_{c3} = \sum_{i=0,2,4} M^i m_i + \sum_{i=2,4,6} P^i p_i$$

The three constants $M^i$ describe relativistic effects, and the $P^i$ encompass electrostatically correlated magnetic interactions. Within the lanthanide series, however, these constants vary in an fixed ratio. In particular, $M^0 : M^2 : M^4 = 100 : 56 : 31$ and $P^2 : P^4 : P^6 = 10 : 5 : 1$ [83]. Thus only one computational constant is required for each, labelled $M^{\text{total}}$ and $P^{\text{total}}$. All of the components of the free-ion Hamiltonian can now be combined into one expression that encompasses twenty free parameters:

$$\begin{aligned} H_{\text{FI}} = &\sum_{k=0,2,4,6} F^k f_k + \zeta_{nl} A_{\text{SO}}(nl) + \alpha L(L+1) + \beta G(G_2) + \gamma G(R_7) \\ &+ \sum_{i=2,3,4,6,7,8} T^i t_i + \sum_{i=0,2,4} M^i m_i + \sum_{i=2,4,6} P^i p_i \end{aligned}$$

As was mentioned at the beginning of Section 2.2, the free-ion interactions vary little between host materials. In fact, accurate predictions of energy levels in new materials are made with most parameters unchanged. For the modelling results in Chapter 5, only the Slater parameters $F^k$ and spin-orbit constant $\zeta_{nl}$ are varied. Moreover, the fitting range is varied by no more than 5%, in line with experimental results for $Er^{3+}$ across several materials [87]. The remaining constants are tabulated by Carnell et al. [83].

### 2.2.2 The crystal-field

The $2J + 1$ degeneracy of each free-ion multiplet is a consequence of spherical symmetry. In a crystalline host, however, this symmetry is broken by the local electric field. This is called the crystal-field interaction $H_{\text{CF}}$. For Kramers ions, this will cause the multiplets to separate into as many as $J + 1/2$ non-degenerate levels. Although $H_{\text{CF}}$ is a much weaker

perturbation than $H_{\mathrm{SO}}$ or $H_{\mathrm{C}}$, it solely determines the spin-lattice dynamics, spin-state mixing and optical transition strengths. Thus, the crystal-field plays a critical role in determining key properties for quantum information processing in rare earth systems[2]. The interaction itself can be expressed succinctly using Wybourne normalisation [80]:

$$H_{\mathrm{CF}} = \sum_{k,q,i} B_q^k C_q^k(i)$$

Where the terms $C_q^k$ were previously defined for $H_{\mathrm{C}}$ in equation (2.9) and the constants $B_q^k$ are determined by experimental fit. The parameters $C_q^k$ required for a given ion depend entirely on the symmetry of the site. The lower the symmetry of a site, the more parameters are required to describe the crystal-field interaction. There are a total of twenty-seven parameters required to describe an arbitrary crystal-field configuration. Expressing these crystal-field parameters as matrix elements of the free-ion Hamiltonian is achieved with equation (1.39) of Liu [81]:

$$\langle n, l, \tau, L, S, J, m_J | H_{\mathrm{CF}} | n, l, \tau', L', S', J', m'_J \rangle = \sum_{k,q,i} B_q^k \left(-1\right)^{J-M} \begin{pmatrix} J & k & J' \\ -m_J & q & m'_J \end{pmatrix} D_J^k$$

Here each $D_J^k$ is described by equation (1.40) of the same reference:

$$D_J^k = \left(-1\right)^{S+L'+J+k} \sqrt{\left(2J+1\right)\left(2J'+1\right)} \begin{pmatrix} l & k & l \\ 0 & 0 & 0 \end{pmatrix} \times \langle l^N \tau L S || \mathbf{U}^{(k)} || l^N \tau' L' S' \rangle \left(-1\right)^l \left(2l+1\right) \begin{Bmatrix} J & J' & k \\ L' & L & S \end{Bmatrix}$$

Once again, the elements of $\mathbf{U}^{(k)}$ are given by Nielson and Koster [86] and the bracketed functions $(\cdots), \{\cdots\}$ correspond to Wigner 3j and 6j symbols, respectively.

Because the number of relevant $C_q^k$ parameters depends on the site symmetry, it is useful to group symmetries into the following three classes: cubic, axial, and lower-than-axial. Magnetic field rotations are a quick way of determining the symmetry class of an ion, and the crystal-field parameters required for modelling each type are stated in Table 1.7 of Liu [81]. It should also be noted that site symmetries generally differ from the crystal symmetry, as ions can form stable bonds in several configurations. Crystal and site

[2]The term 'rare earth system' is used in this thesis to describe a particular combination of host, dopant, temperature and applied magnetic field.

symmetries can only match for lattices with few atomic species and high symmetry, which is particularly the case for silicon.

### 2.2.3 Hyperfine Interactions

For ions with non-zero nuclear spin such as $^{167}$Er ($I = 7/2$), the interaction with the electron-spin further splits the energy levels into hyperfine substates. This hyperfine interaction can be paramaterised using two interaction Hamiltonians, $H_{\mathrm{HF}}$ and $H_{\mathrm{Q}}$. The first Hamiltonian describes the magnetic coupling of the nuclear spin to the electrons. Following Chapter 5 of Wybourne [80], $H_{\mathrm{HF}}$ can be expressed in terms of $N$ single-electron operators. This derivation begins the dipole field at the nucleus from the electrons, each with an orbital radius $r$, spin momentum $s$ and angular momentum $l$:

$$B = 2\mu_B \left( \frac{l - s}{r^3} + \frac{3r\,(s \cdot r)}{r^5} \right)$$

The interaction Hamiltonian can then be expressed as following:

$$\begin{aligned} H_{\mathrm{HF}} &= g_I \mu_N \sum_{i=1}^{N} B_i \cdot I \\ &= \frac{2\mu_B g_I \mu_N}{\langle r^3 \rangle} \sum_{i=1}^{N} \left( l_i - s_i + \frac{3r_i\,(s_i \cdot r_i)}{r_i^2} \right) \cdot I \end{aligned}$$

where $g_I$ is the nuclear g-factor and $\mu_B, \mu_N$ are the Bohr and nuclear magnetons respectively. The matrix elements of this operator are listed in Judd [92]. More importantly, however, the interaction strength is determined by just the single parameter:

$$a_l = \frac{2\mu_B g_I \mu_N}{\langle r^3 \rangle}$$

Fitting $a_l$ alone is simpler than fitting all 9 components of the $A$-tensors, which is required for effective spin-Hamiltonians. This is because the properties of the electronic wavefunction have been largely determined by $H_{\mathrm{FI}}$ and $H_{\mathrm{CF}}$.

The final interaction considered in this section is the nuclear-electronic quadrupole interaction, $H_{\mathrm{Q}}$. For $^{167}$Er the interaction strength of $H_{\mathrm{Q}}$ is similar to that of $H_{\mathrm{HF}}$. This is a form of Coulomb repulsion, and it can be expressed using Equation (2.8).

However, only the $k = 2$ term is required because higher multipole electronic moments are very weak:

$$H_{\mathrm{Q}} = \frac{e^2}{\langle r^3 \rangle} \sum_{i=1}^{N} \sum_{q=-2}^{2} (-1)^q r_I^2 \mathrm{C}_q^2(I) \cdot \mathrm{C}_q^2(i)$$

Here $r_I$ and $C(I)$ represent the orbital radius and charge distribution of the nucleus. The matrix elements of this interaction can be expressed as follows:

$$\langle \tau, L, S, J, m_J I, m_I | H_{\mathrm{Q}} | L', S', J', m'_J I', m'_I \rangle = a_{\mathrm{Q}} \left[ \frac{3/4 K(K+1) - I(I+1) J(J+1)}{2I(I-1) J(2J-1)} \right] \times \langle l^N \tau L S || \mathbf{U}^2 || l^N \tau L' S' \rangle \delta_{S,S'} \left[ \frac{4J(2J-1)}{(J+1)(2J+1)(2J+3)} \right]^{1/2}$$

where $K = F(F+1) - J(J+1) - I(I+1)$ and $F = \boldsymbol{I} + \boldsymbol{J}$. Once again the interaction strength is determined by a single parameter:

$$a_{\mathrm{Q}} = \frac{e^2}{\langle r^3 \rangle} \langle I || r_I^2 C^2(I) || I' \rangle \begin{pmatrix} I & 2 & I \\ -I & 0 & I \end{pmatrix}$$

and so nuclear interactions in rare earths are characterised by just two constants; $a_l$ and $a_{\mathrm{Q}}$.

## 2.3 Inhomogeneous broadening

In solid state materials, effects that broaden the linewidth of a transition can be grouped as either homogeneous or inhomogeneous. In a perfectly ordered crystal, each ion would be subject to identical crystal-fields and so the transition energies of the ensemble would be degenerate. In reality, crystals are not perfect and each individual ion may experience a slightly different local environment, which is the case for both Si and YSO. This disorder is usually random or 'inhomogeneous' across the ensemble of ions. Furthermore, this crystalline disorder often has many different sources and these can be grouped according to their dimensionality.

- 0D point defects such as vacancies, interstitial atoms or substitutional impurities
- 1D line defects, also known as dislocations
- 2D planar defects such as grain boundaries in poly-crystalline materials or stacking faults in layered materials

- 3D volume defects such as voids, fluid inclusions or clusters of point defects

Both the YSO and Si crystals studied here are grown as high -quality single crystals, in which the dominant defects are usually zero or one dimensional.

### 2.3.1 Statistical approximations of inhomogeneous broadening

For large ensembles of ions, the inhomogeneously broadened lineshape can be modelled accurately using a statistical distribution. As several distinct statistical models exist, one must determine the appropriate model for a given material. This choice generally depends on the defect density, and for crystals with defect densities below 1% the continuum model is used [93]. This model gives rise to Lorentzian, Gaussian or Holtzmark distributions, depending on the nature of defects present.

For the YSO crystal studied in this thesis, however, the isotopic impurities of Si and O lead to higher defect densities (a few percent) even though the doping concentration is only 0.005%. These uncharged point defects create a Lorentzian profile at low densities, which transitions to a Gaussian profile at 50% defect density. Thus, the continuum model is not appropriate at these high defect concentrations and a Voigt profile will typically produce a better fit [94, 95]. This profile is a convolution of Gaussian and Lorentzian functions:

$$V(x;\sigma,\rho) = \int_{-\infty}^{\infty} G(x';\sigma)L(x-x';\rho)dx'$$

$$\text{where } G(x;\sigma) = \frac{e^{-x^2/2\sigma^2}}{\sigma\sqrt{2\pi}}$$

$$\text{and } L(x;\rho) = \frac{\rho}{\pi\left(x^2+\rho^2\right)}$$

The linewidths of the Gaussian and Lorentzian distributions represent the only free parameters in the Voigt profile, as the amplitude of each component is scaled to one. Even though the defect density in YSO is high, the broadening of the optical transitions is narrower than the GHz linewidths obtained with other rare-earth dopants at similar concentration in this material [62]. Figure 2.3 in particular shows a spectrum of 0.005% $^{167}$Er:YSO. The convolution of many optical transitions in this figure gives rise to a complicated lineshape, however, the individual absorption lines demonstrate sub-GHz inhomogeneous broadening. These narrow absorption lines represent optical transitions between individual hyperfine states of $^{167}$Er.

While statistical distributions are not particularly relevant for the single Er:Si sites presented in Chapter 5, some discussion regarding inhomogeneous broadening in Er:Si is

presented in Section 5.5.

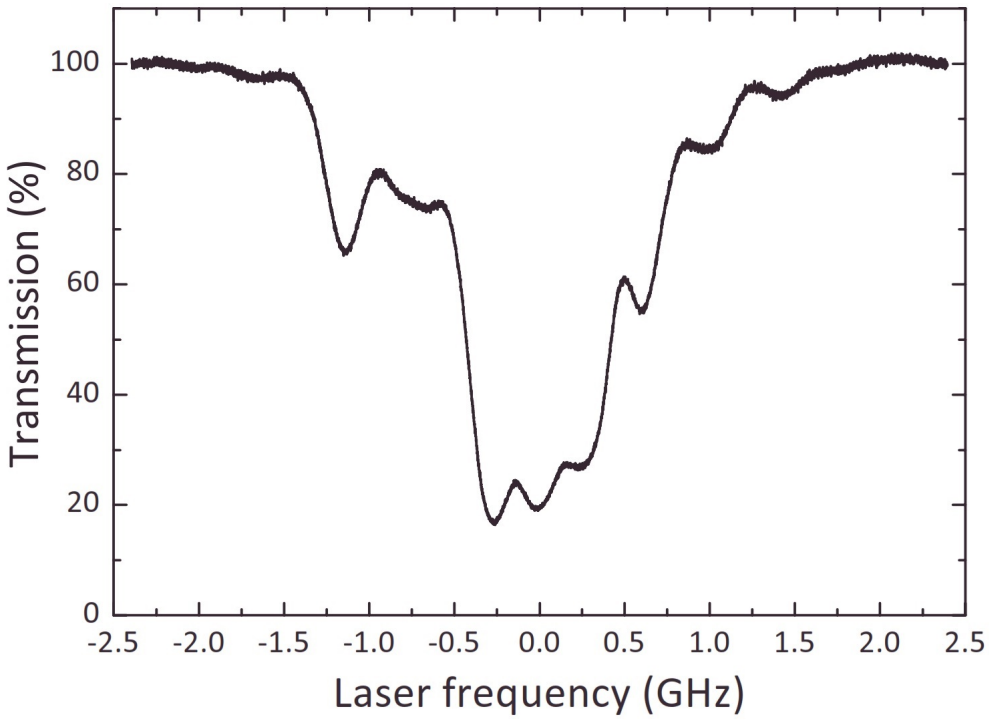


**Figure 2.3:** The inhomogeneous line of the $I_{15/2} \rightarrow I_{13/2}$ transition of $^{167}$Er:YSO site 1 in zero magnetic field, centred at 1536 nm. This spectrum is more complicated than the one observed for natural abundance Er:YSO, where the $I = 0$ isotopes $^{166}$Er and $^{168}$Er produce a single dominant line which lacks any obvious substructure. Here one observes many lines due to the 16 hyperfine states ($\tilde{S} = 1/2$, $I = 7/2$) in both the ground and excited optical levels. A crystal cut from the same boule was used for the experiments in Chapter 4. Spectrum taken from Ref [69].

## 2.4 Transition dynamics of $^{167}$Er

Quantum information processing and storage in rare earth materials is achieved with both optical and spin transitions. Whether these transitions are fit for purpose depends largely on the dynamic interactions within the solid state host. This section begins by introducing two key metrics in this regard; the lifetime ($T_1$) and the coherence time ($T_2$). The rest of the section outlines the important dynamics for rare earth systems, and $^{167}$Er in particular.

### 2.4.1 Population lifetime ($T_1$)

A population of ions in an excited energy state $a$ will decay to the ground state $b$ (or a thermal ratio of $a$ & $b$) at an exponential rate, governed by the decay time-constant $T_1$. For a single ion, the time integral of this function becomes the probability of the ion stochastically decaying. Furthermore, there can be multiple decay paths between states $a$

and $b$, some of which involve intermediate states $c, d$, etc. The relative probability that a decay will occur via a particular transition is called the branching ratio. In general, the lifetime of state $a$ via $n$ branches can be calculated as follows:

$$T_1 = \left( \sum_n \frac{1}{T_1(n)} \right)^{-1} \tag{2.10}$$

where each $T_1(n)$ is the decay time-constant of transitions $n$.

### 2.4.2 Coherence time ($T_2$)

The coherence time $T_2$ of a transition is one of the most important parameters for quantum information processing and storage. It is inversely proportional to the transition linewidth for a single ion, known as the homogeneous linewidth:

$$\Gamma_h = \frac{1}{\pi T_2} \tag{2.11}$$

The homogeneous linewidth is determined entirely by dynamic effects. Such dynamics act as sources of noise, causing transition broadening and dephasing. Even in a noise-free environment, however, the decay time $T_1$ of the transition is still a source of decoherence. In particular, $T_2 \leq 2T_1$, and so the homogeneous linewidth can be rewritten as a function of dephasing and decay:

$$\Gamma_h = \Gamma_\phi + \frac{1}{2\pi T_1}$$

The coherence time of a transition is usually measured using coherent pulse sequences, such as the photon-echo sequence described in Section 3.3.

### 2.4.3 Cross relaxation

We now turn our attention to processes that reduce lifetimes and coherence times. The first dynamic process considered here is spin-spin coupling, which is a type of cross-relaxation. This involves the exchange of energy and angular momentum between ions, and can occur through several different interactions.

For the low doping concentrations dealt with in this thesis, cross-relaxation is predominantly mediated by the magnetic-dipole interaction. At high doping concentrations the overlap of dopant wavefunctions leads to direct spin exchange. These are both resonant

processes where the exchange of energy between ions must be conserved. If the transition energies between two rare earths differ, then cross-relaxation will only take place if additional ions can 'bridge the gap'. This three (or more) body process occurs in YSO due to the dense bath of nuclear spin$-1/2$ Y ions. Their energy splitting can mediate cross-relaxation between two slightly detuned Er ions.

Because a quanta of angular momentum is also exchanged during cross-relaxation, the selection rule obey $\Delta m_S = \pm 1$. This is true for both hyperfine and electronic cross-relaxation. Furthermore, the strength of magnetic-dipole mediated cross-relaxation decreases with $r^{-3}$. For this reason memory demonstrations use very low (ppm) doping concentrations to increase the distance between rare earth ions.

As a final point, one must also consider resonant cross-relaxation between species other than rare earths in the crystal. In crystals used for quantum information processing such as YSO and Si, there is usually a large density of nuclear spin species. As was pointed out already, YSO has 100% abundance of nuclear spin$-1/2$ Y. In both Si and YSO, the Si species also has a 5% abundance of nuclear spin$-1/2$ $^{29}$Si. As these ions cross-relax with each other, they create a rapidly fluctuating magnetic field. This can significantly affect the coherence times of both the optical and spin transitions, and usually sets the limit for nuclear spin coherence in high quality crystals.

### 2.4.4 Spin-lattice coupling

Also known as as phonon coupling, this interaction transfers energy between the vibrational modes of the crystal and the rare earth ions. The crystal is composed of electric charges and so the vibrational modes of the crystal generate oscillatory electric and magnetic fields. Discrete quanta of these oscillatory fields, called phonons, can be emitted or absorbed by the ions. Unlike cross-relaxation, spin-lattice coupling only affects non-degenerate transitions. This is because there are no phonons at zero frequency. Kramers ions exhibit pairs of electronic states, called Kramers doublets, whose degeneracy is only lifted by an external magnetic field. This structure was outlined in Section 2.2.2, and cross-relaxation dominates the dynamics in zero field for this reason.

When addressing the issue of spin-lattice coupling, one must first consider the availability of phonons resonant with the transition of interest. At temperature $t$, the phonon bath

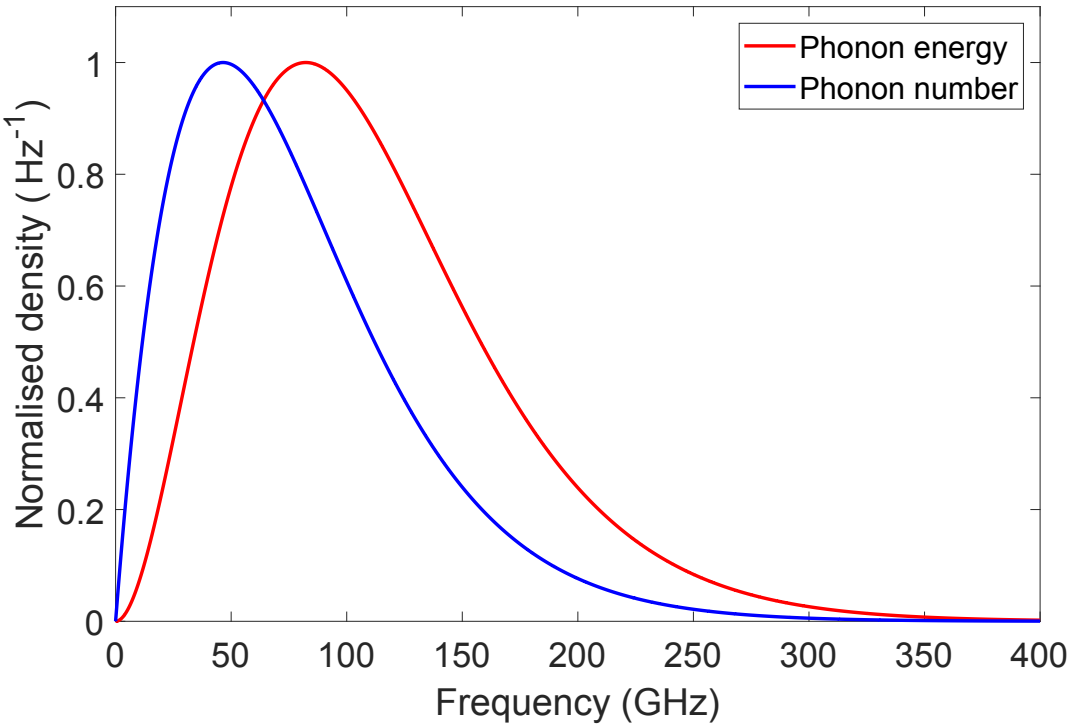


**Figure 2.4:** The theoretical distribution of thermal phonons at 1.4 K. Although it cannot be discerned in this figure, the phonon number density at 360 GHz is one hundredth the peak density at 80 GHz. This is also equivalent to the density at just 20 MHz.

is analogues to a black body spectrum, and can be described by the Planck distribution:

$$\rho_{ph}(\omega) = \frac{3\hbar\omega^3}{2\pi^2 \upsilon^3} \frac{1}{\exp\left(\frac{\hbar\omega}{kt}\right) - 1} \tag{2.12}$$

The phononic interaction is much more important than the equivalent photonic, because the speed of sound in crystals is only ∼2000 m/s. Hence the density of thermal phonons exceeds thermal photons by $(c/\upsilon)^3 \approx 10^{15}$.

Figure 2.4 illustrates the phonon distribution at a temperature of 1.4 K, highly relevant to the experiments described in Chapter 4. The important consideration for these experiments is the density of phonons beyond the peak of the phonon bath.

Reducing the density of available phonons is very important because the rate of electronic spin transitions will be proportional to the density. Depending on the energy of the electronic transition, a variety of phonon processes can occur. The splitting frequency of a Kramers doublet transition is usually GHz or more in fields greater than ∼100mT, and can reach THz with large magnetic fields. In this regime the spin transition is strongly coupled to the lattice, and resonant phonons can drive it directly.

For MHz transition energies, however, there is a lack of resonant phonons to strongly

drive the direct process. Instead two-phonon processes dominate, because they utilise the abundance of phonons at the peak of the thermal distribution (see Figure 2.5).

### The coupling of phonons to spin transitions

Phonons drive transitions in rare earth ions via the oscillatory electromagnetic fields they induce in the crystal. The precise nature of this phonon-ion coupling has a large effect on the transition rates. For the most part, transitions at phonon energies (MHz-THz) involve electronic or nuclear magnetic spins. One would then assume that phonons couple to the magnetic dipole of the spins. Magnetic coupling, however, is very weak. The strongest form of magnetic coupling in rare earths, the Waller process [96], will only induce relaxation on a timescale of days for an electron-spin in YSO[3]. This is much longer than the millisecond lifetimes measured for electronic spin transitions in Er:YSO [98].

Accurate estimates of the spin transition lifetimes are achieved, rather, through the electric-dipole interaction. It was explained in Section 2.2.1 that rare earths ions have large spin-orbit coupling. Furthermore, the interaction of the ion with the crystal-field causes an admixture of distinct spin-orbit levels, such as the $^4I_{13/2}$ and $^4I_{15/2}$. In 1940 Van Vleck discovered how this admixture allows for orbit-lattice coupling in the nominally magnetic spin transitions [99]. As it turns out, electric coupling in Kramers rare earths is actually much stronger than magnetic mechanisms such as the Waller process.

To understand this electric coupling, we turn to the work of Finn, Orbach and Wolf [100]. They describe phonons as oscillating perturbations of the electric crystal-field $H_{\mathrm{CF}}$. Furthermore, the magnitude of perturbation $H'$ induced by phonons is proportional to the crystal strain $\epsilon$. Using the operator notation outlined in Section 2.2.2, the perturbation can be written as follows:

$$\begin{aligned} H_{\mathrm{phonon}} &= \epsilon \frac{d}{dx} H_{\mathrm{CF}} \\ &= \epsilon \frac{d}{d\theta} \sum_{k,q} B_q^k C_q^k(\theta, \phi) \\ &= \epsilon \sum_{k,q} B_q^k \left( C_q^{k+1} \sin\nu + C_q^{k-1} \cos\nu \right) \end{aligned} \tag{2.13}$$

In the above expression, the variable $\nu$ is determined by the angle between the resonant phonon mode and axis of quantisation. It should also be noted that the spherical harmonic

[3]For a 10 GHz energy splitting at 2 K, derived using equation (10.52) of Abragam & Bleaney [97]

operators of $H'$ have odd exponents. Although such operators are not dealt with in crystal-field analysis, this result is not surprising given how they represent derivatives of $k$-even operators. For a spin transition from state $|-s\rangle$ to $|+s\rangle$, the phonon-coupling strength can then be determined precisely:

$$\omega_{\pm s} = \frac{2\pi}{\hbar^2} \left|\langle +s|H_{\text{phonon}}|-s\rangle\right|^2$$

Furthermore, spin-lattice coupling obeys the standard selection rules for electric-dipole transitions. In particular $\Delta m_S = 0, \pm 1$ where $S$ is either the electronic, nuclear or coupled spin basis ($J$, $I$ or $F$).

**Multi-phonon processes**

The discussion so far has focused on the direct process, where a single phonon is exchanged between the spin and the lattice. There are also important multi-phonon processes, which are illustrated in Figure 2.5. The fist of these is the Raman (or virtual phonon) process. Raman phonons form at the beat frequencies of two thermal phonons: $\omega_{vir} = \omega_1 \pm \omega_2$. A whole continuum of low-energy phonons are formed in this process, where the resonance condition is satisfied by $\hbar\omega_{vir} = \hbar(\omega_1 - \omega_2)$. Even though the density of these 'virtual' phonons is small, the continuum of available modes still makes Raman processes strong for low frequency transitions.

The other important two-phonon contribution is called the Orbach process [100]. Much like the Raman process, a transition is driven at the difference of two-phonon energies $\Delta E = \hbar(\omega_1 - \omega_2)$. The coupling can be much stronger in this case, however, as the process is resonant with the electron-spin transition. This is particularly relevant for the hyperfine transitions of $^{167}$Er, which in large fields can be driven indirectly via the high energy Kramers doublet transition. In this case the phonon frequencies $\omega_1$ and $\omega_2$ must precisely match the energies of two Kramers doublet transitions differing by a hyperfine splitting $(\omega_1 - \omega_2)/2\pi \approx 1\,\text{GHz}$. Although this resonant phonon process doesn't admit a continuum of phonon frequencies, it is important when the electronic spin transition energies are near the peak of the phonon bath. This is approximately 80 GHz at 1.4 K, as shown in Figure 2.4.

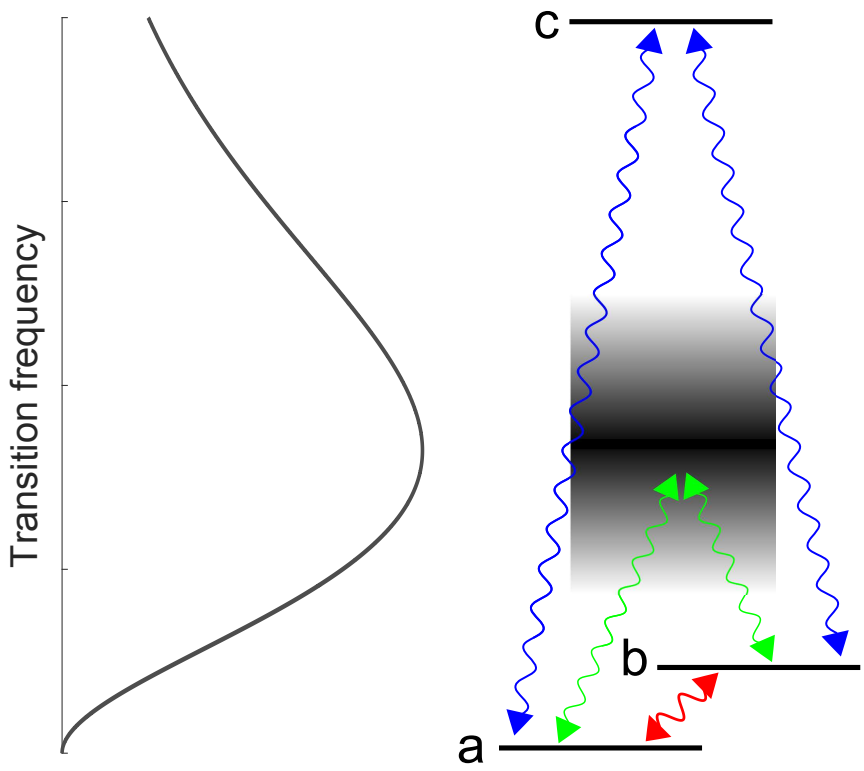


**Figure 2.5:** An illustration of phonon mediated spin-lattice coupling. **The left hand side** shows a thermal phonon distribution. **The horizontal black bars on the right** represent three energy levels of an Er ion labelled **a**,**b** and **c**. Low energy phonons (**red**) are resonant with the **a** ↔ **b** transition, and will drive it directly. A continuum of phonon pairs (**green**) can drive the same transition indirectly, as a Raman process. A higher energy level **c** within the phonon bath will also drive the a ↔ b transition indirectly, via the **blue** phonons. This is a resonant two-phonon process called Orbach coupling.

## 2.5 Energy structure and dynamics of Erbium in Silicon

So far this chapter has focused on the structure and dynamics of rare earths in solid state insulators. When doped into semiconductors, the structure and dynamics become more complicated. These additional properties are key to single-site detection of Er ions in Si, however. This section outlines the properties of Er:Si relevant to the investigations in Chapter 5.

Section 2.5.1 presents an outline of optically stimulated charge transfer in Si. This covers both the energy level structure of Si and the interaction between the lattice and light. Section 2.5.2 then explains how the $4f$-shell levels fit into the Si energy level structure. Section 2.5.3 concludes with a description of the charge dynamics in the Er:Si system, and explains how these dynamics are detected in this thesis.

### 2.5.1 Optical stimulation of charge carriers

Silicon is a semiconductor with a relatively low energy bandgap; 1.15 eV at liquid helium temperatures. This allows optical stimulation to mobilise charge carriers in the lattice. These charges carriers can take the form of electrons in the conduction band or holes in the valence band. The quantity of mobilised charge will also depend on the wavelength of light.

Photons with energies greater than 1.15 eV (1100 nm) can excite electrons from the valence band into the conduction band. This 'above-bandgap' stimulation can mobilise large amount of charge, in the form of free electrons and holes (see Figure 2.6).

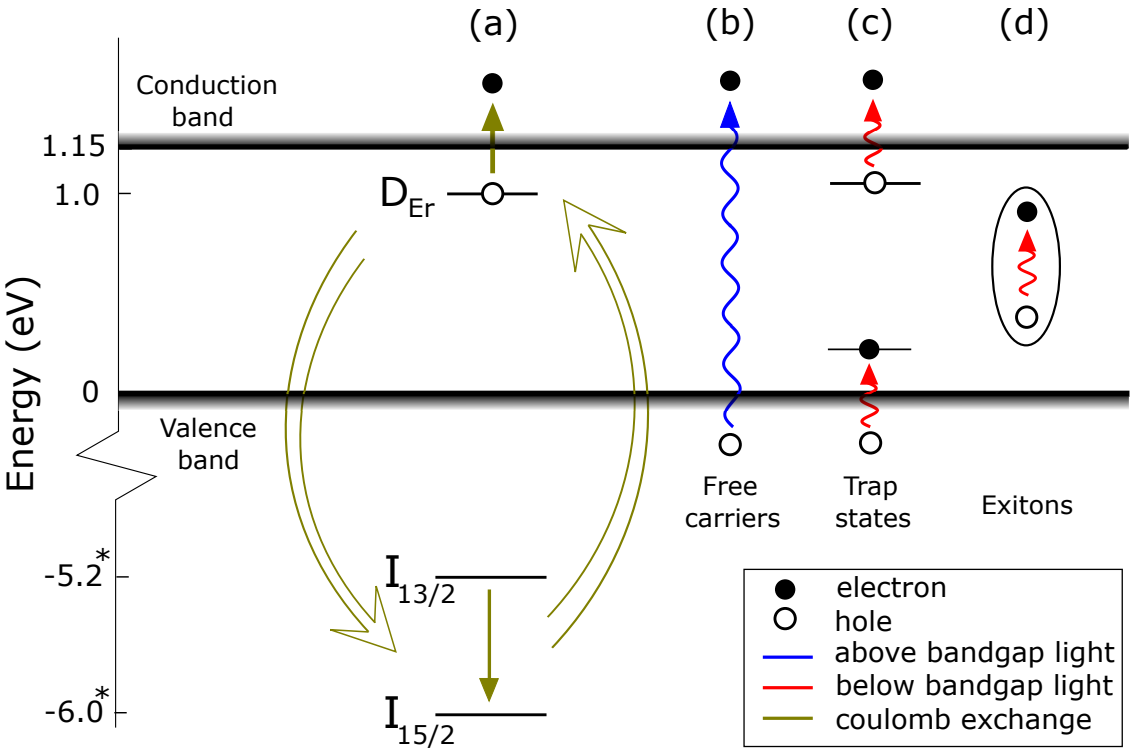


**Figure 2.6:** The energy level structure and dynamics of Er:Si **(a)** Coulomb exchange **(gold)** can transfer energy from the excited $I_{13/2}$ level to an electron that's weakly bound to the erbium related doner level $D_{Er}$ (see Section 2.5.3). This releases the electron to the conduction band. Note also that the relative energy of the 4f levels in Si marked with a **'*'** are not well known (see Section 2.5.2) **(b)** Above bandgap light **(blue)** can excite electrons from the valence band, mobilising both the electron and a hole as a pair of free carriers. **(c)** Below bandgap light **(red)** can mobilise charge carriers from shallow trap states near the valence and conduction bands. **(d)** below bandgap light will also create short lived excitons. These uncharged pseudo-particles exist for only microseconds and carry as little as 14 meV of energy.

Below-bandgap photons can also mobilise charges, but in smaller amounts. Because these photons cannot promote electrons from the valence band, they rely on impurities in the Si to generate charge carriers. These impurities create energy levels in the bandgap,

and this is illustrated in Figure 2.6 (c). Such localised energy levels are called 'trap' states, and are classified as follows:

- 'Donor' states near the conduction band, formed by Group V dopants that release their $5^{\text{th}}$ valence electron.
- 'Acceptor' states near valence band, formed by Group III dopants that capture a $4^{\text{th}}$ valence electron.

Generally speaking, donor traps capture electrons from the conduction band while acceptor traps capture free holes from the valence band. Below-bandgap light mobilises charge by depleting these traps. 1550 nm light mediates this process very effectively, and it's relevance to the Er:Si system will be explained in the next subsection.

Light can also transfer energy to the lattice without mobilising charge. When this occurs an electron-hole pair called an exciton is created, which is illustrated in Figure 2.6 (d). The electron and hole that constitute the exciton are not free carriers. In fact, exciton binding energies can be as low as 14 meV and both above and below-bandgap light can stimulate this process [101]. Although excitons are produced in large amounts by optical illumination, they are short-lived with lifetimes of microseconds. For this reason they don't affect the charge dynamics on the millisecond timescales relevant to the work presented here.

### 2.5.2 Energy structure of Er:Si

Erbium takes on the 3+ configuration in silicon, as in many other materials [102]. The $4f$ levels are also situated well below the bandgap. While the energy level spacing has not been precisely determined, estimates place the $I_{15/2}$ level approximately 6 - 20 eV below the valence band [102–104]. This tight binding is a property unique to the rare earths. The reason was discussed at the start of the chapter, and is illustrated in Figure 2.1. It also prevents light from directly ionising the $4f$ electrons. Instead, an optically excited $4f$ electron can mobilise charge via a coupled trap state [105]. An explanation of this process is covered in the following section, and assumes constant illumination by light resonant with the $I_{15/2} \leftrightarrow I_{13/2}$ optical transition.

### 2.5.3 Charge dynamics of Er:Si

Charge exchange with the Si lattice occurs only if an Er ion forms an impurity complex with other dopants. When this occurs a donor level is created in the bandgap.

For example, Er-O complexes form a donor level about 150 meV below the conduction band [106]. This oxygen-related level ($D_{Er}$) is illustrated in Figure 2.1 (a). $D_{Er}$ comprises an electronic state weakly bound to a 'dangling bond' of the oxygen impurity. Wavefunction overlap between the weakly bound electron and $4f$ electrons mediates energy exchange (see Figure 2.7). This is a very short distance and strongly coupled coulomb exchange interaction. More importantly, the 800 meV potential of the $I_{13/2}$ state is sufficient to ionise this weakly bound electron.

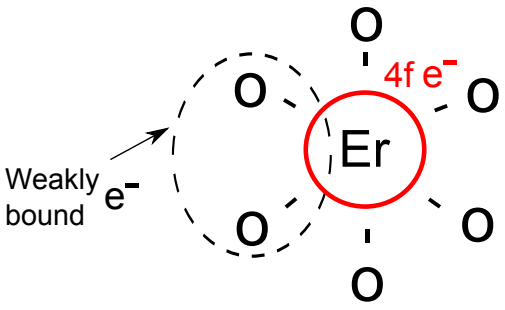


**Figure 2.7:** An example of a tetragonal Er-O complex, whose structure was determined by Carey et al. [104]. Electrons can bind to 'dangling bonds' formed by oxygen dimers, albeit weakly. This creates a donor level $D_{Er}$ in the bandgap of Si. Energy is be passed between the weakly bound electrons of the donor level and the $4f$ electrons through the Coulomb interaction.

Once the $D_{Er}$ level is depleted, the ionisation process should be quenched; there is insufficient energy from a single $I_{15/2} \rightarrow I_{13/2}$ excitation to promote an electron from the valence band. Instead, electrons from the conduction band can fill the $D_{Er}$ level once again. This process is mediated by electrons released from nearby traps. Er:Si photoluminescense studies have shown the lifetime of these traps to be hundreds of milliseconds without light. Below-bandgap light, however, shortens this lifetime to several millisecond (see Chapter 4 of Ref [107]).

An Er complex can also re-ionise captured electrons very efficiently. This is because it possesses a resonant optical absorption process, in the form of the $I_{15/2} \leftrightarrow I_{13/2}$ transition. This enhanced absorption cross-section allows the $D_{Er}$ level to release electrons at a much higher rate than other traps. Thus, the complex is a very efficient charge pump under illumination: Below-bandgap light feeds it electrons and resonant absorption rapidly re-ionises them.

The charge redistribution caused by this process is detected using highly sensitive Single Electron Transistors (SET's) in this thesis. SET's were introduced in Section 1.2, and a detailed summary of their operation is presented in Section 3.4.

## 2.6 Summary

This chapter aimed to provide several key pieces of theoretical knowledge, necessary for understanding and analysing the results of this thesis. Firstly, Section 2.2 presented the $4f$-shell and crystal-field Hamiltonian parameters relevant to rare earth ions. These parameters are used to analyse the crystal-field structure of a single Er:Si ion in Chapter 5.

Section 2.3 then conferred a statistical model for inhomogeneously broadened ensembles in Er:YSO. This model was required for analysing the optical absorption lines presented in Chapter 4. Section 2.4 focused on the dynamic interactions that affect the coherence properties of rare earth ions, both in Si and YSO. An understanding of these interactions is critical to achieving the long lifetimes and coherence times presented in Chapter 4. Finally, the Er:Si energy structure presented in Section 2.5 is useful for understanding the single Er spectra presented in Chapter 5.

Chapter 3

# Experimental techniques

The following chapter outlines the key techniques and equipment required for the spectroscopic investigations presented in Chapter 4. Section 3.1 describes the relevant optical spin-pumping techniques used for manipulating large ensembles of $^{167}$Er ions. Section 3.2 follows with an outline of optical modulation spectroscopy. This outline includes the transfer equations relevant for phase and amplitude modulation, as both are used to obtain $^{167}$Er : YSO spectra. A very brief description of photon echoes in then presented in Section 3.3; this coherent-transient technique is used for the coherence measurements in Section 4.11. The chapter concludes with a description of the charge sensing technique used to detect single Er:Si ions, in Section 3.4.

## 3.1 Optical spin pumping of hyperfine states.

For temperatures greater than a few Kelvin, an ensemble of $^{167}$Er ions will have an equal number of ions in each hyperfine state. Such an ensemble can be described by an equal mixture of hyperfine states $m_I = \{|{-7/2}\rangle, \cdots, |{+7/2}\rangle\}$. Broadly speaking, spin-pumping encompasses methods for creating non-thermal distributions of such hyperfine states. In this thesis, optical spin-pumping via laser absorption is used for spectral holeburning and nuclear spin polarisation. For optical spin-pumping to work effectively with the hyperfine states of $^{167}$Er, there are two basic requirements:

- There must be sufficient mixing between hyperfine states to effectively drive optical $|\Delta m_I| \geq 1$ transitions.
- For efficient pumping, the hyperfine transition lifetimes must be much longer than the optical lifetimes.

These criteria are often met for non-Kramers trivalent rare earths in low symmetry hosts. The results presented in Section 4.10 demonstrate that these requirement have now been met for the hyperfine states of $^{167}$Er also.

### 3.1.1 Spin-based spectral holeburning

Spectral holeburning occurs when $\Gamma_h \ll \Gamma_{inh}$. It is used in this thesis to probe the hyperfine transition energies and dynamics of $^{167}$Er:YSO. It is also an important tool in many quantum memory protocols [47, 50, 57].

Holeburning involves the creation of a spectral transmission window by narrow-band optical excitation. The depletion of resonant ions at the wavelength of the spectral 'hole' creates additional absorption peaks at the excitation wavelengths of adjacent ground-state spin-levels. These absorption peaks are called 'anti-holes', and the entire holeburning process is described in Figure 3.1. Sub-figures a) - c) represent a simplified holeburning scenario, where the difference in ground-state energy spacings is much larger than $\Gamma_{inh}$. In this scenario, burning a single hole will show at most two images of the holes and six anti-holes.

For most rare earth ensembles, however, more complex holeburning spectra are observed. This occurs because $\Gamma_{inh}$ is larger than the spin transition splittings, and thus a single frequency laser will drive multiple transitions. For the system in Figure 3.1, the number of spectral features increases nine-fold because of this overlap. In this case, two side-holes form at wavelengths corresponding to the $|2\rangle \leftrightarrow |1'\rangle$ and $|2\rangle \leftrightarrow |3'\rangle$ transitions. Four more side-holes form because the ions are driven out of each ground-state spin-levels $|1\rangle, |2\rangle$ and $|3\rangle$, and the number of anti-holes will likewise increase. A complete spectrum of holes and anti-holes is presented in Sub-figure e), for large $\Gamma_{inh}$.

With it's eight hyperfine states, $^{167}$Er can potentially exhibit thousands of holes and anti-holes in an optical spectrum. However, the limited mixing of hyperfine states will suppress most transitions. Because of this, holeburning spectra in $^{167}$Er ensembles usually have only a few holes and anti-holes [69]. For $^{167}$Er in large fields, the energy spacings between the largest holes and anti-holes reveal the $I_{15/2}$ hyperfine transition energies. Similarly, the images of the spectral holes are associated with the $I_{13/2}$ hyperfine transitions. This general rule is used to determine the $^{167}$Er:YSO hyperfine transition energies in Section 4.5.

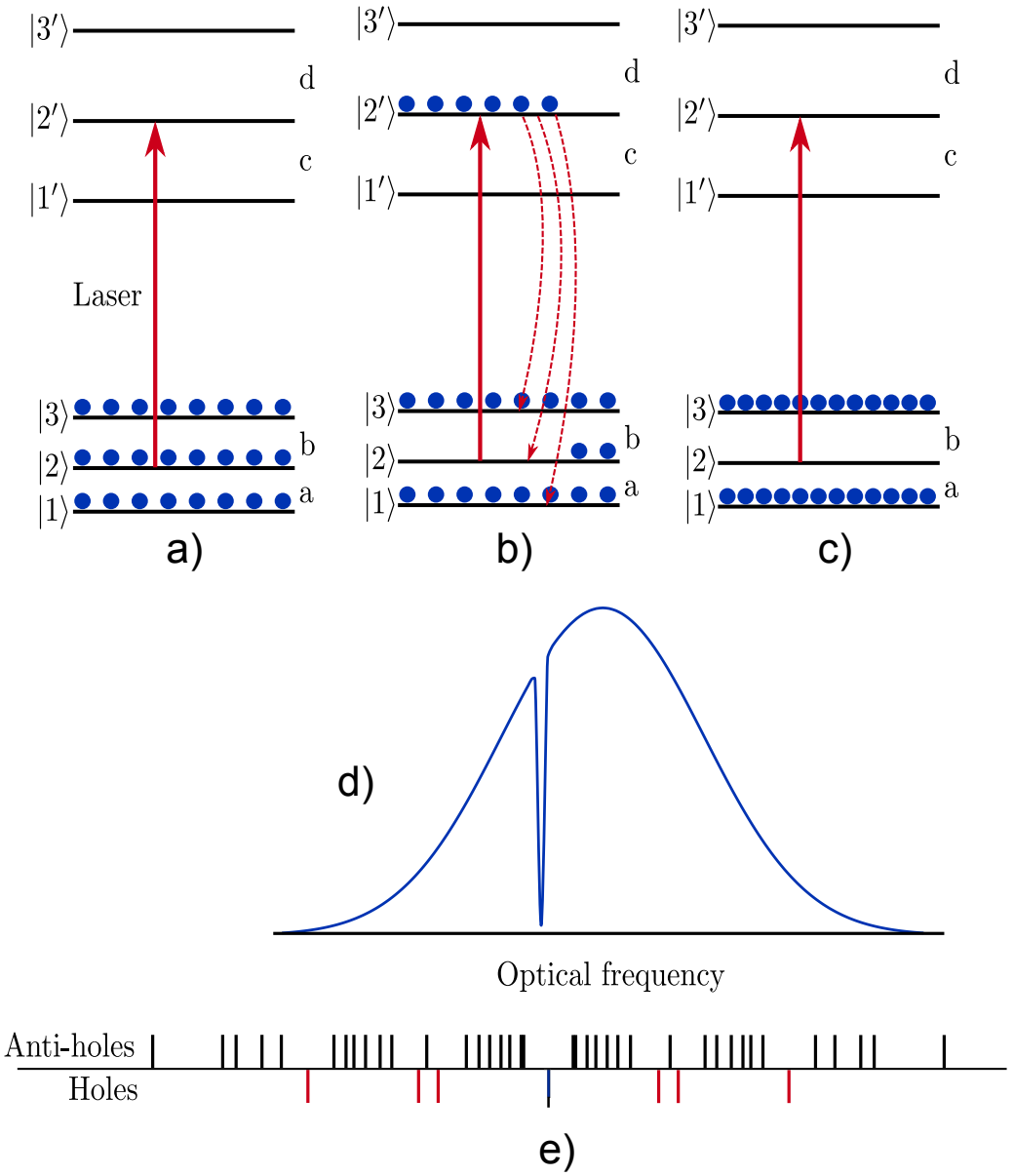


**Figure 3.1:** Spin-state holeburning for an ion with three ground and excited spin-levels. **a)** A laser tuned to the $|2\rangle \leftrightarrow |2'\rangle$ transition will transfer population from ground-state spin-level $|2\rangle$ to the excited state spin-level $|2'\rangle$. **b)** Excited ions will decay to the ground-state spin-levels $|1\rangle, |2\rangle$and $|3\rangle$. Those that decay to spin-level $|2\rangle$ are once again excited by the laser. **c)** Repeated excitation will remove all ions from ground state $|2\rangle$. **d)** A spectral hole in an inhomogeneously broadened ensemble. Side-holes and anti-holes are not shown. **e)** Indication of side-hole and anti-hole wavelengths when $\Gamma_{inh}$ is much larger than the energy splitting between spin-states. Figure reproduced from the thesis of R. Ahlefeldt [78].

### 3.1.2 Measuring transition lifetimes using spectral holeburning

As mentioned above, spectral holeburning is also used in this thesis to probe the dynamics of hyperfine transitions. The sub-ensembles of ions that undergo pumping represent non-thermal states. This imbalance is opposed by spin relaxation, in the form of spin-spin

coupling or spin-lattice coupling (see Section 2.4). These processes act to thermalise the pumped ions with the spin-bath or crystal. Thus, spectral holes fill-in as ions relax into the depleted spin-levels associated with the hole. By recording the amplitude of spectral holes and anti-holes as a function of time, this relaxation rate can be measured. There are, however, two important considerations when interpreting such time-series measurements:

Firstly, burning a spectral hole will often pump population into multiple spin-levels. The hole will then fill at a rate determined by relaxation from each spin-level (see equation 2.10). This makes it difficult to determine the lifetime of a single spin-transitions. However, for quantum memory implementations that require narrow spectral features (such as two-level AFC's), the average rate at which the hole fills is the relevant metric. For $^{167}$Er:YSO, this parameter is investigated experimentally in Section 4.10.

Secondly, spectral holes can broaden if strong dephasing interactions are present. Transition dephasing causes the optical frequencies of the ions to shift, and some of the ions which form the 'walls' of the spectral hole will shift into the burnt region. This process is a type of spectral diffusion (see Ch4 of [81]), and potential mechanisms associated with the spins of the Er ions have already been discussed in Sections 2.4.3 and 2.4.4. The amount of diffusion caused by these short-range interactions depends on the interaction strength; interactions involving the electronic spins usually contribute more diffusion than the equivalent nuclear spin interactions. More specifically, any interactions which flips an Er electronic spin will cause significant dephasing of neighbouring Er ions via the magnetic dipole interaction.

Optical excitation can also contribute significant spectral diffusion in Kramers systems, predominantly through the electronic dipole interaction. Because this diffusion occurs while the spectral feature is being prepared, it's often referred to as Instantaneous Spectral Diffusion (ISD). The 10 ms lifetime of the Er optical transition further limits the timescale on which this diffusion process can act.

Irrespective of the diffusion mechanism, however, the total area of a spectral hole is conserved during (and after) spectral diffusion. Thus, measurements of hole area rather than amplitude should be used if significant spectral diffusion is present.

### 3.1.3 Spin hyper-polarisation

Spin hyper-polarisation is the process of driving a significant fraction of ions into a single spin-state. This phenomenon is exploited for quantum state preparation in atomic vapour systems [74], where polarisation selective optical spin-pumping is used [108]. However,

spin-state mixing in anisotropic rare earth sites inhibits polarisation selectivity. Instead, hyper-polarisation can be achieved with frequency selectivity if the spin-transition energies are larger than $\Gamma_{inh}$. Several rare earth ions have demonstrated this property for hyperfine transitions in solid state, including Er, Nd, and Ho [109–111]. However, the first demonstration of efficient hyper-polarisation of any rare earth system is presented in Section 4.7.

The properties required for frequency-selective optical spin-pumping are investigated in the first half of Chapter 4. With these requirements met, optical pumping is achieved by repeatedly exciting every $\Delta m_I = +1$ (or -1) optical transition within the inhomogeneously broadened population envelope. This will eventually drive all the ions in the ensemble into the $m_I = |{-7/2}\rangle$ (or $|{+7/2}\rangle$) hyperfine state, via the cascade of $\Delta m_I = \pm 1$ transitions. Pumping into a single state can also be achieved by driving with both $|\Delta m_I| = 1$ and $|\Delta m_I| > 1$ transitions; this may lead to faster pumping rates under certain situations. An example of efficient laser-driven optical spin pumping is presented in section 4.7.

## 3.2 Modulation spectroscopy

The previous section introduced the techniques of holeburning and hyper-polarisation. While both are types of optical spin-pumping, their requirements vary greatly when it comes to collecting spectra. Holeburning of hyperfine states reveals structure on the GHz scale in $^{167}$Er:YSO but requires sub-MHz resolution and accuracy. Hyper-polarisation, on the other hand, produces sub-GHz features that lack fine details. However, these absorption features often have exceedingly large optical depth (OD), requiring an imaging technique which avoids saturation.

The difficulty then, is to realise an experimental setup that can fulfil these requirements. As it turns out, modulation spectroscopy is able to satisfy all these requirements.

The approach used in this thesis is a minor tweak of an old technique; optical heterodyne-spectroscopy has been around for many decades [112]. The novel aspect is the use of opto-electronics designed for the 1550 nm telecom band. In particular, GHz bandwidth Electro-optic Modulators (EOMs) and detectors that are readily available and inexpensive at this wavelength[1].

Modulation spectroscopy relies on detecting the sideband-carrier beat generated by the

[1] 10 GHz electro-optic modulators and frequency domain detectors cost approximately $1000 [113, 114]

EOM. Sideband modulation allows the laser to remain locked, which is key to achieving sub-MHz accuracy. While this greatly improves the potential resolution of the scan, it also simplifies experiments where scans are combined with narrow spectral holeburning or coherent pulsing. Two lasers are otherwise required for such experiments; a stabilised laser for holeburning and pulsing, and a free-running laser for scanning. Furthermore, the phase sensitivity of this technique makes it uniquely suited for high OD measurements.

### 3.2.1 An overview of amplitude and phase modulating EOM's

Both Phase Modulating (PM) and Amplitude Modulating (AM) EOM's were used to collect the spectra in Chapter 4, although AM spectra predominated for reasons outlined in the next section. To explain how these spectra were collected, this section presents an analysis of the modulator equations.

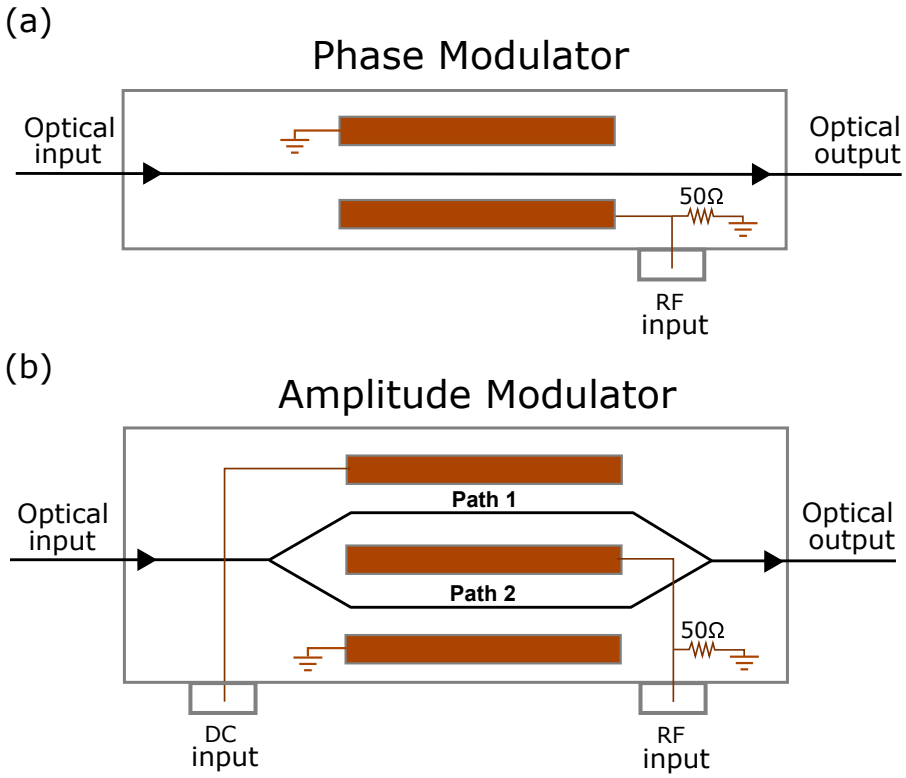


**Figure 3.2:** Physical diagrams of **(a):** PM-EOM and **(b):** AM-EOM. Internally they comprise of $LiNbO_3$ crystals, whose refractive indices are modulated via electrodes (brown). For the AM-EOM the light is split into two paths, forming a Mach-Zehnder interferometer. Applying a bias voltage to the DC input will shift the optical phase $\theta$ of path 1, which determines the carrier amplitude and phase. Applying RF modulation to path 2 generates optical sidebands.

The electric field output from these modulators can be derived from the schematics

presented in Figure 3.2. For low modulation depths, the phase modulator output is:

$$E_{\mathrm{PM}} = \left[ \underbrace{\alpha e^{-i\omega t}}_{\mathrm{SB1}} + \underbrace{\beta}_{\mathrm{carrier}} - \underbrace{\alpha e^{i\omega t}}_{\mathrm{SB2}} \right] e^{if_0 t}$$

The variables in this expression are the sideband amplitudes $\alpha$, the modulation frequency $\omega$, and the laser (carrier) amplitude and frequency $\beta$ and $f_0$. Implicit in this expression is the assumption of slow modulation ($\omega \ll f_0$) and low modulation depth ($\alpha \ll \beta$). This yields an intensity output:

$$\begin{aligned} I_{\mathrm{PM}} &= E^*_{\mathrm{PM}} E_{\mathrm{PM}} \\ &= 2\alpha^2 \left(1 + \cos 2\omega t\right) + \beta^2 \end{aligned}$$

Here the weak amplitude modulation at frequency $2\omega$ is a result of truncating the higher order sidebands in the electric field equation. In-fact, no amplitude modulation is produced with PM because the beat between the carrier and second-order sidebands precisely cancel this term.

The output of an amplitude modulator is slightly more complicated because it has two optical paths:

$$\begin{aligned} E_{\mathrm{AM}} &= \left[ \alpha e^{-i\omega t} + \beta - \alpha e^{i\omega t} + e^{i\theta} \left( -\alpha e^{-i\omega t} + \beta + \alpha e^{i\omega t} \right) \right] e^{if_0 t} \\ &= \left[ \underbrace{-i \sin\left(\theta/2\right) \alpha e^{-i\omega t}}_{\mathrm{SB1}} + \underbrace{\cos\left(\theta/2\right) \beta}_{\mathrm{carrier}} + \underbrace{i \sin\left(\theta/2\right) \alpha e^{i\omega t}}_{\mathrm{SB2}} \right] 2e^{i(f_0 t + \theta/2)} \end{aligned}$$

here an additional term $\theta$ is required to describe the phase between the optical paths, and the intensity output is given by:

$$I_{\mathrm{AM}} = 8\alpha\beta \sin\theta \sin\omega t + 2\left(1 + \cos\theta\right)\beta^2$$

where the $\alpha^2$ terms are ignored. The phase term $\theta$ affects the intensity of both the carrier and amplitude modulation. In particular, maximum AM is achieved with a phase $\theta = \pi/2$.

### 3.2.2 The properties of amplitude and phase modulation

PM is ideal for detecting weak signals, and is used for applications like Pound-Drever-Hall (PDH) laser-stabilisation. This is because the modulation power $\alpha$ can be quite large, and

yet contribute no intensity noise atfrequency $\omega$. Absorption of a single sideband, however, will break the modulation symmetry and generate an AM signal. This is used to detect small absorption with high modulation power at RF frequencies.

The optical depth of 50 ppm Er:YSO, however, produces a clear absorption signal. Because of this, the small-signal sensitivity of PM is not required. Instead, PM has a distinct draw-back for high OD measurements; it's difficult to calibrate the spectral response. Physical EOM's have a frequency dependent power response. This can be parametrised by reformulating the sideband amplitude as $\alpha(\omega)$. Indeed, all the RF equipment used in the experiments of Chapter 4 exhibits frequency dependent transmissivity. To accurately record a spectral absorption profile, the frequency dependent transmission of RF power $P_0(\omega)$ through the system must be accounted for. This background signal can only be measured by recording an AM spectrum, and for this reason AM spectroscopy is predominantly used in this thesis.

### 3.2.3 The modulation power response

Even after compensating for the RF equipment, measuring absorption spectra with modulation spectroscopy is complicated. The remainder of the section outlines the analysis required to extract the real absorption profile $\eta''$ from the spectrum data.

Figure 3.3 illustrates how the three optical fields of the EOM are affected by an absorptive material. The amplitude and phase of each field is transformed differently, depending on their relative optical frequencies. Thus, the sum of the three output fields ($E_{out}$)can be written in the general form:

$$\begin{aligned} E_{out} &= \exp\left(-\eta'' + i\eta'\right) \cdot E_{in} \\ &= \left[\alpha_- e^{-i(\omega t - \phi_-)} + \beta e^{i\varphi} - \alpha_+ e^{i(\omega t + \phi_+)}\right] e^{if_0 t} \end{aligned} \tag{3.1}$$

where the following relationships apply:

$$\begin{aligned} \alpha_\pm &= \alpha_0 e^{-\eta''(f_0 \pm \omega)} \\ \phi_\pm &= \eta'\left(f_0 \pm \omega\right) \end{aligned}$$

The term $\varphi$ determines the phase relationship between the sidebands and carrier, making Equation (3.1) general enough to describe both amplitude and phase modulation. In particular, pure PM is realised with $\varphi = 0$ and AM with $\varphi = \pi/2$. Using the above

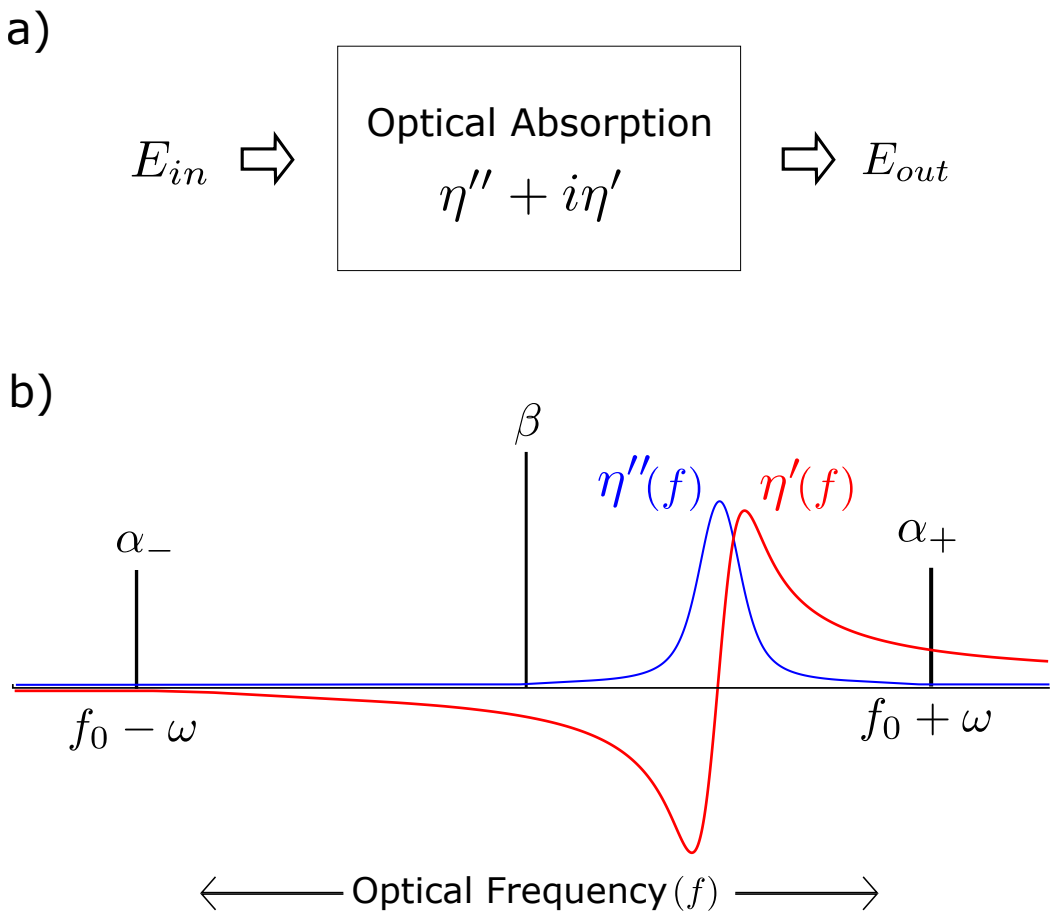


**Figure 3.3:** **a)** The three optical fields of the modulator (collectively referred to as $E_{in}$) pass through an absorptive medium and the collective output field incident on the optical detector is given by $E_{out} = e^{\eta'' + i\eta'} E_{in}$. **b)** For the $^{167}$Er:YSO crystals investigated in this thesis, the real absorption $\eta''$ is narrow enough to fall within the sweep of just one sideband. This simplifies the algebraic form of the output field $E_{out}$, even though the complex absorption $\eta'$ is still quite broad.

expression one can then calcuate the power $P(\omega)$, corresponding to the RF intensity at frequency $\omega$ output from the optical detector (assuming modulation at frequency $\omega$ as well). This is proportional to the square of the optical intensity $I$, because the detector converts optical intensity to electrical voltage:

$$P(\omega) \propto (E^*_{out} E_{out})^2$$

With some algebraic manipulation (see Appendix B) this can be expressed as follows:

$$P(\omega) \propto \alpha_-^2 + \alpha_+^2 - 2\alpha_-\alpha_+ \cos(2\varphi - \phi_- - \phi_+)$$

Assuming the real absorption $\eta''$ is sufficiently narrow in frequency, the lower sideband is

not attenuated and can be treated as constant ($\alpha_- = 1$):

$$\therefore P(\omega) \propto 1 + \alpha_+^2 - 2\alpha_+ \cos\left(2\varphi - \phi_- - \phi_+\right) \tag{3.2}$$

Although it's valid to ignore the absorption of the lower sideband $\alpha_-$, the phase dependence of the lower sideband $\phi_-$ must be accounted for. This is because the dispersive component $\eta'$ tends to cover a much broader frequency range than the absorptive $\eta''$. This is because a Lorentzian absorptive feature falls off with the inverse square of detuning, while the associated dispersion falls off with the inverse detuning (see Figure 3.3). The optical phase-shift due to this dispersive component is evident in the high OD measurements of Chapter 4.

The closed form above does not map the real absorption $\eta''$ to RF power in a linear manner. For AM spectroscopy ($\varphi \approx \pi/2$) there is a background power $P = 2\alpha^2$ when no absorption is present[2]. If the upper sideband is completely absorbed, however, the optical intensity will be halved and the RF power will drop by only 3/4, equivalent to 6 dB. One would think this issue limits the usefulness of modulation spectroscopy. However, the phase dependence makes this method well suited for measuring very high OD's. This will be explained in the next two subsections, and illustrated in Figure 3.4.

### 3.2.4 Determining real and complex absorption

At first glance equation (3.2) seems like a complicated function of phase and amplitude and not suitable for extracting the real-absorption profile $\eta''(f)$. However, the absorptive and dispersive components of any material are related by a one-to-one Fourier map, known as the Kramers-Kronig relations. Hence there is sufficient information in the absorption profile $\eta''(f)$ to determine the RF power $P(\omega)$. More importantly, the reverse is also true and there is direct map between the AM spectrum recorded and the real absorption:

$$P\left(\omega\right) \leftrightarrow \eta''\left(f\right)$$

A precise estimate of $\eta''$ from the spectrum is relatively straight forward when some information about the absorption profile is already available. The optical transition frequencies in $^{167}$Er:YSO are determined in Section 4.5, and an estimate of the transition linewidth

[2]Physical amplitude modulators have some residual PM due to imperfections in the electrodes, causing imbalance in the RF modulation. This can be accounted for with a small phase offset $\delta$, such that $\varphi = \pi/2 + \delta$. For the modulator used in this work, $\delta \approx 5^0$.

is presented in Section 4.6. This information drastically reduces the fitting parameters required to model $\eta''$, so the amplitude of the inhomogeneously broadened absorption profile $\eta''(f)$ is the only free parameter remaining.

### 3.2.5 High optical depth

In 2010 Hedges et al. were the first to demonstrate an efficient quantum memory for light, which required an optical absorption of 140dB [47]. This value had to be inferred by indirect measurements, because their measurement techniques could not resolve more than 30dB of absorption. This resolution floor is also evident for the $^{167}$Er:YSO measurement in Figure 4.3 of Chapter 4. Modulation spectroscopy presents a more direct approach to estimating large OD's. To illustrate this point, Figure 3.4 presents two simulated spectra with large absorption; up to 80dB.

Evident in this figure is the effect of dispersion $\eta'$. Large dispersion creates a 'split peak' in the detected RF power, and the frequency separation between modulation minima is an excellent indicator of optical depth. This effect is also observed for the large optical depth presented in Figure 4.10 .

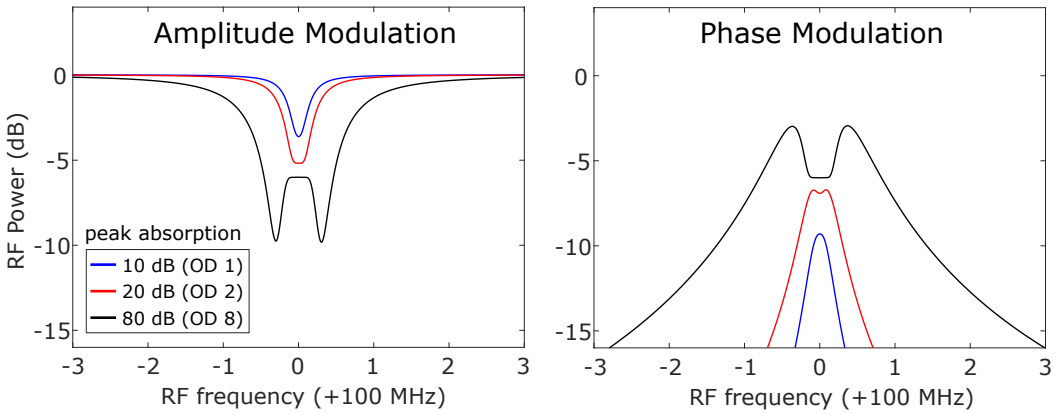


**Figure 3.4:** A model of the RF power output from an optical detector, given a 100 kHz wide optical absorption feature with a Lorentzian profile. This profile is similar to that used by Hedges et al. in their demonstration of an efficient quantum memory for light [47]. **The left hand side** shows the RF power output with AM spectroscopy, while **the right hand side** shows the case for PM spectroscopy. Here we assume the laser (carrier) is detuned from the optical absorption feature by 100 MHz to prevent any dispersive phase-shift of the carrier. Thus, a typical sub-GHz spectrum analyser acting as a RF frequency source and detector can resolve the three traces in either sub-figure.

## 3.3 Photon and spin echoes

Echoes are a widely used technique across many areas of quantum science, and are only described briefly here. Photon echoes are the optical equivalent of spin echoes in NMR [115] and were first demonstrated in ruby in 1964 [116]. In Section 4.11, echo sequences are used to overcome the dephasing of the atomic ensemble due to inhomogeneous broadening. As the name suggests, an 'echo' of the Free Induction Decay (FID) signal is produced, but at a time much longer than the dephasing time $T_2^*$ of the FID.

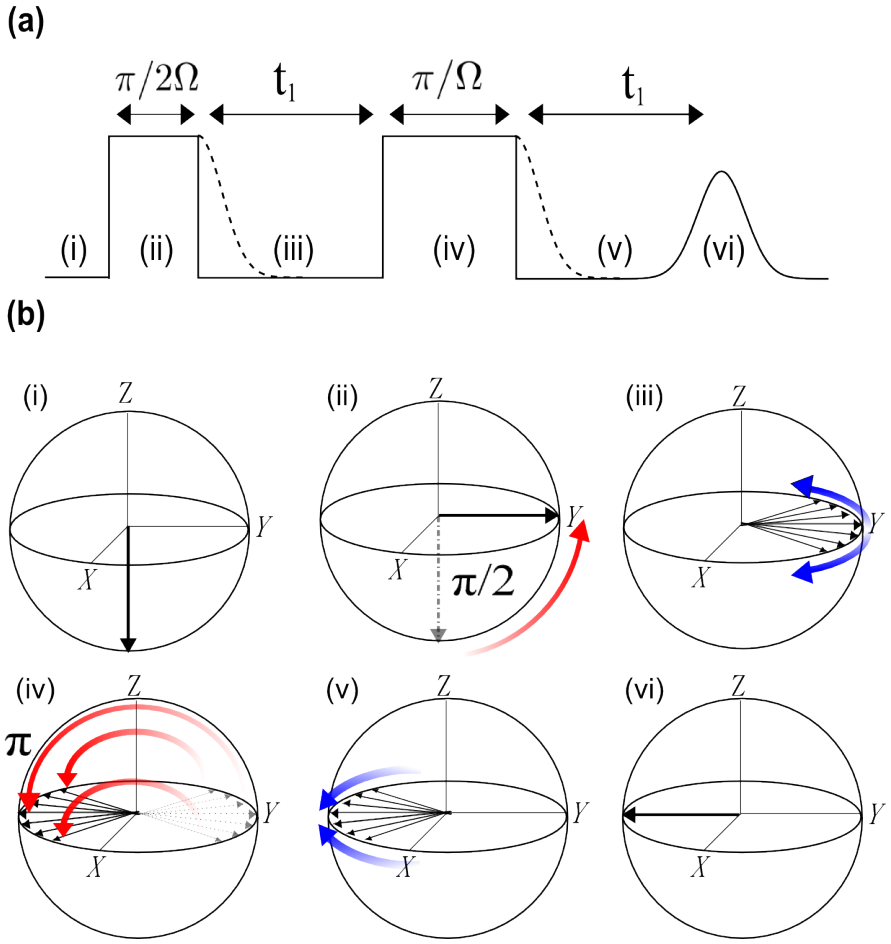


**Figure 3.5:** The photon echo sequence, broken up into six stages, with the solid line showing the applied light pulses and dotted line showing the FID. Part (a) represents the light intensity as a function of time, with the solid line showing the light pulses and echo and the dotted line showing the FID. Part (b) represents the Bloch sphere evolution of the ensemble vectors. Stage (i) shows the initial quantum state, then the $\pi/2$ pulse is applied in stage (ii), detuning occurs in stage (iii) followed by a $\pi$ pulse in stage (iv). Finally rephasing occurs in (v) and a coherent emission is produced in stage (vi) once the ensemble ions are in phase once again.

The two-pulse echo sequence is explained simply if we consider the Bloch sphere representation, where the coherent state of a two level system is represented as a vector on

a unit sphere. This is shown in 3.5 (b). The first pulse, known as a $\pi/2$ pulse, takes the atomic ensemble from the ground state ($-\hat{\mathbf{Z}}$ vector) and rotates it by $\theta = -\pi/2$ to vector $\hat{\mathbf{Y}}$. At this point each ion in the ensemble is in a 50:50 superposition of the ground and excited states. The ensemble is then left to freely evolve for a time $t_1$, and the individual detuning's of the ensemble atoms cause dephasing across $\hat{\mathbf{X}} - \hat{\mathbf{Y}}$ plane. A $\pi$ pulse is then applied to the ensemble, and the vector representing each ion rotates 180 degrees about the $\hat{\mathbf{X}}$ axis. This acts to reverse the time evolution of the ensemble. Hence after another time period of length $t_1$, the ensemble vectors rephase to the $-\hat{\mathbf{Y}}$ vector. At this point in time coherent light is emitted, due to the non-zero net polarisation of the ensemble.

In chapter 4 photon echoes are used to determine the coherence time $T_2$ of a two-level optical transition. This is achieved by measuring the echo amplitude as a function of delay time $t_1$, because decoherence will cause an exponential decrease in echo amplitude $P$ with increasing delay time; $P(t_1) \propto \exp(-2t_1/T_2)$ [117].

More complex pulse sequences can be built up using the same pulses used for the two-pulse echo. In particular, coherent manipulation can extend to multiple levels. In Chapter 4, Raman echoes are used to manipulate hyperfine spin coherence via an intermediary optical level. Conceptually, the spin-evolution of this Raman echo is analogous to the two-pulse echo shown in Figure 3.5, and once again the coherence time of the spin transition can be determined by measuring the optical echo amplitude [118].

## 3.4 Single electron transistors

The ability to detect single ionisation events in solid state is key to resolving individual erbium ions in silicon. This detection is achieved with a device that was developed 30 years ago, known as the Single Electron Transistor (SET) [119]. This section aims to familiarise the reader with the physics of SET's, to better understanding the data presented in Chapter 5.

### 3.4.1 SET structure

An intuitive understanding of SET dynamics can be achieved by first analysing a simpler device. Shown in Figure 3.6, this simplified device exploits the properties of quantum tunnelling. A finite potential well (the island) is formed by placing two insulating layers (the tunnel-junctions) along a circuit path. This differs from a SET only because the energy levels of the island are not quantised. Passing a current through this well relies on

quantum tunnelling, and only occurs if the potentials in this circuit are biased such that $V_S \geq V_I > V_D$. Tunnelling is suppressed if $V_I > V_S$, due to the thick potential barrier between source and drain. This current-blocking effect is called Coulomb-blockade. The potential of the island is controlled by an electrode called the gate, with voltage $V_G$. Not surprisingly, the current-voltage ($I - V_G$) response of this device is similar to a classical transistor.

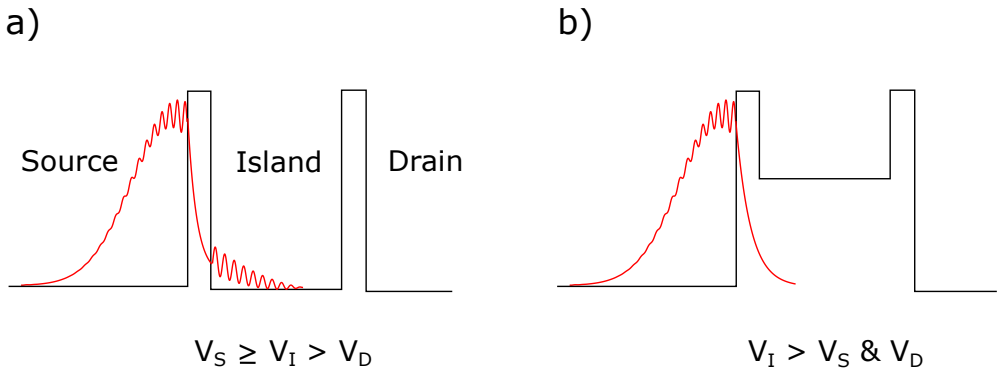


**Figure 3.6:** A conceptual double-barrier device. Quantum tunnelling through such a device was first demonstrated in 1974 [120]. **a)** If the island potential is equal to or less than the source potential, their is a non-vanishing probability that the electron can pass through both tunnel junctions. The tunnel junctions act as resistors while current flows, so the device behaviour is near-Ohmic. **b)** When the island potential becomes sufficiently positive, the double-barrier device blocks current with great efficacy.

A true SET takes this concept one step further, by reducing the size of the island until it forms a quantum dot. In this regime, the capacitance of the island $C_I = q/V_I$ is so small that a single electron can raise the potential of the island above the source potential, causing a self-induced Coulomb-blockade. This concept is illustrated in Figure 3.7, where an additional electron will add a unit of charge to the island $\Delta q = e$ and raise the potential by a uniform amount $\Delta V_e$. This forms a ladder of discrete energy levels, with one 'rung' for each electron.

Just like in the macroscopic case, tuning the gate voltage will also change the potential of the island. The $I - V_G$ trace, however, is considerably more interesting in this case. Current can only tunnel through the quantum dot if the next available energy level or 'rung' on the ladder sits between the source and drain potentials. If the next level is too low, an electron becomes trapped in the dot; too high and Coulomb blockade occurs.

This situation leads to resonant current peaks in the $I-V_G$ trace of the SET, illustrated in Figure 3.8. These resonant peaks, called Coulomb peaks, are spaced precisely $\Delta V = e/C_I$ apart such that each successive peak corresponds to a unit increase in the electronic

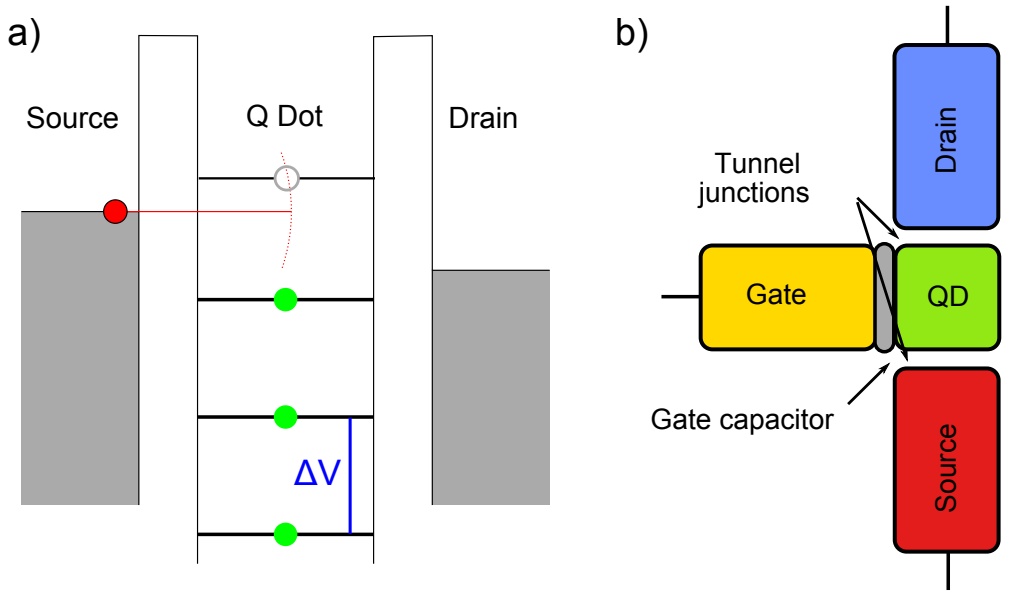


**Figure 3.7:** The single electron transistor. **a)** The quantised electronic energy levels of a quantum dot shown in **green**. Even though the potential of the dot is below the source potential, the next available energy level lies above it. Hence, an electron from the source **(red)** is prevented from tunnelling onto the quantum dot because of self-induced Coulomb blockade. **b)** Simplified SET schematic. Figure reproduced from **[121]**

occupancy of the quantum dot. The capacitance of the quantum dot increases very slowly with the number of electrons, so the peak spacings tend to contract for higher occupancy.

An important parameter for SET operation is the source-drain bias: $V_{\mathrm{SD}} \equiv V_{\mathrm{S}} - V_{\mathrm{D}}$. Quite often the SET is operated in a regime where $V_{\mathrm{SD}}$ is much smaller than the peak spacing $\Delta V$. One would naively expect the Coulomb peaks to be narrower than $V_{\mathrm{SD}}$, given the tunnelling requirement. At finite temperature, however, thermal fluctuations permit a wider continuum of electron energies to pass through the transistor. At temperature $T$, the lineshape of a Coulomb peak is given by equation (2.4) of Kouwenhoven et al. [123]:

$$I(V) \propto \cosh^{-2}\left(\frac{V_{\mathrm{SD}} - V_{\mathrm{peak}}}{2.5 \cdot k_{\mathrm{B}}T/e}\right) \tag{3.3}$$

Although the experimental lineshapes diverge somewhat from this model, the peaks positions and widths are very stable in time. This stability is critical to detecting of individual ionisation events, as will be explained in the following section.

### 3.4.2 Detecting ionisation of a single defect

The I-V characteristics of Coulomb peaks make them ideal for detecting small changes in the quantum dot potential. If one considers the single-occupancy Coulomb peak in Figure

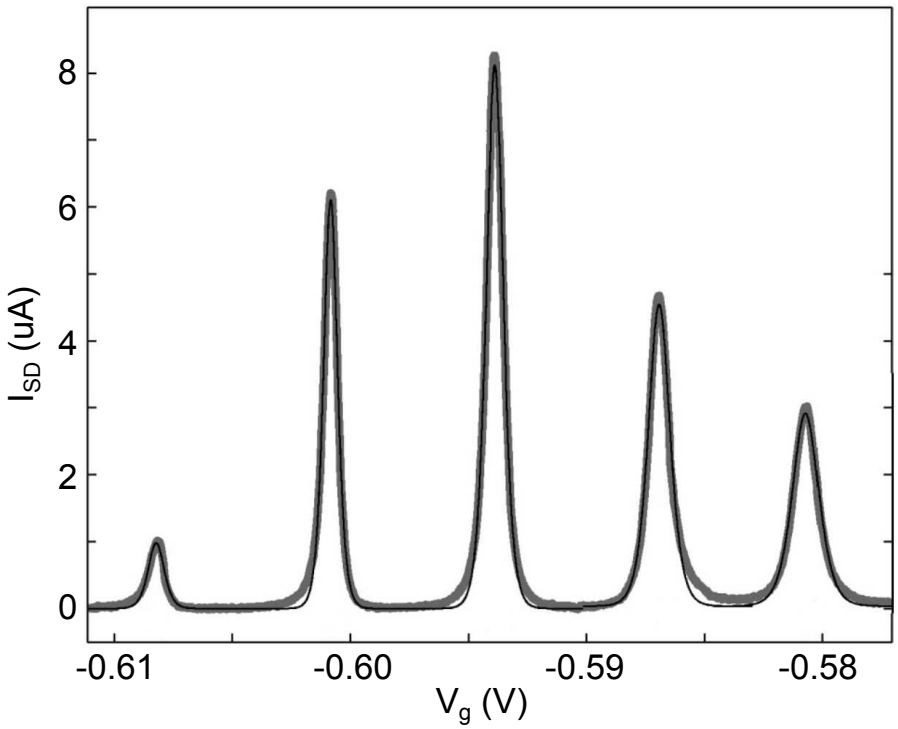


**Figure 3.8:** An $I - V_G$ trace of an SET recorded at 60 mK [122]. The Coulomb peaks are clearly visible, starting with single electron occupancy on the far left. As the dot becomes larger the total capacitance increases, and so the spacing distance reduces towards the right. The **thin black line** shows the fit given by equation 3.3. The first observation of coulomb peak structure in an I-V trace was in 1988 [119]. The phenomenon was poorly understood at first, but this device was eventually dubbed the 'Single Electron Transistor'.

3.8, a 10 mV change in $V_G$ produces 1 $\mu$A of tunnelling current. The quantum dot isn't just capacitively coupled to $V_G$, however. Any nearby source of electrostatic disturbance will have a noticeable effect on the capacitance of the dot. For an $Er^{3+}$ ion within several nm of the dot, the charge redistribution described in Section 2.5 produces such an effect.

To get a sense of scale for this effect, ionisation *within* the dot would shift the potential by an entire Coulomb peak spacing $\Delta V$. For the most part, however, optically stimulated charge redistribution shifts the potential by less than a Coulomb peak width. Figure 3.9 demonstrates the time trace acquired upon charging and discharging of a single Er related level $D_{Er}$ (refer to Subsection 2.5.3).

### 3.4.3 Sensing with FinFET's

Figure 3.10 illustrates the Fin shaped Field Effect Transistor (FinFET) used for the experiments in this thesis. These FinFET's are based on commercial designs and have been used as SET's since 2006 [124]. Unlike planar FET's, the channel in a FinFET looks more

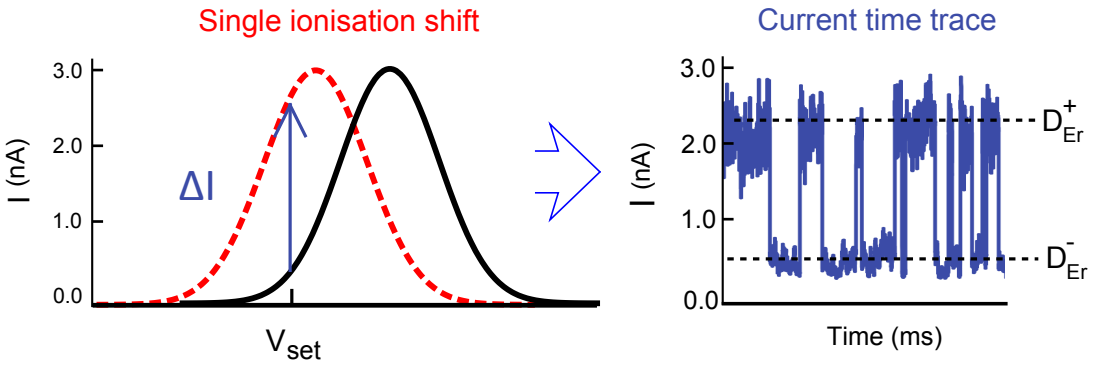


**Figure 3.9: The left side** illustrates the shift of the coulomb peak due to charge redistribution near the quantum dot. With the gate voltage fixed on the wing of the coulomb peak ($V_{set}$), the shift leads to a large change in tunnelling current $\Delta I$. **The right side** shows how the tunnelling current changes in time as the Er related level $D_{Er}$ cycles through electron recovery $\left(D^{-}_{Er}\right)$ and re-ionisation events $\left(D^{+}_{Er}\right)$.

like a nanowire with a gate wrapped around three sides, which yields stronger gate confinements. This is important because it improves the gate tuning sensitivity, allowing for lower operating voltages and increased power efficiency. This also leads to highly elongated quantum dots in these devices, as the gate creates an equipotential along the length of the channel.

FinFET's are also advantageous for measurements that require optical illumination of the SET. Studies of photo-induced current noise in Al-SET devices on silicon and sapphire have shown significantly lower fluctuations in the latter [125]. Charge traps and defects in the silicon substrate below the channel are the most obvious noise source in this situation. Fortunately, the charge sensing quantum dots in a FinFET device are tens of nanometres from the silicon substrate, and are isolated from it by an oxide layer (not shown in Figure 3.10). This makes them less sensitive than planar FET's, where the quantum dots are formed in the bulk silicon itself. The metallic wrap-around gate also screens the channel from similar noise arising from the high density of interfacial defects in the oxide layer beyond the gate.

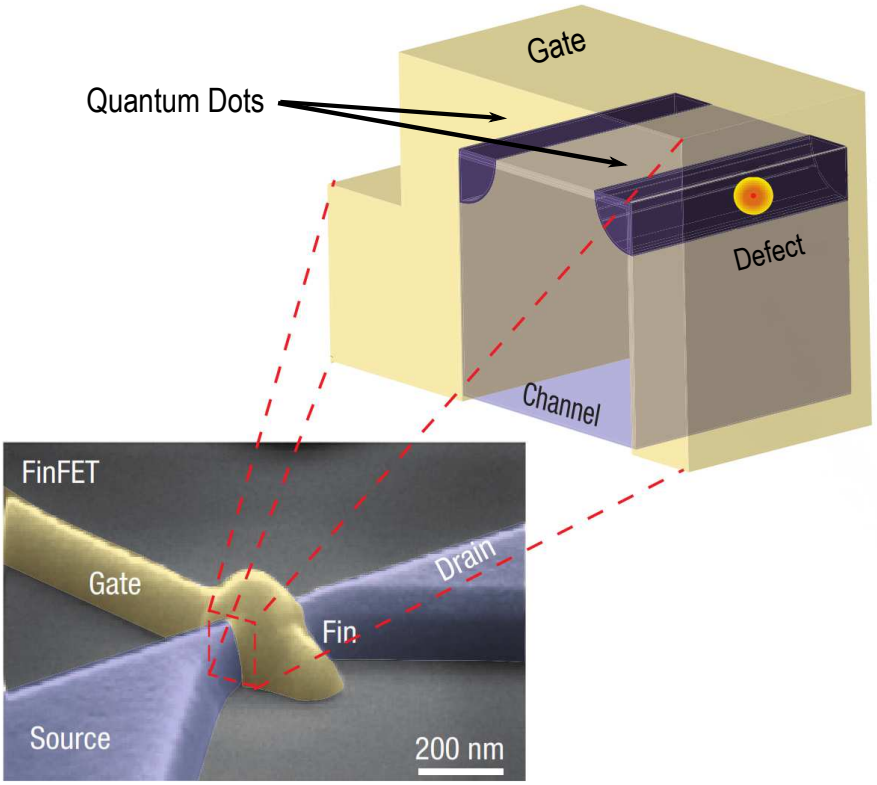


**Figure 3.10:** The **lower left** shows a scanning electron micrograph of a FinFET, identical to those used in this thesis. The **top right** shows a schematic cross-section of the transistor channel, which is approximately $30 \times 30$ nm. By applying a small negative voltage to the gate, elongated quantum dots are formed in the corners of the channel, bounded on the surface by a SiO insulator. The conductive region formed by each dot has a cross-section of only 4 $\text{nm}^2$. Figure reproduced from Ref [124].

Chapter 4

# Properties of $^{167}Er:Y_2SiO_5$ in a large magnetic field

With an optical transition in the 1.5 $\mu$m telecom band, an Er doped crystal might seem the obvious choice for long range quantum communication applications. However, Er based approaches have been impeded by short spin lifetimes and hence short coherence times. In order to address this issue, I investigate the optical and hyperfine transition properties of $^{167}$Er:YSO in large magnetic fields. The properties of the 1.5 $\mu$m transition in Er:YSO have already been extensively studied. In 1997, Macfarlane et al. observed an order-of-magnitude improvement in $Er^{3+}$ dephasing time at 1.5 $\mu$m, by applying a 5T field along the $D1$ direction [67]. This result was reproduced by Scott et al. in 2003, who additionally observed 4 second hole-lifetimes at 0.5T [68]. Six years later Bottger et al. demonstrated a record 4.4 ms coherence time on the same optical transition using a 7T field [26]. These investigations, among others, illustrate that large Er electron spins become thermally polarised with sufficient magnetic field [76, 126].

These investigations did not, however, identify any long lived and coherent hyperfine transitions associated with the Er ions. In zero magnetic field , Baldit et al. investigated the properties of $^{167}$Er hyperfine transitions [69]. They observed hyperfine transition lifetimes and coherence times of only 100 ms and 1 $\mu$s, respectively. The work presented here aims to improve on these hyperfine transitions properties by using large magnetic fields to polarise the electron spins.

The chapter begins with an outline of the previously determined spin-Hamiltonian of $^{167}$Er:YSO. This outline is followed by a description of the equipment and setup used for the experiments presented this chapter, in Section 4.3. The first experiment is presented in Section 4.4, comprising of a 7T absorption spectrum of $^{167}$Er:YSO. This is followed by a holeburning study in Section 4.5. The purpose of this measurement is to determine

the $^{167}$Er hyperfine structure at 7T. In Section 4.1 the experimentally determined energy spacings are compared with the previously estimated values from the spin-Hamiltonian. Using these values, a model of the absorption spectrum is developed and presented in Section 4.6 and spin-polarisation of the $^{167}$Er hyperfine ensemble is investigated in Section 4.7.

The rest of the chapter is devoted to investigating the spin dynamics in $^{167}$Er:YSO, starting with a study of the hyperfine population lifetime in Sections 4.8 and 4.9. The magnetic field dependence of spectral hole lifetimes is then investigated in Section 4.10, and the chapter concludes with optical and hyperfine coherence measurements in Section 4.11.

## 4.1 Previous investigations of $^{167}Er:Y_2SiO_5$

The first investigation into the hyperfine structure of $^{167}$Er:YSO was undertaken by Guillot-Noël et al. at Chimie ParisTech in 2006 [127]. They measured $^{167}$Er ground-state hyperfine transition energies using Electron Paramagnetic Resonance (EPR) in a naturally doped crystal. By recording transition energies in fields up to 1T, they were able to parametrise the tensors of the following ground-state spin Hamiltonian:

$$\mathcal{H} = \beta_e B \cdot g \cdot S + S \cdot A \cdot I + \beta_n g_n B \cdot I + I \cdot Q \cdot I \tag{4.1}$$

These tensors[1] are presented here in units of MHz for spectroscopic site 2:

$$g = \begin{pmatrix} 14.75 & -2.02 & 2.62 \\ -2.02 & 1.89 & -0.93 \\ 2.62 & -0.93 & 0.05 \end{pmatrix}_{(D_1,D_2,b)}$$

$$A = \begin{pmatrix} -1521.40 & 178.11 & -141.76 \\ 178.11 & 172.09 & 212.54 \\ -141.76 & 212.54 & 199.01 \end{pmatrix}_{(D_1,D_2,b)}$$

[1] The g-tensor was also determined by T. Bottger in 2002 [128]

$$Q = \begin{pmatrix} -3.50 & -19.84 & 24.22 \\ -19.84 & 50.40 & 6.73 \\ 24.22 & 6.73 & -46.90 \end{pmatrix}_{(D_1,D_2,b)}$$

The Chimie ParisTech group subsequently investigated the 1.5 $\mu$m transitions of isotopically enriched $^{167}$Er:YSO. During this investigation they recorded an optical absorption spectrum for site 1 at 1.5 $\mu$m with no field applied (see Figure 2.3). Their previous characterisation of the ground-state spin Hamiltonian was in good (but not perfect) agreement with the optical spectrum.

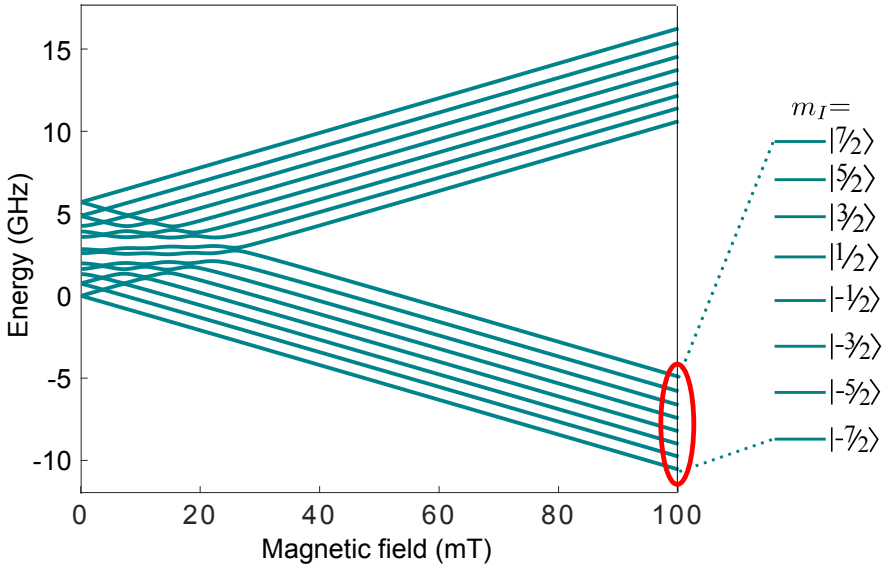


**Figure 4.1:** A simulation of the 16 levels comprising the lowest Kramers doublet of the $I_{15/2}$ ground state for $^{167}$Er:YSO based on spin-Hamiltonian (4.1). **Circled in red** are the eight ground state levels of the lower Zeeman arm relevant to the work here. **On the right hand side** these eight levels are labelled according to the nuclear magnetic quantum number's $m_I = \{|{-7/2}\rangle \cdots |{+7/2}\rangle\}$. This ordering is used throughout the rest of the chapter.

## 4.2 Predictions of the high-field optical absorption profile

The first half of this chapter presents an investigation of the optical structure of the hyperfine transitions in a 7T field oriented along the $D_1$ optical extinction axis. In such a large field the hyperfine transition energies are very different from their zero-field values, and this is illustrated in Figure 4.1. This drastic change occurs between 0-30 mT because the electronic Zeeman interaction dominates over the hyperfine interactions beyond this field. At this point the energy levels of the lowest $I_{15/2}$ Kramers doublet become similarly spaced.

Only the eight levels circled in red are relevant for this work: The upper Zeeman arm is thermally depopulated at low temperatures and large fields. Table 4.1 lists the hyperfine transition frequencies calculated for these eight levels using spin-Hamiltonian 4.1. In a field of 7T along the $D_1$ axis, this presents $\mathcal{O}$(GHz) energy splittings.

| Ground state hyperfine transition | Transition frequency (MHz) |
|---|---|
| $\left\|+5/2\right\rangle \leftrightarrow \left\|+7/2\right\rangle$ | 890 |
| $\left\|+3/2\right\rangle \leftrightarrow \left\|+5/2\right\rangle$ | 836 |
| $\left\|+1/2\right\rangle \leftrightarrow \left\|+3/2\right\rangle$ | 814 |
| $\left\|-1/2\right\rangle \leftrightarrow \left\|+1/2\right\rangle$ | 800 |
| $\left\|-3/2\right\rangle \leftrightarrow \left\|-1/2\right\rangle$ | 784 |
| $\left\|-5/2\right\rangle \leftrightarrow \left\|-3/2\right\rangle$ | 773 |
| $\left\|-7/2\right\rangle \leftrightarrow \left\|-5/2\right\rangle$ | 801 |

**Table 4.1:** Calculated hyperfine transition frequencies for $^{167}$Er:YSO site 2, based on the spin-Hamiltonian determined by Guillot-Noël et al. [127]. The values in column 2 were determined for a field of 7T along the $D_1$ optical extinction axis.

Given these $\mathcal{O}$(GHz) splittings, it was predicted that discrete 'bands' should be visible in the absorption profile assuming the following two things. Firstly, that the small difference in $I_{15/2}$ and $I_{13/2}$ electronic $g$-factors would also lead to $\mathcal{O}$(GHz) splittings in the $I_{13/2}$ levels. Secondly, that the 390 MHz optical linewidth previously measured in Er:YSO would resolve the $\mathcal{O}$(GHz) hyperfine splittings [129].

Such absorption spectra have been observed in $^{167}$Er:$^7$YLiF$_4$ [130], and they look very different to the zero-field $^{167}$Er:YSO profile illustrated in Figure 2.3. Here the resolved bands comprise of the $\Delta m_I = 0, \pm1, \pm2...$ optical transitions. These assumptions were tested here with the optical absorption spectrum in Figure 4.3.

## 4.3 Experimental setup

The following experimental setup was used for all measurements involving $^{167}$Er:YSO, with minor alterations between sections. The crystal under investigation was doped with an Er concentration of 0.005% and purchased from Scientific Materials Corp (Bozeman, Montana). The $^{167}$Er isotopic purity was stated as 91.77 ± 0.04% and the crystal dimensions were $3 \times 4 \times 5$ mm ($D_1$,$D_2$,$b$). The experiment was conducted in an Oxford helium bath cryostat with a unidirectional magnet capable of producing a 15T field. With the exception of measurements in Sections 4.8 - 4.9, the sample was maintained at a temperature of 1.4 K.

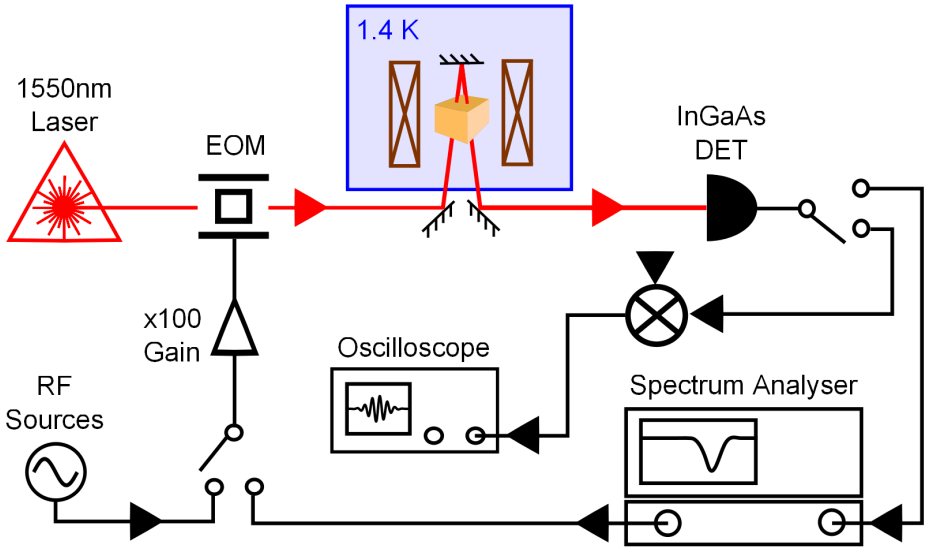


**Figure 4.2:** The general setup for all $^{167}$Er:YSO measurements. There were minor changes to the RF sources and measurement equipment (detectors and spectrum analysers) between experiments. Rapid switching between RF elements was achieved with Mini-circuits 0 - 4GHz absorptive RF switches.

To mount the crystal inside the cryostat, a rigid plastic holder was used. Within the holder, the crystal was placed against a mirror, as shown in Figure 4.2. The probe beam was focused to a 70 $\mu$m waist at the mirror. For all the experiments detailed below, both the magnetic field and light propagating direction were parallel with the $D_1$ optical extinction axis of the crystal. The reflection down the $D_1$ axis gave a total absorption length of 6mm. Only one laser was used for all the experiments; a Thorlabs TLK-1550R stabilised to a fibre reference cavity with a 100 kHz linewidth on a 1 second timescale. This reference cavity was designed and built by myself. It consisted of an optical ring resonator constructed from a Thorlabs 99:1 split 2x2 single mode tap coupler, with a free spectral range of 100 MHz and a finesse of 1 MHz. The resonator was acoustically dampened by immersion in sand, and thermally stabilised using a home-built digital PID feedback unit. This resulted an absolute thermal stability of less than 100 MHz.

Except for the absorption measurements in Section 4.4, frequency modulation of the light was achieved with a 10 GHz EOM. For most measurements, the optical signal was also collected with a 10 GHz Lab Buddy R402-APD optical detector.

The modulation spectroscopy techniques described in Section 3.2 were used to record the spectra in Sections 4.5 - 4.10. For these experiments the AC detector signal was recorded using an RF spectrum analyser. The tracking-generator was also used as the

EOM modulation source in this case.

For the coherence experiments in Section 4.11 only time-domain data was collected. For these experiments the AC detector signal was recorded with an oscilloscope.

## 4.4 Measurement of the optical absorption spectrum at 7T

The figure below presents the optical absorption spectrum of the inhomogeneously broadened $^{167}$Er:YSO line, with a field of 7T along the $D_1$ optical extinction axis. To record this spectrum, neither the EOM or 10 GHz detector shown in Figure 4.2 were required. Instead, the laser-cavity itself was modulated with a piezoelectric actuator fixed to the grating.

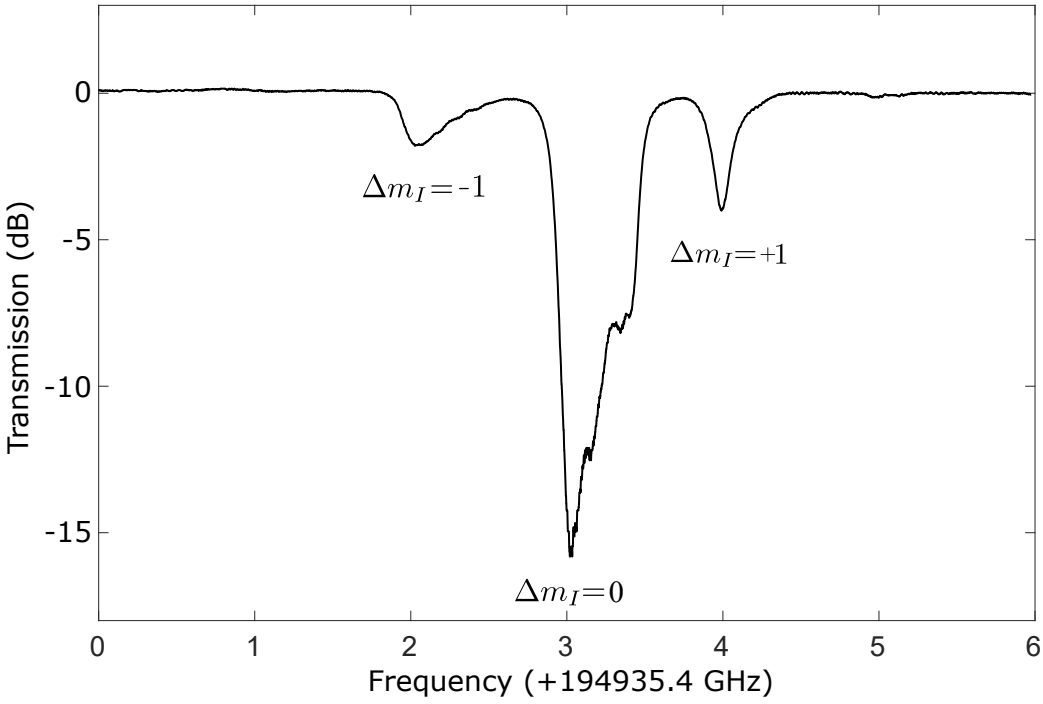


**Figure 4.3:** The optical absorption spectrum of $^{167}$Er:YSO crystallographic site 2, with a field of 7T along the $D_1$ optical extinction axis. The frequency axis was calibrated against the holeburning spectra presented in Section 4.5. The $\Delta m_I = -1$, 0 and +1 absorption bands are also labelled.

The piezo was driven with a 150V saw-tooth at 17 Hz, and the light intensity at the crystal was approximately 50 $\mu$W. The signal was collected with a New-focus 1611 InGaAs detector and output to an oscilloscope.

Three absorption bands are clearly visible in Figure 4.3, confirming the prediction of Section 4.2. These bands at 2, 3 and 4 GHz should encompass the $\Delta m_I = -1$, 0 and +1 optical transitions respectively. As mentioned previously, the hyperfine structure of $^{167}$Er had only been resolved in isotopically enriched YLiF [110,130]. This is the first example of

resolved hyperfine structure[2] in YSO, and the significance of this result is further explored in Sections 4.5 - 4.7.

## 4.5 Determination of hyperfine structure using holeburning

The start of this chapter presented an estimate of the ground-state hyperfine structure, based on low-field measurements. Establishing accurate values for these transition energies at 7T was critical to analysing many of the later results in the chapter. The estimate from Table 4.1 indicated $\mathcal{O}$(GHz) ground-state splittings in a 7T field, where spectral-holeburning and modulation spectroscopy were used to determine these transition energies precisely. Introduced in Chapter 3, these techniques give accurate measurements of hyperfine transition energies, for both the ground and optically-excited states.

Spectral holes were burnt into the optical absorption line using an EOM sideband. During this process the laser was kept locked, approximately 300 MHz blue detuned from the $\Delta m_I = +1$ absorption band. This ensured that any resonant laser absorption was from the lower frequency sideband only. The source of RF to the EOM was the tracking generator output from a HP 4396A spectrum analyser. Holes were burnt using a fixed-frequency (zero-span) output for 100 ms, followed immediately by a 1.8 GHz spectrum sweep with a 50 ms sweep-time (see Figure 4.4). The AC output of a Newfocus 1611 optical detector was connected to the spectrum analyser. This spectrum analyser was also used to digitise the data, and this was downloaded via GPIB.

Holeburning generated a series of holes and anti-holes in the optical absorption line, and these spectra were recorded with AM-spectroscopy (see Section 3.2). These were collated into three figures, which are presented on the following pages and the transition energies calculated from these spectra are tabulated below each figure.

Figure 4.6 presents a cascade plot with five spectra, each with a single hole burnt into the $\Delta m_I = 0$ absorption band. To address every hyperfine state, each of the five spectra had a hole burnt at a different frequency. Previous measurements in 50 ppm Er:YSO indicated an optical inhomogeneous linewidth of 390 MHz [129]. For this reason the holes were separated by 100 MHz increments, and so five spectra were sufficient to cover the entire $\Delta m_I = 0$ absorption band.

The second cascade plot in Figure 4.7 presents a very similar measurement to Figure

[2]For rare earth's such as $Er^{3+}$ & $Nd^{3+}$ in particular, as they are of great interest for quantum applications. $Ho^{3+}$ has large hyperfine splittings which have been resolved in many crystals.

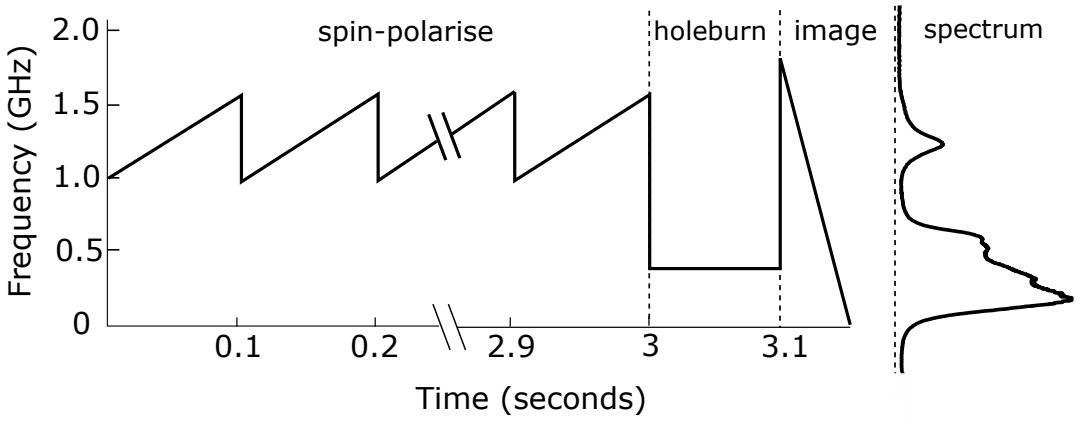


**Figure 4.4:** An example of a pulse sequence used for the holeburning measurements shown in Figures 4.6 - 4.8. This particular time trace illustrates the procedure for the 450 MHz measurement (third spectrum from the top) in Figure 4.7. **Spin polarisation:** A series of sweeps over the $\Delta m_I = +1$ absorption band (100 ms each, 30 in total) were used to push the hyperfine ensemble towards the $|+7/2\rangle$ hyperfine ground state. This absorption band is encompassed by the 1-1.6 GHz region in Figure 4.7. Note that the spin polarisation sequence was not required for the measurements in Figures 4.6 and 4.8. **Holeburning:** The EOM sideband frequency was kept fixed at 450 MHz for 100 ms to burn a spectral hole in the $\Delta m_I = 0$ absorption band. **Imaging:** The EOM sideband was swept over the entire 1.8 GHz range of the spectrum analyser (tracking generator) in 50 ms, and the AM spectrum was recorded using the RF input of the spectrum analyser. **Spectrum:** the $^{167}$Er:YSO absorption spectrum superposed on the RF frequency axis (left) to help illustrate the effect of the optical pulses.

4.6. The difference was that the Er ensemble was spin polarised towards the $m_I = |+7/2\rangle$ ground state (see Section 3.1.3 for more detail on spin polarisation). This was achieved by repeatedly exciting the $\Delta m_I = +1$ absorption band, which drove the hyperfine ensemble towards the $|+7/2\rangle$ hyperfine state through the cascade of $\Delta m_I = +1$ transitions. The pulse sequence for this procedure is shown in Figure 4.4. The purpose of spin polarisation in this measurement was to re-distribute the hyperfine ensemble, so that a different distribution of hole and anti-hole amplitudes would be observed.

Finally, Figure 4.8 once again presents a similar measurement to the previous two. Here the key difference is that holes were burnt into $\Delta m_I = +1$ absorption band, rather than the $\Delta m_I = 0$ band. As the laser was maintained at the same optical frequency for all measurements, this was achieved by simply changing the EOM modulation frequency.

### Guidelines for assigning transitions

Across the following three plots, several 'rules' were applied to determine the hyperfine transition energies. Rules 3-6 are conceptually illustrated in Figure 4.5:

1. Anti-holes can appear in all three absorption bands

2. Side-holes should appear only in adjacent absorption bands

3. The frequency detuning of a side-hole (relative to the burnt hole) is equal to an $I_{13/2}$ hyperfine transition frequency

4. The frequency detuning of an anti-hole in the adjacent absorption band is equal to an $I_{15/2}$ hyperfine transition frequency.

5. The frequency detuning of an anti-hole in the same absorption band is equal to the difference in hyperfine transition frequencies between the $I_{13/2}$ and $I_{15/2}$ states.

6. The sum of transition energies in the $I_{15/2}$ and $I_{13/2}$ levels will determine the ordering of optical transitions. If $\sum I_{15/2} < \sum I_{13/2}$ then the $|{-7/2}\rangle \leftrightarrow |{-7/2}\rangle$ transition will have the lowest optical frequency of the $\Delta m_I = 0$ transitions. Vice-versa if $\sum I_{13/2} < \sum I_{15/2}$ .

7. The change in hole and anti-hole amplitudes from one spectrum to the next (within the same cascade plot) determines the ordering of $I_{13/2}$ and $I_{15/2}$ transition energies. Reasoning: the amplitude of features in each spectrum depends on the population removed from each ground state; this population ratio changes slowly between spectra because the inhomogeneous transition broadening (∼150 MHz) is larger than the 100 MHz spacing between burnt holes.

8. Holes and anti-holes whose frequencies don't shift across the cascade plots are assumed to be artefacts, caused by fixed-frequency harmonics of the tracking generator (or other RF equipment).

By following these rules, 13 out of 14 transition energies were unambiguously determined. This was possible because the three spectra provided a large redundancy of information, evident in the tables below Figures 4.6 - 4.8. The transition energies determined for the upper four hyperfine states ($|+1/2\rangle$ to $|+7/2\rangle$) were verified in later holeburning measurements as well (see Figure D.1).

From the three plots presented in this section, however, no structure was evident for the $|{-7/2}\rangle \leftrightarrow |{-5/2}\rangle$ hyperfine transition in the $I_{15/2}$ state. It was hypothesised that no structure was observed because this transition was degenerate in energy with the $|{-7/2}\rangle \leftrightarrow |{-5/2}\rangle$ hyperfine transition in the $I_{13/2}$ state. (consider transition R.5 on the right hand side of Figure 4.5 (a) when $\beta = \delta$).

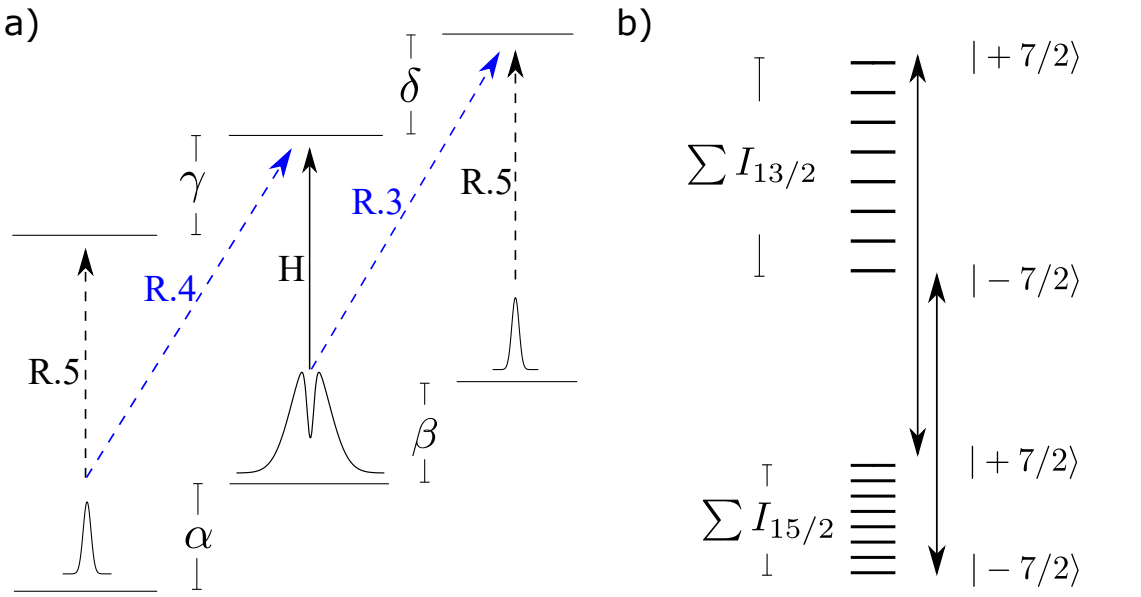


**Figure 4.5:** An illustration to conceptualise the rules used for assigning hyperfine transitions. **(a)** A simplified 3 level spin system where population has been removed from the middle level by spectral holeburning on the $\Delta m_I = 0$ transition (this transition is labelled **H**). Each of the other optical transitions are shown by **dashed lines**, and are labelled according to the corresponding rule. **Rule 3:** Relative to H, a side-hole is observed with frequency detuning $\delta$. **Rule 4:** Relative to H, An anti-hole is observed with frequency detuning $\alpha$. **Rule 5:** Relative to H, two anti-holes are observed with detunings $|\gamma - \alpha|$ and $|\delta - \beta|$.
**(b) Rule 6:** The sum of hyperfine spacings in the $I_{15/2}$ and $I_{13/2}$ states will determine which optical transitions have the highest and lowest energies. Here the $|-7/2\rangle \leftrightarrow |-7/2\rangle$ transition has the lowest energy, while the $|+7/2\rangle \leftrightarrow |+7/2\rangle$ has the highest.

This lack of structure is an outcome of using only two absorption bands for inspecting hole structure (the $\Delta m_I = 0$ and $+1$ bands). This degeneracy is revealed with measurements that additionally include the $\Delta m_I = -1$ transitions, however, as these exhibit frequency detunings corresponding to the sum of $I_{15/2}$ and $I_{13/2}$ hyperfine splittings ($\beta+\delta$). To this end, an additional measurement was performed to determine the $|{-7/2}\rangle \leftrightarrow |{-5/2}\rangle$ ground state transition energy (not shown here). For this measurement a hole was burnt into the $\Delta m_I = -1$ absorption band at the approximate wavelength of the $|{-5/2}\rangle \leftrightarrow |{-7/2}\rangle$ optical transition. Structure in the $\Delta m_I = +1$ band would then reveal the sum of $I_{13/2}$ and $I_{15/2}$ hyperfine transitions. Indeed, an anti-hole was observed in the $\Delta m_I = +1$ band with an energy detuning of 1988.7 MHz. Given that the $|{-7/2}\rangle \leftrightarrow |{-5/2}\rangle$ excited state hyperfine transition was measured to have a frequency of 994 MHz, the $|{-7/2}\rangle \leftrightarrow |{-5/2}\rangle$ ground state frequency was determined to be 994.7 MHz.

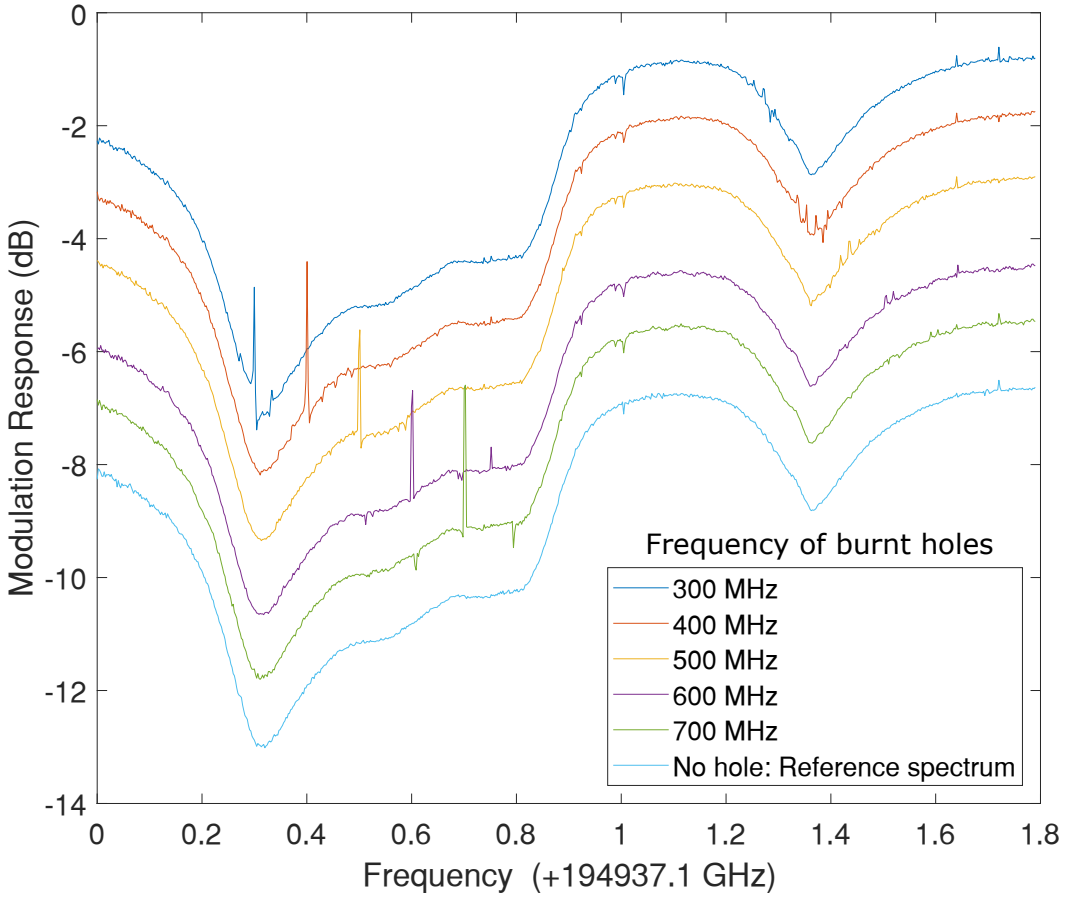


| $\Delta m_I$=0 anti-holes (MHz) | Inferred transition $\lvert I_{15/2} - I_{13/2}\rvert$ | $\Delta m_I$=+1 holes (MHz) | Inferred transition $(I_{13/2})$ |
|---|---|---|---|
| $94 \pm 3$ | $\lvert+5/2\rangle \leftrightarrow \lvert+7/2\rangle$ | $888 \pm 3$ | $\lvert+5/2\rangle \leftrightarrow \lvert+7/2\rangle$ |
| $90 \pm 3$ | $\lvert+3/2\rangle \leftrightarrow \lvert+5/2\rangle$ | $903 \pm 3$ | $\lvert+3/2\rangle \leftrightarrow \lvert+5/2\rangle$ |
| $87 \pm 3$ | $\lvert+1/2\rangle \leftrightarrow \lvert+3/2\rangle$ | $918 \pm 3$ | $\lvert+1/2\rangle \leftrightarrow \lvert+3/2\rangle$ |
| $76 \pm 3$ | $\lvert-1/2\rangle \leftrightarrow \lvert+1/2\rangle$ | $933 \pm 3$ | $\lvert-1/2\rangle \leftrightarrow \lvert+1/2\rangle$ |
| $53 \pm 3$ | $\lvert-3/2\rangle \leftrightarrow \lvert-1/2\rangle$ | $953 \pm 3$ | $\lvert-3/2\rangle \leftrightarrow \lvert-1/2\rangle$ |
| $30 \pm 3$ | $\lvert-5/2\rangle \leftrightarrow \lvert-3/2\rangle$ | $971 \pm 3$ | $\lvert-5/2\rangle \leftrightarrow \lvert-3/2\rangle$ |
| | | $994 \pm 3$ | $\lvert-7/2\rangle \leftrightarrow \lvert-5/2\rangle$ |

**Figure 4.6: Top:** Absorption spectra showing patterns of holes and anti-holes, generated by burning a single hole in each spectrum. The frequency of each burnt hole is stated in the legend. The bottom trace had no holes burnt, and used to identify artefacts in the RF scan. **Bottom:** Table summarising the results observed in the above spectra. The numbers indicate frequency detuning from the burnt holes, and the uncertainties are given by the resolution bandwidth of the RF scan.

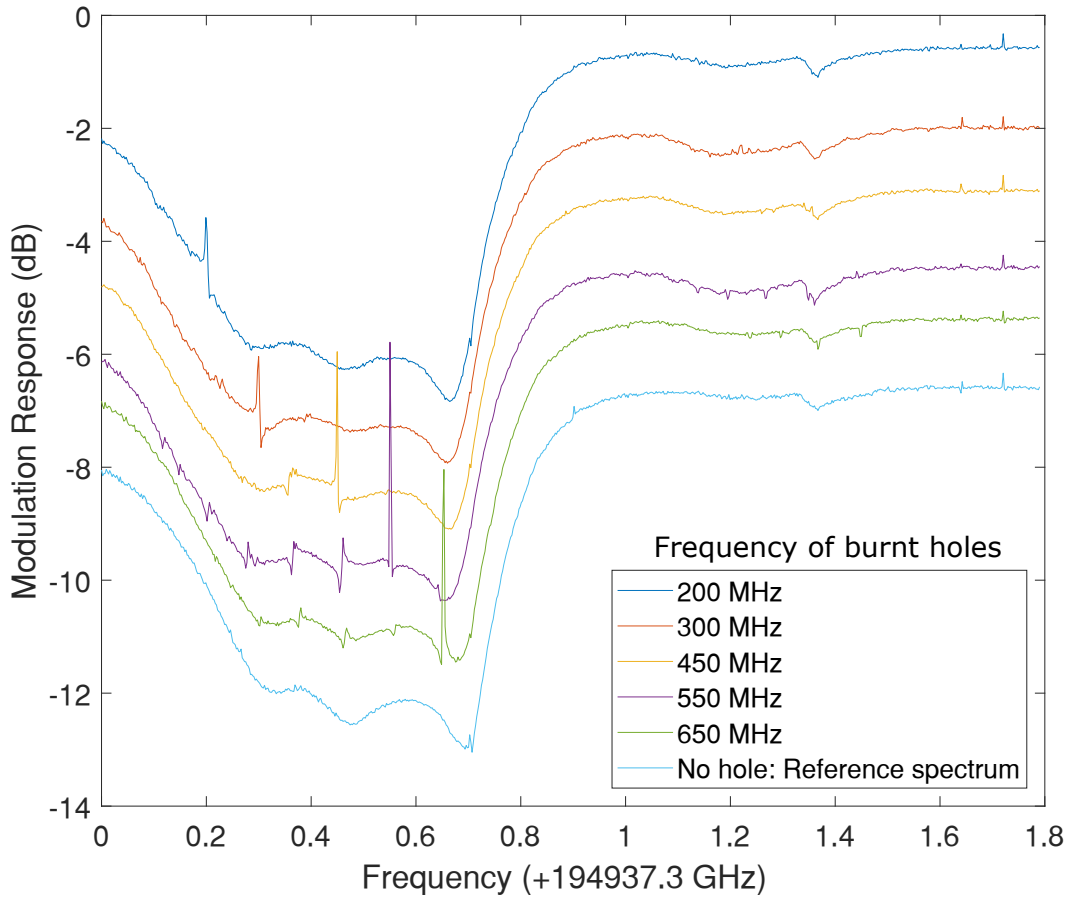


| $\Delta m_I$=0 anti-holes (MHz) | Inferred transition $\lvert I_{15/2} - I_{13/2}\rvert$ | $\Delta m_I$=+1 anti-holes (MHz) | Inferred transition $(I_{15/2})$ |
|---|---|---|---|
| $94 \pm 3$ | $\lvert+5/2\rangle \leftrightarrow \lvert+7/2\rangle$ | $797 \pm 3$ | $\lvert+5/2\rangle \leftrightarrow \lvert+7/2\rangle$ |
| $91 \pm 3$ | $\lvert+3/2\rangle \leftrightarrow \lvert+5/2\rangle$ | $809 \pm 3$ | $\lvert+3/2\rangle \leftrightarrow \lvert+5/2\rangle$ |
| $88 \pm 3$ | $\lvert+1/2\rangle \leftrightarrow \lvert+3/2\rangle$ | $833 \pm 3$ | $\lvert+1/2\rangle \leftrightarrow \lvert+3/2\rangle$ |
| $73 \pm 3$ | $\lvert-1/2\rangle \leftrightarrow \lvert+1/2\rangle$ | $864 \pm 3$ | $\lvert-1/2\rangle \leftrightarrow \lvert+1/2\rangle$ |
| $56 \pm 3$ | $\lvert-3/2\rangle \leftrightarrow \lvert-1/2\rangle$ | | |
| $29 \pm 5$ | $\lvert-5/2\rangle \leftrightarrow \lvert-3/2\rangle$ | | |

**Figure 4.7: Top:** Same as Figure 4.6, except with an additional preparation step: the hyperfine ensemble was optically pumped towards the $|+7/2\rangle$ state. **Bottom:** Table summarising the results observed in the above spectra. The numbers indicate frequency detuning from the burnt holes, and the uncertainties are given by the resolution bandwidth of the RF scan.

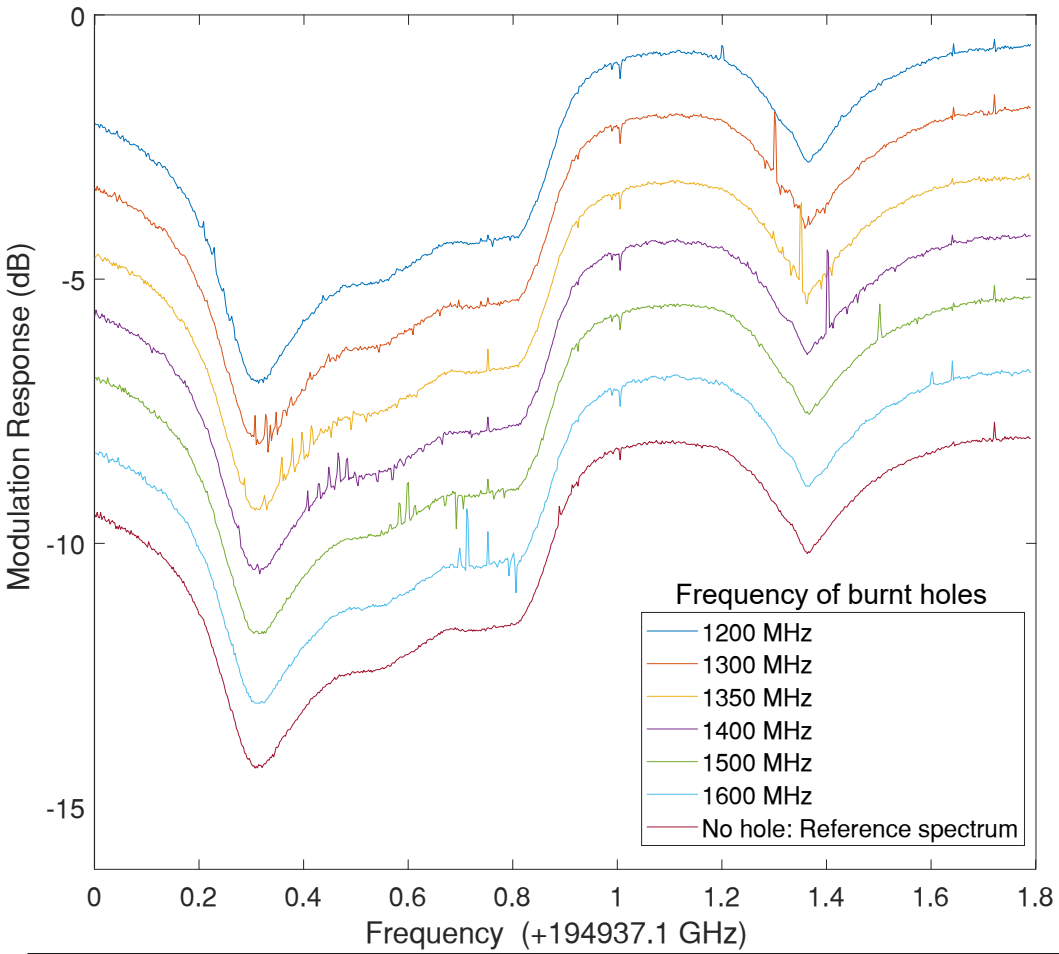


| $\Delta m_I = 0$ anti-holes (MHz) | Inferred transition $(I_{15/2})$ | $\Delta m_I$=0 holes (MHz) | Inferred transition $(I_{13/2})$ |
|---|---|---|---|
| $797 \pm 3$ | $\lvert+5/2\rangle \leftrightarrow \lvert+7/2\rangle$ | $889 \pm 3$ | $\lvert+5/2\rangle \leftrightarrow \lvert+7/2\rangle$ |
| $809 \pm 3$ | $\lvert+3/2\rangle \leftrightarrow \lvert+5/2\rangle$ | $903 \pm 3$ | $\lvert+3/2\rangle \leftrightarrow \lvert+5/2\rangle$ |
| $832 \pm 3$ | $\lvert+1/2\rangle \leftrightarrow \lvert+3/2\rangle$ | $918 \pm 3$ | $\lvert+1/2\rangle \leftrightarrow \lvert+3/2\rangle$ |
| $862 \pm 3$ | $\lvert-1/2\rangle \leftrightarrow \lvert+1/2\rangle$ | $936 \pm 3$ | $\lvert-1/2\rangle \leftrightarrow \lvert+1/2\rangle$ |
| $898 \pm 3$ | $\lvert-3/2\rangle \leftrightarrow \lvert-1/2\rangle$ | $954 \pm 3$ | $\lvert-3/2\rangle \leftrightarrow \lvert-1/2\rangle$ |
| | | $973 \pm 3$ | $\lvert-5/2\rangle \leftrightarrow \lvert-3/2\rangle$ |
| | | $994 \pm 3$ | $\lvert-7/2\rangle \leftrightarrow \lvert-5/2\rangle$ |

**Figure 4.8: Top:** Same as Figure 4.6, except that holes were burnt into the $\Delta m_I = +1$ band instead of the $\Delta m_I = 0$ band. **Bottom:** Table summarising the results observed in the above spectra. The numbers indicate frequency detuning from the burnt holes, and the uncertainties are given by the resolution bandwidth of the RF scan.

### 4.5.1 The hyperfine transition structure

Based on the holeburning results presented in this section, the hyperfine energy splittings of $^{167}$Er were unambiguously determined for both the ground and excited optical states, in a field of 7T along the $D_1$ optical extinction axis. These results are presented on the right-hand side of Figure 4.9.

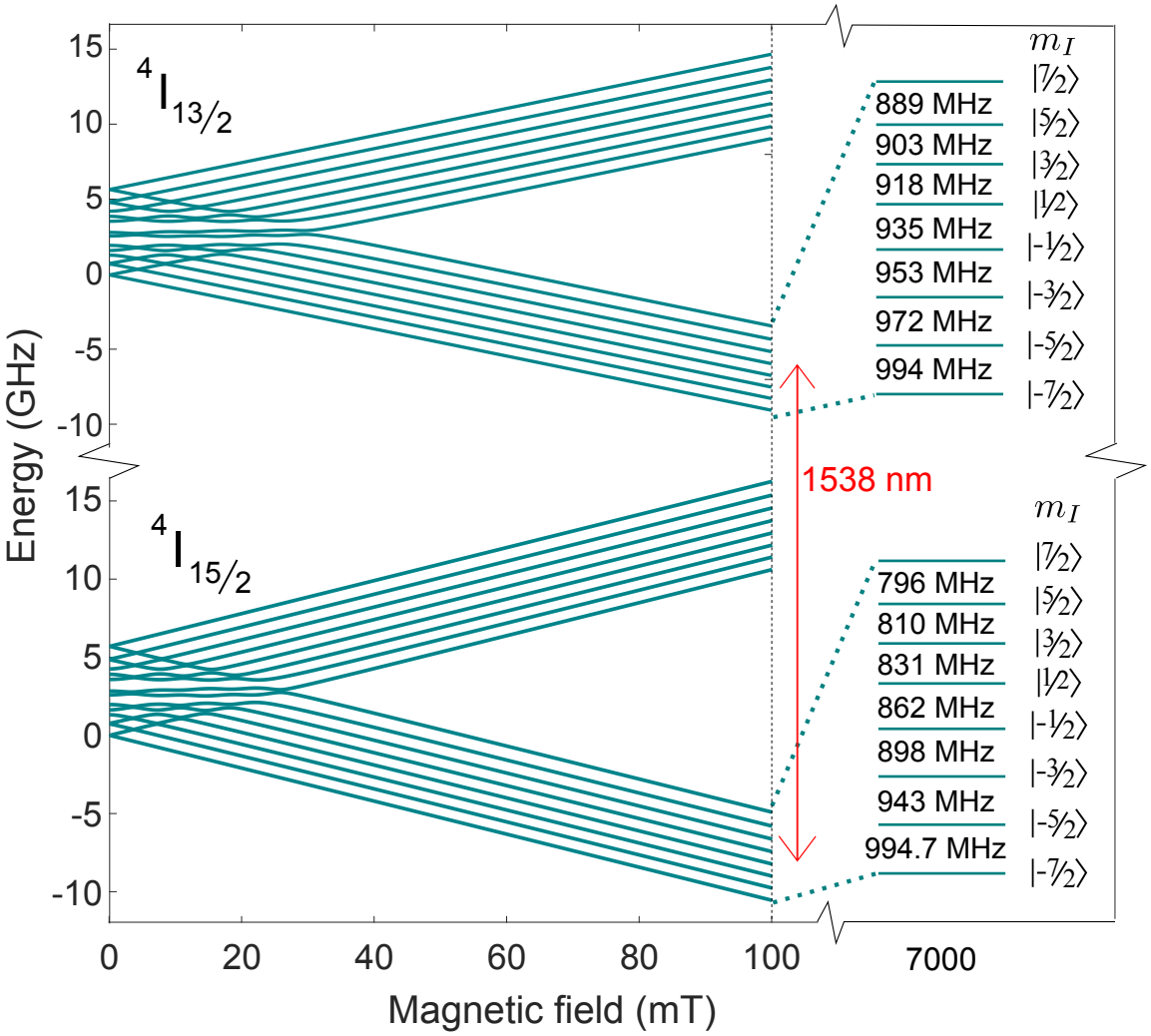


**Figure 4.9:** Energy level diagram of $^{167}$Er:YSO as a function of magnetic field along the $D_1$ optical extinction axis. **The left side** shows a low-field simulation, similar to that shown in Figure 4.1, except here all 32 levels comprising the lowest $I_{13/2}$ and $I_{15/2}$ Kramers doublets are shown. This low-field simulation is for illustrative purposes only, and not used for any calculations. **The right side** shows the energy splittings for the 16 relevant levels in a field of 7T, determined from the holeburning measurements of the previous section. These represent the key parameters of the figure. **The red arrow** illustrates the 1538 nm optical transition used for the holeburning measurements. Refer to Table 4.2 for measurement uncertainties.

These results also highlight the inaccuracy of the parameters determined by Guillot-Noël et al. at high fields. Presented in Table 4.2, the spin-Hamiltonian values are only correct to within 10% and (incorrectly) suggest an increase in energy from the $|-7/2\rangle$ level upwards.

Very recently, however, a new measurement of the spin-Hamiltonian parameters for $^{167}$Er:YSO was undertaken [131]. These new parameters are also presented in Table 4.2, and demonstrate better agreement with our experimental results. However, they still underestimate the largest transition energies by 10%.

| Ground state hyperfine transition | 2006 parameters (MHz) | 2017 parameters (MHz) | Experimental Transition frequency (MHz) |
|---|---|---|---|
| $\|+5/2\rangle \leftrightarrow \|+7/2\rangle$ | 890 | 782 | 796±3 |
| $\|+3/2\rangle \leftrightarrow \|+5/2\rangle$ | 836 | 799 | 810±3 |
| $\|+1/2\rangle \leftrightarrow \|+3/2\rangle$ | 814 | 810 | 831±3 |
| $\|-1/2\rangle \leftrightarrow \|+1/2\rangle$ | 800 | 817 | 862±3 |
| $\|-3/2\rangle \leftrightarrow \|-1/2\rangle$ | 784 | 824 | 898±3 |
| $\|-5/2\rangle \leftrightarrow \|-3/2\rangle$ | 773 | 840 | 943±3 |
| $\|-7/2\rangle \leftrightarrow \|-5/2\rangle$ | 801 | 874 | 994.7±0.1 |

**Table 4.2:** The ground-state hyperfine transition frequencies for $^{167}$Er:YSO site 2, in a magnetic field of 7T along the $D_1$ optical extinction axis. **Column two** shows the values calculated from spin-Hamiltonian (4.1) using the parameters determined by Guillot-Noël et al. in 2006 [127]. **Column three** shows the same calculation using the parameters determined by Chen et al. in 2017 [131] **Column four** presents the values determined experimentally in this section. The uncertainties for the first seven values are given by the resolution bandwidth of the RF scan. The final value was measured with greater precision, where the laser linewidth determined the uncertainty limit.

The spin-Hamiltonian predictions and the measured values could differ due to several reasons. Firstly, the accuracy of predictions will depend on the accuracy and quantity of data taken to paramatrise the $g, A$ and $Q$ tensors. To obtain good fits to their experiment, Chen et al. had to collect significantly more EPR data than Guillot-Noël et al. Secondly, the effective spin-Hamiltonian does not account for changes in electronic mixing as a function of magnetic field (the mixing of $m_J$ states). Both sets of spin-Hamiltonian parameters were measured in sub-Tesla fields, and the $m_J$ components of each electronic spin level will change by several percent by 7T for Kramers ions. This would contribute to similar changes in the effective $g$ and $A$ tensors.

## 4.6 Modelling the optical absorption structure

A model of the optical absorption structure at 7T was required for analysing many of the results in this chapter (see Sections 4.7 - 4.9). In addition to the hyperfine transition energies determined in the previous section, the following parameters were used to construct this model:

- The optical transition frequencies of $^{167}$Er hyperfine levels
- The optical transition frequency of isotopic impurities ($^{166}$Er, $^{168}$Er and $^{170}$Er)
- The inhomogeneous lineshape of the optical transitions[3]
- The relative oscillator strengths of the optical transitions

The $^{167}$Er optical transition frequencies were readily determined from the level structure presented in the previous section[4]. The remaining three parameters were determined by fitting to two separate spectra.

The first fitted spectrum (Figure 4.10) is presented in the next subsection. The fitting to this spectrum is described in Sections 4.6.2 - 4.6.3, and was used to determined both the inhomogeneous lineshape of the optical transitions (Section 4.6.4) and the position of the impurity isotopes in the spectrum (Section 4.6.5).

The final set of parameters, namely the transition oscillator strengths, were estimated from a fit to the absorption spectrum presented earlier in this chapter (Figure 4.3). The results of this fitting are presented in Figure 4.12 of Section 4.6.6. The simulated spectrum from this fitting actually required the complete set of model parameters listed above, and concludes the modelling in this section.

### 4.6.1 The hyper-polarised spectrum

A limited amount of nuclear spin polarisation was demonstrated previously in Figure 4.7. By increasing the EOM sideband intensity nine-fold during spin-pumping, a much higher degree of spin polarisation into the $|+7/2\rangle$ state was subsequently achieved. Once again the EOM sideband was scanned over $\Delta m_I = +1$ absorption band for 3 seconds, illustrated by the pumping sequence in Figure 4.4.

[3]The optical transitions differ only because of nuclear structure, so identical inhomogeneous lineshapes were assumed for all of them.

[4]With the addition of one optical transition frequency as a reference point. This was obtained from $|+7/2\rangle \leftrightarrow |+7/2\rangle$ transition in Figure 4.10

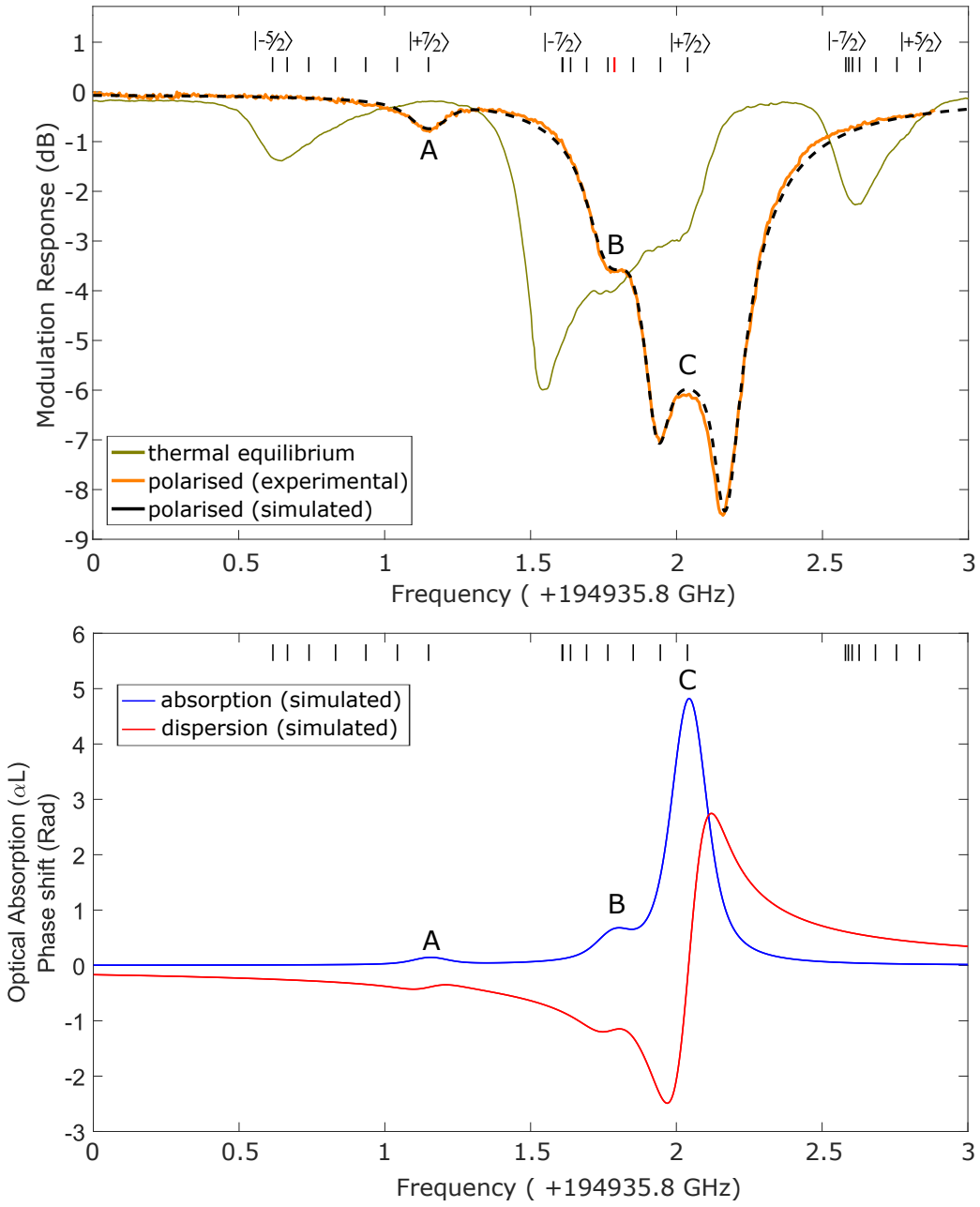


**Figure 4.10: Top:** AM spectra of the Er:YSO optical absorption line. **Gold trace:** A spectrum of the hyperfine ensemble in thermal equilibrium. **Orange trace:** A spectrum showing the $^{167}$Er ensemble polarised into the $|+7/2\rangle$ hyperfine ground state. **Black dashed trace:** A simulated spectrum which gives the best fit to the experimental spectrum in orange. **Vertical black dashes:** centres of each inhomogeneously broadened $^{167}$Er transition. For the outermost transitions in each absorption band, the relevant $I_{15/2}$ hyperfine state is labelled. **Vertical red dash:** centre of the isotopic impurity peak, also marked **B.**

**Bottom:** The absorption and dispersion input used to generate the simulated (black-dashed) AM spectrum **Blue:** The simulated absorption profile, consisting of three absorption peaks marked **A**, **B** and **C**. These three peaks correspond to the $|+7/2\rangle \leftrightarrow |+5/2\rangle$ transition, an isotopic impurity transition, and the $|+7/2\rangle \leftrightarrow |+7/2\rangle$ transition respectively. **Red:** Dispersion calculated from the simulated absortion (blue).

The laser carrier was 700 MHz red-detuned from the $\Delta m_I = -1$ absorption band to prevent unwanted optical excitation. The nine-fold increase in optical intensity was obtained by reducing the beam waist at the crystal from 270 $\mu$m to 90 $\mu$m.

The spectrum illustrating this improved spin-polarisation is presented by the orange trace in Figure 4.10 (a). Here the lack of absorption in the $\Delta m_I = +1$ band is an indicator of a high degree of spin-polarisation into the $|+7/2\rangle$ state. The increased population in the $|+7/2\rangle$ ground state lead to high OD of the $|+7/2\rangle \leftrightarrow |+7/2\rangle$ optical transition (point C in the 4.10 (a)). This manifested as an over-absorbed (inverted) peak in the spectrum, which is a consequence of the dispersion sensitivity in AM spectroscopy (for further detail see Section 3.2.5). As mentioned above, this high degree of spin polarisation was important for accurately determining several parameters in the absorption model. Efficient spin-polarisation is also a key requirement for several broadband quantum memory techniques [47, 74], and one of the major milestones of this thesis.

### 4.6.2 Simulating the hyper-polarised spectrum

The following analysis was used to fit a simulated spectrum (black dashed trace) to the experimental spectrum (orange trace) in Figure 4.10 (a). The first step in developing the simulated spectrum was the construction of a theoretical absorption profile, to base the simulation on. This absorption profile was constructed by combining 23 Voigt profiles, one centred on each optical absorption line. Twenty-two of these profiles were for the $^{167}$Er hyperfine lines: $7 \times (\Delta m_I = -1)$ , $8 \times (\Delta m_I = 0)$ , $7 \times (\Delta m_I = +1)$. The final profile was for an isotopic impurity peak.

While the relative optical transition energies of the hyperfine lines were known, the other absorption parameters (listed at the start of this section) were left as free variables to fit.

### 4.6.3 fitting the parameters

The blue trace in Figure 4.10 (b) shows the theoretical absorption profile which produced the best simulated fit[5] to the experimental AM spectrum in Figure 4.10 (a). Of the 23 peaks in the absorption model, only 3 were predominantly required to achieve an accurate

[5]In addition to the absorption (blue), the simulated AM spectrum (black dashed) required knowledge of the optical dispersion (see Section 3.2 for more detail on simulating AM spectra). This dispersion was calculated from the absorption (blue) using the Kramers-Kronig relations, and is shown by the red trace in Figure 4.10 (b).

fit. These peaks are labelled **A** , **B** and **C** in Figure 4.10 (b). In the same order, they correspond to the following three transitions:

- **A**: The $|+7/2\rangle \leftrightarrow |+5/2\rangle$ optical transition
- **B**: An isotopic impurity transition
- **C**: The $|+7/2\rangle \leftrightarrow |+7/2\rangle$ optical transition

This association between peaks and transitions was later confirmed by holeburning at the centre of peak **C** with the ensemble polarised, and this measurement is shown in Appendix D. Thus, the simplicity of this hyper-polarised spectrum made it suitable for determining three parameters in the absorption model.

The first parameter was the lineshape of the Voigt profiles, determined from the lineshape of peak **C** and discussed in the next section. The second parameter was the optical transition frequency of the hyperfine lines, determined from the centre of peaks **A** and **C**. The third parameter was the optical transition frequency of the isotopic impurity, determined from the position of peak **B**, and discussed in Section 4.6.5.

### 4.6.4 The inhomogeneous lineshape of the optical transitions

A Voigt distribution is a convolution of Gaussian and Lorentzian distributions, and has two free parameters corresponding to the linewidths $\sigma$ and $\rho$.

As mentioned in Section 4.6.2, the fit to the optical transitions in Figure 4.3 was made using a Voigt distribution. This distribution is needed to take into account the high density of isotopic impurities in YSO (see Section 2.3 for more detail). In particular, the fit to the highly absorbing $|+7/2\rangle \leftrightarrow |+7/2\rangle$ optical transition gave the most accurate estimate of the Gaussian and Lorenzian broadening contributions. This is because the shape of the absorption wings in the fit are very sensitive to the ratio $\sigma : \rho$ and these wings are clearly visible with this high OD. The inferred Voigt distribution is presented in Figure 4.11. Both $\rho$ and $\sigma$ were estimated to be $45 \pm 5$ MHz, giving a FWHM of $150 \pm 10$ MHz.

#### Comparison with published lineshapes for Er:YSO

The narrowest linewidth observed for natural abundance 0.005% Er:YSO was measured in 2006 by Bottger et al. [129]. They observed a FWHM of 390 MHz, and inferred a Lorentzian inhomogeneous absorption profile. This is significantly broader than the 150

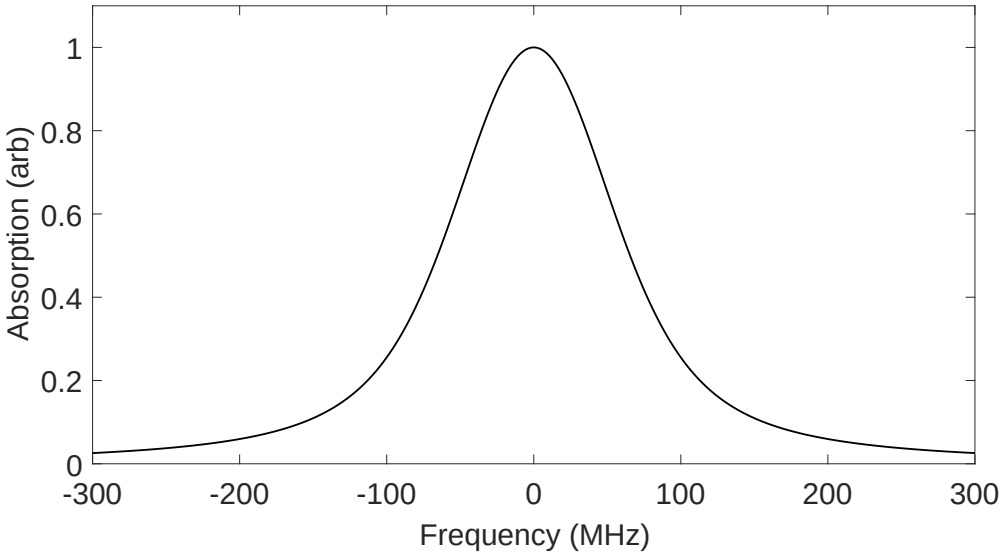


**Figure 4.11:** The estimated inhomogeneous distribution for an optical transition of Er:YSO (50 ppm doped). This distribution is described by a Voigt profile with equal Gaussian and Lorentzian contributions ($\rho = \sigma = 45$ MHz)

MHz determined here, and would exhibit more pronounced absorption wings. The discrepancy between the two inferred distributions can be attributed to the difference between isotopically enriched and natural abundance Er.

The spectrum recorded by Bottger et al. included a natural mix of four major Er isotopes: $^{166}$Er (33%), $^{167}$Er (23%), $^{168}$Er (27%) and $^{170}$Er (15%). The optical frequencies of these isotopes differ by 75 MHz per atomic number [111]. Out of these four isotopes, only $^{167}$Er exhibits hyperfine structure. The natural mix of the three $I = 0$ isotopes gives rise to a line much broader than from a single isotope. This explains the large absorption width observed by Bottger et al.

The $^{167}$Er hyperfine structure then gives rise to eight dominant lines spread over hundreds of MHz. These relatively weak lines produce a broad absorption background, leading to an approximately Lorentzian lineshape.

### 4.6.5 The transition frequencies of isotopic impurities

The isotopically enriched $^{167}$Er:YSO crystal used in this work contained a significant proportion of isotopic impurities; 8.23% as stated by the manufacturer. These impurities can consist of $^{166}$Er and $^{168}$Er and $^{170}$Er, none of which exhibit hyperfine structure. Their abundance in natural samples is given by the ratio 10:8:5 (in the same order).

Determining the optical frequencies of these transitions is complicated because they

are enveloped by the $\Delta m_I = 0$ absorption band of $^{167}$Er. In thermal equilibrium this absorption band exhibits 8 strong hyperfine peaks. An estimate based on isotope shifts could not be easily made because the 'centre' of the $^{167}$Er absorption profile was not well defined.

Instead, Figure 4.10 presented a means to accurately determine the isotopic frequencies. By pumping the $^{167}$Er into a single hyperfine state, a small side-peak originating from impurity absorption became clear (the side-peak B). The dashed line in the same figure illustrates a fit to the spectrum which includes an impurity contribution. This contribution assumed a single absorption peak, with a relative population of 8%. Achieving a good fit with one impurity peak suggests that the major isotopic impurity contribution came from predominantly one species. This could occur if the purification process distorted the ratio of even isotopes from the natural ratio of 10:8:5.

### 4.6.6 The transition oscillator strengths

The final set of parameters required for the absorption model were the transition oscillator strengths. As stated previously, these were determined by fitting a simulated spectrum to the first experimental absorption spectrum presented in this chapter (Figure 4.3). This simulated fit required all of the optical transition properties determined so far, and is presented in Figure 4.12. As before, this simulation consisted of 23 overlapped Voigt distributions (see Section 4.6.2).

| $\Delta m_I = -1$ | | $\Delta m_I = +1$ | |
|---|---|---|---|
| Hyperfine transitions | Oscillator strength (%) | Hyperfine transitions | Oscillator strength (%) |
| $\lvert+7/2\rangle \rightarrow \lvert+5/2\rangle$ | 2.5 | $\lvert+5/2\rangle \rightarrow \lvert+7/2\rangle$ | 3.0 |
| $\lvert+5/2\rangle \rightarrow \lvert+3/2\rangle$ | 6.3 | $\lvert+3/2\rangle \rightarrow \lvert+5/2\rangle$ | 4.6 |
| $\lvert+3/2\rangle \rightarrow \lvert+1/2\rangle$ | 10 | $\lvert+1/2\rangle \rightarrow \lvert+3/2\rangle$ | 9.9 |
| $\lvert+1/2\rangle \rightarrow \lvert-1/2\rangle$ | 14 | $\lvert-1/2\rangle \rightarrow \lvert+1/2\rangle$ | 15 |
| $\lvert-1/2\rangle \rightarrow \lvert-3/2\rangle$ | 17 | $\lvert-3/2\rangle \rightarrow \lvert-1/2\rangle$ | 21 |
| $\lvert-3/2\rangle \rightarrow \lvert-5/2\rangle$ | 21 | $\lvert-5/2\rangle \rightarrow \lvert-3/2\rangle$ | 26 |
| $\lvert-5/2\rangle \rightarrow \lvert-7/2\rangle$ | 25 | $\lvert-7/2\rangle \rightarrow \lvert-5/2\rangle$ | 31 |

**Table 4.3:** The oscillator strengths of the $\Delta m_I = \pm 1$ transitions, relative to the $\Delta m_I = 0$ transitions. A strength of 100% would yield 6.66 dB/cm of absorption. The uncertainty in the oscillator strength for each of the the $\Delta m_I = -1$ transitions is 10 percent of the stated strength. For the $\Delta m_I = +1$ transitions it is 15 percent. These uncertainties indicate a Root Mean Square Deviation (RMSD) which is twice the RMSD of the optimal fit.

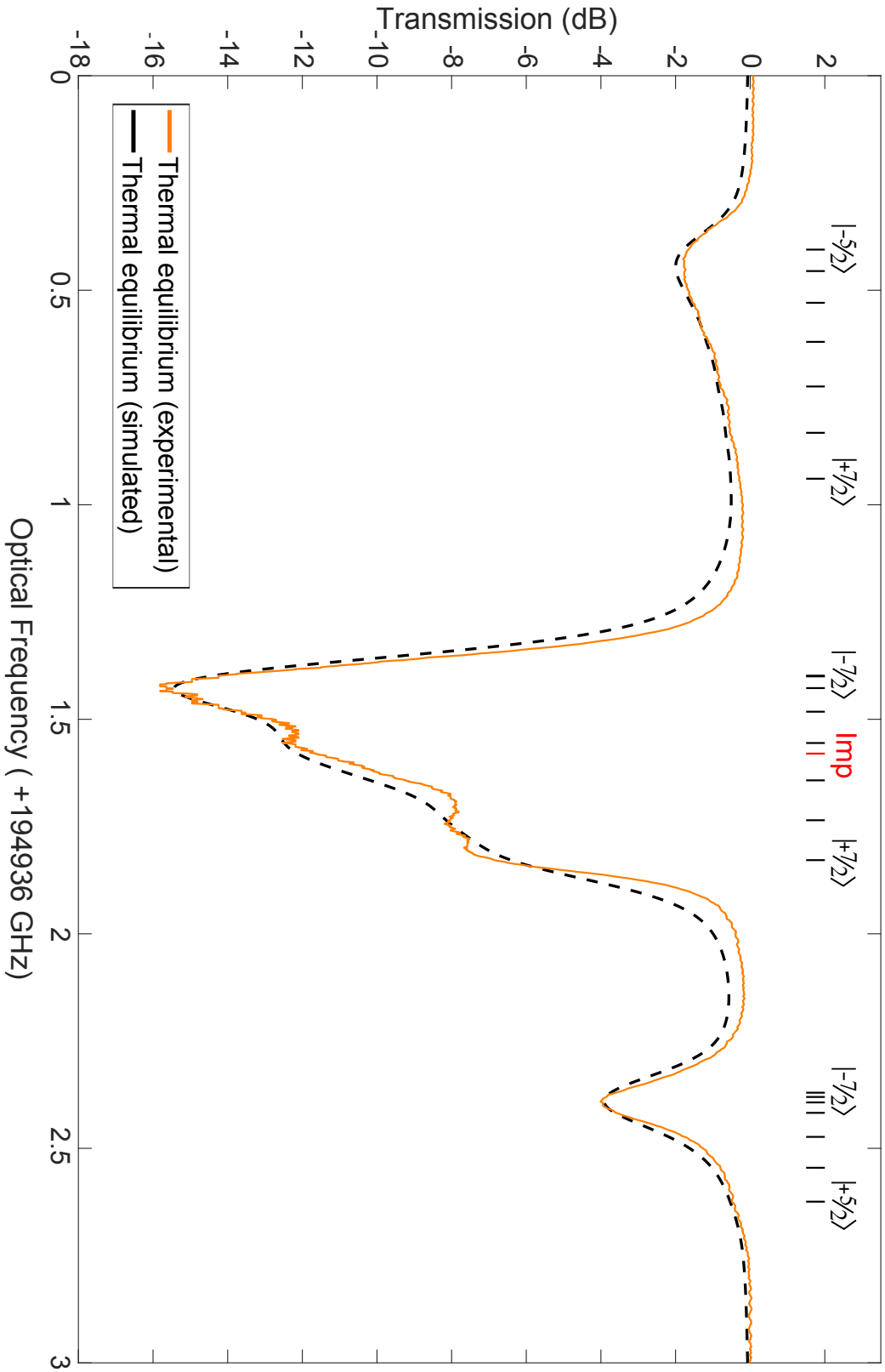


**Figure 4.12:** Optical absorption of $^{167}$Er:YSO with the ensemble of ions equally distributed amongst the hyperfine states (thermal equilibrium). **Orange trace**: Absorption spectrum taken from Figure 4.3. **Black dashed trace**: A fit to the optical absorption spectrum, based on the absorption model derived in this section. **Vertical black dashes:** centres of each inhomogeneously broadened $^{167}$Er transition. For the outermost transitions in each absorption band, the relevant $I_{15/2}$ hyperfine state is labelled. **Vertical red dash:** centre of the isotopic impurity transition.

In this simulation the eight $\Delta m_I = 0$ peaks had identical absorption (4 dB). This approximation of uniformity was based on the assumption of weak mixing between hyperfine states and thermal equilibrium. The oscillator strength of the isotopic impurity peak was assumed to equal the $\Delta m_I = 0$ peaks. Scaled by the relative impurity concentration, this gave a peak absorption of 2.8 dB.

The relative oscillator strengths of the fourteen $\Delta m_I = \pm 1$ transitions were then estimated by fitting to the envelopes of the $\Delta m_I = \pm 1$ absorption bands. The result is illustrated in Table 4.3, where a gradient of oscillator strengths is observed. To simplify the fitting, the gradient was assumed to be linear for both the $\Delta m_I = -1$ and $+1$ transitions. Such a gradient has previously been observed for the hyperfine levels of $Ho^{3+}$ in a low-symmetry sites [132], and is consistent with the gradient of hyperfine transition energies measured in Section 4.5.

Although not considered here, a more accurate determination of the $\Delta m_I = 0$ oscillator strengths could be also obtained from Table 4.3. While the approximation of equal strength yielded a good fit to the $\Delta m_I = 0$ absorption band in Figure 4.12, Table 4.3 would suggest that the $|-7/2\rangle \leftrightarrow |-7/2\rangle$ transition is about half the strength the $|+7/2\rangle \leftrightarrow |+7/2\rangle$ transition. This is because the sum of oscillator strengths in the $\Delta m_I = -1$, 0 and $+1$ bands should be conserved for transitions from the same hyperfine ground states.

## 4.7 Determining the degree of spin polarisation

The hyper-polarised spectrum in Figure 4.10 proved very useful for determining the optical absorption parameters in the previous Section. Hyper-polarisation is also important for many quantum memory schemes. It allows for large-bandwidth absorption in off-resonant Raman and CRIB memories [47, 74], and high efficiencies in AFC delay lines [133].

To apply these schemes to $^{167}$Er:YSO, it is important to quantify the degree of polarisation achieved in this work. Thus, the degree of spin polarisation in Figure 4.10 was determined using the oscillator strengths for the $\Delta m_I = -1$ transitions presented in Table 4.3, and the fitting procedure described in Section 4.6.3.

In particular, the fit to the $\Delta m_I = -1$ absorption band was used to determine the relative population in each hyperfine state. An exploded view of Figure 4.10 covering only the 0.5 to 1.3 GHz range (the $\Delta m_I = -1$ band) is presented in Figure 4.13.

The reason for only using the $\Delta m_I = -1$ absorption band in this fitting was two-fold. Firstly, there was no absorption from isotopic impurities at this wavelength. Secondly, the

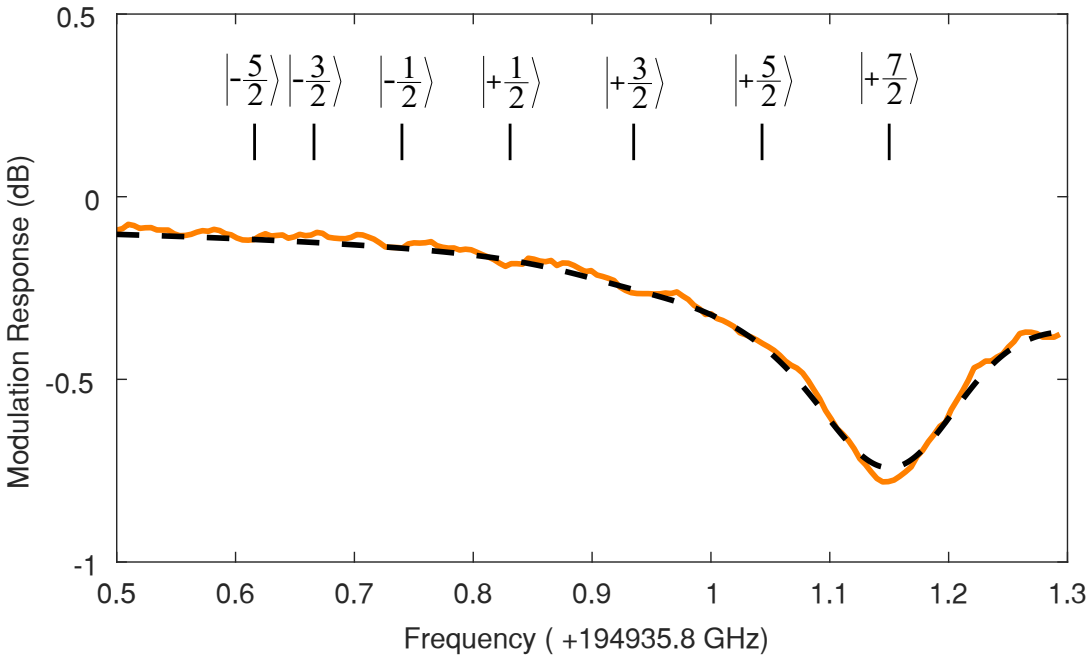


**Figure 4.13:** An exploded view of the $\Delta m_I = -1$ absorption band from Figure 4.10. **Orange trace:** AM spectrum with the $^{167}$Er ensemble polarised into the $|+7/2\rangle$ hyperfine ground state. **Black-dashed trace:** A simulated spectrum which gives the best fit to the experimental spectrum in orange. **Vertical black dashes:** centres of inhomogeneously broadened $^{167}$Er optical transitions, labelled by hyperfine ground state.

shape of the $\Delta m_I = -1$ absorption band was more sensitive to the relative population in each state, compared with the $\Delta m_I = 0$ band. This second point was inferred from the oscillator strengths presented in Table 4.3, which shows a considerable decrease in oscillator strengths across the series of $\Delta m_I = -1$ optical transitions. This meant that any population remaining in the $|+5/2\rangle$, $|+3/2\rangle$ (etc) states would give rise to stronger optical absorption than the $|+7/2\rangle$ state.

From this fitting it was determined that $95 \pm 3\%$ of the nuclear spin population was polarised into the $|+7/2\rangle$ state.

## 4.8 Hyperfine population lifetime at 1.6 K

Polarising the population into a single hyperfine state produces a non-thermal distribution. This distribution will eventually decay back to thermal equilibrium because of spin-lattice coupling [134]. This section presents set of measurements[6] used to determine the rate of polarisation decay at 1.6 K.

[6]In the previous sections the data was taken at 1.4 K. Here a 1.6 K data set is presented, as more measurement time-steps and longer delays were collected at this temperature than at 1.4 K

For these measurements the hyperfine ensemble was repeatedly polarised into the $|+7/2\rangle$ hyperfine state and then allowed to decay. For each experimental run an AM spectrum was recorded at a set time after polarisation, and these spectra are shown in Figure 4.14. During each decay period the laser light was also turned off until a spectrum was recorded. This was achieved by adjusting the DC voltage bias of the AM-EOM and turning off the RF input.

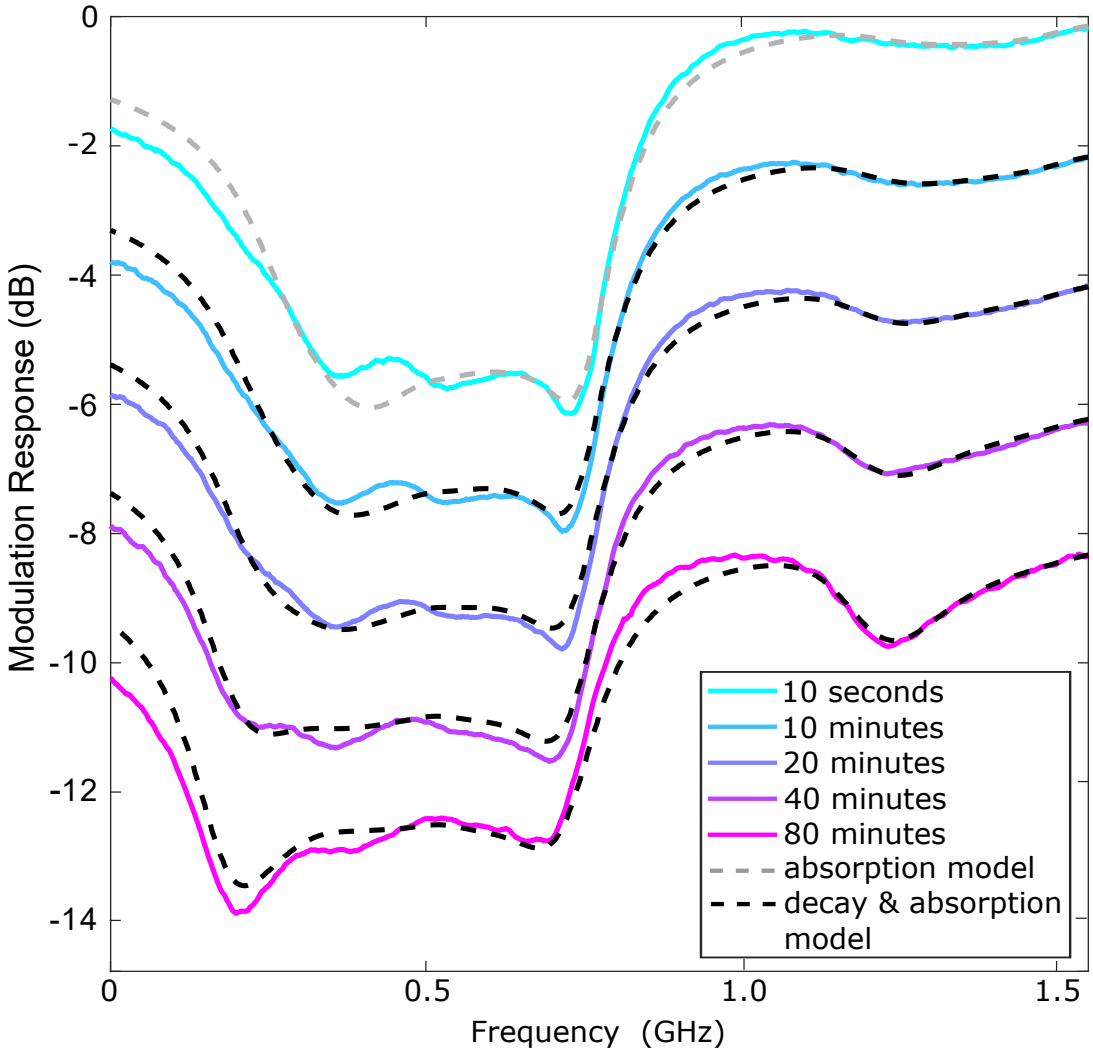


**Figure 4.14:** Waterfall plot illustrating the rate of depolarisation of the nuclear-spin ensemble at 1.6 K. The AM spectra shown here include only the $\Delta m_I = 0$ and $+1$ absorption bands. The black dashed lines show the spectrum model at each time delay. The free parameters for the the model are the time constant $\gamma^{-1}$ (750 seconds) and hyperfine population distribution at $t = 10$ sec.

As in the previous section, the recorded spectra were fit using the absorption model developed in Section 4.6. In the first instance, this was used to determine the hyperfine ensemble distribution $\{N_{-7/2}, \cdots N_{+7/2}\}$ immediately after polarisation. The results of

this fit is shown by the grey dashed trace in Figure 4.14, and the ensemble distribution is presented in Table 4.4

In addition to the absorption model used in the last section, a decay rate model was also used to fit the spectra recorded after a non-zero delay $t$. This model estimated the amount of spin-depolarisation after time delay $t$, in order to generate a simulated population distribution $N(t)_{m_I}$ for each state $m_I$. For this decay rate model it was assumed that spin-lattice coupling would drive only $\Delta m_I = \pm 1$ hyperfine transitions (ie: transitions between adjacent hyperfine states). This is because the weak hyperfine state mixing would suppress transitions between non-adjacent hyperfine states (see Section 2.4.4). It was also assumed that all the $\Delta m_I = \pm 1$ transitions were equally strong, and so a common decay rate $\gamma$ was used across all the rate equations.

Thus, the decay rate model comprised of the following rate-equations for hyperfine states $m_I = \{|-5/2\rangle, \cdots, |+5/2\rangle\}$:

$$\frac{dN(t)_{m_I}}{dt} = -\gamma \cdot (2N_{m_I}(t) - N_{m_I-1}(t) - N_{m_I+1}(t)) \tag{4.2}$$

where the decay rate $\gamma$ determined the hyperfine population lifetime of each state $T_1(m_I) = \frac{1}{2}\gamma^{-1}$. The two $|\pm 7/2\rangle$ states, however, could couple to only one neighbouring level each:

$$\frac{dN(t)_{\pm 7/2}}{dt} = -\gamma \cdot \left(N(t)_{\pm 7/2} - N(t)_{\pm 5/2}\right)$$

and so these present a population lifetime twice that of the other six $m_I$ states. Using this model, a value of $\gamma$ was found which minimised the RMS deviation between the simulated and measured spectra. This was achieved by fitting the simulated spectra (black dashed traces) simultaneously to all four measurements between 10 and 80 minutes. Here the fitting was only applied to the $\Delta m_I = +1$ absorption band (approx 1.2 - 1.3 GHz in Figure 4.14). The $\Delta m_I = 0$ band was not fit because the absorption model had less accurate values for the relative strengths of $\Delta m_I = 0$ transitions[7].

| Hyperfine state | $\|-7/2\rangle$ | $\|-5/2\rangle$ | $\|-3/2\rangle$ | $\|-1/2\rangle$ | $\|+1/2\rangle$ | $\|+3/2\rangle$ | $\|+5/2\rangle$ | $\|+7/2\rangle$ |
|---|---|---|---|---|---|---|---|---|
| $N(t \approx 0)$ (%) | 0 | 0 | 0 | 4 | 6 | 17 | 25 | 48 |

**Table 4.4:** Distribution of hyperfine population upon hyper-polarisation at 1.6 K, inferred from the $t = 10$ sec spectrum in Figure 4.14. The degree of spin-polarisation is not as great as was demonstrated in Section 4.7, as this was an earlier measurement.

[7]The model simply assumed that all $\Delta m_I = 0$ transitions were equally strong, an issue that was discussed at the end of Section 4.6.6

Based on this fitting, the spectra at 1.6 K demonstrated a decay rate $\gamma^{-1} = 750 \pm 180$ seconds. As stated above, this decay rate is equivalent the population lifetime $T_1$ for the $m_I = |\pm 7/2\rangle$ states, while $T_1 = \frac{1}{2}\gamma^{-1}$ for $m_I = |^{-5}/_2\rangle, \cdots, |^{+5}/_2\rangle$.

It should also be noted that the values inferred here represent lower bound estimates for the population lifetime, as the decay rate model only included $\Delta m_I = \pm 1$ hyperfine transitions. The fitting should not be sensitive to small amounts of $\Delta m_I = \pm 2$ transitions, but the inferred population lifetime will be longer if they are included.

## 4.9 Temperature dependence of hyperfine population lifetime

The previous section presented a method for estimating the hyperfine population lifetime at a given temperature. This experiment was repeated for six temperatures from 1.4 K to 3.2 K, and the spectra collected from those measurements are shown in Appendix C. By studying the change in population lifetime as a function of temperature, it was possible to determine which type of spin-lattice interaction mediated the polarisation-decay. This investigation was similar to previous temperature-dependence studies of Er:YSO spin relaxation in low fields [134].

In large magnetic fields and cryogenic temperatures, spin-lattice relaxation can be mediated by three different processes. These are the Raman, Orbach and Direct processes that were outlined in Section 2.4. Thus, $\gamma$ can be expressed as a sum of these three contributions:

$$\gamma = \gamma_{Direct} + \gamma_{Raman} + \gamma_{Orbach}$$

These processes can be distinguished by their temperature dependence. The Direct process is driven by phonons at the hyperfine energy splittings, corresponding to a frequency of $\mathcal{O}$(GHz). This process is linear with temperature $T$ in the range accessible by these experiments. Conversely, the Raman and Orbach processes have much stronger temperature dependencies ($T^9$ and exponential) and the sum temperature dependence is presented on page 565 of Abragam & Bleaney [97]:

$$\gamma = A_d T + A_r T^9 + A_{or} f^3 \left(e^{hf/kT} - 1\right)^{-1} \tag{4.3}$$

where $h$ represents the Planck constant, $k$ is the Boltzmann constant and $f$ is the linear

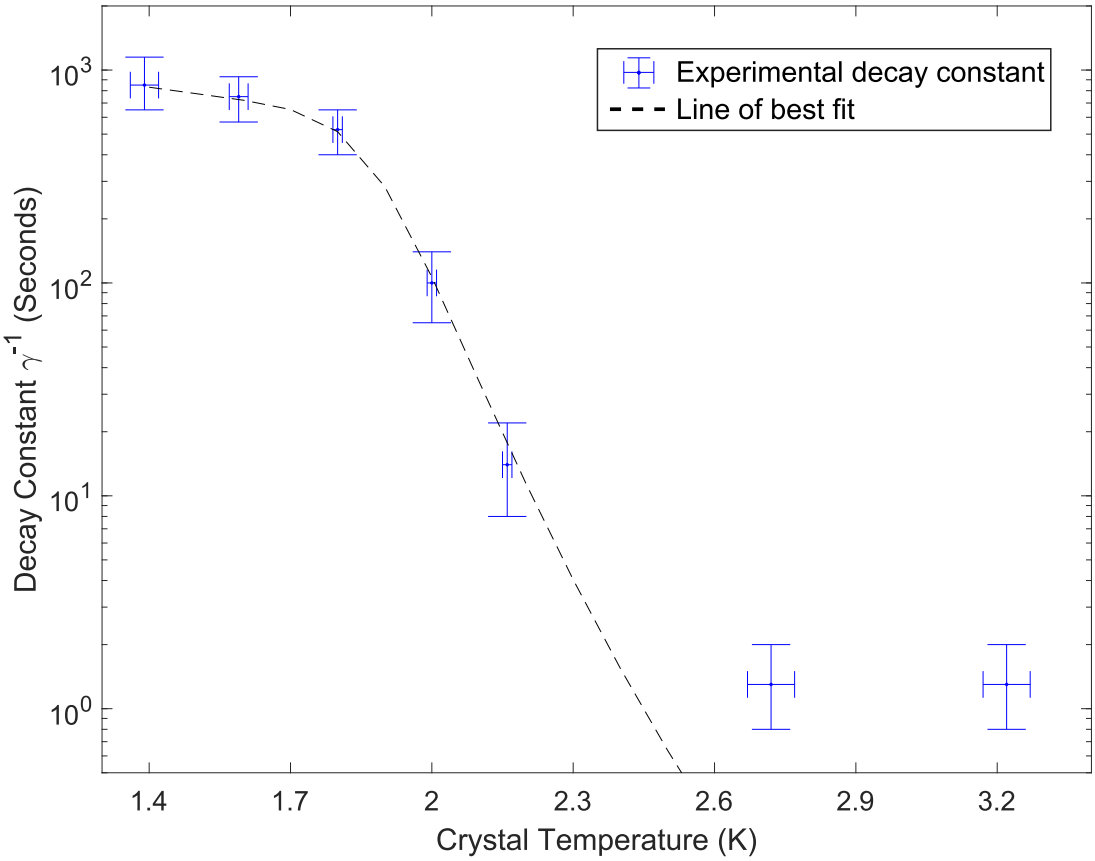


**Figure 4.15:** The decay rate of $^{167}$Er nuclear spin hyper-polarisation as a function of temperature, in a field of 7T. The value of $\gamma^{-1}$ is equivalent to the hyperfine population decay rate ($T_1$). $x$-axis error bars show the maximum temperature variation during the measurement. $y$-axis error bars are given by the fit whose Root Mean Square Deviation (RMSD) is twice as large as the RMSD of the optimal fit to the spectrum. The line-of-best-fit only includes the five data points up to 2.16 K; beyond this temperature it was assumed that the decay rate was limited by a phonon bottleneck.

spin transition frequency.

This equation shows that the Orbach process depends on the ground state electronic spin transition frequency $f$, which varies with magnetic field. At 7T, this splitting can be accurately determined from the crystal field Hamiltonian of Er:YSO [82]. This gives a value of $f = 1108$ GHz (see Figure 4.16).

The experimentally measured decay below 2.2 K fit well to Equation (4.3). This fit is shown by the dashed in Figure 4.15, and has the following parameters:

| $A_D$ | $A_R$ | $A_{Or}$ |
|---|---|---|
| $9 \cdot 10^{-4}\,\mathrm{K}^{-1}.\mathrm{s}^{-1}$ | $0\,\mathrm{K}^{-9}.\mathrm{s}^{-1}$ | $8 \cdot 10^{-30}\,\mathrm{s}^2$ |

Here the plateau in population lifetime below 1.8 K indicates that the Direct process dominates at low temperature. The steep decay in lifetimes between 1.8 K - 2.2 K is an order-of-magnitude greater than expected for the Raman process, and indicates that the

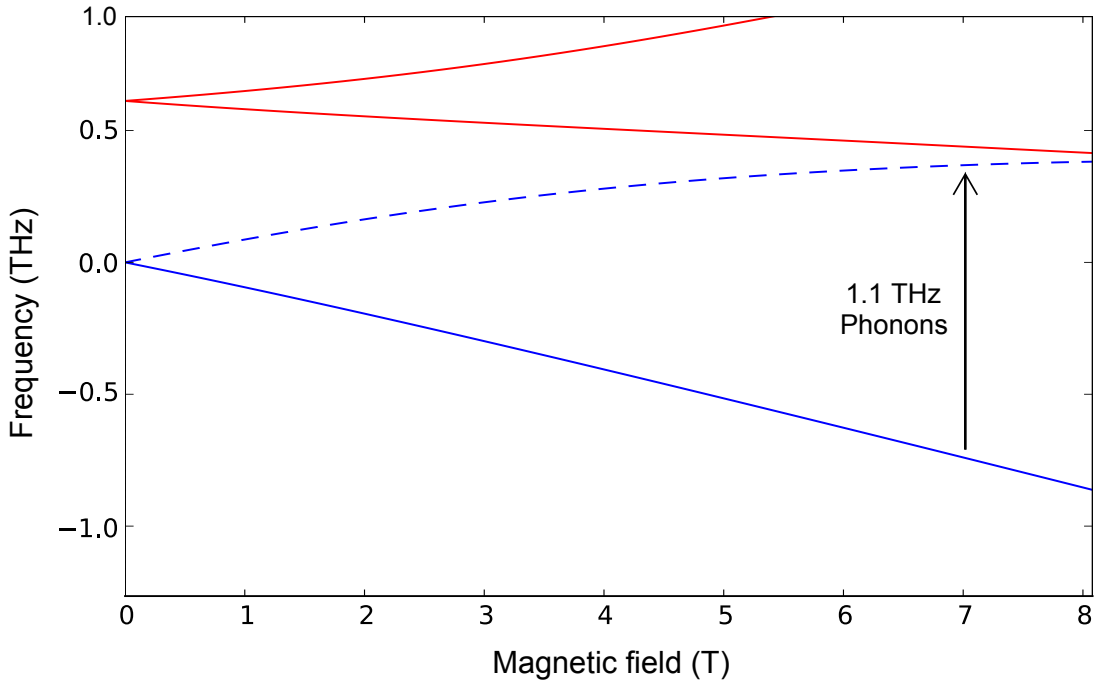


**Figure 4.16:** The energy level diagram of the two lowest crystal field levels of the $I_{15/2}$ ground state multiplet, as a function of magnetic field along the $D_1$ axis and without hyperfine structure. **The solid blue line** shows the $\tilde{S} = |{-1/2}\rangle$ projection the lowest Kramers doublet, whose field dependence is slightly non-linear across the plotted range. **The dotted blue line** shows the field dependence of the $\tilde{S} = |{+1/2}\rangle$ projection, which curves strongly as it anti-crosses with the lower arm of the 2nd lowest Kramers doublet in red. Above 1.8 K the ground state hyperfine transitions are driven indirectly by phonons that excite the $\tilde{S} = |{-1/2}\rangle \leftrightarrow |{+1/2}\rangle$ transition (and higher) at 7T. This is a $\Lambda$-type process called Orbach coupling.

Orbach process dominates in this range. This result is consistent with previous measurements in Er:YSO that demonstrated strong electronic spin-lattice relaxation in non-zero magnetic fields [98, 134].

### 4.9.1 Population lifetime measurements above 2.2 K

Figure 4.15 shows a plateau in the measured population lifetime above 2.2 K, which is inconsistent with the processes in Equation (4.3). It was hypothesised that a phonon 'bottleneck' could cause this plateau, based on similar observations in other materials [135, 136]. To investigate this hypothesis, two estimates for the population lifetime limit were developed. The first estimate was based on the relative heat capacities of the spins and phonons, and second on phonon diffusion in the crystal.

**A phonon bottleneck due to heat capacity**

It is possible to deplete the crystal of resonant phonons if the number of electron spins is large compared to the production rate of phonons. In particular, this will occur if all the resonant phonons are absorbed by the hyper-polarised ions. The observed population lifetime is then determined by the rate of phonon production; the faster phonons are produced, the faster the $^{167}$Er ensemble can relax via the Orbach process.

This analysis follows closely the derivation in Section 10.6 of Abragam & Bleaney. They first determine the ratio of heat capacities of the spins $C_{\mathrm{S}}$ and phonons $C_{\mathrm{Ph}}$, equivalent to the ratio of polarised spins $N$ to resonant phonon modes $\Sigma_{\mathrm{Ph}}$:

$$\begin{aligned}\frac{C_{\mathrm{S}}}{C_{\mathrm{Ph}}} &\approx \frac{N}{\Sigma_{\mathrm{Ph}}} \\ &= N \cdot \frac{\upsilon^3}{12\pi V f^2 df}\end{aligned}$$

where $f = 1108$ GHz is the resonant frequency of the spin transition, $df = 20$ MHz is the spin transition linewidth, $\upsilon = 2 \cdot 10^6$ mm/s is the speed of sound in crystal and $V = 60\,\mathrm{mm}^3$ is the volume of the crystal. The number of polarised spins $N$ can be estimated from the density of Er ions and the pumping volume (a beam waist of $290 \pm 20\,\mu$m). This gives a value of:

$$\begin{aligned}\frac{C_{\mathrm{S}}}{C_{\mathrm{Ph}}} &= \frac{3\pi\,(0.29)^2 \cdot 8.5 \cdot 10^{13} \cdot \left(2 \cdot 10^6\right)^3}{12\pi \cdot 60 \cdot \left(1.108 \cdot 10^{12}\right)^2 \cdot 2 \cdot 10^7} \\ &= 0.17\end{aligned}$$

which indicates that the heat capacities of spin and phonons are very similar. This is a consequence of the THz spin transition frequency; at lower frequencies the heat capacity of the phonon bath would be much smaller than the spins. Assuming that all the phonons are absorbed by spins, the spin relaxation lifetime $T_1$ can then be estimated from the phonon lifetime $\tau_{\mathrm{Ph}}$:

$$\begin{aligned}T_1 =& \tau_{\mathrm{Ph}} \frac{C_{\mathrm{S}}}{C_{\mathrm{Ph}}} \\ =& \frac{L}{\upsilon} \cdot \frac{C_{\mathrm{S}}}{C_{\mathrm{Ph}}}\end{aligned} \tag{4.4}$$

here $L$ is the mean free path of phonons in the crystal. Assuming negligible scattering (a low number of crystal defects) then $L$ is equivalent to the mean crystal length of 4 mm. This would yield a very short lifetime of $T_1 \approx 10^{-6}$ seconds, which suggests that phonon production is not the limiting factor in the observed relaxation rate.

#### A phonon bottleneck due to diffusion

While the previous analysis demonstrated that there were insufficient spins in the crystal to absorb all the phonons, there might still be sufficient spins to impede their movement through the crystal. Assuming that spin hyper-polarisation removes a significant portion of the resonant phonons, then a return to thermal equilibrium could be slowed if phonons have to diffuse into the hyper-polarised region. In particular, slow diffusion would occur if the phonon absorption cross-section of the electron spins was large.

Terahertz phonons have a wavelength of 2 nm, which is much shorter than the mean distance between Er ions in the crystal. Assuming that phonons are scattered in random directions after interacting with a spin, the RMS distance travelled by a phonon $d$ over a period of time $t$ can then be estimated using the Einstein diffusion equation [137]:

$$d = \sqrt{3\varepsilon r^2 t} \tag{4.5}$$

In this equation, $r$ is the phonon mean free path and $\varepsilon$ is the mean scattering time (the time between absorption events). The value of $r$ can be determined by the density of Er ions $\rho$ and the phonon absorption cross-section $\sigma$, such that $r = (\sigma\rho)^{-1/3}$. The value of $\varepsilon$ is equivalent to the electron spin transition lifetime, as it only takes femtoseconds for phonons to move between Er ions. While equation (4.5) is very simple, neither the absorption cross-section nor transition lifetime are easily estimated from recorded measurements. However, a value of $d/t \approx$1 mm/s (which would be consistent with the observed rate of relaxation) can be obtained with $\sigma = 0.05$ and $T_{1\,(e\,spin)} = 10$ ns. This diffusion hypothesis could be experimentally interrogated by studying the rate of spin depolarisation as a function of pumping volume.

## 4.10 Spectral hole lifetime

Chapter 2 introduced two important relaxation processes in rare earth systems: spin-lattice and spin-spin relaxation. The first process, namely spin-lattice relaxation, was character-

ised by the measurements in the previous two sections. The second process was masked in the previous measurement because it did not redistribute the hyperfine population, and therefore did not change the population envelope. However, it will affect any measurements operating on a subgroup of the entire ensemble. This is particularly the case for spectral holeburning, which is a vital component of many quantum memory applications. Therefore, it is important to characterise the cross-relaxation process.

This section presents a study of cross-relaxation, through measurements of spectral hole lifetimes as a function of magnetic field along the $D_1$ optical extinction axis. For these measurements the $^{167}$Er ensemble was initialised in thermal equilibrium at 1.4 K, instead of a hyper-polarised state. Spectral features were then burnt into the centre of the $\Delta m_I = +1$ absorption band, in order to avoid isotopic impurities while maintaining good optical depth. It should be noted that all three bands overlapped (to varying degrees) for fields less than 1T, as indicated by Figure 2.3.

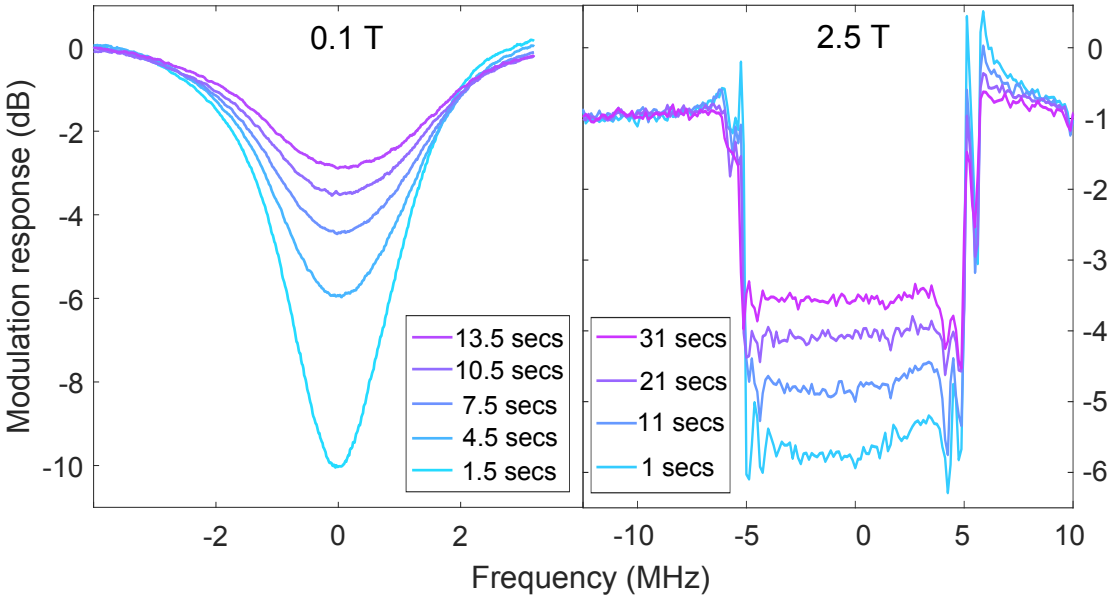


**Figure 4.17:** PM spectra of features burnt at 0.1T and 2.5T. The modulation response is inverted with respect to AM spectroscopy (see Figure 3.4). While the trench at 2.5T is wider, it's sharp edges illustrate reduced spectral diffusion. Some ringing is also evident at the sharp edges of the trench, caused by the fast sweep of the tracking generator.

For fields greater than 1.5T, 10 MHz wide spectral trenches were burnt by sweeping the EOM sideband over a 10 MHz range. This width was chosen as it was considerably broader than the laser linewidth of 100 kHz, resulting in a flat trench. This sweeping was performed for 10 seconds to reach steady state spin-redistribution, as the duty cycle of the sweep was only 10 Hz. A fixed time after a trench was burnt, PM spectra were recorded

with a 50 ms sweep of the EOM sideband over the trench. This burn-scan process was repeated for several fixed delays (up to 6) to determine the trench lifetime, and the series of trenches burnt at 2.5T are shown on the right hand side of Figure 4.17 as an example.

Faster relaxation and increased hole broadening made it difficult to burn deep trenches for fields less than 1.5T. At these low fields spectral holes were instead generated using a fixed-frequency RF source. Even with a fixed-frequency EOM sideband, however, the holes broadened to several MHz due to spectral diffusion (see Section 3.1.2). As an example, the holes burnt at 0.1T are shown on the left hand side of Figure 4.17. For both the trench and hole burning, the laser carrier was 1.5 GHz blue detuned from the $\Delta m_I = +1$ band to prevent unwanted absorption. In both cases lifetimes were determined by fitting a single exponential to the depth of the trench or hole.

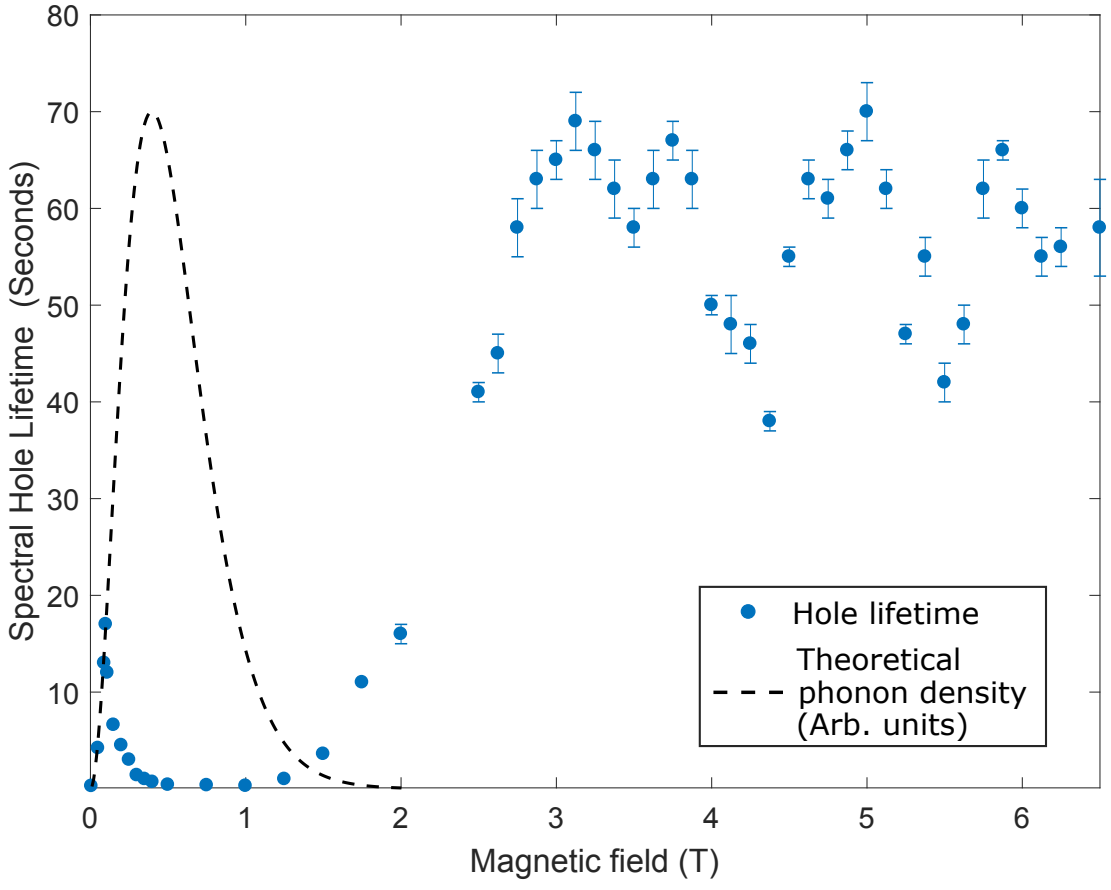


**Figure 4.18: Blue:** The lifetime of spectral features burnt into the $\Delta m_I = +1$ absorption band, as a function of magnetic field along the $D_1$ optical extinction axis. $y$-axis error bars are the standard error in the fit to each point. **Black dashed:** The theoretical phonon density at the electronic transition frequency, defined by Equation (2.12) and equivalent to the Orbach process in Equation (4.3).

The trend in lifetimes shown in Figure 4.18 can be explained by three effects dominating at different magnetic fields. In order of increasing field, these are electronic cross-relaxation, electronic spin-lattice relaxation and hyperfine cross-relaxation. The following three subsections outline the justifications for these conclusions.

### 4.10.1 Electronic cross-relaxation

Rapid electronic cross-relaxation between neighbouring Er ions limits the electronic spin lifetime at low field in Er:YSO [98]. This also shortens hyperfine transition lifetimes to 100 ms in low field, because of the Orbach process described in Section 2.4.4 [69].

Fortunately, electronic cross-relaxation can be suppressed by increasing the magnetic field. In an applied field the Zeeman splitting of the Kramers doublet causes the electron spin ensemble to polarise into the $\tilde{S} = |-1/2\rangle$ state, at a rate determined by the Boltzmann factor. This suppresses the electron-spin cross-relaxation because the density of resonant ions in the $\tilde{S} = |+1/2\rangle$ state is reduced. The rate of hyperfine transitions is then also reduced, which causes the increase in hole lifetimes observed between 0 and 0.1T

### 4.10.2 Spin-lattice relaxation

Beyond 0.1T the spectral holes lifetimes begin to shorten, even though electronic cross-relaxation should be quenched ($e^{-\Delta E/kT} = 0.0006$ at 1T and 1.4 K). This suggests that another process mediates hyperfine transitions beyond this point. In Section 4.9 it was determined that the Orbach spin-lattice process drives hyperfine transitions in large fields at higher temperatures. Because this process is mediated by thermal phonons, it also becomes strong at low temperatures if the magnetic field is reduced. This is illustrated by the black dashed trace in Figure 4.18, which plots the density of thermal phonons at the electron spin transition frequency (Eq 2.12). Moreover, the trend in lifetimes between 0.1-3.0T is anti-correlated with this distribution. Based on this observation and the results of the previous section, it was inferred that Orbach spin-lattice relaxation dominates between 0.1 - 3.0T

### 4.10.3 Hyperfine cross-relaxation

Figure 4.15 from the previous section shows that direct nuclear spin-lattice relaxation limits the hyperfine lifetime at high fields, resulting in a hyperfine $T_1$ of 12 minutes at 1.4 K. However, this lifetime is an order of magnitude longer than the ∼60 sec plateau in

hole lifetimes observed here. This implies that spin-lattice relaxation no longer limits hole lifetimes above 3T. Instead, we infer that hyperfine cross-relaxation is dominant based on several observations.

Firstly, the complicated field dependence above 3T suggests some form of resonant coupling. For hyperfine cross-relaxation, this is consistent with a change in the density of resonant nuclear spins as a function of magnetic field. For certain magnetic fields the hyperfine transition energies of site 1 will be sufficiently similar to those of site 2, such that hyperfine cross-relaxation between the sites can be mediated by Y spins. This increases the effective spin density, causing some regions above 3T to exhibit shorter lifetimes.

Furthermore, this is the only remaining interaction (of the usually considered mechanisms described in Section 2.4) which can reduce hole lifetimes below the hyperfine population lifetime; Electronic cross-relaxation was ruled out due to Boltzmann statistics.

It should also be noted that the lifetimes in Figure 4.18 were measured with the hyperfine population in thermal equilibrium. Measurements with a hyper-polarised ensemble should yield significantly shorter lifetimes at high field, due to the four-fold increase in resonant spins.

### 4.10.4 Spectral diffusion

An additional consideration for shaping narrow absorption features is spectral diffusion. Figure 4.17 presents spectral features burnt at 0.1T and 2.5T. While they both exhibit the long lifetimes necessary for efficient holeburning, the spectrum at 0.1T shows increased spectral broadening. This broadening is consistent with the process of spectral diffusion, which was introduced in Section 3.1.2.

More specifically, the increase is due to the change in electron spin dynamics. For fields greater than 2T the electron-spins are highly polarised. In this regime a phonon-mediated spin flip (spin-lattice coupling) is rapid and short lived; the large density of phonon modes implies that an electron spin will fall back quickly to the ground state. Thus, each electron spin flip contributes only a small contribution to optical transition dephasing.

In a field of 0.1T, however, the electron spins spend appreciable time in either spin state. This produces large dephasing, even though the lifetime (and hence rate of electron spin transitions[8]) is similar to the 2.5T regime. For this reason quantum memory schemes

[8]In the previous subsections it was described how spectral hole lifetimes below 3T are limited by the electronic spin transition rate

requiring narrow linewidths cannot be realised at low fields. Large dephasing will also shorten optical and hyperfine coherence times in the low field regime.

## 4.11 Coherence measurements

On-demand quantum memories require long optical and spin coherence times for qubit manipulation and storage. This section investigates the coherence properties of these transitions in $^{167}$Er:YSO, through two sets of measurements.

Section 4.11.1 presents two-pulse photon echo measurements of the $I_{15/2} \leftrightarrow I_{13/2}$ optical transition; this well-known technique was introduced in Section 3.3.

Section 4.11.2 then presents a Raman echo measurement of the $|{-7/2}\rangle \leftrightarrow |{-5/2}\rangle$ ground state hyperfine transition. Much like the photon echo, the Raman echo technique used here requires only optical pulses. However, the implementation is slightly more involved as it requires optical fields at two frequencies [118].

The magnetic sensitivity of the $|{-7/2}\rangle \leftrightarrow |{-5/2}\rangle$ hyperfine transition is then investigated in Section 4.11.3, and Section 4.11.4 concludes with a discussion of the frozen core effect.

### 4.11.1 Optical coherence measurements

This section presents a measurement of two-pulse echoes of the $|{-7/2}\rangle \leftrightarrow |{-7/2}\rangle$ optical transition. As in previous experiments, an EOM sideband was used to spin-polarise the $^{167}$Er ensemble before the measurement, and the carrier was kept several hundred MHz detuned from the $^{167}$Er absorption.

The optical pulse sequence is shown in Figure 4.19 (b). The polarising-sideband (green) was used to prepare the hyperfine ensemble into $|{-7/2}\rangle$ ground state. This was achieved by sweeping the sideband over the $\Delta m_I = -1$ absorption band, using the same method described in Section 4.7. While previous demonstrations in this chapter involved polarisation to the $|{+7/2}\rangle$ state, here the ensemble was polarised into the $|{-7/2}\rangle$ state instead. This change was motivated by the larger oscillator strength of the associated $\Delta m_I = -1$ transition, relative to the $|{+7/2}\rangle$ state. This allowed for shorter optical pulses during the Raman echo measurements described in the following subsection (see Table 4.3). The degree of spin polarisation achieved here was not measured quantitatively, as it had been for the $|{+7/2}\rangle$ ground state in Section 4.7. Nevertheless, the larger $\Delta m_I = -1$ oscillator strengths should improve the spin polarisation efficiency, compared with polarisation into the $|{+7/2}\rangle$ state.

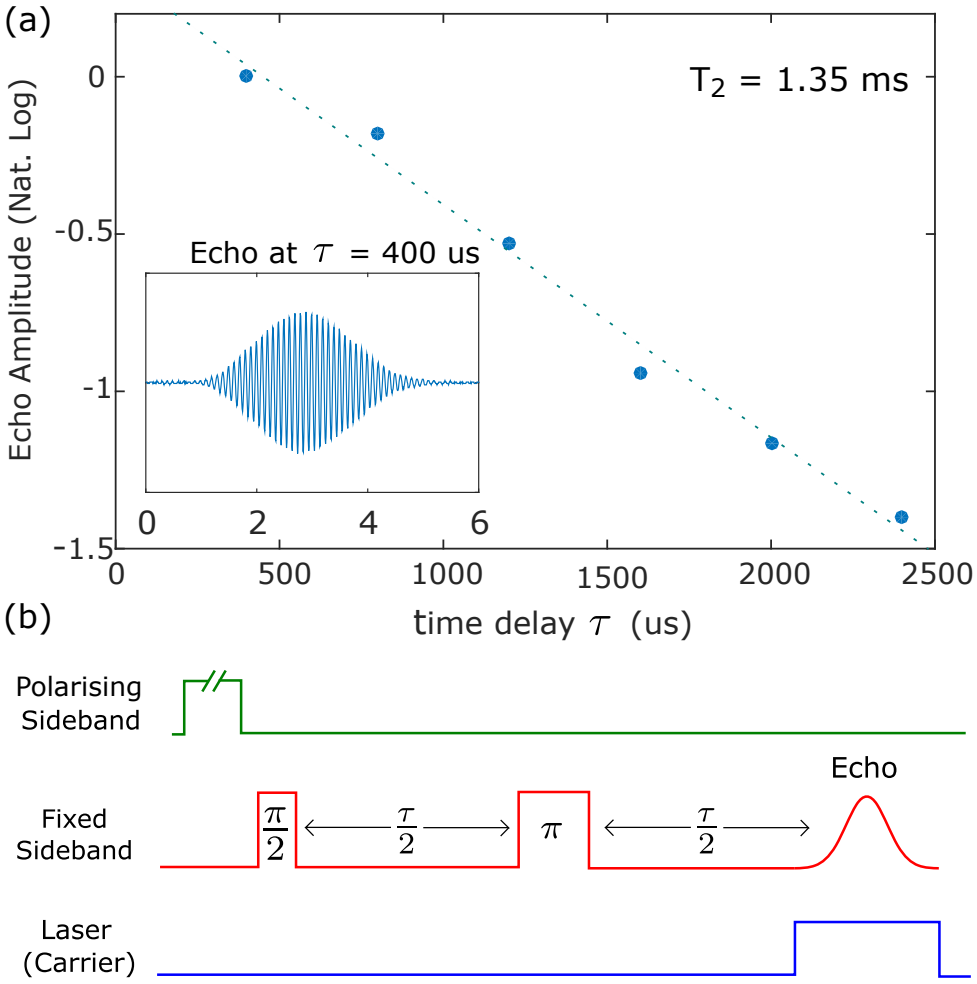


**Figure 4.19:** Coherence measurement on the $|{-7/2}\rangle \leftrightarrow |{-7/2}\rangle$ optical transition at 1.4 K and 7T. **(a)** The decay of two-pulse echo amplitude as a function of total time delay $\tau$. **Inset:** Oscilloscope trace of an echo at $\tau = 400\,\mu s$.
**(b)** A schematic of the optical pulse sequence. **Polarising Sideband:** A VCO drives the sideband over the $\Delta m_I = -1$ absorption band, to polarise the $^{167}$Er ensemble into the $m_I = |{-7/2}\rangle$ ground state (see method in Sec 4.7). **Fixed Sideband:** Centred on the wing of the $|{-7/2}\rangle \leftrightarrow |{-7/2}\rangle$ optical transition and used to coherently drive the same optical transition. **Laser (carrier)**: Approximately 1 GHz red detuned from the $\Delta m_I = -1$ absorption band. When a photon echo forms, the laser-carrier acts as a Local Oscillator (LO) to generate an optical heterodyne beat with the Fixed Sideband.

A fixed-frequency EOM sideband at 2150 MHz was used to coherently drive the $|{-7/2}\rangle \leftrightarrow |{-7/2}\rangle$ optical transition, and this is shown by the middle trace in Figure 4.19 (b). This fixed-frequency sideband excited ions in the wing of the $|{-7/2}\rangle \leftrightarrow |{-7/2}\rangle$ absorption peak, to mitigate pulse propagation issues caused by large optical depth. Photon echoes formed at the wavelength of this sideband at time $t = \tau$. The $\pi$-pulse length which maximised echo amplitude was determined to be $1.5 \pm 0.25\,\mu s$ for 1.5 mW of optical driving power.

To detect the echoes, a local oscillator (the laser carrier) was switched on just before

they were due. This intensity control of the laser carrier was achieved with the DC-bias input to the AM-EOM (see Figure 3.2). Thus, the echo signal took the form of a 2150 MHz heterodyne beat on the optical detector. The 2150 MHz RF signal output from the detector was then mixed down to 10 MHz using a 2140 MHz fixed frequency RF source. The mixer output was then filtered through a 10 MHz bandpass filter, and recorded on the scope shown in Figure 4.2.

These echoes were recorded for a series of time delays from 400 $\mu$s to 2400 $\mu$s, illustrated in Figure 4.19 (a). For each time delay the optical pulse sequence was repeated 30 times. The data points in Figure 4.19 show the average amplitude of the 5 largest echoes for each time delay. From the rate of echo decay we determine a coherence time for the $|-7/2\rangle \leftrightarrow |-7/2\rangle$ optical transition of $T_2 = 1.35$ ms.

Although this value is an order of magnitude greater than zero field coherence times, it falls short of the 4.4 ms achieved by Bottger et al. at 7T [26]. This is likely due to differences in site structure and magnetic field orientation. In particular, Bottger et al. oriented their field 40 degrees to the $D_1$ axis, and performed their measurement on Site 1 rather than Site 2. From a practical standpoint, however, the orientation used by Bottger et al. is difficult to realise with the cryostat used in this work. For this reason, and the fact that it would not necessarily yield any improvement in hyperfine coherence times, the optimal configuration determined by Bottger et al. was not used here.

### 4.11.2 Hyperfine coherence measurements

Optical transitions are required for capturing flying qubits. However, optical coherence times are generally to short for quantum repeater applications. This holds true for Er:YSO, even though it has demonstrated the longest optical coherence time of any rare earth doped material [26].

In other rare earths systems storage times are extended using hyperfine transitions instead [48,138]. The coherence time of the $|-7/2\rangle \leftrightarrow |-5/2\rangle$ ground state hyperfine transition is interrogated here for this reason. This is achieved using the Raman echo technique; equivalent to an optically detected spin-echo measurement (see Ref [118] for a detailed description).

The optical pulse sequence for this experiment is shown in Figure 4.20 (b). The experimental setup was similar to the photon echo measurements in the previous section, except that an additional optical field $\Omega_2$ was used to address the to the $|-5/2\rangle \leftrightarrow |-7/2\rangle$ optical

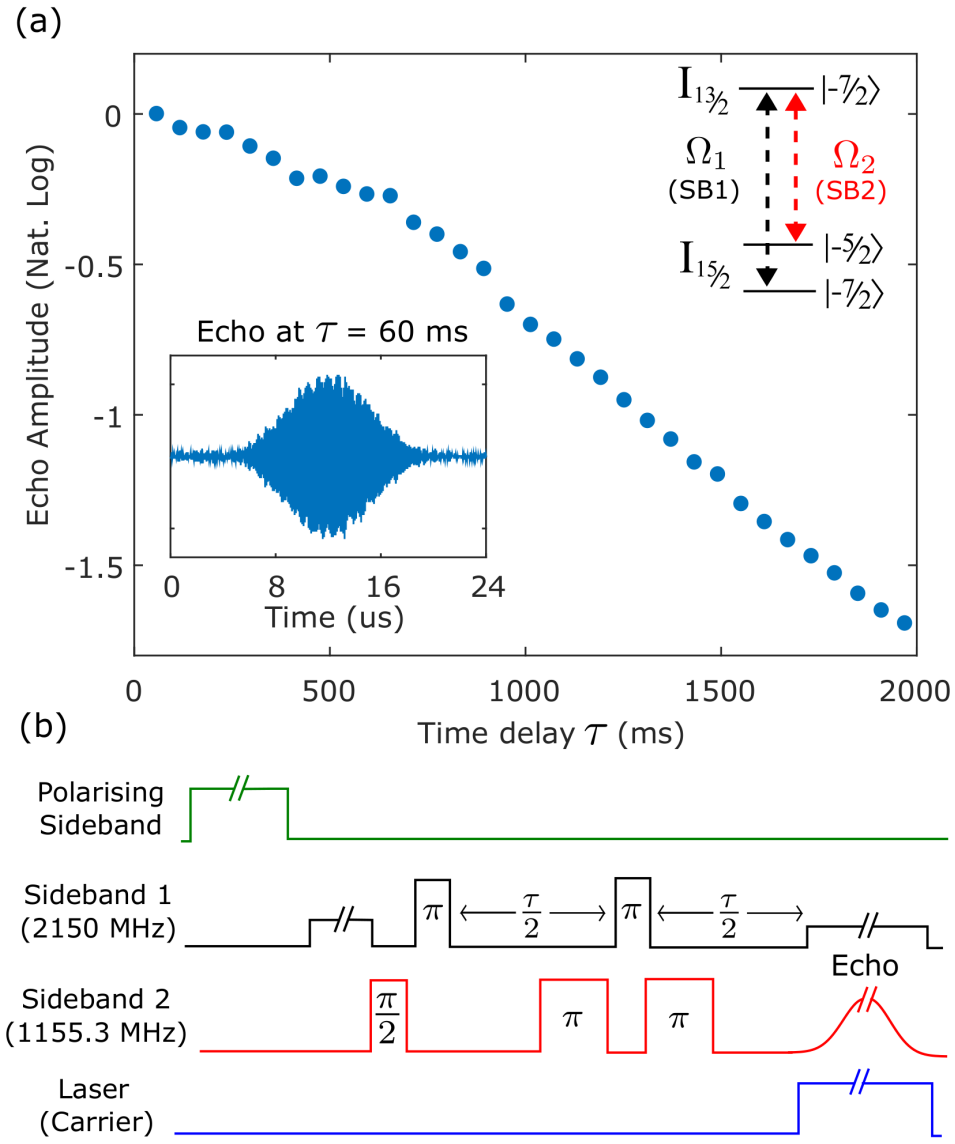


**Figure 4.20:** Coherence measurements on the $|-5/2\rangle \leftrightarrow |-7/2\rangle$ hyperfine transition at 1.4 K and 7T **(a)** normalised Raman echo intensity as a function of total delay $\tau$, at 1.4 K and 7T. *Inset:* Raman echo at $\tau = 60$ ms. **(b)** Pulse sequence for Raman Echoes. *Polarising Sideband:* A VCO drives the sideband over the $\Delta m_I = -1$ absorption band, to polarise the $^{167}$Er ensemble into the $m_I = |-7/2\rangle$ ground state (see method in Sec 4.7). *Sideband 1 ($\Omega_1$):* Centred on the $|-7/2\rangle \leftrightarrow |-7/2\rangle$ optical transition. *Sideband 2 ($\Omega_2$):* Centred on the $|-5/2\rangle \leftrightarrow |-7/2\rangle$ optical transition, at optical frequency $\Omega_2$. *Laser (carrier):* Approximately 2 GHz red detuned from the $\Delta m_I = 0$ absorption band. When a Raman echo forms, the laser-carrier acts as a Local Oscillator (LO) to generate an optical heterodyne beat with SB1.

transition[9]. Combined with the previous field that drove the $|-7/2\rangle \leftrightarrow |-7/2\rangle$ optical trans-

[9]The optimal $\pi$ pulse length for the $|-5/2\rangle \leftrightarrow |-7/2\rangle$ optical transition was measured to be $4 \pm 0.5\,\mu s$ using 1.5 mW of optical power. This value was determined using the method described in Section 4.11.1.

ition, this formed a resonant 3-level system that could indirectly drive the $|{-7/2}\rangle \leftrightarrow |{-5/2}\rangle$ ground state hyperfine transition. For this purpose it was also important that the frequency difference between $\Omega_1$ and $\Omega_2$ match the $|{-7/2}\rangle \leftrightarrow |{-5/2}\rangle$ ground state transition frequency of 994.7 MHz.

Here Raman echoes were performed on a narrow anti-hole in the $\Delta m_I = -1$ band, as opposed to the $\Delta m_I = 0$ band used for the photon echoes. This was done to prevent the pulse distortion from the large OD of the $|{-7/2}\rangle \leftrightarrow |{-7/2}\rangle$ optical transition. The anti-hole was prepared by holeburning with 100 $\mu$W of optical power with $\Omega_1$ for 100 ms. Both optical fields $\Omega_1$ and $\Omega_2$ were generated using fixed-frequency EOM sidebands at 2150 MHz and 1155.3 MHz, respectively.

Upon completion of the Raman echo pulse sequence, optical heterodyne detection was again used to collect the Raman echo signal. Here the optical modulation frequency of the echo was 1155.3 MHz, as it reformed at the optical frequency of $\Omega_2$. Observing the Raman echoes at frequency $\Omega_2$ also relied on having population in the $|{-7/2}\rangle$ optically excited state at the time of coherent rephasing[10]. This was achieved with another long weak pulse at the frequency of $\Omega_1$, which slowly pumped the sub-ensemble in the $|{-7/2}\rangle$ ground state to the $|{-7/2}\rangle$ excited state at time $t = \tau$ .

Using this method, Raman echoes were recorded for a series of time delays from 60 ms to 1980 ms. For every time delay the optical pulse sequence was repeated 30 times. Each data point in Figure 4.20 (a) shows the average amplitude of the 5 largest echoes for the given time delay. This data selection was necessary to filter out transient issues due laser frequency instability. As the laser wasn't sufficiently stable to rephase the entire coherent ensemble in each measurement, there were many recorded echoes with reduced intensity.

In this plot the rate of echo decay is not exponential for delays shorter than a second. This trend is consistent with previous spin-echo measurements for Er doped materials in large fields, and is attributed to slow Y spin dynamics (see Section 4.11.4 and Ref [139]). For this reason we define the coherence time of the $|{-7/2}\rangle \leftrightarrow |{-5/2}\rangle$ ground state hyperfine transition by $e^{-1}$ attenuation of the echo amplitude. This gives a value of $T_2^{\text{hyp}} = 1300 \pm 10$ ms, which is 300 times greater than any previously measured coherence in Er:YSO [26].

[10] Attempts to optically excite the population just prior to rephasing (rather an during) yielded significantly attenuated echoes due to the short lifetime of the optical transition. Additionally, it should be possible to form an echo on any related optical transition ($\Delta m_I = \pm 1, \pm 2$, etc) if either coherent ground state populations is transferred to the appropriate optical excited state at the time of rephasing.

### Hyperfine inhomogeneous broadening

In general, an echo time-envelope represents the Fourier transform of the inhomogeneously broadened ensemble on which the echo is performed. For the photon echo measurements of Section 4.11.1, the echo rephased $\mathcal{O}$(MHz) optical inhomogeneous broadening. This width was determined by the bandwidth of the optical pulses, and is consistent with the $\mu$s echo time-envelope shown in Figure 4.11.1. For the Raman echo sequence, the echo rephased the inhomogeneously broadened hyperfine ensemble, rather than the optical. Although the Raman echo was performed on a sub-MHz wide anti-hole in the optical transition, the associated hyperfine ensemble contained ions from across the entire inhomogeneous hyperfine line. The reason for this difference is that the optical and hyperfine inhomogeneous broadening is largely uncorrelated.

Thus, the Raman echo time-envelope was used to determine the hyperfine inhomogeneous broadening. In particular, the FWHM of the time and frequency linewidths obey the following Fourier relationship (assuming a Gaussian echo):

$$\mathrm{FWHM}(t) = \frac{4\ln 2}{\pi \mathrm{FWHM}(f)}$$

From the Inset of Figure 4.20 we obtain a FWHM of $7 \pm 1\,\mu s$ for the time-envelope. This implied that the inhomogeneous hyperfine line had a FWHM of $130 \pm 20$ kHz.

## 4.11.3 Magnetic sensitivity of the $|-7/2\rangle \leftrightarrow |-5/2\rangle$ ground state hyperfine transition

Magnetic sensitivity is a large determining factor for coherence times. For field vectors at which transitions exhibit zero magnetic sensitivity (called 3D turning points) exceptionally long coherence times can be achieved [48, 138]. To investigate whether such a regime had been achieved (accidentally) in the previous section, the magnetic sensitivity of the $|-7/2\rangle \leftrightarrow |-5/2\rangle$ hyperfine transition was measured.

For this experiment a series of holeburning spectra were recorded as a function of magnetic field along the $D_1$ optical extinction axis (not shown here). At each field the $|-7/2\rangle \leftrightarrow |-5/2\rangle$ hyperfine transition frequency was determined using the method described at the end of Section 4.5.

The resulting field dependence is presented in Figure 4.21, where a linear frequency gradient of $11.3 \pm 0.1$ MHz/T is observed. This proved that the measured hyperfine co-

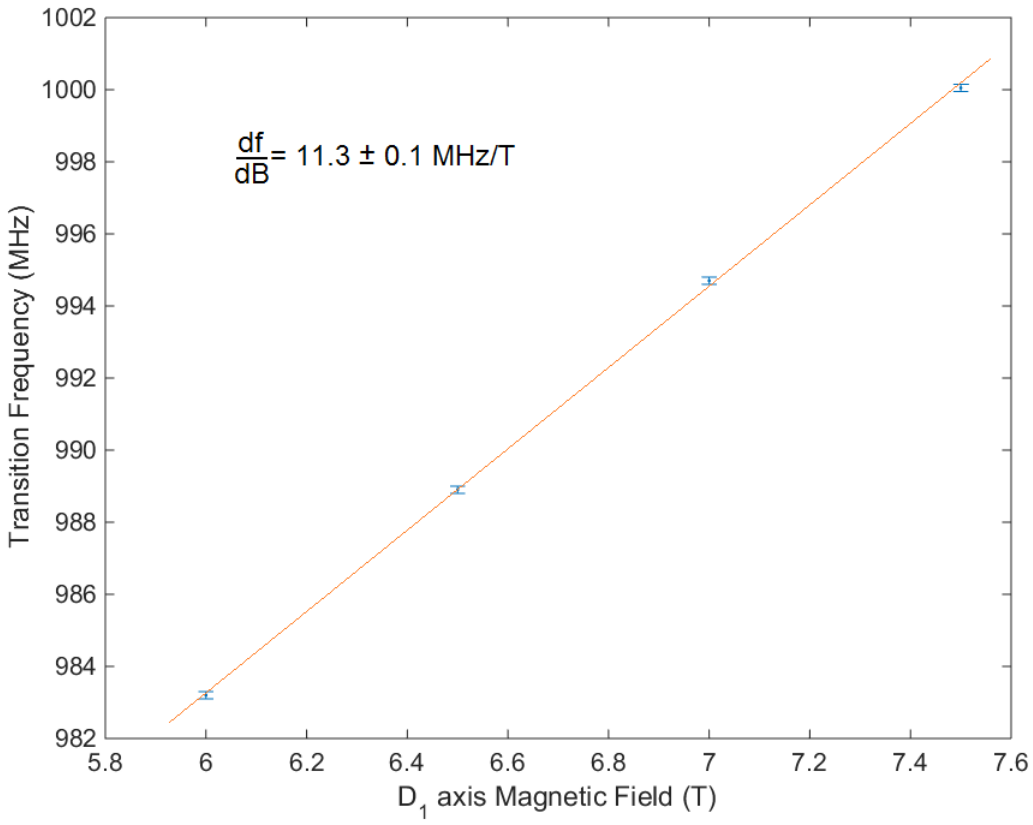


**Figure 4.21:** Frequency of the $|-7/2\rangle \leftrightarrow |-5/2\rangle$ ground state hyperfine transition as a function of magnetic field along the $D_1$ axis. The $y$-axis error bars indicate the linewidth of the spectral holes used to measure the transition frequency. The data fits well to the straight line shown in orange, with a gradient of $11.3 \pm 0.1$ MHz/T. The stated uncertainty is the standard error in the fit.

herence time wasn't exceptionally long, as there was no turning point at 7T. At best the magnetic sensitivity at 7T could be a saddle point, if the sensitivity in the the $D_2$ and $b$ directions are zero. The constant gradient also suggested that long coherence might be achieved at lower fields, and this is investigated further in the following section.

### 4.11.4 The frozen core effect

In the high field and low temperature regime, polarised electron spins should contribute negligible magnetic noise [67, 76, 126]. Instead, the major contribution to decoherence should be nuclear spins in the crystal, primarily the nuclear spin$-1/2$ $^{89}$Y ions, as they exist in 100% abundance.

The amount of decoherence on the $|-7/2\rangle \leftrightarrow |-5/2\rangle$ transition caused by Y ions can be estimated from the magnetic sensitivity measured in the previous section. This estimate

is obtained as follows[11] [48, 140]:

$$\frac{1}{\pi T_2} = \nabla f \cdot \mathbf{\Delta B}$$

where $\nabla f$ is the magnetic sensitivity of the transition and $\mathbf{\Delta B}$ is the FWHM field fluctuation caused by the Y ions. Previous calculations for undoped YSO have estimated magnetic fluctuations of $8\,\mu T$, caused by Y cross-relaxation [48]. By taking $\frac{\delta f}{\delta D_1} = 11.3\,\mathrm{MHz/T}$ as a lower-bound for $\nabla f$ , the hyperfine coherence time is then:

$$\begin{aligned} \nabla f \cdot \mathbf{\Delta B} &\geq 11.3 \cdot 10^6\,\mathrm{Hz/T} \times 8 \cdot 10^{-6}\,\mathrm{T} \\ \therefore T_2 &\leq 3.6\,\mathrm{ms} \end{aligned}$$

This value is well below the experimentally observed coherence time of 1.3 seconds, which indicates that the Y cross-relaxation must be heavily suppressed under the experimental conditions. Observed in many other materials, this suppression was dubbed the 'frozen core' effect [141]. Here the Y ions close to the polarised Er spins are detuned from the bulk, slowing the rate of Y cross-relaxation and reducing the magnetic fluctuations.

The slowed Y dynamics also lead to the non-exponential decay observed in Figure 4.20. This implies that longer coherence times can be achieved by using dynamic decoupling techniques [142].

## 4.12 Summary

Er based approaches to quantum information storage have been impeded by short spin lifetimes and coherence times. To address these issues, this chapter investigated the optical and hyperfine transition properties of $^{167}$Er:YSO in large magnetic fields.

Sections 4.4 introduced the optical absorption spectrum of this material in a field of 7T. The holeburning measurements in Section 4.5 were then used to determine the underlying hyperfine structure of the optical absorption line. Based on these measurements, a model of the absorption spectrum was developed and presented in Section 4.6.

The rest of the chapter delivered the major experimental milestones of the thesis. Firstly, efficient nuclear spin polarisation of the entire $^{167}$Er ensemble was presented in Section 4.7. This was the first such demonstration in rare earth systems, and a key re-

[11] This equation is only valid if the Y spins cross-relax faster than the rate of Er decoherence. In this case it is valid as the Y cross-relaxation rate was measured to be 8 Hz in Er:YSO [76].

quirement for broadband optical storage. A hyperfine population lifetime of 14 minutes at a temperature of 1.4 K was subsequently measured in Section 4.9. The magnetic field dependence of spectral hole lifetimes was then investigated in Section 4.10. These measurements illustrated the effect of spin-lattice relaxation in this system, and how it can be mitigated. The final result of the chapter is detailed in Section 4.11, where a 1.3 second coherence time was achieved for an $^{167}$Er hyperfine transition. This is an improvement of several orders-of-magnitude over previous coherence measurements for spin transitions in Er doped solids, and the implication of these results for future quantum memory development will be discussed in Chapter 6.

Chapter 5

# Single Erbium ions in Silicon

**The Er:Si research presented in this chapter is a highly collaborative effort, spanning several research institutions[1]. Experimental data was collected by Dr C. Yin, G. de Boo and Q. Zhang, and relevant figures are duly annotated. However, all the subsequent analysis and modelling presented here is my own.**

The development of a practical quantum computer hinges on the realisation of DiVicenzo's seven criteria [9,10]. In this respect, great progress has been made with a computing architecture based on single defects in silicon. Most of this work has focused on individual P:Si dopants, in order to address the first five criteria [13–15, 17, 18]. With an optical transition at 1.5 $\mu$m, Er is an ideal candidate to fulfil the final two [10]. In particular, single Er ions could be used to develop an optical-spin bus, allowing P:Si qubits to access the future quantum Internet.

Long spin lifetimes and coherence times are important requirements for such a bus. This chapter aims to address these requirements, by investigating the optical transition properties and energy level structure of single Er:Si ions. Section 5.1 begins with an outline of a novel optical detection method developed for measuring these single Er centres. The experimental setup used for these optical measurements is introduced in Section 5.2. The first recorded examples of single Er:Si absorption spectra are then presented in Section 5.3 and these homogeneously broadened absorption lines are analysed in Section 5.4. The inhomogeneous absorption profile of Er:Si is then investigated in Section 5.5 and the chapter concludes with a characterisation of the crystal field Hamiltonian for an individual Er ion in Section 5.6.

[1] **Devices implantation was performed at ANU by Prof J. McCallum and Dr B. Johnson of the University of Melbourne. The experiment was setup up by Dr C. Yin, G. de Boo and Myself at the University of New South Wales (UNSW). Experimental investigations were conducted by Dr C. Yin, G. d Boo, Q. Zhang and Myself at UNSW. Data analysis was undertaken by Dr C. Yin and G. Deboo at UNSW and Myself at ANU. Analysis software and advice was provided by Dr S. Horvath and Prof M. Reid of Canterbury University, NZ.**

## 5.1 Single defect detection in solid state

A key requirement for an optical-spin bus, and single defect quantum computing more generally, is the ability to detect or 'read-out' the energy state of the defect. The first detection of an individual defect in solid state relied on an all-optical approach, where a single pentacene molecule in a p-terphenyl crystal was detected using absorption spectroscopy [143]. All-optical approaches have since been extended to other solid state defects, although they generally suffers from low detection efficiency [144–146].

Instead, 100% detection efficiency has been achieved using solely electrical readout. In particular, Single Electron Transistor (SET) technology has been used to readout the electronic spin state of a P:Si dopant [13]. The downside of this approach is poor energy resolution, which is limited to several GHz at mK temperatures. This would make nuclear spin readout difficult for $^{167}$Er, given the sub-GHz hyperfine spacings.

To overcome these issues, a novel approach to single defect detection was developed for the Er:Si experiments detailed here. Informed by previous observations of light induced ionisation in SET's and a rich history of Er:Si spectroscopy, this approach combines optical excitation and electrical detection to achieve high resolution and detection efficiency. The following two subsections describe this approach in more detail, and Section 5.3 presents the first demonstration of single Er detection using this approach.

### 5.1.1 Resonant optical excitation

When interrogating the optical transition of a single centre, the frequency resolution is ultimately limited by the transition lifetime or dephasing time. Although optical dephasing has not been investigated in Er:Si, millisecond lifetimes have been observed for the 1.5 $\mu$m optical transition in bulk samples. This suggested that sub-KHz resolution might be achieved using an optical approach in a noise-free environment. Unfortunately, detecting emission from the $I_{15/2} \leftrightarrow I_{13/2}$ transition of single Er centres is made difficult by the weak fluorescence in silicon [27]. Thus, an approach based on resonant 1.5 $\mu$m absorption (rather than emission) was proposed.

### 5.1.2 High efficiency electrical readout

Previous investigations in silicon informed the concept of electrical readout by optical excitation. Er related defects in silicon are known to form 'donor' levels in the Si bandgap.

Detailed in Section 2.5, this structure presents an energy pathway between Er ions and charge carriers. While this pathway has previously been used to generate 1.5 $\mu$m emission by electroluminescence, our aim was to drive this process in reverse [147]. In particular, it was assumed than an electric current could be induced in the silicon by optically exciting the $I_{15/2} \leftrightarrow I_{13/2}$ transition.

Even with a pathway for electrical readout, this technique still required a very sensitive charge detector. To satisfy this requirement, the same SET technology used for single P:Si detection was employed. These nano-scale transistors are described in Section 3.4, and their applicability was further motivated by previous demonstrations of (non resonant) photo-ionisation detection [125].

With sufficiently low density of Er ions, it was believed that single centres could be spectrally resolved by combining SET detection and a narrow wavelength laser. It was also thought the signal collected by the SET should provided a means to distinguish between single and multiple defects (see Figure 3.9). Such measurements are analogous to photon statistics measurements on optically detected single centres.

## 5.2 Experimental setup

Investigated in this chapter are Er implanted Fin-shaped Field Effect Transistors (FinFETs). When negatively biased, these FinFETs operate as SETs at liquid He temperatures. An example of such a transistor is shown in Figure 3.10, and the n-p-n FinFETs used here were fabricated by IMEC [124]. Each device had a p-type silicon channel passing under a poly-crystalline silicon gate separated by a gate dielectric. The p-type channel had a boron doping of $10^{18}\,\mathrm{cm}^{-3}$. Following device fabrication, erbium and oxygen co-implantation was performed with implantation energies of 400 keV and 55 keV and ion fluences of $4 \cdot 10^{12}$ and $3 \cdot 10^{13}\,\mathrm{cm}^{-2}$ respectively.

The presence of oxygen and boron impurities is known to enhance erbium luminescence in silicon, and this doping produced an Er:O ratio of about 1:6 in the channel region [27]. The isotopic composition of the erbium ion beam was estimated by J. McCallum to be 70–80% $^{168}$Er and 20–30% $^{167}$Er, allowing both species to be studied. The dimension of the device channels were 100×50×20 nm (length×width× height). Stopping and Range of Ions in Matter (SRIM) simulations of the ion implantation gave estimates of approximately 30–40 Er ions within the charge sensing region of the channel.

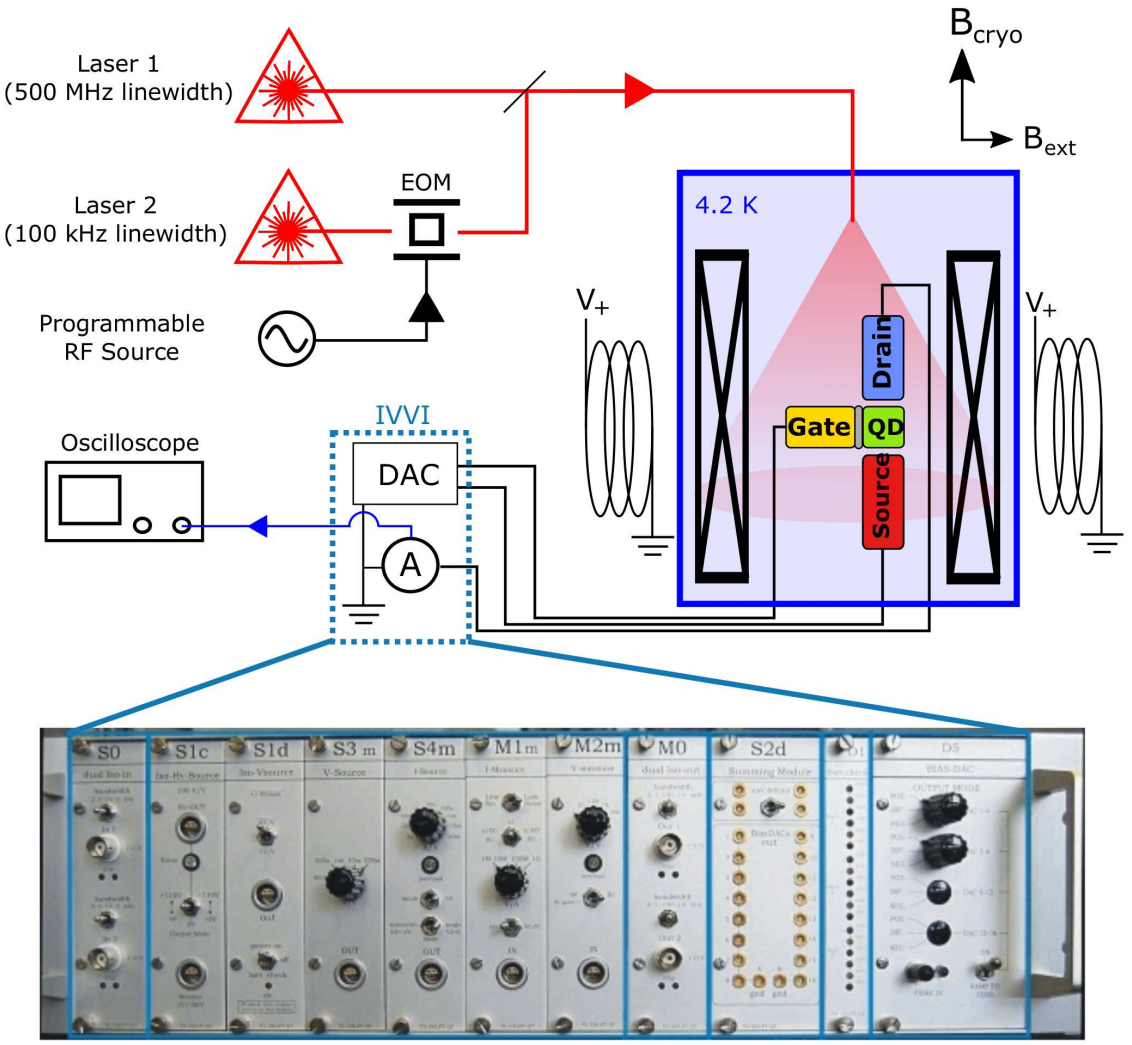


**Figure 5.1:** The experimental setup for the Er:Si investigations. Either laser (1 or 2) was used non-consecutively to illuminate the sample. **The lower section** shows an image of the specialised rack mount electronics (IVVI) used for controlling and measuring current in the FinFET devices. This image was reproduced from [148].

The experimental setup shown in Figure 5.1 was used for all the experiments described in this chapter. The Er-implanted FinFETs were maintained at a temperature of 4.2 K, in an Oxford helium bath cryostat with a 15T super-conducting magnet. Perturbation coils were added to the cryostat (externally) to provide a small perpendicular field (2 mT) at the sample. The sample stick was equipped with bare single mode fibre (smf-28e) connected to a fibre feed-though at the top. The fibre was cleaved at the bottom end (the sample end). Illumination of the FinFET was achieved by fixing the cleaved end of the fibre perpendicular to the sample, producing a beam waist of approximately 1 mm on the FinFET.

To illuminate the sample, two 1550 nm fibre-coupled lasers were used non-concurrently. The first laser was a 5 mW JDSU SWS15101, with a 500 MHz linewidth over 1 second. The JDSU laser was designed with remote wavelength control, so it was possible to program 100 nm spectral scans with 50 MHz steps. For spectral scans that covered wide wavelength ranges or required several hours to complete, an external wavemeter (Angstrom WS-7) was used as an absolute frequency reference to compensate for thermal drift.

The second laser was a 50 mW Thorlabs TLK-1550R, stabilised to my home-built reference cavity (100 kHz linewidth on a 1 second timescale). For this laser, spectral scans up to 10 GHz wide were achieved with a 10 GHz Covega AM-EOM, driven by a Agilent programmable high frequency RF source. In this case the laser (carrier) was maintained at a fixed frequency, and either of the two EOM sidebands were used to scan over the optical absorption line. The two lasers complemented each other well in wavelength resolution and scan range. For the experiments documented in this chapter only a single laser was used at any one time, depending on the experimental requirements.

Control and read-out of the FinFET current was achieved with an I-V and V-I measurement (IVVI) unit, shown in the lower half of Figure 5.1. This is a battery-operated (low electrical noise) rack-mount unit composed of several add-in boards, designed and built at the University of Technology (TU) Delft [148]. As only one FinFET was measured at any time and no RF was applied to the FinFET gates, the IVVI unit was rather under-utilised in the experiments described here.

Voltage to the source-drain channel and gate were supplied by two channels of a computer controlled DAC (the S2d board). An ammeter (the M1m board) was also placed in series with the drain lead to measure the source-drain current. The M1m board generated a voltage proportional to the source-drain current, which was then amplified and digitised via an ADC in 1 ms time-steps. This digital signal was sent to a buffer-board (the S0 board), which was then connected to a scope for data acquisition. The purpose of the S0 board was to isolate the measurement electronics (the scope) from the sensitive FinFET control and read-out electronics.

## 5.3 Detection of single Er ions

Section 5.1 introduced a novel approach to single defect detection in solid state. Here this approach is realised with Er:Si, and illustrated though the optical absorption spectrum in Section 5.3.1. In particular, this spectrum was collected using photo-ionisation in the

Er implanted SET, rather than a measurement of optical attenuation. This measurement technique is further utilised to detect the electronic and nuclear spin states of Er ions in Sections 5.3.2 - 5.3.3.

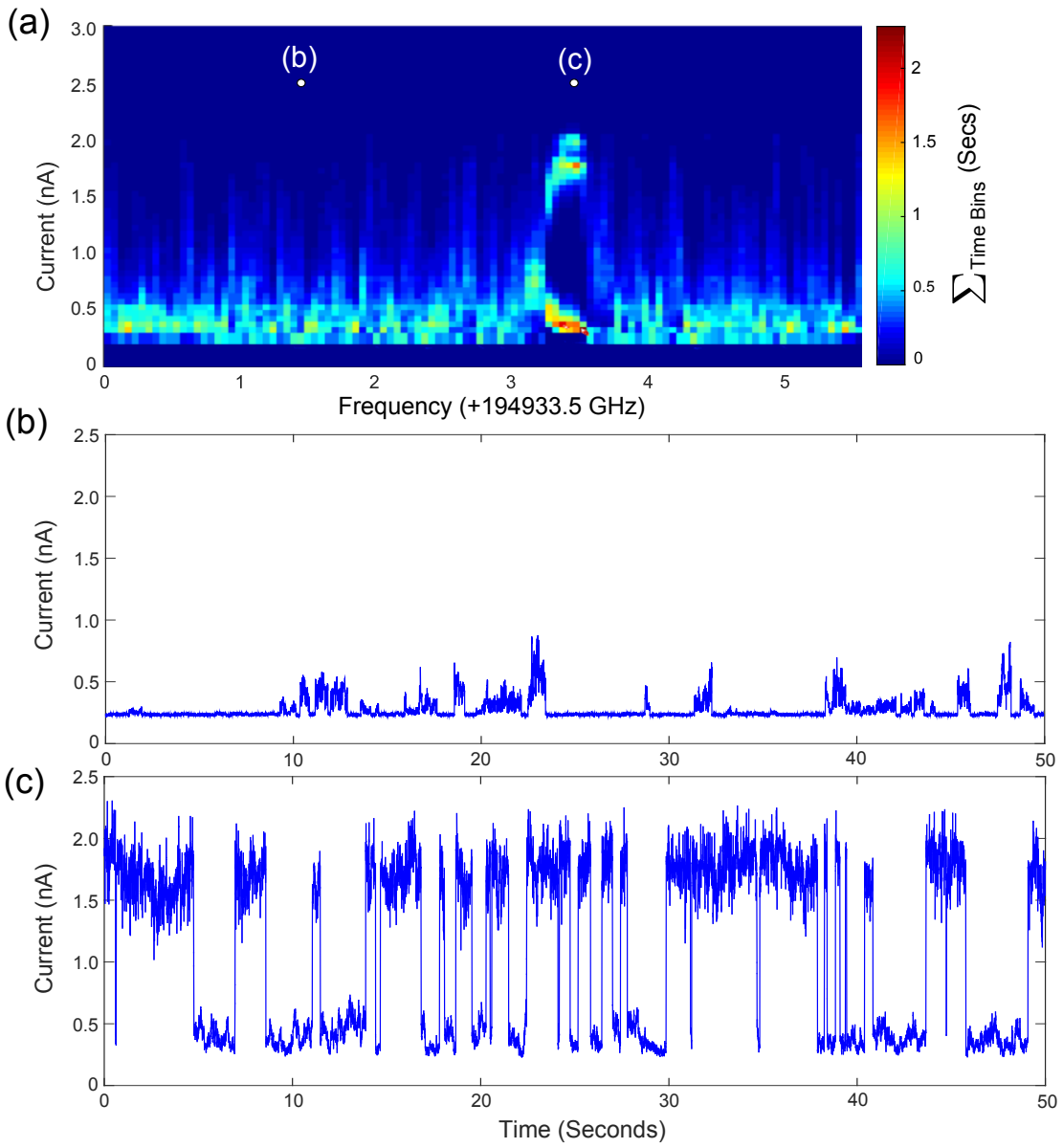


**Figure 5.2:** The first detection of optical absorption from a single Er ion in a FinFET device. **(a)** Absorption spectrum comprised of 110 vertical current histograms plotted side-by-side. The $x$-axis represents the laser frequency and the $y$-axis represents FinFET current. The colour intensity shows the time integral at each current level (binned in 50 pA steps) for a 50 sec current time-trace. **(b)** An example current time-trace with 194935.0 GHz laser illumination. **(c)** An example current time-trace with 194936.4 GHz laser illumination. **Data collected by Dr C. Yin.**

### 5.3.1 Electrically detected absorption of single Er ions

Using the experimental setup described in the previous section, an absorption spectrum was collected using the JDSU laser. This spectrum was developed by stepping the laser wavelength in 50 MHz increments from 1520 - 1550 nm, with 1 mW of optical power incident on the FinFET. This wavelength region was chosen because it covered the strongest known emission lines observed in bulk Er:Si [27, 149–151]. At each wavelength step the recorded data consisted of 50 second time-traces of the FinFET source-drain current. To maximise the charge detection sensitivity, the FinFET gate voltage was biased to the wing of the first coulomb peak (see Figure 3.9).

Figure 5.2 (a) shows a spectrum from this absorption scan covering a 5.5 GHz region around 1537.9 nm. The plotted data at each wavelength step in this spectrum is a histogram of FinFET current recorded during the 50 second exposure. Two examples of these current time-traces are shown in Figure 5.2 (b) and (c).

The 500 MHz wide Er absorption peak centred at 3.4 GHz in Figure 5.2 (a) is the first example of optically resonant charge detection in an SET device. Illustrated in Subfigure (c), the FinFET current undergoes discrete two-level fluctuations observed when the laser is resonant with this absorption peak. This is the signature of a single charge trap oscillating between two charge states, and consistent with absorption from a single defect [125].

### 5.3.2 Electron spin detection

To resolve the electron spin states of Er in an optical spectrum, one must break the degeneracy of the $\tilde{S} = 1/2$ Kramers doublets. This can be achieved using a magnetic field; Zeeman splitting of Kramers doublets has been observed in bulk Er:Si spectra [152].

In a similar way, Figure 5.3 demonstrates Zeeman splitting of a single Er absorption line[2] centred at 194807.6 GHz. The two visible Zeeman arms were inferred to be $\Delta m_{\tilde{S}} = 0$ optical transitions, while the two $\Delta m_{\tilde{S}} = \pm 1$ transitions were too weak to be observed. While this is consistent with Zeeman split lines recorded in Er:YSO spectra (Ch5 of Ref [128]), it meant that the $g$-factors of the $I_{15/2}$ and $I_{13/2}$ states could not be determined. Rather, the Zeeman splitting in Figure 5.3 informed the value of $|g_{15/2} - g_{13/2}| = \Delta g = 4.8$. This is larger than the isotropic $\Delta g = 1.9$ for cubic Er:Si sites [27], and consistent with

[2]To illustrate magnetic field dependence, this colour plot presents slightly different data to that of Figure 5.4 (a). Here the $y$-axis shows applied field rather than current, and each pixel indicates the total time for which the current was greater than 1 nA (by colour) for the specified field and wavelength.

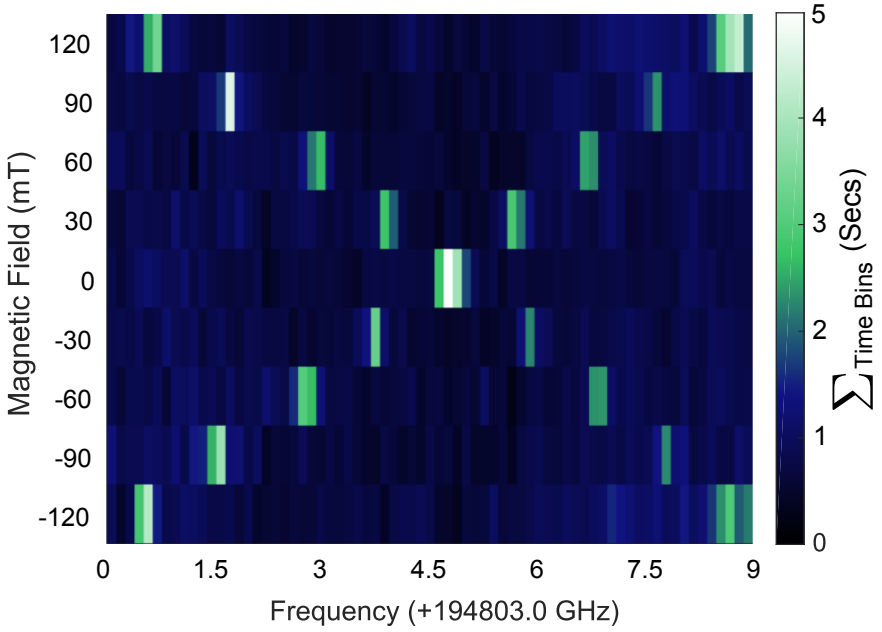


**Figure 5.3:** Magnetic field dependence of Er absorption peaks. The $x$-axis represents laser frequency and the $y$-axis represents applied field. The colour shows the total time the current remained above 1 nA for the 50 second recording at each pixel. **Data collected by Dr C. Yin.**

the assumption that low-symmetry Er complexes are required for the electroluminescence pathway (see Section 5.5).

### 5.3.3 Nuclear spin detection

As mentioned in Section 5.2, $^{167}$Er constituted approximately one quarter of the ions implanted in the FinFET. Resolving the hyperfine structure of these ions was not possible with the 500 MHz linewidth of the JDSU laser. Instead, several absorption spectra were recorded using the cavity-locked Thorlabs laser to achieve sub-MHz resolution. With the laser locked, spectral scans were recorded by sweeping the optical sidebands of a high frequency EOM.

The left hand side of Figure 5.4 shows an example spectrum recorded using this method. The overall structure is identical to the Kramers-doublet spectrum shown in Figure 5.3, although only one Zeeman arm has been developed up to 140 mT (the red arrow). Superposed on the electronic Zeeman shift are narrow hyperfine absorption peaks, indicating the presence of $^{167}$Er.

The right hand side of Figure 5.4 shows the developed Zeeman arm replotted with the linear magnetic dependence (approx 10 GHz/T) subtracted. This shows more clearly the hyperfine state evolution as a function of magnetic field, and here it can be observed that

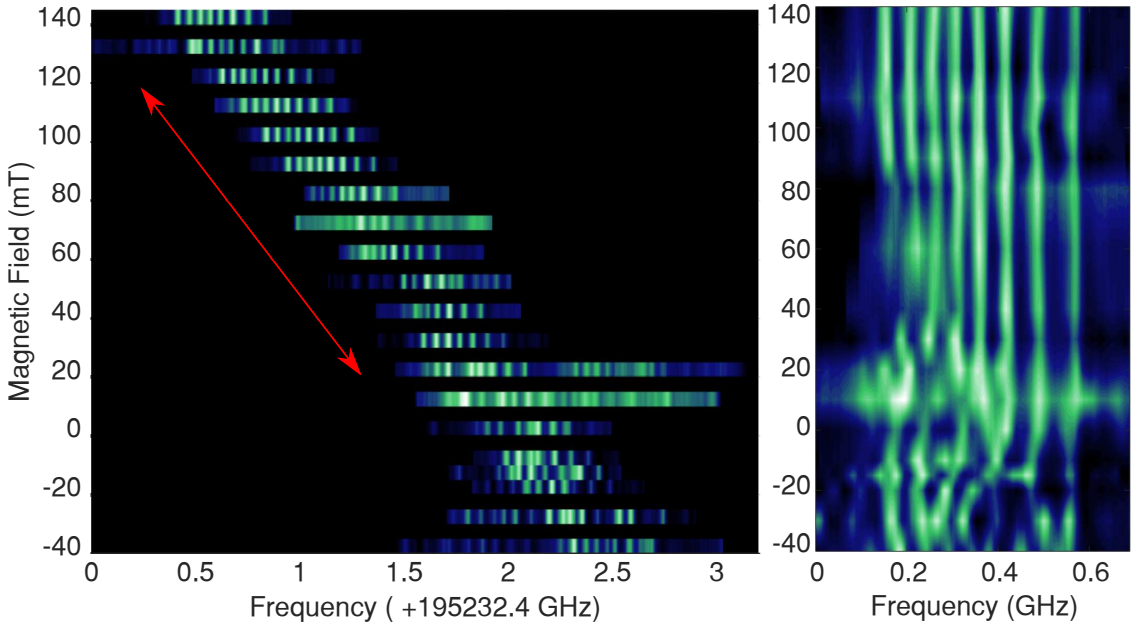


**Figure 5.4:** Magnetic field dependence of FinFET tunnelling current for an $^{167}$Er ion. **Left side:** demonstrates the typical X shape for the set of Kramers doublet optical transitions. No data was collected for the regions in black. **Right side** shows the hyperfine substructure for the optical transition indicated by the red arrow. The magnetic field dependence of this Zeeman arm (10 GHz/T) has been subtracted to highlight the change in hyperfine structure with magnetic field. Beyond 80 mT there are eight clear hyperfine peaks at this point. **Data collected by G. de Boo.**

the optical transition exhibits eight strong peaks above 80 mT. These are inferred to be the eight $\Delta m_I = 0$ transitions of $^{167}$Er, illustrated by the energy level diagram in Figure 4.1. The complicated field dependence below 80 mT in Figure 5.4 is indicative of hyperfine level anti-crossings, also consistent with Figure 4.1.

## 5.4 Properties of the homogeneous absorption line

The previous figure illustrated homogeneously broadened optical transitions in a FinFET device. Here we study the homogeneous transition lineshape, to better understand the Er optical coherence properties. This is achieved by developing a model of the optical absorption process in Sections 5.4.1 - 5.4.3, and fitting simulated spectra to experimental data in Section 5.4.4.

The first step to developing the absorption model was to assume a Lorentzian absorption profile. Detailed in Section 5.4.1, this absorption profile was modulated by slowly-varying electric field noise: a known noise source in FinFET devices.

The next step involved a description of the ionisation process due to optical excitation, and this is presented in Section 5.4.2. The final step required a simulation of the FinFET time-trace data, described in Section 5.4.3.

Using this model, a simulated $^{167}$Er absorption spectrum was constructed in Section 5.4.4. This simulation was fit to an experimental $^{167}$Er spectrum, and the fitted parameters are presented and discussed in Section 5.4.5.

### 5.4.1 The optical absorption profile

A homogeneously broadened optical transition can described by a Lorentzian profile:

$$\varphi(f) = \frac{\varphi_0 \sigma^2}{(f - f_0)^2 + \sigma^2}$$

where $f_0$ is the peak frequency, $\varphi_0$ is the peak absorption, and $\sigma = \Gamma_\phi + (2\pi T_1)^{-1}$ is the homogeneous linewidth detailed in Section 2.4.2. A slowly varying electric field perturbation $\Delta E(t)$ will shift the frequency of the optical transition via the Stark effect. In FinFET devices such perturbations often arise from voltage fluctuations in the gate electrodes, or the charging and discharging of trap states. As these perturbations are small, the transition frequency will shift linearly with applied field ($\Delta f = \alpha \Delta E$) and so the absorption profile is be modified accordingly:

$$\varphi(f, t) = \frac{\varphi_0 \sigma^2}{(f + \alpha \Delta E(t) - f_0)^2 + \sigma^2} \tag{5.1}$$

In the next section, this distribution will be used to determine the probability of optical excitation at a given laser wavelength $f$.

### 5.4.2 Simulating the ionisation process

In these FinFET devices, optical excitation of Er ions is detected through ionisation of the Si donor level $D_{Er}$ (see Section 2.5). More specifically, the FinFET current changes a discrete amount each time the $D_{Er}$ level is emptied or filled. To simulate this behaviour, a Boolean variable *charge_state* was used to represent the state of $D_{Er}$ at any given time $t$. The following commented pseudo-code shows how *charge_state* was determined in a single time instance.

Prior to excitation the $D_{Er}$ level remains filled, so we initialise with 0 to represent this :

$$charge\_state(f,t) = 0$$

optical absorption is a probabilistic process, so compare $\varphi$ with a random number:

$$If : \varphi(f,t) > random\_number(0,1)$$

if a photon is absorbed , $D_{Er}$ is emptied:

$$charge\_state(f,t) = 1$$

if absorption did not occur, $D_{Er}$ remains filled:

$$Else :$$

$$charge\_state(f,t) = 0$$

In order to create a simulated FinFET current time-trace for a given wavelength $f$, it was necessary to re-calculate value of *charge_state* many times using a loop. The implementation of this loop is the focus of the next section.

### 5.4.3 Simulating the FinFET current time-trace

The absorption spectra shown in this chapter were developed by recording FinFET current time-traces. It was assumed that the current $I(t)$ would depend only on the voltage $V(t)$ in the FinFET channel. As the transistor is biased to operate as an SET, the voltage dependence can be well approximated by the Coulomb peak lineshape described in Section 3.4:

$$I(t) = \cosh^{-2}\left(\frac{eV(t)}{2.5 \cdot k_{\mathrm{B}}T}\right)$$

where $T = 4.2$ K. A simple model of the voltage $V(t)$ was then developed by assuming that only two effects could alter the channel voltage.

The first was ionisation of the $D_{Er}$ level, described in the previous section. Ionisation was assumed to create a discrete shift in the channel voltage $\Delta V_{\mathrm{Er}}$, consistent with observations of single defect ionisation in other FinFET devices [13, 125]. This shift was also assumed to be large, so that $\Delta V_{\mathrm{Er}}$ was similar in magnitude to the Coulomb peak linewidth of $2k_BT/e$.

The second effect was the electric field noise $\Delta E$ introduced in Section 3.4. Under the

operating conditions of the FinFET, this small perturbation should modulate the channel voltage linearly: $\Delta V_{\mathrm{E\,field}} = \beta \Delta E$ .

Combining these two effects, a model was obtained for the FinFET channel voltage as a function of time $t$ and excitation frequency $f$:

$$V(f,t) = V_0 + \beta \Delta E(t) + \Delta V_{\mathrm{Er}} \cdot charge\_state(f,t) \tag{5.2}$$

Using this voltage model, one can construct a current time-trace for a particular laser frequency: $I(f,t)$. This is achieved by repeatedly calling the functions derived in the previous two sections, and assuming Gaussian electric noise with standard deviation $\delta E$:

$$\begin{aligned}
&For\, t = t_0 \ to\ t_{final}: \\
&\quad \Delta E(t) = gaussian_noise_function(\delta E) \\
&\quad Call:\ \varphi(f,t) \\
&\quad Call:\ charge_state(f,t) \\
&\quad I(f,t) = cosh^{-2}\left( [V_0 + \beta \Delta E(t) + \Delta V_{\mathrm{Er}} \cdot charge_state(f,t)] \cdot \frac{e}{2.5 k_B T} \right)
\end{aligned}$$

here the variable $t$ was iterated 50,000 times in order to simulate a 1 KHz detection bandwidth (see Section 5.2) over a 50 second time-trace.

### 5.4.4 Simulating an absorption spectrum

Using the code in the previous section, a simulated absorption spectrum of a single $^{167}$Er ion was constructed. Shown in Figure 5.5 (b), this simulation combined eight Lorentzian profiles from Equation 5.1, one for each $\Delta m_I = 0$ transition. The simulated current time-traces were then plotted in the same way as the experimental spectrum in Figure 5.2. In particular, each simulated time-trace $I(f,t)$ was converted into a vertical current histogram, and plotted side-by-side as a function of laser frequency $f$.

This simulated spectrum was fit-by-inspection to the experimental $^{167}$Er spectrum in Figure 5.5 (a). This Figure shows data taken at 90 mT, representing a subset of data taken during the magnetic field dependence study presented in Figure 5.4. Here the spectrum does not exhibit two discrete charge levels, as was previously observed in Figure 5.2. Rather, optical excitation resulted in a continuum of current levels in Figure 5.5.

The most probable cause for this change in current dynamics was a change in the charge

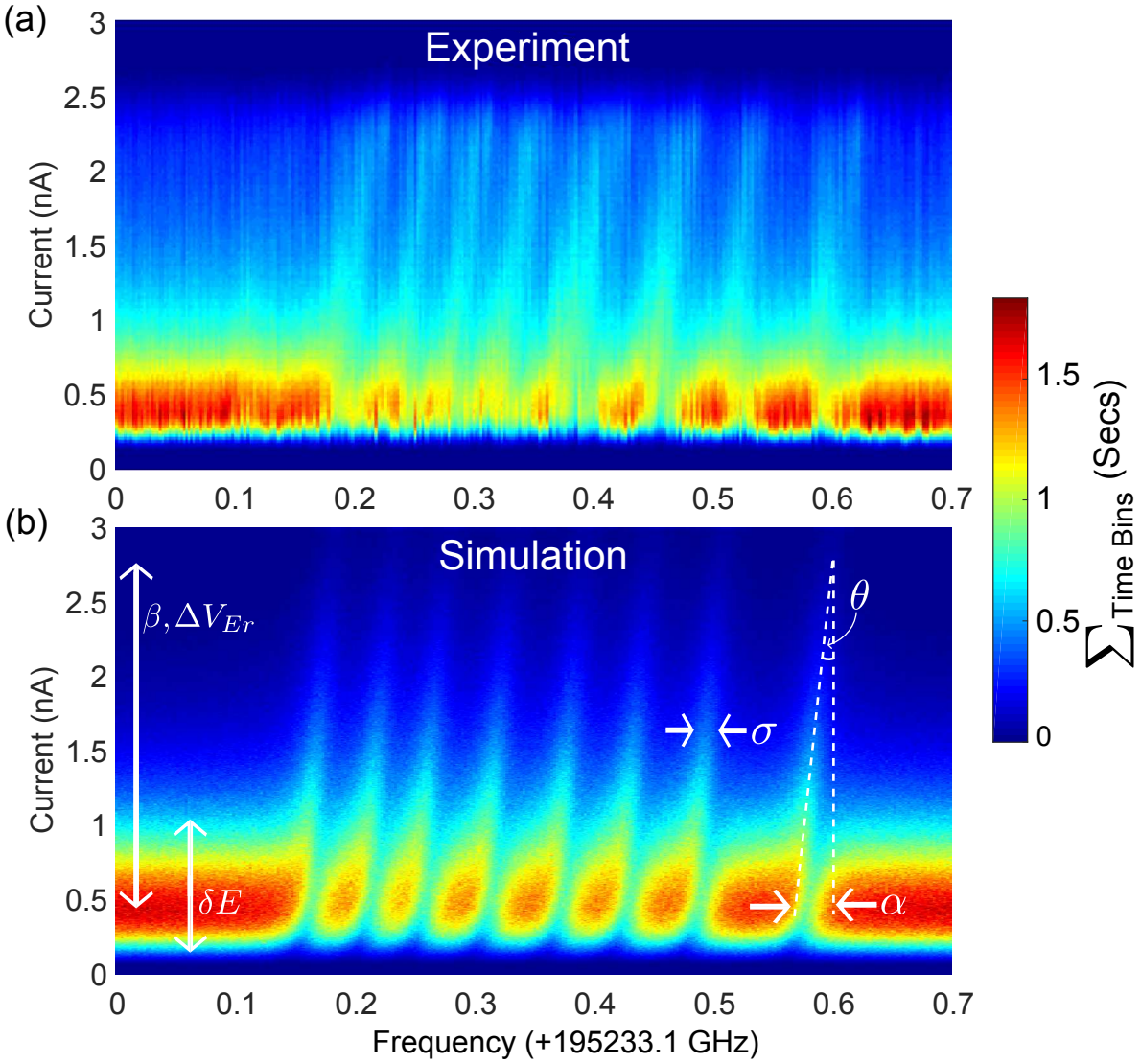


**Figure 5.5:** Experimental and simulated absorption spectra of a $^{167}$Er transition in a field of 90 mT. **(a)** The experimental spectrum, centred at 195.233 THz (1535.6 nm). The $x$-axis corresponds to the wavelength of the laser illuminating the FinFET. The $y$-axis shows a current histogram, where the 50 sec current time-traces recorded for each wavelength are binned in 20 pA steps. **(b)** A simulated fit to the experimental absorption spectrum in part (a). The fitted parameters are listed in Table 5.1. **Experimental data collected by G. de Boo.**

environment around the single Er defect. Prior to the measurements in Figures 5.4 and 5.5, the FinFET was thermally cycled to room temperature. This could have created strain-induced damage within the FinFET, forming localised charge defects and traps. Electrons released from the $D_{Er}$ trap would then get trapped in any one of several nearby defects, rather than being released into the drain lead.

### 5.4.5 Interpretation of the fit

Even with the FinFET in this damaged state, the fitting to Figure 5.5 (a) provided useful information on the optical coherence properties. Firstly, the experimental spectrum showed a noticeable asymmetry, or slant, in the hyperfine absorption peaks. This phenomenon was also reproduced in the simulated spectrum, where it was quantified by the angle $\theta$. This angle arose from the correlation between the absorption frequency and the FinFET voltage. In particular, their susceptibilities can be equated because they are modulated by the same charge noise $\Delta E(t)$ :

$$\frac{\Delta f}{\alpha} = \Delta E = \frac{\Delta V}{\beta}$$

which implies that:

$$\frac{\Delta f}{\Delta V} = \frac{\alpha}{\beta}$$
$$\therefore \tan\theta \propto \frac{\alpha}{\beta}$$

This quirk of the FinFET absorption spectrum was used to determine the homogeneous line broadening due to charge noise alone, by fitting for the parameters $\alpha$ and $\beta$. Using the parameters $\alpha$ and $\Delta E$, one could then determine the contributing stark noise:

$$\begin{aligned}\langle\varphi(f)\rangle &= \left\langle \frac{\varphi_0\sigma^2}{(f - f_0 - \alpha\Delta E(t))^2 + \sigma^2} \right\rangle \\ &= \frac{\varphi_0\sigma^2}{(f-f_0)^2 - 2(f-f_0)\,\alpha\langle\Delta E(t)\rangle + \alpha^2\langle\Delta E(t)^2\rangle + \sigma^2} \\ &= \frac{\varphi_0\sigma^2}{(f-f_0)^2 + \alpha^2\delta E^2 + \sigma^2}\end{aligned}$$

Table 5.1 lists the parameters $\alpha$, $\beta$, $\delta E$ and $\sigma$ determined from the fit to Figure 5.5 (a). These values yielded an estimate of the electric noise broadening; $2\alpha\delta E \approx 15$ MHz, which was comparable to the underlying broadening $2\sigma \approx 30$ MHz. Hence, the sum broadening from these interactions resulted in the 50 MHz homogeneous linewidths observed in Figure 5.4.

Decomposing the line broadening into separate components gave key insights into the dynamics of these FinFET devices. Firstly, we could confirm that electric noise contributed an appreciable amount to the optical broadening. This noise affected both the Er ion and SET tunnelling current in a correlated manner, indicating a macroscopic source.

| Parameter Label | Parameter Value |
|---|---|
| $\alpha$ | 7 MHz·m·V$^{-1}$ |
| $\beta$ | 0.3 m$^{-1}$ |
| $\sigma$ | 15 MHz |
| $\varphi_0$ | 0.5 |
| $\Delta V_{\mathrm{Er}}$ | 0.4 mV |
| $\delta E$ | 1 V·m$^{-1}$ |

**Table 5.1:** Parameters used to generate the simulated spectrum in Figure 5.5 (b). These parameters were estimated through a fitting-by-inspection to Figure 5.5 (a).

Such sources could include voltage noise generated by the FinFET gates, or distant charge traps in the silicon below the transistor channel.

However, the dominant source of noise was not due to the macroscopic electric fields. Indeed, broadening due to $\sigma$ alone would yield an optical coherence time of $T_2 \approx 10$ ns. This is much shorter than the millisecond optical lifetimes typical of bulk Er:Si, suggesting that the transition width is not lifetime limited [107]. Instead, the linewidth is most likely dominated by magnetic or highly-localised electric dephasing, and potential sources include charge traps and two-level systems formed by impurities and crystal defects. These impurities and defects play a central role in the subsequent investigations presented in this chapter, and further evidence of their effect on the Er ions is presented in the next section.

## 5.5 Properties of the inhomogeneous absorption line

The previous section focused on the narrowest features of the optical absorption spectra. We now turn our attention to the other extreme, by considering the inhomogeneous distribution of optical transitions shown in Figure 5.6.

The inhomogeneous absorption profile of this Er:Si FinFET device looks very different to that of bulk Er:Si. Here the concentration of Er is so low that individual ions are clearly resolved, so inhomogeneous broadening is a moot point in some respects. Furthermore, the variety of spectroscopic splitting factors in Figure 5.6 suggests that several different Er sites are optically active.

Given these observations, an accurate estimate of the inhomogeneous broadening cannot be made using spectra developed with a single field direction, such as Figure 5.6. Instead, an accurate measurement of the inhomogeneous broadening in these FinFET devices has been performed by G. de Boo, using magnetic rotation experiments.

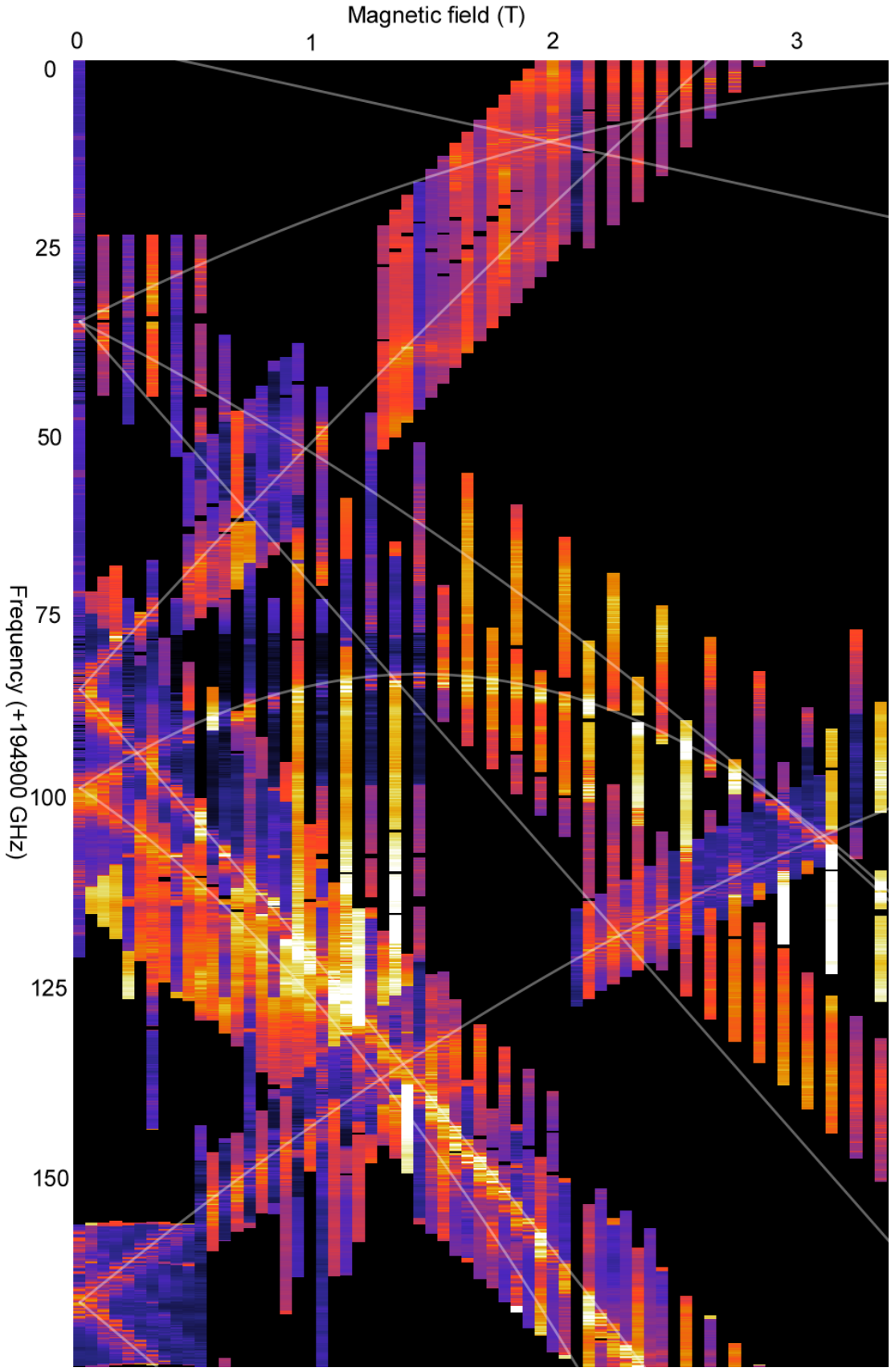


**Figure 5.6:** A wide-scan absorption spectrum developed over 0-3.5T. Absorption lines of individual $Er^{3+}$ ions are observed over a range of 100 GHz, each with a unique magnetic field dependence. This particular device was implanted with only $^{167}Er$, so the lines also exhibit hyperfine structure. White lines are a guide to the eye. **Data collected by G. de Boo.**

He observed three Er sites with the same $I_{15/2}$ and $I_{13/2}$ electronic g-tensors, spread across 25 GHz (see Table B.5 of Ref [153]). In Section 2.3 it was explained that large inhomogeneous broadening is often a consequence of higher-dimensional defects, such as dislocations and plane boundaries. As the FinFET devices are composed of composite layers, the existence of 2D plane boundaries is inevitable. Indeed, Figure 3.10 illustrates that the detectable Er ions are no more than 15 nm from a Si-SiO interface.

Another potential source of lattice defects is the ion-beam implantation process, described in Section 5.2. The implantation process can cause severe damage to the crystal because of erbium's large atomic number ($n = 68$). Moreover, thorough annealing is not possible without damaging the FinFET device. Collectively, this can result in voids and other high dimensional defects in the neighbourhood of the implanted ions [154].

Because of the large inhomogeneous broadening of Er:Si in FinFET devices, certain dynamics which greatly affect the coherence properties of Er spins cannot be estimated a-priori. For example, predicting spin-lattice coupling depends on knowledge of the energy level structure, and achieving long hyperfine lifetimes times in Er:YSO relies on such information. For this reason individual Er ions can only be considered for spin-qubits once their site structure is determined, which is the focus of the following (and final) section. Chapter 6 then introduces several fabrication techniques that could mitigate the large inhomogeneous broadening in these devices, and so improve the optical and hyperfine coherence times.

## 5.6 A high symmetry Er site

The spectrum presented in Figure 5.6 is just one example of several wide-field spectra recorded with this FinFET device. At a lower frequency of 194463 GHz, a rather unique optical transition was observed in one of these spectral scans. Presented in Figure 5.7 (a) this optical transition showed almost zero field dependence in the direction of the superconducting magnet field. This observation was interesting because optical transitions of Kramers rare earths usually exhibit strong magnetic field dependence. In fact, no other Er absorption line has shown this property in a FinFET device.

The reason for this unique behaviour was determined from a high resolution spectrum recorded at low-field, which is shown in Figure 5.7 (b). Here one can see hyperfine-level anti-crossings, which indicate that the 3 parallel lines seen in Figure 5.7 (a) correspond to $\Delta m_I = 0, \pm 1$ absorption bands.

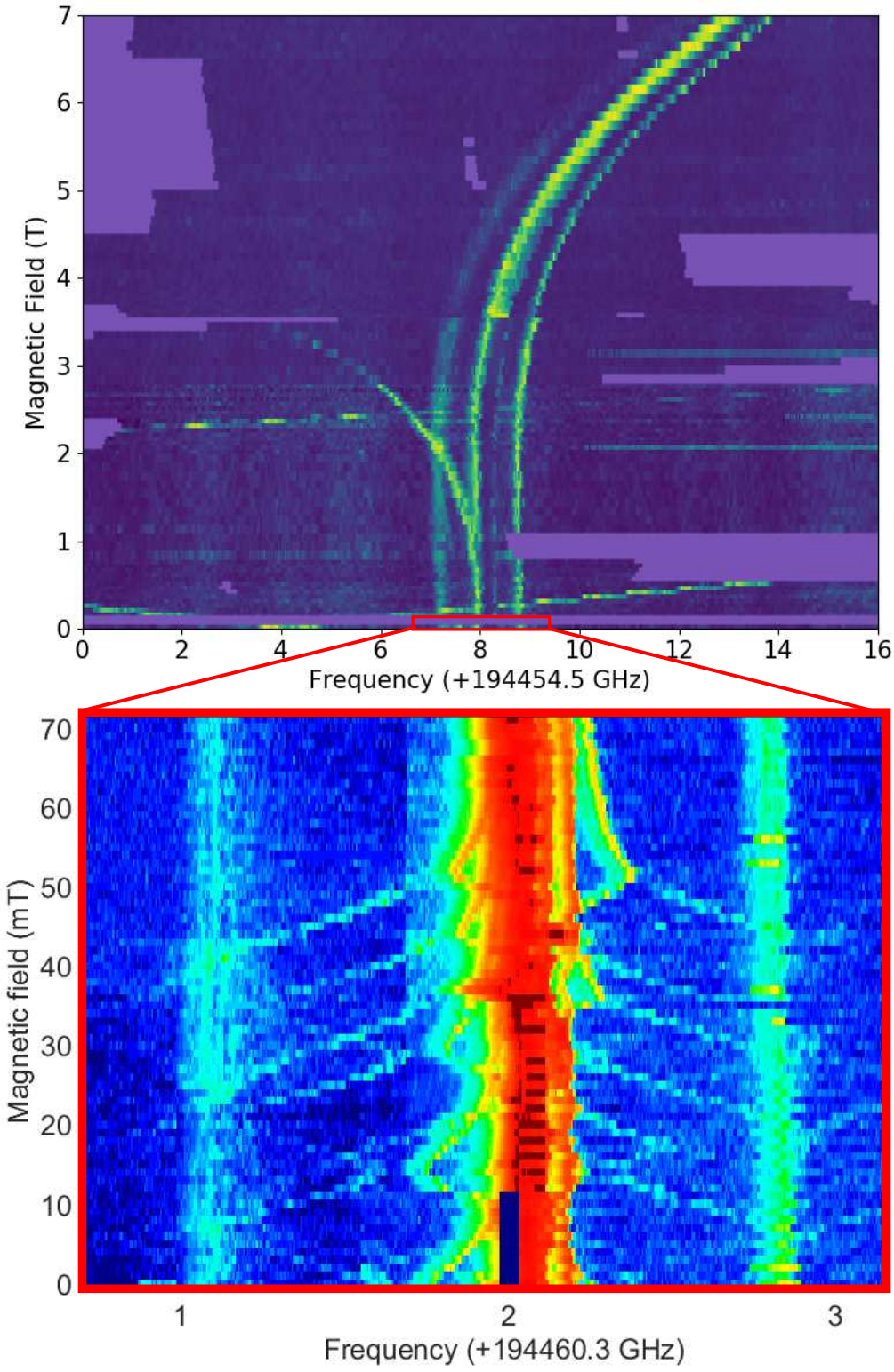


**Figure 5.7:** Two spectra of an $^{167}$Er absorption line centred at 194462.4 GHz. **(a)** Wide-field spectrum (0-7T). The arm curving to the left (right) shows the $\Delta m_{\tilde{S}} = 0$ transition from the $m_{\tilde{S}} = |+\frac{1}{2}\rangle$ $(m_{\tilde{S}} = |-\frac{1}{2}\rangle)$ state of the $I_{15/2}$ Kramers doublet. The three parallel lines correspond to the $\Delta m_I = -1, 0$ & $+1$ hyperfine absorption bands, respectively. Sections of the spectrum which were not developed are masked in purple. **(b)** Narrow-field spectrum (0-70 mT). Hyperfine anti-crossings between the electronic $m_{\tilde{S}} = |\pm\frac{1}{2}\rangle$ levels can be observed. The hyperfine transition gradients reveal the $I_{15/2}$ and $I_{13/2}$ electronic g-factors: approximately 60 GHz/T. **Data collected by G. de Boo and Q. Zhang.**

More importantly, they reveal equal field dependence for the Zeeman levels in both the $I_{15/2}$ and $I_{13/2}$ in this field direction. In particular, the strong magnetic field dependence shown by some of the hyperfine levels indicated that the Zeeman levels in both the $I_{15/2}$ and $I_{13/2}$ states had a spectroscopic splitting factor of $g \approx 4$ in this direction. This implied that some symmetry must exist in the $I_{15/2}$ and $I_{13/2}$ $g$-factors, and hence the Er site.

In Section 2.2.2 it was explained that a site with high symmetry can be characterised using a reduced set of crystal-field Hamiltonian parameters. This presented an opportunity to determine the electronic level structure of this Er:Si site, as only a small amount of data might be required for a crystal-field Hamiltonian fit. This also made the site particularly appealing to study, as many important spin dynamics can be estimated once the crystal-field Hamiltonian is known (see Section 2.4.4). Moreover, knowledge of this Hamiltonian is critical to realisation of long hyperfine coherence times in Kramers ions, as explained in Sections 4.9 and 6.3.

To determine which crystal-field parameters would be required for this fitting, a magnetic rotation experiment was first performed. Detailed in Sections 5.6.1 - 5.6.2, this study determined the overall site symmetry. The fitting to the electronic Hamiltonian is then described in Section 5.6.3. The Hamiltonian parameters determined from this fit were used to simulate the hyperfine substructure in Figure 5.7 (b), and this is presented in Section 5.6.4.

### 5.6.1 Magnetic field rotation study

In an effective spin-Hamiltonian such as (4.1), the anisotropic Zeeman interaction is described by a 3 dimensional $g$-tensor. To determine the components of this tensor, one can record the Zeeman splitting as a function of field orientation; this type of measurement is commonly known as a magnetic field rotation study. It can also be used to determine the symmetry of the crystal-field interaction, because anisotropy in the Zeeman interaction is a consequence of an anisotropic crystal-field interaction.

Unfortunately the weak $\Delta m_{\tilde{S}} = \pm 1$ transitions made it difficult to determine the $g$-tensors of the $I_{15/2}$ or $I_{13/2}$ Kramers doublets. Thus a measurement of $|g_{15/2} - g_{13/2}| = \Delta g$ was made instead, using the strong $\Delta m_{\tilde{S}}$ & $\Delta m_I = 0$ transition at 194.4624 THz. This measurement was performed under the assumption that the optical $\Delta g$-tensor would reveal the symmetry of the crystal field interaction, much like the electronic $g$-tensor.

For this measurement a single-axis rotation was performed in the $X-Y$ plane; the plane

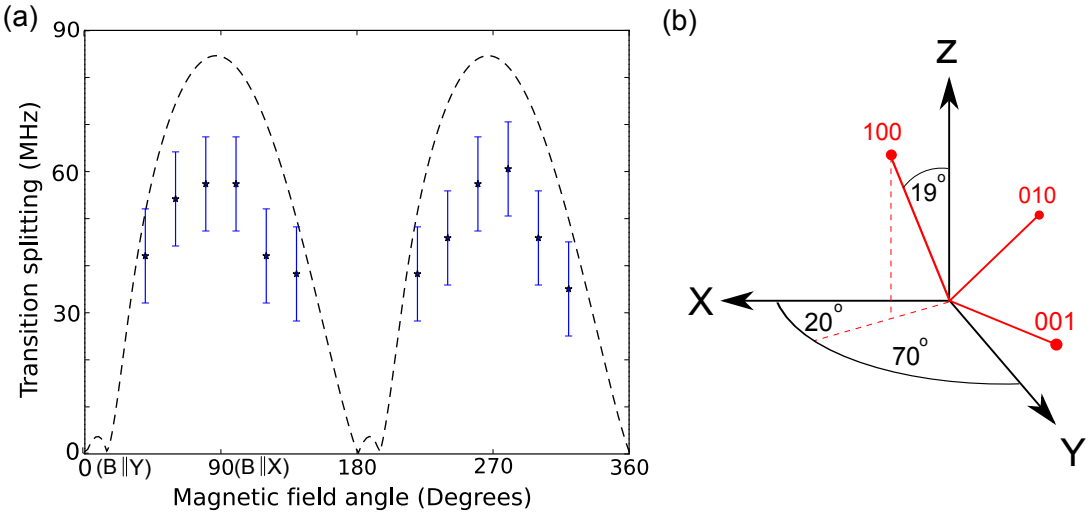


**Figure 5.8: (a)** Magnetic field rotation pattern of the $\Delta m_{\tilde{S}}$ & $\Delta m_I = 0$ absorption line in the $X - Y$ plane. *black stars:* experimentally observed splitting of hyperfine sublevels within the transition. The uncertainty in the splitting is determined by the width of the optical transitions. *Dashed black line:* Simulated rotation pattern of the $\Delta m_{\tilde{S}} = 0$ optical transition, assuming a field amplitude of 2 mT and Hamiltonian parameters from Table 5.3. **(b)** Orientation of the $X, Y, Z$ co-ordinate frame *(black)* with respect to the principle axes of the silicon wafer *(red)*. In this co-ordinate frame the $Z$ direction is aligned with the superconducting magnet and cryostat (refer to Figure 5.1), while the axis of the Er site is oriented along the $X$ direction. **Data collected by G. de Boo and Q. Zhang.**

perpendicular to the superconducting magnet axis (see Figure 5.1). This was achieved using perturbation coils external to the cryostat, which applied a field of $2 \pm 0.2$ mT. The resulting field rotation pattern is presented in Figure 5.8 (a). Note that for certain angles the optical Zeeman splitting was much less than the transition linewidth, hence too small to be observed.

### 5.6.2 Interpretation of the site symmetry

By combining the data from Figure 5.7 and Figure 5.8 (a), it was possible to estimate the $\Delta g$-tensor for this optical transition at zero field. With respect to the $X, Y, Z$ co-ordinate frame presented in Figure 5.8 (b), the tensor has only one non-zero component:

$$\Delta g \approx \begin{pmatrix} 2 & 0 & 0 \\ 0 & 0 & 0 \\ 0 & 0 & 0 \end{pmatrix}_{X,Y,Z}$$

This determined that the Er site possessed approximately axial symmetry in the Zeeman interaction. The relatively high symmetry restricted the number of crystal field parameters

required to characterise the crystal-field Hamiltonian (see Section 2.2.2). More specifically, axial symmetry in the Zeeman tensor results from either hexagonal (six-fold), tetragonal (four-fold) or trigonal (three-fold) point group symmetries. These symmetries can be further decomposed into five distinct point groups, and the parameters required to describe the associated crystal-field Hamiltonians are listed in Table 5.2

| | | |
|---|---|---|
| Hexagonal | $C_6$ | $B_0^2$, $B_0^4$, $B_0^6$, Re($B_6^4$) |
| Tetragonal | $C_{4v}$ | $B_0^2$, $B_0^4$, $B_0^6$, Re($B_4^6$, $B_4^4$) |
| | $C_4$ | $B_0^2$, $B_0^4$, $B_0^6$, $B_4^6$, Re($B_4^4$) |
| Trigonal | $C_{3v}$ | $B_0^2$, $B_0^4$, $B_0^6$, Re($B_3^6$, $B_6^6$, $B_3^4$) |
| | $C_3$ | $B_0^2$, $B_0^4$, $B_0^6$, $B_3^6$, $B_6^6$, Re($B_3^4$) |

**Table 5.2:** The five point groups which exhibit axial symmetry. Here each $B_0^k$ is a real valued constant, while the $B_q^k$'s with $q \neq 0$ can be complex. Parameters taken from Table 1.7 from Ref [81].

This analysis determined that the crystal-field Hamiltonian $\mathcal{H} = \sum B_q^k C_q^k$ would have at most eight free parameters.

### 5.6.3 Determining the crystal-field Hamiltonian

To determine the crystal-field parameters $B_q^k$, we utilised a Hamiltonian solver program called PYCF. Described in Appendix A, this program minimises the least-squares difference between experimental transition energies and calculated Hamiltonian eigenvalues. The Hamiltonian used for the fitting included only the electronic components of the 4f-shell Hamiltonian (2.1):

$$H_{\mathrm{PYCF}} = H_{\mathrm{FI}} + H_{\mathrm{CF}} + H_{\mathrm{Z}} \tag{5.3}$$

Generally speaking, this fitting requires spectra of multiple crystal field levels (Kramers doublets) for a unique solution to be obtained. Three spectra were collected for this purpose, encompassing optical transitions of the lowest two Kramers doublets in the $I_{13/2}$ state[3]. Two of these spectra were already presented in Figure 5.7, and show the optical transitions from the lowest Kramers doublet in the $I_{15/2}$ state to the lowest doublet in the

[3]Every optical transition was assumed to originate from the lowest $I_{15/2}$ crystal field level, due to the thermal distribution in the $I_{15/2}$ state.

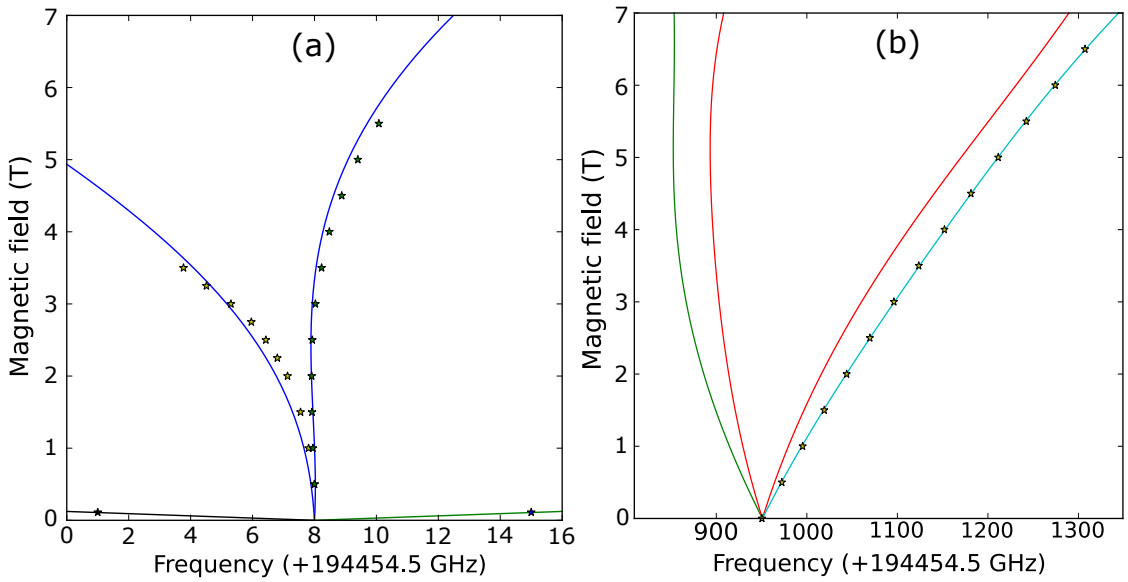


**Figure 5.9:** Fitting of the lowest energy optical transitions. **(a)** The optical transitions from the lowest energy Kramers doublet in the $I_{15/2}$ state to the lowest energy Kramers doublet in the $I_{13/2}$ state. **(b)** The lowest-to-second-lowest Kramers doublet optical transitions. *Stars* represent the data points used for the fitting. *Solid lines* show the fitted transitions based on Hamiltonian (5.3) with the parameters from Table 5.3.

$I_{13/2}$ state. The third spectrum shows the lowest-to-second-lowest doublet transition, and is presented in Appendix E.

Collectively, these spectra contained less data than is usually required for a unique Hamiltonian fit [82]. The data was sufficient in this case because of the high symmetry of the Er site. Figure 5.9 shows the fitted optical transitions based on these spectra.

### The fitting process

The first step in the fitting process was to input transition energy data into the PYCF program. This data consisted of transition energies at 17 different fields (0-7T in 500mT steps plus 2.25T, 2.75T and 3.25T), shown by the stars in Figure 5.9. The fitting then proceeded by selecting some initial Hamiltonian parameters[4], and allowing PYCF to find a solution (fit) using the basin-hopping algorithm. This process was repeated many times, with different combinations of starting values (positive and negative) for the free parameters listed in Table 5.3. These parameters were taken from either the tetragonal or the trigonal subsets of Table 5.2, as they were mutually exclusive. No solution was found for any tetragonal set. For the trigonal set the program would always converge to one of two

[4]Most of the free-ion parameters were left fixed (not fit) in this process, for reasons explained in Section 2.2.1. Only the Slater parameters $F^k$ and spin-orbit parameter $\zeta$ were varied (by just a few percent).

degenerate solutions, indicating uniqueness in the fit.

| Hamiltonian Parameter | Value ($cm^{-1}$) |
|---|---|
| $\alpha$ | [17.79] |
| $\beta$ | [-582.1] |
| $\gamma$ | [1800] |
| $T^2$ | [400] |
| $T^3$ | [43] |
| $T^4$ | [73] |
| $T^6$ | [-271] |
| $T^7$ | [308] |
| $T^8$ | [299] |
| $M_{tot}$ | [3.86] |
| $P_{tot}$ | [594] |
| $F^2$ | 97483 |
| $F^4$ | 67904 |
| $F^6$ | 54010 |
| $\zeta$ | 2325 |
| $B_0^2$ | 10 |
| $B_0^4$ | 798 |
| $B_0^6$ | 233 |
| $B_3^4$ | $\pm$1930 |
| $B_4^4$ | -335-117i |
| $B_3^6$ | $\pm$617$\pm$34i |
| $B_6^6$ | -180-63i |

**Table 5.3:** The electronic Hamiltonian parameters for the axial Er:Si site, determined using the PYCF fitting program. Two degenerate solutions were identified, due to degeneracy in the $q = 3$ crystal-field parameters. Values in square brackets were not varied during the fit.

Once this overall solution was found, small amounts of additional crystal-field parameters were added in an attempt to improve the fit. Here it was found that adding the $B_4^4$ term improved the fitting, and the complete list of fitted Hamiltonian parameters are presented in Table 5.3.

As stated above, the fit indicates approximately trigonal ($C_3$) symmetry. For the common interstitial cubic Er site in silicon, trigonal distortions can only arise from stress along perpendicular crystal axes such as the 111, $\bar{1}11$, etc. However, the site orientation shown in Figure 5.8 (b) illustrates that this is not the case here. Instead, this symmetry has

likely arisen from a more complicated Er-host interaction, consistent with the observation that Er complexes are required for electroluminescence.

To further test the fit, a simulation of the experimental rotation pattern in Figure 5.8 (a) was constructed, and is shown by black dashed trace in the same figure. This simulation exhibits larger splittings than the experimental data, which shows that the fit could be improved. This could be done by increasing the number of crystal field parameters in the fitting and collecting more spectroscopic data, such as transitions to higher $I_{13/2}$ crystal field levels.

Nevertheless, the parameters listed in Table 5.3 should be sufficiently accurate to determine a regime in which long hyperfine lifetimes are achieved at liquid helium temperatures, and this analysis will be presented in Section 6.4.

### 5.6.4 Simulating the hyperfine structure

With the electronic Hamiltonian parameters determined, it was possible to simulate the hyperfine structure in Figure 5.7 (b) using the hyperfine coupling parameters $a_l$ and $a_q$ (see Section 2.2.3). These parameters have previously been estimated from the crystal field fitting of Er:YSO [82]. As the hyperfine interaction should be independent of host, the same parameters were applied here to test the electronic Hamiltonian fit:

$$a_l = 0.008, \qquad a_q = 0.08$$

For this set of energy levels the hyperfine substructure yielded 256 optical transition. Thus, it was necessary to also determine the optical transition strengths in order to simplify the simulated spectrum. This was achieved using a program developed by M. Reid, which determined both the magnetic and electric dipole transition strengths (refer to Sec 2.4 of Ref [82]).

Figure 5.10 (b) shows this simulated spectrum, under illumination by $\pi$ and $\sigma$ polarised light in equal amounts. While the simulated transition strengths show noticeable discrepancy from the experimental data[5], the energy splitting between the parallel $\Delta m_I = -1, 0$ and $+1$ transitions is in good agreement. This further supports the validity of the crystal field fit.

[5] Accurate estimates of transition strengths are usually difficult to obtain, as there are many approximations necessary for calculating the interaction Hamiltonians. Moreover, the polarisation of incident light was unknown as the experiment fibre was not polarisation maintaining.

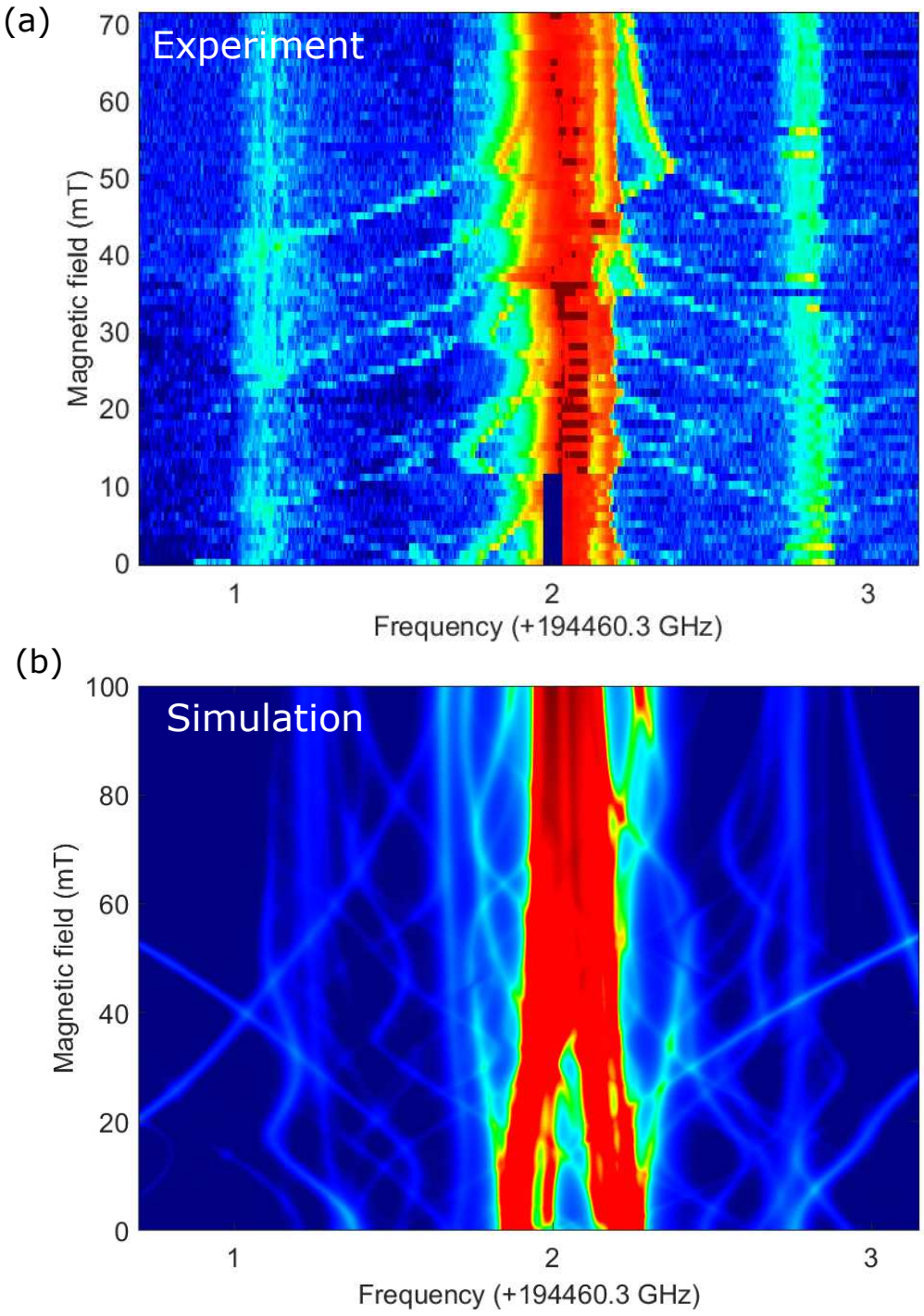


**Figure 5.10:** Optical absorption spectra showing the hyperfine substructure of the lowest-to-lowest Kramers doublet transition of the trigonal $^{167}$Er site, with the magnetic field along the $Z$ direction. **(a)** Experimental absorption spectrum, reproduced from Figure 5.7. **(b)** Simulated absorption spectrum, constructed using the approach detailed in Sec 2.4 of Ref [82]. **Transition strengths calculated by S. Horvath.**

### 5.6.5 Extending the approach to other Er:Si sites

The axial site studied here was chosen because of symmetry considerations which simplified the crystal-field Hamiltonian fitting. However, this site is not representative of most Er:Si sites identified so far (see Table B.5 of Ref [153]). The Er:Si sites with lower symmetry will require a much larger set of experimental data for a unique fit to be obtained. To put this in context, the crystal-field fitting of Er:YSO sites with $C_2$ symmetry required the zero-field transition energy of 37 crystal field levels up to the $^2H_{11/2}$ multiplet and several magnetic field dependence studies of optical and spin transitions [82].

Collecting such a large volume of information for single Er:Si centres presents several challenges. Firstly, spectra are developed relatively slowly with a typical dwell time per data point of $\mathcal{O}(10\text{ sec})$. This can be significantly improved, however, by recording the SET voltage using RF-reflectometry rather than directly measuring the tunnelling current [155]. This AC measurement technique can potentially improve the measurement bandwidth (which is currently several KHz) by three order of magnitude or more.

Secondly, silicon is not transparent to optical wavelengths which excite transitions to higher energy multiplets such as the $^4I_{11/2}$, $^4I_{9/2}$, etc. Developing spectra of these higher energy levels will require two-colour stimulation via intermediary levels. For instance, spectra of the $^4I_{9/2}$ multiplet can be developed by exciting to a resonant level in the $I_{13/2}$ using 1550 nm laser light and sweeping with a second laser in the 1700 nm region.

## 5.7 Summary

This chapter presented results of the first spectroscopic investigation of individual erbium ions in silicon. This was achieved using a novel approach to single ion detection, which was introduced in Section 5.1. Using this approach it was possible to develop high resolution optical spectra of these ions, such that both the electronic and hyperfine levels of single Er ions were resolved in Section 5.3. An investigation of the optical absorption lineshape and homogeneous broadening was then presented in Section 5.4. Here it was concluded that noise from both the FinFET electrodes and impurities in the silicon contributed to the homogeneous linewidth, which totalled approximately 50 MHz. The inhomogeneous broadening in the FinFET devices was then discussed in Section 5.5. The large inhomogeneous broadening was attributed to lattice damage caused by ion implantation. Finally, the site structure of an individual Er ion was analysed in Section 5.6. Such studies are

required to determine the magnetic field regime in which the Er electrons spin can be polarised, which is necessary for realising long transition lifetimes and coherence times in Er:Si.

# Conclusion

The digital Internet has been a powerhouse of social and economic development in the 21st century; Internet related commerce accounted for 21 percent of GDP growth in mature economies between 2006-2011 [29]. This digital revolution has now spurred billion dollar investments in quantum technologies, aimed at unlocking similar economic potential [30]. Along with quantum computing, the future 'quantum Internet' will play a major role in this technological platform [31, 32].

This will require quantum memories for light with storage times longer than the transmission times across the network, and coherent optical interfaces for entangling distant quantum computers. Rare earth ions have shown great promise in this regard, with demonstrations of long coherence times, broadband absorption, and high storage efficiencies [47–50].

Among the rare earth ions, Er centres uniquely possess optical transitions in the 1.5 $\mu$m region. This wavelength region lies within the transparency window of both silicon and silica fibres, making Er an obvious candidate for these quantum telecommunications technologies. Although there have been numerous demonstrations of quantum information devices based on rare-earth doped crystals, it has proven difficult to realise these devices with Er centres. This thesis has investigated the key underlying obstacle to deploying Er based quantum information devices, the dynamics associated with the ion's electron spin. Two systems were investigated, Er doped YSO and individual Er ions in FinFET transistors.

It was shown in Chapter 4 that the rapid electron spin relaxation in Er:YSO, which shortened both hyperfine lifetimes and coherence times, could be suppressed with the application of a large magnetic field. By polarising the Er electron spins in YSO, the hyperfine transition lifetime was extended to approximately 10 minutes and the coherence was increased to $1.3 \pm 0.01$ seconds. Section 6.1 of this chapter briefly explores the impact of this result on quantum communication applications.

I also discuss the possibility of extending the coherence time further in this system in Section 6.2, and highlight the potential of applying these techniques to other Kramers systems such as Nd:YSO in Section 6.3.

In Chapter 5 I described experiments demonstrating the detection of single Er ions in a FinFET transistor using a hybrid electronic/optical scheme. The long term goal of this work was to demonstrate the readout of a single Er spin qubit, as a prerequisite for a spin-optical quantum bus. While it proved possible to detect single ions and resolve both the electronic Zeeman and hyperfine levels, state readout was not achieved. This would require long spin lifetimes, sufficient for maintaining a spin state during readout. With the kHz bandwidth in FinFET devices, millisecond spin transition lifetimes should be satisfactory for the purpose. As a first step in understanding the spin dynamics of these single centres, I have further investigated techniques used to identify the site symmetries of these single centres, and characterise their Hamiltonians. One centre in particular was characterised as having trigonal ($C_3$) symmetry. In Section 6.4 of this chapter I suggest strategies for extending the transition lifetimes and coherence times of these single centres.

## 6.1 Quantum repeater networks

In 2009, Razavi et al. undertook a thorough analysis into entanglement generation rates for fibre based quantum links, assuming that many parallel memories are available for multiplexing [59]. The light propagation time $L/c$ was one of the key considerations in their approach to calculating entanglement rates. In particular, memories with coherence times $T_2 \gg L/c$ were deemed to have effectively infinite storage times, and entanglement rates could be calculated simply in this regime (see Eq (1) of Ref [59]).

To put this in context, $L$ =1000 km is often used as a benchmark distance for repeater protocols [156]. The hyperfine coherence time measured in Section 4.11 is 200 times greater than $L/c$ over this range. This is well within the 'infinite' memory regime, and the per-memory entanglement rate for repeater nodes spaced 125 km (using the Razavi protocol) is:

$$R_3^3 = 0.5\, bits/s$$

This is a large improvement over a direct (repeater-less) entanglement rate of $10^{-5}\, bits/s$ for a THz single photon source. Moreover, this rate scales linearly with the number of

parallel memory channels. This is an advantage for rare earth doped solid state memories, as the large density of ions opens the path for massive multiplexing. By using standard fabrication techniques, YSO waveguide circuits with millions of parallel memory channels could be realised [62].

While this would yield data rates of $Kbits/s$ for a 1000 km network, it is also interesting to consider data rates over global distances. To this end we consider a distance of $L$ =10000 km, for which the the light propagation time is 65 ms. Although this is still shorter than $T_2$, there will inevitably be data loss due to decoherence over this time-scale. This loss can be calculated for repeater nodes spaced 156 km apart, using equation (4) of Ref [59]:

$$E_c\left(\hat{\rho}^{+}_{XY}\left(t_6^6\right)\right) = 0.82$$

This shows that data rates are reduced by only 18% compared with an 'infinitely' coherent memory, which is quite good. A caveat to this result, however, is how poorly current repeater protocols scale over such long distances:

$$R_6^6 = 0.008\, bits/s$$

Although the protocol of Razavi et al. is not the only choice for future repeater implementation, it is indicative of the state-of-the-art. Irrespective of which protocol is eventually utilised though, this analysis illustrates an important point: There now exists a telecom-compatible storage material whose coherence time is more than sufficient for entanglement over global distances.

## 6.2 Quantum hard-drives

This primary goal of this thesis was to investigate Er doped materials for quantum communication applications. However, the results of Chapter 4 suggest that $^{167}$Er:YSO also has potential for long-term quantum information storage. Here several techniques are introduced which together might achieve this goal. Section 6.2.1 covers the ZEFOZ technique, whose purpose is to reduce transition dephasing. Implementing this technique is very important, as the hyperfine coherence times are currently limited by dephasing mechanisms. Section 6.2.2 then describes several approaches to extending transition lifetimes, which could open the path to hour long storage times.

### 6.2.1 ZEFOZ

Section 4.11.2 explained that magnetic perturbations limited the hyperfine coherence times in the high field regime studied here. This issue could be addressed by moving the magnetic field to a 'turning point', where the hyperfine transition becomes magnetically insensitive in three dimensions. This is called the Zero First-Order Zeeman (ZEFOZ) technique, and is especially useful when combined with the frozen-core effect in YSO [157].

For non-Kramers ions, the location of high field turning points are accurately estimated using effective-spin Hamiltonians measured in low fields [140,158–160]. However, the results of Section 4.5 show that this approach cannot be used for $^{167}$Er:YSO. Instead, one would have to parametrise the spin Hamiltonian in high field or utilise a crystal-field Hamiltonian [82].

If a sufficiently shallow turning-point can be found in this way, coherence times might be extended to the six hours observed in Eu:YSO. This is because the small frozen-core of Eu limited the coherence times to 5 ms in high fields: a 1.3 second coherence time suggests a much a quieter magnetic environment. None-the-less, hour long coherence times can only be achieved if the hyperfine transition lifetimes are also improved, and approaches to solving this issue are discussed in the following section.

### 6.2.2 Improving the hyperfine transition lifetimes

Hour long coherence times in $^{167}$Er:YSO cannot be achieved using ZEFOZ alone. If the magnetic perturbations are sufficiently attenuated, the coherence times will be limited by the hyperfine transition lifetimes (see Sections 4.8 - 4.10).

The first issue which must be addressed in this regard is nuclear spin cross-relaxation, which occurs on a minute timescale. By taking advantage of the transition selection rules, however, this process is readily suppressed. In particular, the weak hyperfine state mixing in this system will suppress $|\Delta m_I| > 1$ transitions. Thus, one can initialise the system into non-adjacent hyperfine levels such as the $|{-7/2}\rangle \leftrightarrow |{-3/2}\rangle$ , and use the $\Delta m_I = 2$ transition for information storage.

This approach to state preparation should suppress cross-relaxation below the spin-lattice relaxation rate. However, reducing the spin-lattice coupling is rather more involved and here we introduce three techniques to address this problem.

From a technical standpoint, the simplest approach would involve lowering the sample temperature. In Section 4.9 it was determined that the spin-lattice relaxation rate was limited by the direct process at low temperatures. This involved $\mathcal{O}$(GHz) phonons, whose density in the crystal scale linearly with temperature. Thus, simply moving to a 300 mK dilution fridge should raise the transition lifetime to approximately 60 minutes.

The second approach would aim to suppress only those phonons resonant with the hyperfine transitions. This idea is based on recent demonstration of phononic bandgap films that achieved 30 dB of phonon suppression in the 2.4-3.2 MHz range [161]. With this approach, a phononic bandgap in the 800-1000 MHz range could be achieved using standard fabrication equipment. Demonstrating just 10 dB of attenuation in the frequency range could yield transition lifetimes of 120 minutes.

The third approach would focuses on minimising the hyperfine spin-lattice coupling, rather than reducing the phonon density. For an electron-spin transition $|-s\rangle \leftrightarrow |+s\rangle$, the spin-lattice interaction is described by Eq (2.13) :

$$\omega_{\pm s} = \frac{2\pi}{\hbar^2} \left|\langle +s|H_{\text{phonon}}|-s\rangle\right|^2$$

where the matrix elements of $H_{\text{phonon}}$ vary with magnetic field direction (see Section 2.4.4). This equation is readily extended to the hyperfine transitions, as they couple to the lattice via admixture with the electronic spin. The mixing caused by this interaction is so weak that's its usually ignored, and for this reason the hyperfine spin-lattice coupling is orders of magnitude weaker than the electronic. Nonetheless, one can determine the magnetic field direction for which the hyperfine spin-lattice coupling is minimised, using the Hamiltonian parameters from Ref [82].

## 6.3 Kramers ions in large fields

The issues of spin-relaxation addressed in this thesis are not just relevant to erbium. Indeed, the transition lifetimes and coherence times of many other Kramers ions are shortened by the same dynamics. To investigate whether large fields can be used for other Kramers ions, here I consider the applicability to $^{145}$Nd:YSO. This material has been used in several high profile memory demonstrations, and exhibits millisecond long hyperfine coherence in small magnetic fields [57, 162].

To determine whether efficient spin-polarisation can be achieved with $^{145}$Nd, one must first consider the crystal field structure in the host material. If the lowest energy Kramers doublets are too close together, level anti-crossings will occur before sufficient spin-polarisation is reached for the lowest Kramers doublet. This is not an issue for Nd:YSO, however, as the lowest Kramers doublets are separated by 88 cm$^{-1}$ (2.6 THz) for site 1 [163]. This is three times larger than the equivalent splitting in Er:YSO [82].

The measurements in Section 4.10 showed that Er spins in YSO are highly polarised in a field of 3T, equivalent to a spin transition frequency of 630 GHz. However, reaching this transition frequency with Nd would require a field of 10T due to its small ground-state electronic moment (see supplementary materials of Ref [162]). Assuming similar spin-lattice coupling, this would be sufficient to reduce the spin-lattice relaxation rate to $\mathcal{O}$(1 min). Although it's difficult to estimate the hyperfine cross-relaxation rate at this field, the smaller electronic moment of Nd would suggest lower relaxation rates than observed in Er (for the same doping concentration).

This simple analysis shows that long transition lifetimes might be achievable in Nd:YSO with a commercial cryostat. As Nd has the smallest ground state moment of any Kramers ion, this approach should have merit for other Kramers ions as well.

## 6.4 Er:Si optical-spin bus

The long term goal of the Er:Si research program is to realise a telecom wavelength bus for future silicon based quantum computers. With this goal in mind, several of the device requirements details in Section 1.2.1 are currently being addressed. These include the development of high Q optical resonators that are compatible with FinFET technology, and investigations of Stark tunability for the optical transitions [164,165]. In line with this goal, this thesis has focused on the issues of Er spin-readout and coherence, both of which require further investigation.

### 6.4.1 Improving transition lifetimes and coherence times of single Er ions

Materials such P:Si and Bi:Si have shown great promise for quantum information processing, with the observation of exceedingly long coherence times for these dopants [16,166]. The same should hold true for the Er:Si devices studied here, if several key improvements are made.

Firstly, the large homogeneous and inhomogeneous optical linewidths measured in Sections 5.4 - 5.5 suggest poor Si crystal quality. This issue could be mitigated with high temperature annealing, which was not performed for reasons detailed in Section 5.5. Annealing could be used, however, if dopants are implanted into the Si wafer prior to FinFET fabrication. If applied, this change in the manufacturing process should greatly reduce both the homogeneous and inhomogeneous linewidths. With regards to the second point, the number of unique spectroscopic sites should be reduces.

Homogeneous broadening could further be reduced by utilising isotopically enriched $I = 0$ materials (in particular $^{28}$Si) to eliminate nuclear magnetic noise. To put this in context, the isotopic enrichment of Si yielded a 5000-fold improvement in spin coherence times of individual P:Si dopants [17].

Finally, long coherence times and lifetimes in Er:Si will require the Er electron spins to be polarised, for much the same reasons as Er:YSO. Spin-lattice coupling is the major concern here, as the ultra low Er density should help to suppress both electronic and hyperfine cross-relaxation. If we consider the trigonal Er site for which the 4f-Hamiltonian was determined in Section 5.6, a maximum electronic $g$-factor of 11.4 is achieved along the axis of the site. This would suggest a field of 4T will be required to reduce the spin-lattice relaxation rate below $\mathcal{O}(1\text{ min})$, based on the results achieved with Er:YSO in Chapter 4. If no other dynamics are present, then hyperfine state readout should be achieved in this regime, which would represent an important milestone on the path to an Er based optical-spin bus.

**Appendix A**

# Python Crystal Field

PYCF is a software suite developed by S. Horvath at the University of Canterbury. A detailed description of the software and print-outs of the code can be found in reference [82]. Here it is used primarily for fitting the experimental data from Chapter 5 to the $4f$-shell Hamiltonian detailed in Chapter 2. PYCF builds upon the $4f$-shell Hamiltonian solver developed by M. Reid in the 1980's. In particular, the two scripts `SLJCALC` and `JMCALC` from the 1980's solver form the basis of program, and their python equivalents are critical sub-routines. These two scripts calculate the matrix elements of the following Hamiltonian in the $\tau, L, S, J$ and $\tau, L, S, J, m_J$ basis, respectively:

$$H = H_{FI} + H_{CF} + H_Z$$

The components of the first two terms are described in Sections 2.2.1 and 2.2.2. The Zeeman interaction is required because the spectroscopic data is presented as a function of magnetic field. It should also be noted that `JMCALC` comes in two variants, selected by user input. The variant used most often provides a faster 'truncated' method of calculating matrix elements. This truncated approach follows the method of Carnall et al. [83], and diagonalises the free-ion and crystal-field components in separate (de-coupled) bases. This approximation leads to order-of-magnitude improvements in fitting speed, while only introducing deviations of a few percent compared with the coupled-basis variant of `JMCALC`.

### The crystal field library

Once the relevant matrix elements have been determined using `SLJCALC` and `JMCALC`, the next step is to fit the Hamiltonian parameters to the recorded spectra. This fitting is performed by the crystal field library (`cfl`) subroutine. Based on the `CFIT` algorithm developed by M. Reid, `cfl` takes advantage of modern high-performance computing algorithms [167–170]. As suggested by the title, PYCF is optimised for fitting the crystal

field parameters $B_q^k$, as opposed to free-ion parameters. In-fact, the only free-ion parameters which are varied during the fitting process are the Slater terms $F^k$ and the spin-orbit term $\zeta$.

Starting with an initial set of parameters, `cfl` performs an iterative optimisation by minimising the least-squares difference between the calculated eigenvalues and experimental transition energies. As mentioned previously, the spectroscopic data are taken at multiple magnetic field values. Thus, the `cfl` routine simultaneously fits the data for each magnetic field value to a separate Hamiltonian, and fitting-weights can be assigned to the optimisation for these individual Hamiltonians.

As with many optimisation programs, PYCF solutions can converge to different (and non-degenerate) local minima. In order to identify the best global solution, `cfl` employs the basinhopping algorithm [171]. Basinhopping employs random steps, whose size and frequency and defined by the user, followed by local minimisation. Then, the metropolis criterion is applied to decide whether the algorithm should move to the newly found local minimum [172]. The bounds on parameter space are defined by user input: if a sufficiently converged solution is not found, `cfl` will continue to execute until the union of these bounds is reached.

# Modulator equations

Presented here is the derivation of the modulator power response $P$. This derivation is based on the physical modulator description presented in Section 3.2. Firstly, the output electric field $E$ is described as follows:

$$E = \left[\alpha_- e^{-i(\omega t-\phi_-)} + \beta e^{i\varphi} - \alpha_+ e^{i(\omega t+\phi_+)}\right] e^{if_0 t}$$
$$E^*E = \left[\alpha_- e^{i(\omega t-\phi_-)} + \beta e^{-i\varphi} - \alpha_+ e^{-i(\omega t+\phi_+)}\right] e^{-if_0 t} \times$$
$$\left[\alpha_- e^{-i(\omega t-\phi_-)} + \beta e^{i\varphi} - \alpha_+ e^{i(\omega t+\phi_+)}\right] e^{if_0 t}$$

If we only consider components at the modulation frequency $\omega$:

$$\begin{aligned}
E(\omega)^*E(\omega) &= \alpha_-\beta\left[e^{i(\omega t-\phi_-+\varphi)} + e^{-i(\omega t-\phi_-+\varphi)}\right] - \alpha_+\beta\left[e^{-i(\omega t+\phi_+-\varphi)} + e^{i(\omega t+\phi_+-\varphi)}\right] \\
&= 2\alpha_-\beta\cos(\omega t - \phi_- + \varphi) - 2\alpha_+\beta\cos(\omega t + \phi_+ - \varphi) \\
&= 2\alpha_-\beta\left[\cos(\omega t)\cos(-\phi_- + \varphi) + \sin(\omega t)\sin(-\phi_- + \varphi)\right] \\
&\quad - 2\alpha_+\beta\left[\cos(\omega t)\cos(\phi_+ - \varphi) + \sin(\omega t)\sin(\phi_+ - \varphi)\right] \\
&= 2\beta\cos(\omega t)\left[\alpha_-\cos(-\phi_- + \varphi) - \alpha_+\cos(\phi_+ - \varphi)\right] \\
&\quad + 2\beta\sin(\omega t)\left[\alpha_-\sin(-\phi_- + \varphi) - \alpha_+\sin(\phi_+ - \varphi)\right]
\end{aligned}$$

The expressions in the square-brackets are now substituted for the terms $u$ and $v$. This simplifies the form of the equation to:

$$I = 2\beta u\cos(\omega t) + 2\beta v\sin(\omega t)$$

The two terms $u$ and $v$ can then be substituted for trigonometric identities, by assuming

the following relations:

$$\sin\gamma = \frac{u}{\sqrt{u^2+v^2}}$$
$$\cos\gamma = \frac{v}{\sqrt{u^2+v^2}}$$

The intensity can then be re-expressed using the effective 'angle' $\gamma$:

$$\begin{aligned} I &= 2\sqrt{u^2+v^2}\left(\sin\gamma\cos\left(\omega t\right)+\cos\gamma\sin\left(\omega t\right)\right) \\ &= 2\sqrt{u^2+v^2}\sin\left(\gamma+\omega t\right) \end{aligned}$$

Expressed in this manner, the RF power $P$ can be described by the RMS amplitude of the optical intensity, squared:

$$P \propto u^2+v^2$$

Where:

$$\begin{aligned} u^2+v^2 &= \left[\alpha_-\cos\left(-\phi_-+\varphi\right)-\alpha_+\cos\left(\phi_+-\varphi\right)\right]^2+\left[\alpha_-\sin\left(-\phi_-+\varphi\right)-\alpha_+\sin\left(\phi_+-\varphi\right)\right]^2 \\ &= \alpha_-^2\cos^2\left(-\phi_-+\varphi\right)+\alpha_+^2\cos^2\left(\phi_+-\varphi\right)+\alpha_-\alpha_+\cos\left(-\phi_-+\varphi\right)\cos\left(\phi_+-\varphi\right) \\ &\quad +\alpha_-^2\sin^2\left(-\phi_-+\varphi\right)+\alpha_+^2\sin^2\left(\phi_+-\varphi\right)-\alpha_-\alpha_+\sin\left(-\phi_-+\varphi\right)\sin\left(\phi_+-\varphi\right) \\ &= \alpha_-^2+\alpha_+^2+\alpha_-\alpha_+\left[\cos\left(-\phi_-+\varphi\right)\cos\left(\phi_+-\varphi\right)-\sin\left(-\phi_-+\varphi\right)\sin\left(\phi_+-\varphi\right)\right] \\ \therefore P &\propto \alpha_-^2+\alpha_+^2+2\alpha_-\alpha_+\cos\left(2\varphi-\phi_+-\phi_-\right) \end{aligned}$$

**Appendix C**

# Population lifetime data

Presented in the following two figures are AM spectra recorded in a field of 7T along the $D_1$ optical extinction axis of $^{167}$Er:YSO. Each Subfigure was recorded at the temperature indicated, following the method described at the beginning of Section 4.8. The temperature for each measurement was inferred from a low pressure vacuum gauge, in equilibrium with the sample space of the cryostat. Temperature regulation of the sample was achieved with a series of valves between the sample space and vacuum pump.

For temperature range of 1.4 K - 1.8 K, a population model was fit assuming the initial population distribution in Table 4.4. For the measurements at 2.0 K and 2.16 K, the level of initial spin polarisation was described by the following distribution:

| Hyperfine state | $\|-7/2\rangle$ | $\|-5/2\rangle$ | $\|-3/2\rangle$ | $\|-1/2\rangle$ | $\|+1/2\rangle$ | $\|+3/2\rangle$ | $\|+5/2\rangle$ | $\|+7/2\rangle$ |
|---|---|---|---|---|---|---|---|---|
| $N(t=0)$ (%) | 0 | 2 | 1 | 3 | 8 | 18 | 27 | 41 |

For the measurements at 2.77 K and 3.22 K, the level of initial spin polarisation was described by the following distribution:

| Hyperfine state | $\|-7/2\rangle$ | $\|-5/2\rangle$ | $\|-3/2\rangle$ | $\|-1/2\rangle$ | $\|+1/2\rangle$ | $\|+3/2\rangle$ | $\|+5/2\rangle$ | $\|+7/2\rangle$ |
|---|---|---|---|---|---|---|---|---|
| $N(t=0)$ (%) | 6 | 6 | 6 | 6 | 12 | 18 | 18 | 29 |

The decrease in initial spin-polarisation with increasing temperature occurs due to the increase in phonons. In particular, the optical spin-pumping achieves equilibrium with the spin depolarising effect of the phonons. Hence the equilibrium level of spin-polarisation reduces with increasing phonon density and temperature.

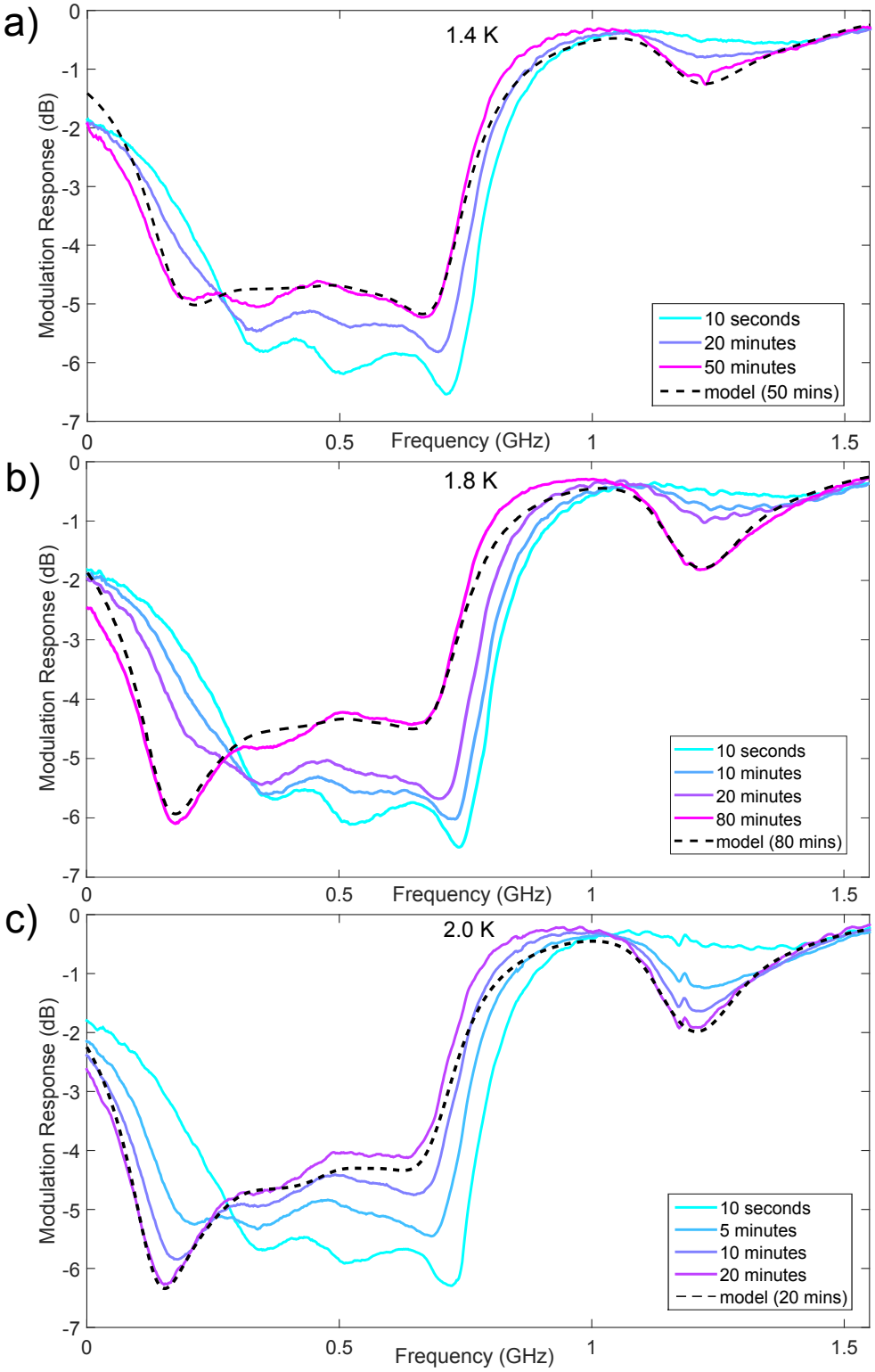


**Figure C.1:** Amplitude modulation spectra of the $\Delta m_I = 0$ and $+1$ optical absorption bands in a field of 7 T along the $D_1$ axis in $^{167}$Er:$Y_2SiO_5$. Sub-figures **a)**, **b)** and **c)** were recorded at helium temperatures of 1.4 K, 1.8 K and 2.0 K respectively. The nuclear spin population is initially pumped into the $|+7/2\rangle$ hyperfine ground state, and the legend entries indicate the time delay of the recorded spectra after spin-pumping. The black dashed traces indicate the fit to spectrum for the longest time delay trace, based on the decay rates plotted in Figure 4.15.

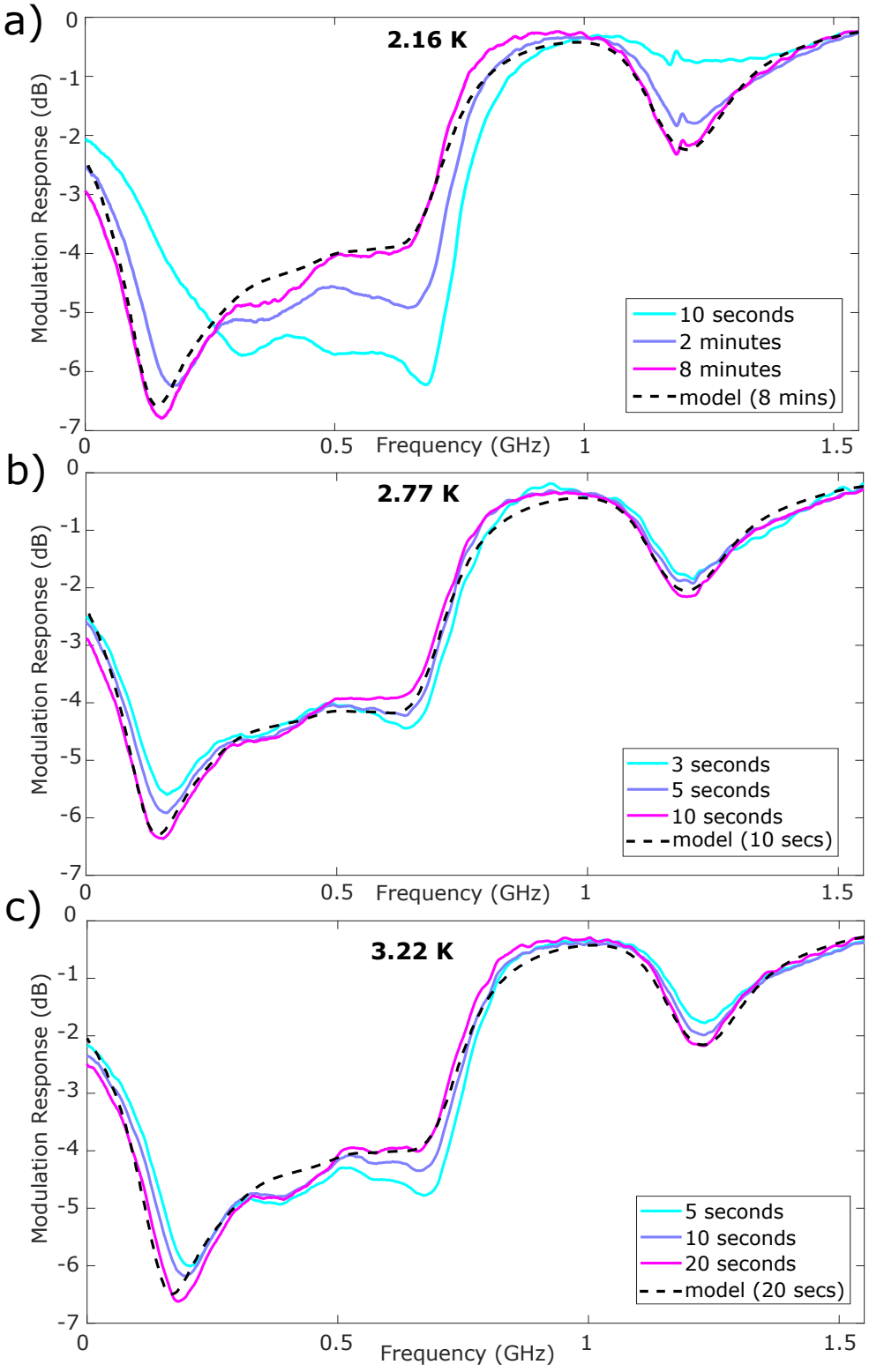


**Figure C.2:** Amplitude modulation spectra of the $\Delta m_I = 0$ and $+1$ optical absorption bands in a field of 7 T along the $D_1$ axis in $^{167}$Er:$Y_2SiO_5$. Sub-figures **a)**, **b)** and **c)** were recorded at helium temperatures of 2.16 K, 2.77 K and 3.22 K respectively. The nuclear spin population is initially pumped into the $|+7/2\rangle$ hyperfine ground state, and the legend entries indicate the time delay of the recorded spectra after spin-pumping. The black dashed traces indicate the fit to spectrum for the longest time delay trace, based on the decay rates plotted in Figure 4.15.

Appendix D

# Holeburning of the hyper-polarised ensemble

With the nuclear spin ensemble hyper-polarised, a holeburning spectrum was subsequently recorded. This measurement aimed to create a narrow anti-hole with a low absorbing background, as this type of spectral feature is useful for quantum memory applications. This measurement also confirmed the hyperfine energy structure that was investigated in Section 4.5.

For this experiment the EOM sideband was used to burn a single hole in the centre of the $|+7/2\rangle \leftrightarrow |+7/2\rangle$ transition (the downwards pointing arrow). The hole was burnt with a weak 100 $\mu$W pulse for 100 ms, to mitigate hole broadening.

Figure D.1 shows the hole-burning spectrum acquired by AM spectroscopy. The image of the spectral hole in centre of the $|+7/2\rangle \leftrightarrow |+5/2\rangle$ transition indicates that about one third of the resonant ions had been removed from the $|+7/2\rangle$ ground state[1]. Three narrow anti-holes were also visible at the frequencies corresponding to the $|+5/2\rangle \leftrightarrow |+3/2\rangle$, $|+3/2\rangle \leftrightarrow |+1/2\rangle$ and $|+1/2\rangle \leftrightarrow |-1/2\rangle$ optical transitions. These anti-holes correspond to subsets of the population pumped into the $|+5/2\rangle$, $|+3/2\rangle$ and $|+1/2\rangle$ ground states, via the $\Delta m_I$ =-1, -2 & -3 optical decay paths. The relative height of the anti-holes presented a means to estimate the oscillators strengths for these $\Delta m_I$ =-2 & -3 transitions, using Table 4.3. This gave estimates of 0.7% and 0.3% for the $|+7/2\rangle \leftrightarrow |+3/2\rangle$ and $|+7/2\rangle \leftrightarrow |+1/2\rangle$ optical transitions, respectively.

[1]The hole in the $|+7/2\rangle \leftrightarrow |+7/2\rangle$ transition (the downwards pointing arrow) could not be used to infer this value. The large OD caused small modulation-depth for the hole at this wavelength.

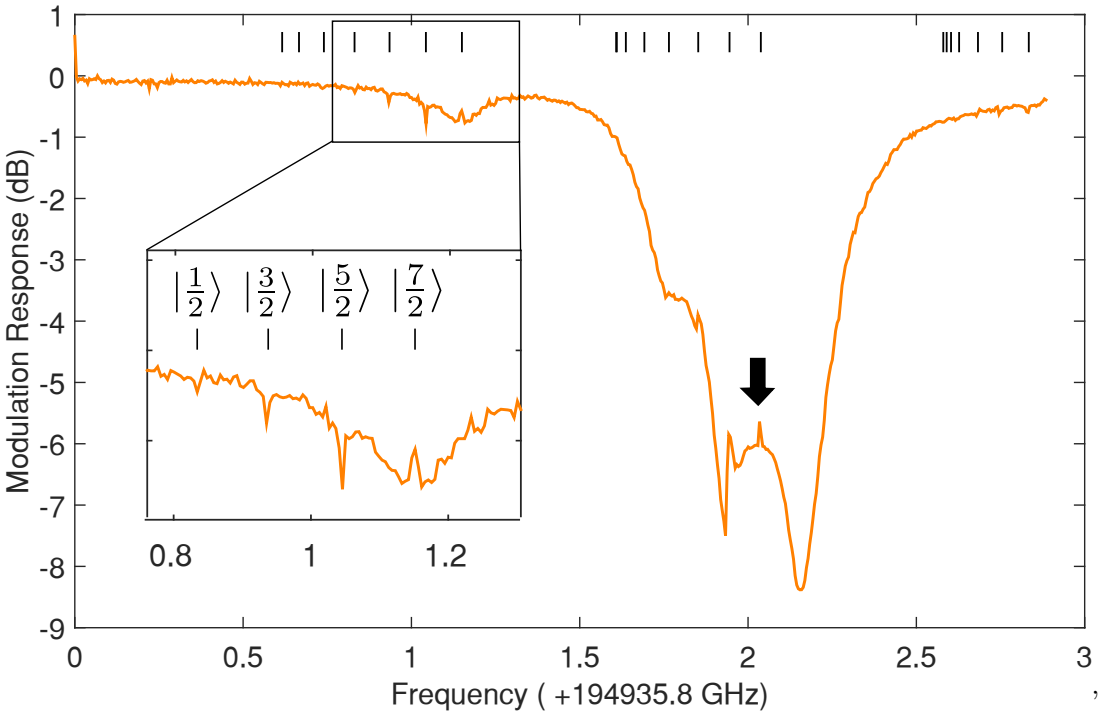


**Figure D.1:** AM spectrum with 95% of the hyperfine ensemble pumped into the $|+7/2\rangle$ ground state. **Arrow:** the frequency where a spectral hole was subsequently burnt, in the centre of the $|+7/2\rangle \leftrightarrow |+7/2\rangle$ optical transition. **Vertical black dashes:** The centres of the inhomogeneously broadened $^{167}$Er optical transitions. **Inset**: Exploded view of the $\Delta m_I = -1$ absorption band, showing side-holes and anti-holes formed by the holeburning. The transitions are labelled according to their corresponding hyperfine ground states.

**Appendix E**

# An additional spectrum of the axial site

Fitting a crystal-field Hamiltonian generally requires spectra of multiple crystal field levels (Kramers doublets) for a unique solution to be obtained. The spectra developed in Section 5.6 included only optical transitions from the lowest energy Kramers doublet in the $I_{15/2}$ state to the lowest doublet in the $I_{13/2}$ state.

As expected, attempts to determine the Hamiltonian with this limited data gave several non-degenerate solutions. While this meant that more data (spectra) would be required to obtain a unique fit, all the solutions determined at that stage indicated that the next crystal field level in the $I_{13/2}$ state would be approximately 30 $cm^{-1}$ (1 THz) higher in energy. This presented a narrow bandwidth (several hundred GHz) over which to develop further optical spectra, in order to identify the second $I_{13/2}$ level.

Figure E.1 shows the spectrum developed for this purpose, where four sets of absorption lines were identified. However, only the transitions marked in blue gave a good fit when added to the previous data. This suggested that the second $I_{13/2}$ crystal field level for the axial site had been identified.

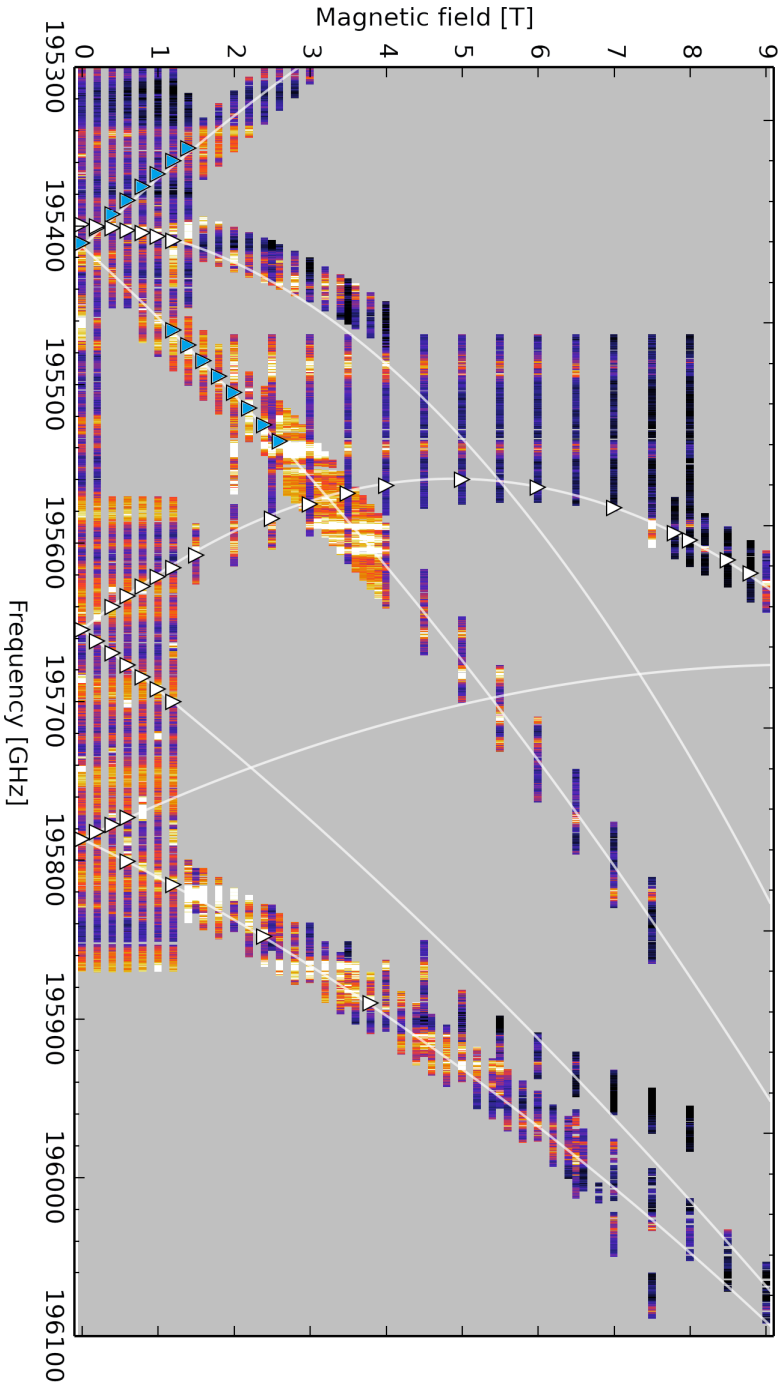


**Figure E.1:** A wide-scan absorption spectrum developed over a 0-9T. Absorption lines are observed over a range of 800 GHz, each with a unique magnetic field dependence. Only the transitions with blue triangles demonstrated good convergence when added to the previous data for fitting. White lines are a guide to the eye. **Data collected by Dr C. Yin.**

# Bibliography

[1] R. L. Rivest, A. Shamir, and L. Adleman. A method for obtaining digital signatures and public-key cryptosystems. *Communications of the ACM*, 21(2):120–126, feb 1978.
(Cited on page 1)

[2] P.W. Shor. Algorithms for quantum computation: discrete logarithms and factoring. In *Proceedings 35th Annual Symposium on Foundations of Computer Science*, pages 124–134. IEEE Comput. Soc. Press, 1994.
(Cited on page 2)

[3] R. P. Feynman. Simulating physics with computers. *International Journal of Theoretical Physics*, 21(6-7):467–488, 1982.
(Cited on page 2)

[4] D. Deutsch. Quantum Theory, the Church-Turing Principle and the Universal Quantum Computer. *Proceedings of the Royal Society A: Mathematical, Physical and Engineering Sciences*, 400(1818):97–117, jul 1985.
(Cited on page 2)

[5] Gregoire Ribordy. ID Quantique, Geneva, Switzerland.
(Cited on page 3)

[6] Vikram Sharma. Quintessence Labs, Canberra, Australia.
(Cited on page 3)

[7] Thomas Monz, Philipp Schindler, Julio T. Barreiro, Michael Chwalla, Daniel Nigg, William A. Coish, Maximilian Harlander, Wolfgang Hänsel, Markus Hennrich, and Rainer Blatt. 14-Qubit Entanglement: Creation and Coherence. *Physical Review Letters*, 106(13):130506, mar 2011.
(Cited on pages 3 and 4)

[8] David Beckman, Amalavoyal N. Chari, Srikrishna Devabhaktuni, and John Preskill. Efficient networks for quantum factoring. *Physical Review A*, 54(2):1034–1063, aug

1996.
(Cited on page 3)

[9] Daniel Loss and David P. DiVincenzo. Quantum computation with quantum dots. *Physical Review A*, 57(1):120–126, jan 1998.
(Cited on pages 3, 4, and 109)

[10] D. P. DiVincenzo. The Physical Implementation of Quantum Computation. *Fortschritte der Physik*, 48(9-11):771–783, sep 2000.
(Cited on pages 3 and 109)

[11] A. Goban, C.-L. Hung, S.-P. Yu, J.D. Hood, J.A. Muniz, J.H. Lee, M.J. Martin, A.C. McClung, K.S. Choi, D.E. Chang, O. Painter, and H.J. Kimble. Atom-light interactions in photonic crystals. *Nature Communications*, 5:1023–1030, may 2014.
(Cited on page 4)

[12] P. J. J. O'malley, R. Babbush, I. D. Kivlichan, J. Romero, J. R. Mcclean, R. Barends, J. Kelly, P. Roushan, A. Tranter, N. Ding, B. Campbell, Y. Chen, Z. Chen, B Chiaro, A. Dunsworth, A. G. Fowler, E. Jeffrey, E. Lucero, A. Megrant, J. Y. Mutus, M. Neeley, C. Neill, C. Quintana, D. Sank, A. Vainsencher, J. Wenner, T. C. White, P. V. Coveney, P. J. Love, H. Neven, A. Aspuru-Guzik, and J. M. Martinis. Scalable Quantum Simulation of Molecular Energies. *Physical Review X*, 6:031007, 2016.
(Cited on page 4)

[13] Andrea Morello, Jarryd J. Pla, Floris A. Zwanenburg, Kok W. Chan, Kuan Y. Tan, Hans Huebl, Mikko Möttönen, Christopher D. Nugroho, Changyi Yang, Jessica A. van Donkelaar, Andrew D. C. Alves, David N. Jamieson, Christopher C. Escott, Lloyd C. L. Hollenberg, Robert G. Clark, and Andrew S. Dzurak. Single-shot readout of an electron spin in silicon. *Nature*, 467(7316):687–691, sep 2010.
(Cited on pages 4, 109, 110, and 119)

[14] Martin Fuechsle, Jill A. Miwa, Suddhasatta Mahapatra, Hoon Ryu, Sunhee Lee, Oliver Warschkow, Lloyd C. L. Hollenberg, Gerhard Klimeck, and Michelle Y Simmons. A single-atom transistor. *Nature nanotechnology*, 7(4):242–246, apr 2012.
(Cited on pages 4 and 109)

[15] Jarryd J Pla, Kuan Y Tan, Juan P Dehollain, Wee H Lim, John J L Morton, David N Jamieson, Andrew S Dzurak, and Andrea Morello. A single-atom electron spin qubit in silicon. *Nature*, 489(7417):541–545, sep 2012.
(Cited on pages 5 and 109)

[16] Kamyar Saeedi, Stephanie Simmons, Jeff Z Salvail, Phillip Dluhy, Helge Riemann, Nikolai V Abrosimov, Peter Becker, Hans-Joachim Pohl, John J L Morton, and Mike L W Thewalt. Room-temperature quantum bit storage exceeding 39 minutes using ionized donors in silicon-28. *Science (New York, N.Y.)*, 342(6160):830–3, 2013.
(Cited on pages 6 and 142)

[17] Juha T Muhonen, Juan P Dehollain, Arne Laucht, Fay E Hudson, Rachpon Kalra, Takeharu Sekiguchi, Kohei M Itoh, David N Jamieson, Jeffrey C McCallum, Andrew S Dzurak, and Andrea Morello. Storing quantum information for 30 seconds in a nanoelectronic device. *Nature nanotechnology*, 9(12):986–91, dec 2014.
(Cited on pages 6, 109, and 143)

[18] M. Veldhorst, C. H. Yang, J. C. C. Hwang, W. Huang, J. P. Dehollain, J. T. Muhonen, S. Simmons, A. Laucht, F. E. Hudson, K. M. Itoh, A. Morello, and A. S. Dzurak. A two-qubit logic gate in silicon. *Nature*, pages 410–414, oct 2015.
(Cited on pages 6, 8, and 109)

[19] P. Zeeman. On the influence of Magnetism on the Nature of the Light emitted by a Substance. *Philosophical Magazine*, 43:226, 1897.
(Cited on page 6)

[20] Guilherme Tosi, Fahd A. Mohiyaddin, Vivien Schmitt, Stefanie Tenberg, Rajib Rahman, Gerhard Klimeck, and Andrea Morello. Silicon quantum processor with robust long-distance qubit couplings. *Nature Communications*, 8:1038, dec 2017.
(Cited on page 7)

[21] B M Maune, M G Borselli, B Huang, T D Ladd, P W Deelman, K S Holabird, A A Kiselev, I Alvarado-Rodriguez, R S Ross, A E Schmitz, M Sokolich, C A Watson, M F Gyure, and A T Hunter. Coherent singlet-triplet oscillations in a silicon-based double quantum dot. *Nature*, 481(7381):344–7, jan 2012.
(Cited on page 7)

[22] Ian Appelbaum, Biqin Huang, and Douwe J Monsma. Electronic measurement and control of spin transport in silicon. *Nature*, 447(7142):295–8, may 2007.
(Cited on page 7)

[23] A Yang, M Steger, T Sekiguchi, M L W Thewalt, T D Ladd, K M Itoh, H Riemann, N V Abrosimov, P Becker, and H-J Pohl. Simultaneous subsecond hyperpolarization of the nuclear and electron spins of phosphorus in silicon by optical pumping of exciton transitions. *Physical review letters*, 102(25):257401, jun 2009.
(Cited on page 7)

[24] Chunming Yin, Milos Rancic, G.G. Gabriele G. de Boo, Nikolas Stavrias, J.C. Jeffrey C J.C. Jeffrey C. McCallum, M.J. Matthew J M.J. Matthew J. Sellars, and Sven Rogge. Optical addressing of an individual erbium ion in silicon. *Nature*, 497(7447):91–94, may 2013.
(Cited on pages 7 and 8)

[25] J Stark. Observations of the effect of the electric field on spectral lines I. Transverse effect. *Annalen der Physik*, 43:965–983, 1914.
(Cited on page 9)

[26] Thomas Böttger, C. W. Thiel, R. L. Cone, and Y. Sun. Effects of magnetic field orientation on optical decoherence in $Er^{3+}$:$Y_2SiO_5$. *Physical Review B*, 79(11):115104, 2009.
(Cited on pages 9, 15, 65, 102, and 104)

[27] H. Przybylinska, W. Jantsch, Yu. Suprun-Belevitch, M. Stepikhova, L. Palmetshofer, G. Hendorfer, a. Kozanecki, R. Wilson, and B. Sealy. Optically active erbium centers in silicon. *Physical Review B*, 54(4):2532–2547, 1996.
(Cited on pages 9, 110, 111, and 115)

[28] A. J. Kenyon. Erbium in silicon. *Semiconductor Science and Technology*, 20:R65–R84, 2005.
(Cited on page 9)

[29] James Manyika and Charles Roxburgh. The great transformer: The impact of the Internet on economic growth and prosperity. *McKinsley Global Institute*, 2011.
(Cited on pages 10 and 137)

[30] Kai Kupferschmidt. Europe to bet up to 1 billion on quantum technology. *Science*, apr 2016.
(Cited on pages 10 and 137)

[31] H. J. Kimble. The quantum internet. *Nature*, 453(7198):1023–1030, 2008.
(Cited on pages 10 and 137)

[32] N. Gisin and R. Thew. Quantum communication. *Nature Photonics*, 1(3):165–171, 2007.
(Cited on pages 10 and 137)

[33] Kevin Günthner, Imran Khan, Dominique Elser, Birgit Stiller, Omer Bayraktar, Christian R Müller, Karen Saucke, Daniel Tröndle, Frank Heine, Stefan Seel, Peter Greulich, Herwig Zech, Björn Gütlich, Ines Richter, Michael Lutzer, Sabine Philipp-May, Rolf Meyer, Christoph Marquardt, and Gerd Leuchs. Quantum-limited measurements of optical signals from a geostationary satellite. *Optica*, 4(6):611–616, 2017.
(Cited on page 10)

[34] Elizabeth Gibney. Chinese satellite is one giant step for the quantum internet. *Nature*, 535(7613):478–479, jul 2016.
(Cited on page 10)

[35] Juan Yin, Yuan Cao, Yu-Huai Li, Sheng-Kai Liao, Liang Zhang, Ji-Gang Ren, Wen-Qi Cai, Wei-Yue Liu, Bo Li, Hui Dai, Guang-Bing Li, Qi-Ming Lu, Yun-Hong Gong, Yu Xu, Shuang-Lin Li, Feng-Zhi Li, Ya-Yun Yin, Zi-Qing Jiang, Ming Li, Jian-Jun Jia, Ge Ren, Dong He, Yi-Lin Zhou, Xiao-Xiang Zhang, Na Wang, Xiang Chang, Zhen-Cai Zhu, Nai-Le Liu, Yu-Ao Chen, Chao-Yang Lu, Rong Shu, Cheng-Zhi Peng, Jian-Yu Wang, and Jian-Wei Pan. Satellite-based entanglement distribution over 1200 kilometers. *Science*, 356(6343):1140–1144, 2017.
(Cited on page 10)

[36] R. Ursin, F. Tiefenbacher, T. Schmitt-Manderbach, H. Weier, T. Scheidl, M. Lindenthal, B. Blauensteiner, T. Jennewein, J. Perdigues, P. Trojek, B. Ömer, M. Fürst, M. Meyenburg, J. Rarity, Z. Sodnik, C. Barbieri, H. Weinfurter, and A. Zeilinger. Entanglement-based quantum communication over 144km. *Nature*

*Physics*, 3(7):481–486, jun 2007.
(Cited on page 10)

[37] Ming-Fang Huang, Akihiro Tanaka, Ezra Ip, Yue-Kai Huang, Dayou Qian, Yequn Zhang, Shaoliang Zhang, Philip N. Ji, Ivan B. Djordjevic, Ting Wang, Yoshiaki Aono, Shuji Murakami, Tsutomu Tajima, Tiejun J. Xia, and Glenn A. Wellbrock. Terabit/s Nyquist Superchannels in High Capacity Fiber Field Trials Using DP-16QAM and DP-8QAM Modulation Formats. *Journal of Lightwave Technology*, 32(4):776–782, feb 2014.
(Cited on page 10)

[38] E Temprana, E Myslivets, B.P.-P. Kuo, L Liu, V Ataie, N Alic, and S Radic. Overcoming Kerr-induced capacity limit in optical fiber transmission. *Science*, 348(6242):1445–1448, jun 2015.
(Cited on page 10)

[39] T. Izawa, N. Shibata, and A. Takeda. Optical attenuation in pure and doped fused silica in the ir wavelength region. *Applied Physics Letters*, 31(1):33, aug 1977.
(Cited on page 10)

[40] V. Woollaston. Interactive map reveals the 550,000 mile-long network of underwater cables that carry world's web traffic. *Dailymail UK*, 2014.
(Cited on page 10)

[41] R.J. Mears, L. Reekie, I.M. Jauncey, and D.N. Payne. Low-noise erbium-doped fibre amplifier operating at 1.54 $\mu$m. *Electronics Letters*, 23(19):1026–1028, sep 1987.
(Cited on page 10)

[42] R.J. Mears, L. Reekie, S.B. Poole, and D.N. Payne. Low-threshold tunable CW and Q-switched fibre laser operating at 1.55 $\mu$m. *Electronics Letters*, 22(3):159, 1986.
(Cited on page 10)

[43] L. M. Duan, M. D. Lukin, J. I. Cirac, and P Zoller. Long-distance quantum communication with atomic ensembles and linear optics. *Nature*, 414(6862):413–8, 2001.
(Cited on page 11)

[44] N. Sangouard, C. Simon, H. de Riedmatten, and N. Gisin. Quantum repeaters based on atomic ensembles and linear optics. *Reviews of Modern Physics*, 83(1):33–80, mar

2011.
(Cited on page 11)

[45] Charles H. Bennett and Gilles Brassard. Quantum cryptography: Public key distribution and coin tossing. *International conference on Computers, Systems & Signal Processing*, 560:175–179, dec 1984.
(Cited on page 11)

[46] Sreraman Muralidharan, Linshu Li, Jungsang Kim, Norbert Lütkenhaus, Mikhail D. Lukin, and Liang Jiang. Optimal architectures for long distance quantum communication. *Scientific Reports*, 6(1):20463, apr 2016.
(Cited on page 12)

[47] Morgan P. Hedges, Jevon J. Longdell, Yongmin Li, and Matthew J. Sellars. Efficient quantum memory for light. *Nature*, 465(7301):1052–1056, jun 2010.
(Cited on pages 12, 14, 16, 17, 48, 57, 82, 87, and 137)

[48] Manjin Zhong, Morgan P Hedges, Rose L Ahlefeldt, John G Bartholomew, Sarah E Beavan, Sven M Wittig, Jevon J Longdell, and Matthew J Sellars. Optically addressable nuclear spins in a solid with a six-hour coherence time. *Nature*, 517(7533):177–180, 2015.
(Cited on pages 12, 102, 105, 107, and 137)

[49] Erhan Saglamyurek, Neil Sinclair, Jeongwan Jin, Joshua A. Slater, Daniel Oblak, Félix Bussières, Mathew George, Raimund Ricken, Wolfgang Sohler, and Wolfgang Tittel. Broadband waveguide quantum memory for entangled photons. *Nature*, 469(7331):512–515, jan 2011.
(Cited on pages 12, 13, 16, and 137)

[50] Erhan Saglamyurek, Jeongwan Jin, Varun B. Verma, Matthew D. Shaw, Francesco Marsili, Sae Woo Nam, Daniel Oblak, and Wolfgang Tittel. Quantum storage of entangled telecom-wavelength photons in an erbium-doped optical fibre. *Nature Photonics*, 9(2):83–87, 2015.
(Cited on pages 12, 15, 16, 48, and 137)

[51] Boris Albrecht, Pau Farrera, Xavier Fernandez-Gonzalvo, Matteo Cristiani, and Hugues de Riedmatten. A Waveguide Frequency Converter Connecting Rubidium Based Quantum Memories to the Telecom C-Band. *Nature Communications*, 5:3376,

2014.
(Cited on page 12)

[52] Y. O. Dudin, A. G. Radnaev, R. Zhao, J. Z. Blumoff, T. A B Kennedy, and A. Kuzmich. Entanglement of light-shift compensated atomic spin waves with telecom light. *Physical Review Letters*, 105(26):1–4, 2010.
(Cited on page 12)

[53] A. G. Radnaev, Y. O. Dudin, R. Zhao, H. H. Jen, S. D. Jenkins, A. Kuzmich, and T. A. B. Kennedy. A quantum memory with telecom-wavelength conversion. *Nature Physics*, 6(11):894–899, 2010.
(Cited on page 12)

[54] Nicolas Maring, Kutlu Kutluer, Joachim Cohen, Matteo Cristiani, Margherita Mazzera, Patrick M. Ledingham, and Hugues de Riedmatten. Storage of up-converted telecom photons in a doped crystal. *New Journal of Physics*, 16(113021), 2014.
(Cited on page 12)

[55] Pau Farrera, Nicolas Maring, Boris Albrecht, Georg Heinze, and Hugues de Riedmatten. Nonclassical correlations between a C-band telecom photon and a stored spin-wave. *Optica*, 3(9):1019, 2016.
(Cited on page 12)

[56] Paritosh Manurkar, Nitin Jain, Michael Silver, Yu-Ping Huang, Carsten Langrock, Martin M. Fejer, Prem Kumar, and Gregory S. Kanter. Multidimensional mode-separable frequency conversion for high-speed quantum communication. *Optica*, 3(12):1300, dec 2016.
(Cited on page 13)

[57] Félix Bussières, Christoph Clausen, Alexey Tiranov, Boris Korzh, Varun B. Verma, Sae Woo Nam, Francesco Marsili, Alban Ferrier, Philippe Goldner, Harald Herrmann, Christine Silberhorn, Wolfgang Sohler, Mikael Afzelius, and Nicolas Gisin. Quantum teleportation from a telecom-wavelength photon to a solid-state quantum memory. *Nature Photonics*, 8(10):775–778, sep 2014.
(Cited on pages 13, 16, 48, and 141)

[58] C. Clausen, F. Bussières, A. Tiranov, H. Herrmann, C. Silberhorn, W. Sohler, M. Afzelius, and N. Gisin. A source of polarization-entangled photon pairs interfacing quantum memories with telecom photons. *New Journal of Physics*, 16(9):093058, sep 2014.
(Cited on page 13)

[59] M. Razavi, M. Piani, and N. Lütkenhaus. Quantum repeaters with imperfect memories: Cost and scalability. *Physical Review A*, 80(3):032301, 2009.
(Cited on pages 13, 138, and 139)

[60] Masaaki Hirano. Manufacturable Ultra-Low Loss Pure-Silica-Core Fiber for Trans-Oceanic Telecommunication. In *Frontiers in Optics 2014*, page FTh1B.1, Washington, D.C., oct 2014. OSA.
(Cited on page 13)

[61] Kate R. Ferguson, Sarah E. Beavan, Jevon J. Longdell, and Matthew J. Sellars. Generation of Light with Multimode Time-Delayed Entanglement Using Storage in a Solid-State Spin-Wave Quantum Memory. *Physical Review Letters*, 117(2):020501, 2016.
(Cited on page 13)

[62] Sara Marzban, John G. Bartholomew, Stephen Madden, Khu Vu, and Matthew J. Sellars. Observation of Photon Echoes From Evanescently Coupled Rare-Earth Ions in a Planar Waveguide. *Physical Review Letters*, 115(1):013601, jul 2015.
(Cited on pages 14, 34, and 139)

[63] John. Bartholomew. *Investigation of the Scalability of Rare-earth Quantum Hardware*. PhD thesis, Australian National University, 2014.
(Cited on pages 14 and 20)

[64] S. J. Madden and K. T. Vu. Very low loss reactively ion etched Tellurium Dioxide planar rib waveguides for linear and non-linear optics. *Optics Express*, 17(20):17645, sep 2009.
(Cited on page 14)

[65] Bjorn Lauritzen, Jiri Minár, Hugues de Riedmatten, Mikael Afzelius, Nicolas Sangouard, Christoph Simon, and Nicolas Gisin. Telecommunication-Wavelength Solid-State Memory at the Single Photon Level. *Physical Review Letters*, 104(8):080502,

2010.
(Cited on page 14)

[66] Julián Dajczgewand, Jean-Louis Le Gouët, Anne Louchet-Chauvet, and Thierry Chanelière. Large efficiency at telecom wavelength for optical quantum memories. *Optics Letters*, 39(9):2711, 2014.
(Cited on page 15)

[67] R. M. Macfarlane, T. L. Harris, Y. Sun, R. L. Cone, and R. W. Equall. Measurement of photon echoes in $Er^{3+}$:$Y_2SiO_5$ at 1.5 $\mu$m with a diode laser and an amplifier. *Optics Letters*, 22(12):871, jun 1997.
(Cited on pages 15, 65, and 106)

[68] Darryl Scott. *All-Optical Real Time RF Signal Processing In Rare Earth Ion Doped Crystals*. PhD thesis, Australian National University, 2003.
(Cited on pages 15, 17, and 65)

[69] E. Baldit, K. Bencheikh, P. Monnier, S. Briaudeau, J. A. Levenson, V. Crozatier, I. Lorgeré, F. Bretenaker, J. L. Le Gouët, O. Guillot-Noël, and Ph. Goldner. Identification of Λ-like systems in $Er^{3+}$:$Y_2SiO_5$ and observation of electromagnetically induced transparency. *Physical Review B*, 81(14):144303, 2010.
(Cited on pages 15, 35, 48, 65, and 98)

[70] Paul G. Kwiat, Klaus Mattle, Harald Weinfurter, Anton Zeilinger, Alexander V. Sergienko, and Yanhua Shih. New High-Intensity Source of Polarization-Entangled Photon Pairs. *Physical Review Letters*, 75(24):4337–4341, dec 1995.
(Cited on page 16)

[71] P. C. Maurer, G. Kucsko, C. Latta, L. Jiang, N. Y. Yao, S. D. Bennett, F. Pastawski, D. Hunger, N. Chisholm, M. Markham, D. J. Twitchen, J. I. Cirac, and M. D. Lukin. Room-temperature quantum bit memory exceeding one second. *Science (New York, N.Y.)*, 336(6086):1283–6, jun 2012.
(Cited on page 16)

[72] M. Hosseini, B.M. Sparkes, G. Campbell, P.K. Lam, and B.C. Buchler. High efficiency coherent optical memory with warm rubidium vapour. *Nature communications*, 2:1175, feb 2011.
(Cited on pages 16 and 17)

[73] Duncan G. England, Kent A. G. Fisher, Jean-Philippe W. MacLean, Philip J. Bustard, Rune Lausten, Kevin J. Resch, and Benjamin J. Sussman. Storage and Retrieval of THz-Bandwidth Single Photons Using a Room-Temperature Diamond Quantum Memory. *Physical Review Letters*, 114(5):053602, feb 2015.
(Cited on page 17)

[74] P. S. Michelberger, T. F. M. Champion, M. R. Sprague, K. T. Kaczmarek, M. Barbieri, X. M. Jin, D. G. England, W. S. Kolthammer, D. J. Saunders, J. Nunn, and I. A. Walmsley. Interfacing GHz-bandwidth heralded single photons with a warm vapour Raman memory. *New Journal of Physics*, 17(4):043006, apr 2015.
(Cited on pages 17, 50, 82, and 87)

[75] Roger M. Macfarlane. High-resolution laser spectroscopy of rare-earth doped insulators: a personal perspective. *Journal of Luminescence*, 100(1-4):1–20, mar 2002.
(Cited on page 19)

[76] Thomas Böttger, C. W. Thiel, Y. Sun, and R. L. Cone. Optical decoherence and spectral diffusion at 1.5 $\mu$m in $Er^{3+}$:$Y_2SiO_5$ versus magnetic field, temperature, and $Er^{3+}$ concentration. *Physical Review B*, 73(7):075101, 2006.
(Cited on pages 20, 65, 106, and 107)

[77] R. D. Shannon and C. T. Prewitt. Effective ionic radii in oxides and fluorides. *Acta Crystallographica Section B Structural Crystallography and Crystal Chemistry*, 25(5):925–946, may 1969.
(Cited on page 21)

[78] Rose Ahlefeldt. *Evaluation of a stoichiometric rare earth crystal for quantum computing.* PhD thesis, Australian National University, 2013.
(Cited on pages 21 and 49)

[79] Mitchel Weissbluth. *Atoms and molecules.* Academic Press, New York, 1st edition.
(Cited on pages 22 and 25)

[80] Brian G Wybourne. *Spectroscopic Properties of Rare Earths.* John Wiley and Sons, New York, 1st edition, 1965.
(Cited on pages 22, 29, 31, and 32)

[81] G. Liu and B. Jacquier. Spectroscopic Properties of Rare Earths in Optical Materials.

2005.
(Cited on pages 22, 26, 27, 28, 29, 31, 50, and 129)

[82] Sebastian Horvath. *High-resolution spectroscopy and novel crystal-field methods for rare-earth based quantum information processing.* PhD thesis, University of Canterbury, 2016.
(Cited on pages 22, 28, 92, 130, 132, 133, 134, 140, 141, 142, and 145)

[83] W. T. Carnall, G. L. Goodman, K. Rajnak, and R. S. Rana. A systematic analysis of the spectra of the lanthanides doped into single crystal LaF3. *The Journal of Chemical Physics*, 90(7):3443–3457, apr 1989.
(Cited on pages 23, 30, and 145)

[84] Robert Withnall and Jack Silver. Physics of Light Emission from Rare-Earth Doped Phosphors. In *Handbook of Visual Display Technology*, pages 1019–1028. Springer Berlin Heidelberg, Berlin, Heidelberg, 2012.
(Cited on page 23)

[85] David Griffiths. *Introduction to Quantum Mechanics.* Prentice Hall, New York, 1st edition, 1995.
(Cited on page 24)

[86] C. Nielson and G. F. Koster. *Spectroscopic Coefficients for the $p^n, d^n$, and $f^n$ Configuration.* M.I.T press, Cambridge, MT, 1st edition, 1963.
(Cited on pages 28, 29, and 31)

[87] H. U. Rahman. Optical intensities of trivalent erbium in various host lattices. *Journal of Physics C: Solid State Physics*, 5(3):306–315, 1972.
(Cited on pages 28 and 30)

[88] R. E. Trees. Configuration Interaction in Mn II. *Physical Review*, 83(4):756–760, aug 1951.
(Cited on page 29)

[89] K. Rajnak and B. G. Wybourne. Configuration Interaction Effects in $l^N$ Configurations*. *Physical Review*, 132(1):280–290, oct 1963.
(Cited on page 29)

[90] J.E. Hansen, B. R. Judd, and H. Crosswhite. Matrix elements of scalar three-electron operators for the atomic f shell. *Atomic data and nuclear data tables*, 62(1):1–49, 1996.
(Cited on page 30)

[91] B. R. Judd. Optical Absorption Intensities of Rare-Earth Ions. *Physical Review*, 127(3):750–761, aug 1962.
(Cited on page 30)

[92] B. R. Judd. *Operator Techniques in Atomic Spectroscopy.* McGraw Hill, New York, 1st edition, 1963.
(Cited on page 32)

[93] A. M. Stoneham. Shapes of Inhomogeneously Broadened Resonance Lines in Solids. *Reviews of Modern Physics*, 41(1):82–108, jan 1969.
(Cited on page 34)

[94] D. L. Orth, R. J. Mashl, and J. L. Skinner. Optical lineshapes of impurities in crystals: a lattice model of inhomogeneous broadening by point defects. *Journal of Physics: Condensed Matter*, 5(16):2533–2544, apr 1993.
(Cited on page 34)

[95] R. Jaaniso, H. Hagemann, and H. Bill. Inhomogeneous broadening of optical spectra in mixed crystals: Basic model and its application to Sm <sup>2+</sup> in SrFCl <sub> x </sub> Br <sub> 1âĹŠ x </sub>. *The Journal of Chemical Physics*, 101(12):10323–10337, dec 1994.
(Cited on page 34)

[96] I. Waller. Uber die Magnetisierung von paramagnetischen Kristallen in Wechselfeldern. *Zeitschrift fur Physik*, 79(5-6):370–388, may 1932.
(Cited on page 39)

[97] A. Abragam and B. Bleaney. *Electron Paramagnetic Resonance of Transition Metal Ions.* Dover Publications, ch10, 2nd edition, 1970.
(Cited on pages 39 and 91)

[98] S. R. Hastings-Simon, B. Lauritzen, M. U. Staudt, J. L. M. van Mechelen, C. Simon, H. de Riedmatten, M. Afzelius, and N. Gisin. Zeeman-level lifetimes in $Er^{3+}$:$Y_2SiO_5$.

*Physical Review B*, 78(8):085410, 2008.
(Cited on pages 39, 93, and 98)

[99] J. H. Van Vleck. Paramagnetic Relaxation Times for Titanium and Chrome Alum. *Physical Review*, 57(5):426–447, mar 1940.
(Cited on page 39)

[100] C. B. P. Finn, R. Orbach, and W. P. Wolf. Spin-Lattice Relaxation in Cerium Magnesium Nitrate at Liquid Helium Temperature: A New Process. *Proceedings of the Physical Society*, 77(2):261–268, feb 1961.
(Cited on pages 39 and 40)

[101] G Davies. The optical properties of luminescence centres in silicon. *Physics Reports*, 176:83–188, 1989.
(Cited on page 43)

[102] C. Delerue and M. Lannoo. Description of the trends for rare-earth impurities in semiconductors. *Physical Review Letters*, 67(21):3006–3009, nov 1991.
(Cited on page 43)

[103] Jun Wan, Ye Ling, Qiang Sun, and Xun Wang. Role of codopant oxygen in erbium-doped silicon. *Physical Review B*, 58(16):10415–10420, oct 1998.
(Cited on page 43)

[104] J D Carey. Structure of multi-oxygen-related defects in erbium-implanted silicon. *Journal of Physics: Condensed Matter*, 14(36):8537–8547, sep 2002.
(Cited on pages 43 and 44)

[105] I N Yassievich and L C Kimerling. The mechanisms of electronic excitation of rare earth impurities in semiconductors. *Semiconductor Science and Technology*, 8(5):718–727, may 1993.
(Cited on page 43)

[106] F Priolo, G Franzi, Dipartimento Fisica, Universita Catania, and Corso Italia. The erbium-impurity-interaction of Er3 + In crystalline silicon. *Journal of Applied Physics*, 78(6):3874–3882, 1995.
(Cited on page 44)

[107] Forcales Fernandez. *Two-Colour Spectroscopy of Energy Transfers in Er:Si.* PhD thesis, Univeristy of Amsterdam, 2004.
(Cited on pages 44 and 123)

[108] William Happer. Optical Pumping. *Reviews of Modern Physics*, 44(2):169–249, apr 1972.
(Cited on page 50)

[109] M. N. Popova. Investigations of hyperfine and isotope structures in optical spectra of crystals with rare-earth ions. *Optics and Spectroscopy*, 119(4):544–550, oct 2015.
(Cited on page 51)

[110] R. M. Macfarlane, R. S. Meltzer, and B. Z. Malkin. Optical measurement of the isotope shifts and hyperfine and superhyperfine interactions of Nd in the solid state. *Physical Review B*, 58(9):5692–5700, sep 1998.
(Cited on pages 51 and 70)

[111] R. M. Macfarlane, A. Cassanho, and R. S. Meltzer. Inhomogeneous broadening by nuclear spin fields: A new limit for optical transitions in solids. *Physical Review Letters*, 69(3):542–545, jul 1992.
(Cited on pages 51 and 84)

[112] G. C. Bjorklund, M. D. Levenson, W. Lenth, and C. Ortiz. Frequency modulation (FM) spectroscopy. *Applied Physics B Photophysics and Laser Chemistry*, 32(3):145–152, nov 1983.
(Cited on page 51)

[113] OEMarket. 10GHz Bandwidth PIN Photodetector, 2017.
(Cited on page 51)

[114] OEQuest. 10GHz Bandwidth Electro Optic Modulator with DC bias. *https://www.oequest.com/getproduct/20591/cat/1164/page/1.*
(Cited on page 51)

[115] E. L. Hahn. Spin Echoes. *Physical Review*, 80(4):580–594, nov 1950.
(Cited on page 58)

[116] N. A. Kurnit, I. D. Abella, and S. R. Hartmann. Observation of a Photon Echo. *Physical Review Letters*, 13(19):567–568, nov 1964.

(Cited on page 58)

[117] I. D. Abella, N. A. Kurnit, and S. R. Hartmann. Photon Echoes. *Physical Review*, 141(1):391–406, jan 1966.
(Cited on page 59)

[118] S. Hartmann. Photon, spin, and Raman echoes. *IEEE Journal of Quantum Electronics*, 4(11):802–807, 1968.
(Cited on pages 59, 100, and 102)

[119] M. A. Kastner. The single-electron transistor. *Reviews of Modern Physics*, 64(3):849–858, jul 1992.
(Cited on pages 59 and 62)

[120] L. L. Chang, L. Esaki, and R. Tsu. Resonant tunneling in semiconductor double barriers. *Applied Physics Letters*, 24(12):593–595, 1974.
(Cited on page 60)

[121] D. Schwen and F. Bianco. Single electron transistor schematic and Coulomb blockade effect https://en.wikipedia.org/wiki/Coulomb_blockade, 2006.
(Cited on page 61)

[122] S. Lindemann, T. Ihn, S. Bieri, T. Heinzel, K. Ensslin, G. Hackenbroich, K. Maranowski, and A. C. Gossard. Bouncing states in quantum dots. *Physical Review B*, 66(16):161312, oct 2002.
(Cited on page 62)

[123] L. P. Kouwenhoven, C. M. Marcus, P. L. Mceuen, S. Tarucha, R. M. Westervelt, and N. S. Wingreen. Electron transport in quantum dots. *Proceedings of the Advanced Study Institute on Mesoscopic Electron Transport*, pages 105–214, 1997.
(Cited on page 61)

[124] G. P. Lansbergen, R. Rahman, C. J. Wellard, I. Woo, J. Caro, N. Collaert, S. Biesemans, G. Klimeck, L. C. L. Hollenberg, and S. Rogge. Gate-induced quantum-confinement transition of a single dopant atom in a silicon FinFET. *Nature Physics*, 4(8):656–661, aug 2008.
(Cited on pages 62, 64, and 111)

[125] Hubert C George. *Studies of visible light illumination and substrate material effects on aluminium SET's.* PhD thesis, University of Notre Dame, 2011.
(Cited on pages 63, 111, 115, and 119)

[126] O. Guillot-Noël, H. Vezin, Ph. Goldner, F. Beaudoux, J. Vincent, J. Lejay, and I. Lorgeré. Direct observation of rare-earth-host interactions in $Er^{3+}$:$Y_2SiO_5$. *Physical Review B*, 76(18):180408, nov 2007.
(Cited on pages 65 and 106)

[127] O. Guillot-Noël, Ph. Goldner, Y. Le Du, E. Baldit, P. Monnier, and K. Bencheikh. Hyperfine interaction of $Er^{3+}$ ions in $Y_2SiO_5$: An electron paramagnetic resonance spectroscopy study. *Physical Review B*, 74(21):214409, 2006.
(Cited on pages 66, 68, and 79)

[128] Thomas Böttger. *Laser frequency stabilization to spectral hole burning frequency references in erbium-doped crystals : material and device optimization.* PhD thesis, Montana State University, 2002.
(Cited on pages 66 and 115)

[129] Thomas Böttger, Y. Sun, C. W. Thiel, and R. L. Cone. Spectroscopy and dynamics of $Er^{3+}$:$Y_2SiO_5$ at 1.5 $\mu$m. *Physical Review B*, 74(7):75107, aug 2006.
(Cited on pages 68, 71, and 83)

[130] K. I. Gerasimov, M. M. Minnegaliev, B. Z. Malkin, E. I. Baibekov, and S. A. Moiseev. High-resolution magneto-optical spectroscopy of $^{7}LiYF_4$ : $^{167}Er^{3+}$, $^{166}Er^{3+}$ and analysis of hyperfine structure of ultranarrow optical transitions. *Physical Review B*, 94(5):54429, aug 2016.
(Cited on pages 68 and 70)

[131] Yu-Hui Chen, Xavier Fernandez-Gonzalvo, Sebastian P. Horvath, Jelena V. Rakonjac, and Jevon J. Longdell. Hyperfine interactions of $Er^{3+}$ ions in $Y2SiO5$: electron paramagnetic resonance in a tunable microwave cavity. *arXiv*, oct 2017.
(Cited on page 79)

[132] J. Pelzl, S. Hüfner, and S. Scheller. Hyperfine structure in holmium ethylsulfate and holmium trichloride. *Zeitschrift für Physik A Hadrons and nuclei*, 231(4):377–396, aug 1970.
(Cited on page 87)

[133] Hugues de Riedmatten, Mikael Afzelius, Matthias U. Staudt, Christoph Simon, and Nicolas Gisin. A solid-state light-matter interface at the single-photon level. *Nature*, 456(7223):773–777, 2008.
(Cited on page 87)

[134] I.N. Kurkin and K.P. Chernov. EPR and spin-lattice relaxation of rare-earth activated centres in $Y_2SiO_5$ single crystals. *Physica B+C*, 101(2):233–238, 1980.
(Cited on pages 88, 91, and 93)

[135] J. H. Van Vleck. Paramagnetic Relaxation and the Equilibrium of Lattice Oscillators. *Physical Review*, 59(9):724–729, may 1941.
(Cited on page 93)

[136] B.W. Faughnan and M.W.P. Strandberg. The role of phonons in paramagnetic relaxation. *Journal of Physics and Chemistry of Solids*, 19(1-2):155–166, apr 1961.
(Cited on page 93)

[137] Albert Einstein. On the Motion of Small Particles Suspended in a Stationary Liquid, as Required by the Molecular Kinetic Theory of Heat. *Annalen der Physik*, 322:549–560, 1905.
(Cited on page 95)

[138] J. J. Longdell, E. Fraval, M. J. Sellars, and N. B. Manson. Stopped Light with Storage Times Greater than One Second Using Electromagnetically Induced Transparency in a Solid. *Physical Review Letters*, 95(6):063601, 2005.
(Cited on pages 102 and 105)

[139] R. M. Macfarlane, R. Wannemacher, D. Boye, Y. P. Wang, and R. S. Meltzer. Non-exponential photon echo decay of Er3+ in fluorides. *Journal of Luminescence*, 48-49:313–317, 1991.
(Cited on page 104)

[140] E. Fraval, M. J. Sellars, and J. J. Longdell. Method of Extending Hyperfine Coherence Times in $Pr:Y_2SiO_5$. *Physical Review Letters*, 92(7):077601, feb 2004.
(Cited on pages 107 and 140)

[141] R. M. Shelby, C. S. Yannoni, and R. M. Macfarlane. Optically Detected Coherent Transients in Nuclear Hyperfine Levels. *Physical Review Letters*, 41(25):1739–1742,

dec 1978.
(Cited on page 107)

[142] Elliot Fraval. *Minimising the Decoherence of Rare Earth Ion Solid State Spin Qubits*. Phd thesis, Australian National University, 2005.
(Cited on page 107)

[143] W. Moerner and L. Kador. Optical detection and spectroscopy of single molecules in a solid. *Physical Review Letters*, 62(21):2535–2538, 1989.
(Cited on page 110)

[144] Lachlan J. Rogers, Kay D. Jahnke, Mathias H. Metsch, Alp Sipahigil, Jan M. Binder, Tokuyuki Teraji, Hitoshi Sumiya, Junichi Isoya, Mikhail D. Lukin, Philip Hemmer, and Fedor Jelezko. All-Optical Initialization, Readout, and Coherent Preparation of Single Silicon-Vacancy Spins in Diamond. *Physical Review Letters*, 113(26):263602, dec 2014.
(Cited on page 110)

[145] Darin J. Sleiter, Kaoru Sanaka, Y. M. Kim, Klaus Lischka, Alexander Pawlis, and Yoshihisa Yamamoto. Optical Pumping of a Single Electron Spin Bound to a Fluorine Donor in a ZnSe Nanostructure. *Nano Letters*, 13(1):116–120, jan 2013.
(Cited on page 110)

[146] R. Kolesov, K. Xia, R. Reuter, R. Stöhr, A. Zappe, J. Meijer, P.R. Hemmer, and J. Wrachtrup. Optical detection of a single rare-earth ion in a crystal. *Nature Communications*, 3(May):1029, 2012.
(Cited on page 110)

[147] G. Franzò, F. Priolo, S. Coffa, A. Polman, and A. Carnera. Room temperature electroluminescence from Er doped crystalline Si. *Applied Physics Letters*, 64(17):2235–2237, apr 1994.
(Cited on page 111)

[148] Raymond Schouten. QTRay IVVI rackmount designs and specifications http://qt.tn.tudelft.nl/∼schouten/ivvi/index-ivvi.htm, 2017.
(Cited on pages 112 and 113)

[149] H. Przybylinska, G. Hendorfer, M. Bruckner, L. Palmetshofer, and W. Jantsch. On the local structure of optically active Er centers in Si. *Applied Physics Letters*,

490(1995):490, 1995.
(Cited on page 115)

[150] C. A. J. Ammerlaan, D. T. X. Thao, and T. Gregorkiewicz. Photoluminescence of erbium-doped silicon: Excitation power dependence. *Journal of Applied Physics*, 88(3):1443–1455, 2000.
(Cited on page 115)

[151] M. V. Stepikhova, B. A. Andreev, V. B. Shmagin, Z. F. Krasil'nik, V. P. Kuznetsov, V. G. Shengurov, S. P. Svetlov, W. Jantsch, L. Palmetshofer, and H. Ellmer. Properties of optically active Si:Er and $Si_{1-x}Ge_x$ layers grown by the sublimation MBE method. *Thin Solid Films*, 381:164–169, 2001.
(Cited on page 115)

[152] N. Q. Vinh, H. Przybylińska, Z. F. Krasil'nik, and T. Gregorkiewicz. Microscopic structure of Er-related optically active centers in crystalline silicon. *Physical review letters*, 90(6):066401, 2003.
(Cited on page 115)

[153] Gabriele de Boo. *Optically Addressing Individual Dopants in Silicon.* Phd thesis, University of New South Wales, 2017.
(Cited on pages 125 and 134)

[154] J.F. Gibbons. Ion implantation in semiconductors - Part II: Damage production and annealing. *Proceedings of the IEEE*, 60(9):1062–1096, 1972.
(Cited on page 125)

[155] B. J. Villis, A. O. Orlov, S. Barraud, M. Vinet, M. Sanquer, P. Fay, G. Snider, and X. Jehl. Direct detection of a transport-blocking trap in a nanoscaled silicon single-electron transistor by radio-frequency reflectometry. *Applied Physics Letters*, 104:233503, 2014.
(Cited on page 134)

[156] N. Sangouard, Christoph Simon, Hugues de Riedmatten, and Nicolas Gisin. Quantum repeaters based on atomic ensembles and linear optics. *Review of Modern Physics*, 83(1):33–34, mar 2011.
(Cited on page 138)

[157] C. Langer, R. Ozeri, J. Jost, J. Chiaverini, B. DeMarco, A. Ben-Kish, R. Blakestad, J. Britton, D. Hume, W. Itano, D. Leibfried, R. Reichle, T. Rosenband, T. Schaetz, P. Schmidt, and D. Wineland. Long-Lived Qubit Memory Using Atomic Ions. *Physical Review Letters*, 95(6):060502, aug 2005.
(Cited on page 140)

[158] J. J. Longdell, A. L. Alexander, and M. J. Sellars. Characterization of the hyperfine interaction in europium-doped yttrium orthosilicate and europium chloride hexahydrate. *Physical Review B*, 74(19):195101, nov 2006.
(Cited on page 140)

[159] D. L. McAuslan, J. G. Bartholomew, M. J. Sellars, and J. J. Longdell. Reducing decoherence in optical and spin transitions in rare-earth-metal-ion-doped materials. *Physical Review A*, 85(3):032339, 2012.
(Cited on page 140)

[160] Marko Lovrić, Philipp Glasenapp, Dieter Suter, Biagio Tumino, Alban Ferrier, Philippe Goldner, Mahmood Sabooni, Lars Rippe, and Stefan Kröll. Hyperfine characterization and spin coherence lifetime extension in $Pr^{3+}$:$La_2(WO_4)_3$. *Physical Review B*, 84(10):104417, sep 2011.
(Cited on page 140)

[161] Yeghishe Tsaturyan, Andreas Barg, Anders Simonsen, Luis Guillermo Villanueva, Silvan Schmid, Albert Schliesser, and Eugene S Polzik. Demonstration of suppressed phonon tunneling losses in phononic bandgap shielded membrane resonators for high-Q optomechanics. *Optics express*, 22(6):6810–21, 2014.
(Cited on page 141)

[162] Gary Wolfowicz, Hannes Maier-Flaig, Robert Marino, Alban Ferrier, Hervé Vezin, John J. L. Morton, and Philippe Goldner. Coherent Storage of Microwave Excitations in Rare-Earth Nuclear Spins. *Physical Review Letters*, 114(17):170503, apr 2015.
(Cited on pages 141 and 142)

[163] R Beach, M D Shinn, L Davis, R W Solarz, and W F Krupke. Optical absorption and stimulated emission of neodymium in yttriumorthosilicate. *IEEE J. Quantum*

*Electron*, 26(August):1405–1412, 1990.
(Cited on page 142)

[164] Bin-Bin Xu, Alvaro C. Bedoya, Milos Rancic, Chunming Yin, Gabriele de Boo, Blair Morrison, Brett C. Johnson, Jeffrey C. Mcallum, Benjamin J. Eggleton, Matthew J. Sellars, and Sven Rogge. High Q phosphorus doped optical cavity for qubit devices. *Manuscript in Preparation*.
(Cited on page 142)

[165] Qi Zhang, Chunming Yin, Guangchong Hu, Gabriele de Boo, Milos Rancic, Brett C Johnson, Jeffrey C McCallum, Jiangfeng Du, Matthew J Sellars, and Sven Rogge. Single rare-earth ions as a probe of electric fields and strain in nano-transistors. *Manuscript in Preparation*.
(Cited on page 142)

[166] Gary Wolfowicz, Alexei M. Tyryshkin, Richard E. George, Helge Riemann, Nikolai V. Abrosimov, Peter Becker, Hans-Joachim Pohl, Mike L. W. Thewalt, Stephen A. Lyon, and John J. L. Morton. Atomic clock transitions in silicon-based spin qubits. *Nature Nanotechnology*, 8(8):561–564, aug 2013.
(Cited on page 142)

[167] Stefan van der Walt, S Chris Colbert, and Gael Varoquaux. The NumPy Array: A Structure for Efficient Numerical Computation. *Computing in Science and Engineering*, 13(2):22–30, mar 2011.
(Cited on page 145)

[168] Stefan Behnel, Robert Bradshaw, Craig Citro, Lisandro Dalcin, Dag Sverre Seljebotn, and Kurt Smith. Cython: The Best of Both Worlds. *Computing in Science and Engineering*, 13(2):31–39, mar 2011.
(Cited on page 145)

[169] E. Anderson, Z. Bai, C. Bischof, S. Blackford, J. Demmel, J. Dongarra, J. Du Croz, A. Greenbaum, S. Hammarling, A. McKenney, and D. Sorensen. *LAPACK Users Guide*. Society for Industrial and Applied Mathematics, Philadelphia, PA, 3rd edition, 1999.
(Cited on page 145)

[170] S. G. Johnson. The NLopt nonlinear-optimization package, 2017.
(Cited on page 145)

[171] David J. Wales and Jonathan P. K. Doye. Global Optimization by Basin-Hopping and the Lowest Energy Structures of Lennard-Jones Clusters Containing up to 110 Atoms. *J. Phys. Chem. A*, 101(28):5111–5116, 1997.
(Cited on page 146)

[172] Nicholas Metropolis, Arianna W. Rosenbluth, Marshall N. Rosenbluth, Augusta H. Teller, and Edward Teller. Equation of State Calculations by Fast Computing Machines. *The Journal of Chemical Physics*, 21(6):1087–1092, jun 1953.
(Cited on page 146)